Acoustic streaming around a sharp edge : fundamentals and mixing applications

Chuanyu Zhang

Université de Paris

Thèse de doctorat

de l'Université de Paris

École doctorale [nº 564 : Physique en Île-de-France]

Laboratoire Interdisciplinaire des Energies de Demain/Matière Système Complexe

Acoustic streaming around a sharp edge: fundamentals and mixing applications

Par Chuanyu ZHANG

Thèse de doctorat de Physique

Dirigée par Philippe Brunet et Laurent Royon

présentée et soutenue publiquement à Paris le 30 Septembre 2020

Rapporteure,	Mme Aubin, Joelle/Chargée de recherche au CNRS/Université de Toulouse
Rapporteur,	M Thibault, Pierre/Professeur/Université Grenoble Alpes
Examinateur,	M Gallaire, François/Professeur/École Polytechnique Fédérale de Lausanne
Examinateur,	M Limat, Laurent/Directeur de recherche au CNRS/Université de Paris
Directeur de thèse,	M Royon, Laurent/Professeur/Université de Paris
Co-Directeur de thèse,	M Brunet, Philippe/Chargé de recherche au CNRS/Université de Paris
Encadrant,	M Guo, Xiaofeng/Maître de Conférences/Université Gustave Eiffel - ESIEE Paris

Abstract

Abstract

This thesis presents studies of acoustic streaming in the vicinity of sharp structures in microchannels. Sharp Edge Acoustic Streaming (SEAS) is a steady flow induced by the coupling of low-frequency acoustic wave and fluid around sharp edge. The four-paper thesis includes experimental and numerical investigation on influence of the geometrical features, viscosity and frequency on SEAS intensity and pattern, the interaction of SEAS with the throughput in the microchannel and its application in the mixing process. This research is motivated by the fact that the mechanism of the very strong streaming phenomenon with audible or lower acoustic is still not clear and its promising application in process intensification. Besides developing a Direct Numerical Simulation scheme for the fundamental study, some practical information on how to obtain strong streaming by optimal design sharp-edge geometries and operating condition adjustments are provided.

Keywords: *Acoustofluidics, Sharp Edge Acoustic Streaming, Microchannel, Mixing enhancement*

Résumé

Le streaming acoustique peut être généré par un champ acoustique autour d'une singularité géométrique. Ce streaming à effet géométrique est quantitativement plus intense que le classique streaming de Rayleigh à énergie injectée égale et peut être généré à basse fréquence. Cette thèse, à travers ces quatre articles, étudie différents aspects de ce phénomène en allant d'interprétation fondamentale de son origine jusqu'à son application pour intensifier le mélange liquide-liquide grâce à l'écoulement induit par champs acoustique. Des approches numériques et expérimentales sont déployées pour résoudre ce phénomène multi-physique et en fournir les conditions optimales en termes de géométrie, de viscosité du fluide, des conditions d'écoulement et acoustiques.

Mots Clés: *Acoustofluidiques, Streaming Acoustique, Singularité, Micro-canal, Intensification du mélange*

Preamble

The main text of this thesis serves to give an introduction to the theory background and corresponding methodology (Chapter 2) utilized in four journal papers attached in Appendices, which constitute this thesis work. Chapter 3 summarized the main results in a brief way, followed by a general conclusion and perspectives in Chapter 4.

The sharp-edge acoustic streaming is quantitatively investigated via the direct resolution of the full Navier-Stokes equation, using Finite Element Method. The influence of viscous boundary layer δ , curvature radius r_c and viscosity ν on the acoustic streaming performance are quantified. Our results suggest choices of operating conditions and geometrical parameters, via dimensionless quantities r_c/δ and δ/w and provide guidelines on how to obtain strong, optimal sharp-edge acoustic streaming. These issues have been discussed in Appendix A and Appendix C.

Further, several experiments have been conducted. Vibration velocities are characterized by directly visualizing the displacement of tracing particles and the generated acoustic streaming is observed using particle image velocimetry. With a microchannel patterned with a single sharp edge, by measuring the concentration of a fluorescence dye, we evaluate the mixing performance for different values of tip angle, vibration amplitude, and flow rate. The sharper the edge tip is, the larger the vortices size and the spatial extent of the induced streaming are. The Mixing index, jumps from 0.73 (without acoustic excitation) to 0.38 (with acoustic excitation), resulting in a highly mixed homogeneous fluid just after the sharp edge. Then experiments are done to quantify this streaming flow through the influence of liquid viscosity ν, from 1 mm^2/s to 30 mm^2/s, and acoustic frequency from 500 Hz to 3500 Hz. Both quantities supposedly influence the thickness of the viscous boundary layer $\delta = (\nu/\pi f)^{1/2}$. Globally, the streaming velocity is dramatically weakened by a higher viscosity, whereas the flow pattern and the disturbance distance remain similar regardless of viscosity. Besides viscosity, the frequency also strongly influences the maximal streaming velocity. Details of the above results can be found in Appendix B.

Finally, three Sharp-Edge Acoustic Streaming (SEAS) micromixers with multiple sharp edge patterns are investigated as in Appendix D. Simulation with direct numerical simulation (DNS) and experiments through dye visualizations as well as Iodide-Iodate Reactions are carried out to unveil the interaction between acoustic streaming and main flow, and to evaluate micromixing performances. Following this, an optimal structure is found among the three mixers which allows achieving a decrease of micromixing time from 0.3 s to 0.04 s. A comparison with literature on passive mixers confirms the equivalent micromixing performance of SEAS mixer in terms of energy dissipation rate.

Acknowledgement

This thesis is submitted for obtaining the degree of Doctor of Philosophy (PhD) at the Université de Paris. The research was carried out at the Le Laboratoire Interdisciplinaire des Energies de Demain (LIED,UMR 8236) and Laboratoire Matière et Systèmes Complexes (MSC,7057) during three years from September 2017 to August 2020. This study was supervised by Dr.Philippe Brunet (Researcher, CNRS), Dr. Xiaofeng GUO (Associate professor, ESIEE Paris) and Prof. Laurent Royon (Professor, Université de Paris). The PhD project was financed by the Chinese Scholarship Council(CSC).

First and foremost I wish to thank my advisors: Philippe, Xiaofeng and Laurent, for their support, patience, encouragement and immense knowledge. Their guidance helped me in all the time of research, writing of this thesis and my life. Many thanks to Xiaofeng who provided the opportunity for me to start this interesting research, who was always patient and spent a lot of time on discussing with me and who helped me a lot in my life in France. Big thanks to Philippe who is so nice and always shared the insightful ideas with me and gave the great guidance to my research. Great thanks to Laurent who gave me the warm smile every time I met him and tried to give me the support in every aspect of my study and life.

Dozens of people have helped and taught me and I would like to thank the great people in the labs: Remy is so funny guy who brought a lot smiles to the lab and helped me a lot when I came to the lab. Many thanks to Grabriel, Ania and Mathieu, they are so great friends. We together have had so many wonderful lunches and dinners. I never forget the interesting time we spent on Denmark. Great thanks to Prof. Eric Falcon, he gave me a lot of support to measure the vibration of my chip. Many thanks to Martin, who helped me order the computer and organised so many wonderful activities of the Lab. I am also very grateful to my friends, Bo WANG, Xuan Chen, Bin NI, Tao ZHU etc for their support in my life.

I also thank an organization: Chinese Scholarship Council(CSC). I greatly appreciate their supports and their insistence on encouraging more academic communications between China and France.

I would also like to say a heartfelt thank you to my Mum, Dad for helping in whatever way they could during this challenging period.

And finally to my dear Dan, who has been by my side throughout this PhD, living every single minute of it, and without whom, I would not have had the courage to embark on this journey and write this thesis.

Contents

Abstract I

Preamble II

Acknowledgement IV

Contents VII

1 Introduction 1
- 1.1 Acoustic Streaming: basics and theory . . . 2
- 1.2 Micro- and mini-fluidics . . . 12
- 1.3 Question to answer in this thesis . . . 18
- 1.4 References . . . 20

2 Methodology 25
- 2.1 Experimental characterization . . . 26
- 2.2 Numerical investigation . . . 36
- 2.3 References . . . 42

3 Results and Discussions 45
- 3.1 Unveiling the mechanism of SEAS phenomenon by DNS . . . 46
- 3.2 Hydrodynamic interpretation by direct visualization . . . 49
- 3.3 Coupling Influence of Frequency and Viscosity on SEAS . . . 51
- 3.4 SEAS and mixing enhancement in microchannel with multiple sharp edges . . . 53
- 3.5 References . . . 56

4 Conclusions and Perspectives 57
- 4.1 Conclusions . . . 58
- 4.2 Perspectives . . . 59
- 4.3 References . . . 60

A Paper under revision with Physics Review E 61

B Paper appeared in Microfluidics and Nanofluidics 97

C Paper appeared in Micromachines 113

D Paper under review in Chemical Engineering Journal 129

Chapter 1

Introduction

1.1 Acoustic Streaming: basics and theory

1.1.1 A brief classification of acoustofluidic studies

The perception and interpretation of sound by humans, as a type of entertainment, started from the music, as early as the ancient Greek time GEISSLER et HUNT [1980]. Then, since the 18^{th} century, the understanding of sound and acoustics as a scientific endeavor has been rapidly developed FRIEND et YEO [2011]; RAYLEIGH [2013], during which many phenomenons were recorded and studied. Related to an ancient phenomenon, Chinese spouting bowl, water spouts out from the resonant vibration bowl, shown in Fig.1.1(a), was studied by John Tyndall SCHUFLE [1981]. Instabilities of fluid free surface, fluid jet and mechanism of human hearing, acoustic streaming were studied by RAYLEIGH [1945]. Studies of resonant acoustic cavities and the observation of quartz wind and surface wave were achieved by FARADAY [1831] and HELMHOLTZ [2009] respectively. In more recent times, various phenomenons were also observed and studied, such as the resonant vibration field in Kundt's tube and as shown in Fig.1.1(b), the complex motion and deformations of sessile droplets on a substrate where surface acoustic wave are induced.

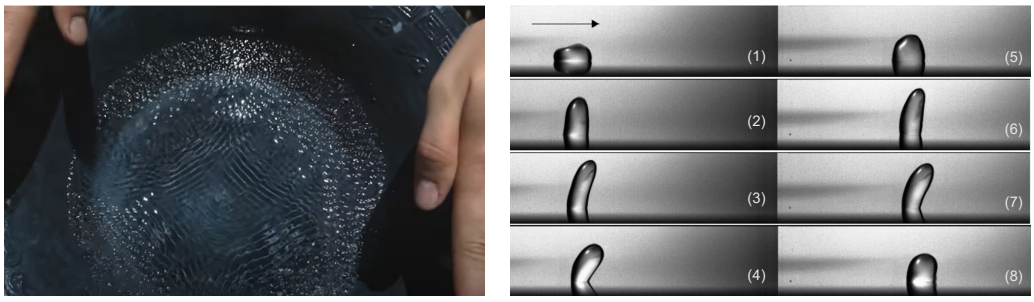

Figure 1.1 – Examples of interactions between acoustic waves and a fluid (a) vibration waves formed in a resonant bowl filmed by FREE et GRUCHY [2017]; (b) successive snapshots of a water drop displaced by surface acoustic wave, showing a periodic creeping and jumping motion BRUNET et collab. [2010]; RENAUDIN et collab. [2007].

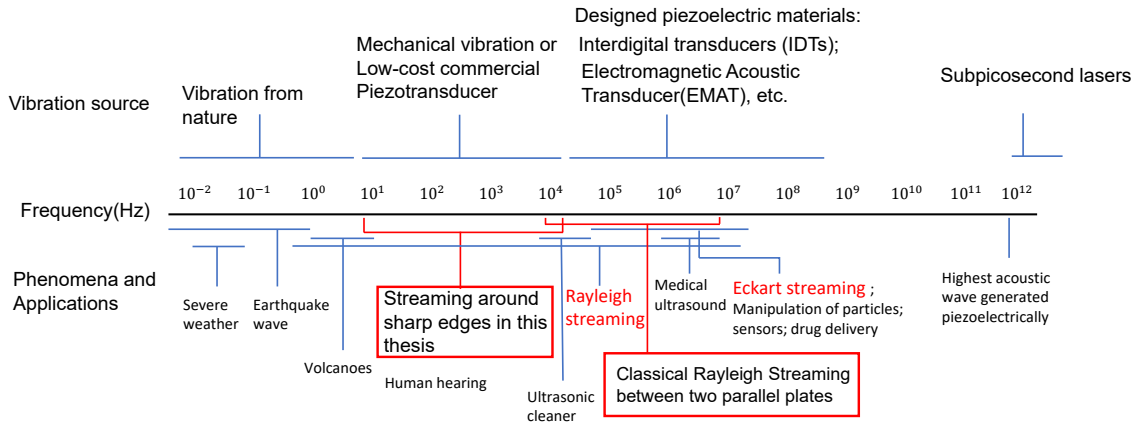

Figure 1.2 – Spectrum of acoustics from different sources and their applications. Acoustic streaming is roughly divided into classical Rayleigh streaming and sharp-edge streaming (in red box), the latter being the main subject of the thesis.

So far, the frequency range of acoustics applied in scientific research spans 15 orders of magnitude, as shown in Fig.1.2. Most geophysical phenomena appear in the infrasound range below the limit of human hearing ($< 20\mathrm{H}z$), like the earthquakes waves and the low-frequency acoustic emission by volcanoes. In Fig.1.2, the frequencies of which the most current prominent man-made applications of acoustics for measurement and manipulations of fluids, reside in the ultrasonic range (above 20 kHz), specifically in the range between 20 kHz to 10 MHz; these applications involve different types of mixing enhancement, particle manipulation, pumping, sensors, imaging, and medical surgery [MITRAGOTRI [2005]], as shown in Fig.1.2. One obvious feature shown in Fig.1.2 is that fewer previous studies were based on the audible frequency range. However, recently, more and more pioneering studies take advantage of acoustics and vibration fields with low-frequency at human hearing range. For example, low-frequency fluid oscillation (range 5Hz ~ 200Hz) could accelerate the fluid mixing in microplate well as well as in microchannel GLASGOW et AUBRY [2003]; OBERTI et collab. [2009]; PETKOVIC-DURAN et collab. [2009]. WHITEHILL et collab. [2011] demonstrated the droplet spreading on the vibrating surface at 200Hz and particle focusing in a channel at 1 kHz VAINSHTEIN et SHAPIRO [2008]; interesting phenomenons were observed by BRUNET et collab. [2007], where droplet moved against gravity on a vertically vibrating inclined plate at 30 ~ 200 Hz; in LANGELIER et collab. [2009]'s study, the specific cavities were designed to absorb the outside vibration and then the audible music as a vibration source was introduced into the microchannel. Although it is difficult to control the vibration field from low-frequency source because of its long wavelength, a significant advantage of low frequency actuation is the simple instrumentation needed, which is in keeping with the recent trend to develop low cost microfluidic "lab-on-a-chip" systems for various applications WHITEHILL et collab. [2011].

1.1.2 Acoustic streaming phenomenon

The studies of streaming phenomenon started with several observations. FARADAY [1831] and Savart BOLURIAAN et MORRIS [2003] observed streaming shown by fine powders, appeared in air adjacent to a vibration surface of a plate. The trajectory of the particles began from the nodal point toward to anti-nodal site then outward and moved back to the nodal line. DVOŘÁK [1874] also observed similar flow circulation while following the opposite direction. The theory behind such phenomena was not built up until Lord Rayleigh, who first came up with the adequate theoretical model to analyze the acoustic streaming phenomena. He utilized a perturbation method to successively solve first-order equations as a linear problem, then worked out the second-order ones with the forcing term from the first-order solution. Since then, such approach has become the dominant analytical tool for the studies of acoustic streaming. Progresses have been continuously made in this area until today: much work has been done on the topic of streaming flow involving analytical and numerical models, experimental studies and, more recently, the applications of acoustic streaming to existing problems within microfluidics, which will be presented in the next section. Hermann Schlichting, after which the 'Schlichting streaming' was named, first modelled the inner streaming within the stoke boundary layer SCHLICHTING [1932]. NYBORG [1958] developed an approximate solution for the steady streaming flow near any portion of fluid-solid interface. LIGHTHILL [1978] derived Navier-Stokes equations describing the streaming flow as a time-averaged momentum flux in the fluid, caused by a spatial gradient in the oscillatory Reynolds stress. Other researchers like in Henrik Bruus's group, extended the fundamental treatment of the governing equations and solved the equations for various open and closed geometries MULLER et BRUUS [2015].

Qualitatively, the streaming flow comes from the dissipation of acoustic vibrations within the fluid. When the acoustic wave propagates through a fluid medium, the velocity and pressure of the volume elements are described by oscillating terms. With an ideal condition where viscous attenuation is null, the time-average displacement of any volume element is zero everywhere. However, in a real fluid, viscous dissipation combined with nonlinear inertial terms leads to a time-averaged acoustic momentum flux (analogous as the so-called Reynolds stress well known in turbulence) and a resulting steady force in the fluid LIGHTHILL [1978]. These streaming flows, by nature, are

caused by the attenuation of the acoustic wave WIKLUND et collab. [2012]. As we shall see later, dissipation can occur either near walls or boundaries, either in the fluid bulk, leading to various types of streaming flows. Singular geometries are susceptible to enhance these effects. The relative importance of both effects depends on the frequency, fluid viscosity, but also geometrical dimensions.

Streaming flows vary greatly in terms of velocity, flow configuration and length scale under different acoustic excitation conditions. To the best of my knowledge, for slow streaming, its velocity can be as low as μ m/s, while for fast streaming, it can reach as high as 2 m/s ZACHARIAS et OHL [2013]. However, the terms "slow" and "fast" are not just qualitative description of scale of velocity with an ambiguous bench. If the amplitude of the streaming velocity is considerably smaller than that of fluid particle (acoustic) velocity, it is called "slow streaming". Otherwise, the streaming with comparable or even larger velocity than the fluid particle velocity is called "fast streaming". For the length scale of streaming flow, its value varies from being on the order of μm as microstreaming up to the order of cm in bulk-streaming BOLURIAAN et MORRIS [2003]. With respect to the flow configuration, it mainly consists of jet and vortices. It worth noting that, the above characterizations of the streaming flow are highly influenced by the frequency and amplitude of the acoustic excitation and the geometry where the acoustic field is applied. So the features of the various streaming flows are just descriptive, not definitive and they are just a reflection of acoustic excitation and the mechanism of attenuation of acoustic energy WIKLUND et collab. [2012]. The above features may extend with the advancement of acoustic excitation in novel geometry. Following this section, inner and outer boundary layer streaming, Eckart streaming will be reviewed. Before this, let's start with viscous attenuation of an acoustic wave.

In general, the mechanism of the attenuation of the acoustic wave through fluid can be attributed to dissipation of energy either directly into the fluid during passing through fluid or in viscous stokes boundary layer near the interface between solid and fluid. This classification leads to two types of streaming. For the latter, the dissipation into the boundary layer is comparatively larger in comparison to bulk dissipation because of the steep velocity gradient that is formed perpendicular to the solid boundary as the acoustic wave propagates parallel to it. The strong velocity gradient results from the presence of non-slip boundary. This results in an acoustic velocity that varies from zero at the solid surface, to its free-stream value at a distance $\delta = \sqrt{2\nu/\omega}$ away from the surface (the scale order is 1μm for ultrasound in water and 10 μm for audible sound in water)

Then two types of streaming are usually distinguished: the first is the Eckart streaming, also called quartz wind, which significantly arises within the fluid, during which acoustic energy dissipates; the second is labeled as Rayleigh streaming (this name specifically refers to the outer streaming). As mentioned above, acoustic energy dissipates within the viscous Stokes layer. Then Reynolds stress within the layer induces the inner streaming and a slip velocity along the outer side of the Stokes layer, which in turn drives the outer streaming outside of the Stokes layer, in the main flow.

Eckart streaming

As an acoustic wave propagates through a fluid, a part of the acoustic energy is absorbed by the fluid at a rate that is typically proportional to the square of its frequency, as specified in Stokes's law of sound attenuation STOKES [2010]. The amplitude of the acoustic wave becomes attenuated causing the acoustic pressure amplitude to decrease as the distance from the acoustic source increases. The dissipation of acoustic energy results in a steady momentum flux, forming a jet of fluid inside the acoustic beam in the direction of acoustic propagation. For the case of a fluid jet formed within the confinement of a microfluidic chamber, vorticity will typically ensue, resulting in fluid circulation within either part of or the entire chamber. As shown in Fig.1.3, the travelling wave originating from the vibration source, is attenuated and induces the significant large scale streaming flow along the direction of its propagation.

Rayleigh streaming

For Rayleigh streaming, the second-order steady flow comes up with the creation of vorticity in a viscous boundary layer near the boundary along solid wall and fluid. Due to the no-slip boundary condition, the vibration or acoustic motion must vanish along the wall, while at a certain distance form the wall the acoustic vibration is generally parallel to the wall direction. Hence this type of streaming is also named as "boundary layer driven streaming". Unlike Eckart Streaming, this type of streaming is at relatively steady state, since the little variations from higher order coupling can usually be ignored. Since such streaming is closely related to the boundary layer, it can show up around various geometry walls or obstacles in fluid with acoustic wave or vibration field, resulting in various configurations of streaming flow under different conditions. As in Fig.1.4(a), when the piezo-transducer with a 2.17MHz actuation below the chamber turns on, vortices were formed between pressure node and antinode and the pairs of streaming vortices were symmetrical to the pressure nodes. Due to the periodic momentum gradient between antinodes and nodes, the size of a single vortex is equal to the half wavelength of the acoustic wave BRUUS [2007]. Fig.1.4(b) shows the particles' trajectories from the stack image near a vibrating beam inserted into a Hele-Shaw cell. The experiment was performed in a high-viscosity water/glycerin mixture (108.2 mPa·s) at 200Hz. For the outer streaming flow, the part corresponding to the middle part of the end, was likely being jetted out, without coming back while the parts near the two edges flowed back to the edges after bursting out. Fig.1.4(c) gives a schematic presentation of streaming near a channel wall. With a vibrating boundary condition, inter and outer streaming flows theoretically appear along the wall with a characterized size of half wavelength, like in Fig.1.4(a). In Fig.1.4(d), the streamline in which streaming flow around a hemispherical bubble superposed over a certain throughput, is shown. For Fig.1.4(e), image stack of a vibrating cylinder inserted into silicon oil (dynamic viscosity: 9.3 mPa·s) is presented. The vibration's frequency of the cylinder is as low as 5 ~ 60Hz, which gives rise to a relatively thick boundary layer. The inner streaming flow within the layer can be very clearly depicted under this low-frequency conditions. From the point of view of the application, limited by the vibration source, the above streaming flow is usually characterized with the low-intensity and high-cost, restricting its usage in many areas like mixing process in microchannel.

Acoustic Streaming near a Sharp Edge or Sharp Edge Acoustic Streaming(SEAS)

Acoustic steaming near a sharp edge was firstly observed by ZACHARIAS et OHL [2013] in eye surgery around high-speed vibrating needles. Its origin is associated with the boundary layer, so it belongs to the Rayleigh streaming. Known as high intensity and low frequency acoustic condition, SEAS has been studied extensively NAMA et collab. [2014]; OVCHINNIKOV et collab. [2014], as the picture captured by us shown in Fig.1.5(a) and the one obtained from DOINIKOV et collab. [2020] shown in Fig.1.5(b) in recent years. High intensity means the SEAS can be applied in many area where the traditional Rayleigh streaming can't reach, like high-speed streaming near a tip is used to suppress the cavitation bubbles in eye surgery ZACHARIAS et OHL [2013] and Lab-on-a-Chip device with SEAS is utilized as sputum liquefier in medical test HUANG et collab. [2015]. Low frequency means more choices of acoustic or vibration source. Much cheaper and simpler piezoelectric transducer (like low-cost commercial Piezotransducer used in this thesis), even possible vibration source from natural environment, instead of the complex and expensive one, like the interdigitated transducer(IDT), can be used to induce SEAS. Based on these advantages, the current thesis concentrates on the streaming phenomenon near a sharp edge structure in a microchannel.

1.1.3 Theoretical background of acoustic streaming

After showing the streaming phenomena, the thesis should further review the various situations in which the streaming can be induced and present the relevant fluid mechanics in terms of equations to be a base to understand the following part of this thesis.

Figure 1.3 – Eckart streaming formed along propagation of acoustic wave from the vibration source: (a) image captured by J.M. Lenoir and V.Botton of LMFA lyon; (b)image captured by NOWICKI et collab. [1998]

Oscillatory flow

Let's start with the equations of a linear sound wave in a fluid, coupled to a flow. The velocity $\boldsymbol{u}$ and pressure p then contain both the fast acoustic and the slow flow terms. For a compressible flow, without considering the boundary condition of the fluid domain. Continuity and momentum equations are flowing respectively:

$$\frac{\partial \rho}{\partial t} + \nabla \cdot (\rho \mathbf{u}) = 0 \tag{1.1}$$

$$\rho(\frac{\partial \boldsymbol{u}}{\partial t} + \boldsymbol{u} \cdot \nabla \boldsymbol{u}) = -\nabla p + \mu \nabla^2 \boldsymbol{u} + (\beta^{'} + \frac{1}{3}\mu)\nabla(\nabla \cdot \boldsymbol{u}) \tag{1.2}$$

the compression and rarefaction of a compressible fluid caused by sound wave can be treated as a oscillatory motion with a small amplitude. The small disturbances to the pressure and density can be defined as following:

$$p = p_0 + p^{'}; \rho = \rho_0 + \rho^{'} \tag{1.3}$$

with $p^{'} \ll p$ and $\rho^{'} \ll \rho$. Similarly, the velocity is also defined as:

$$\boldsymbol{u} = \boldsymbol{u_0} + \boldsymbol{u}^{'} = \boldsymbol{u}^{'} \tag{1.4}$$

the $\boldsymbol{u_0}$ means the undisturbed state $\boldsymbol{u_0} = 0$. In addition, since the $\boldsymbol{u}^{'}$ is considered to be small and in the focused region (without solid boundary), there aren't large changes in the region, the nonlinear inertial term $\boldsymbol{u} \cdot \nabla \boldsymbol{u}$ can be neglected. By ignoring the viscous terms, Eqn.1.1, Eqn.1.2 can be reduced to:

$$\frac{\partial \rho^{'}}{\partial t} + \rho_0 \nabla \cdot \boldsymbol{u}^{'} = 0 \tag{1.5}$$

$$\rho_0 \frac{\partial \boldsymbol{u}^{'}}{\partial t} = -\nabla p^{'} \tag{1.6}$$

Further, assuming the flow is irrotational, potential function $\nabla\phi = \boldsymbol{u}^{'}$ can be used to describe the velocity field. Then Eqn.1.6 can be transformed to:

$$\rho_0 \frac{\partial \phi}{\partial t} = -p^{'} \tag{1.7}$$

If the process of the compression and rarefaction is adiabatic, the relation between $\rho^{'}$ and $p^{'}$ is linear:

$$p^{'} = c^2 \rho^{'} \tag{1.8}$$

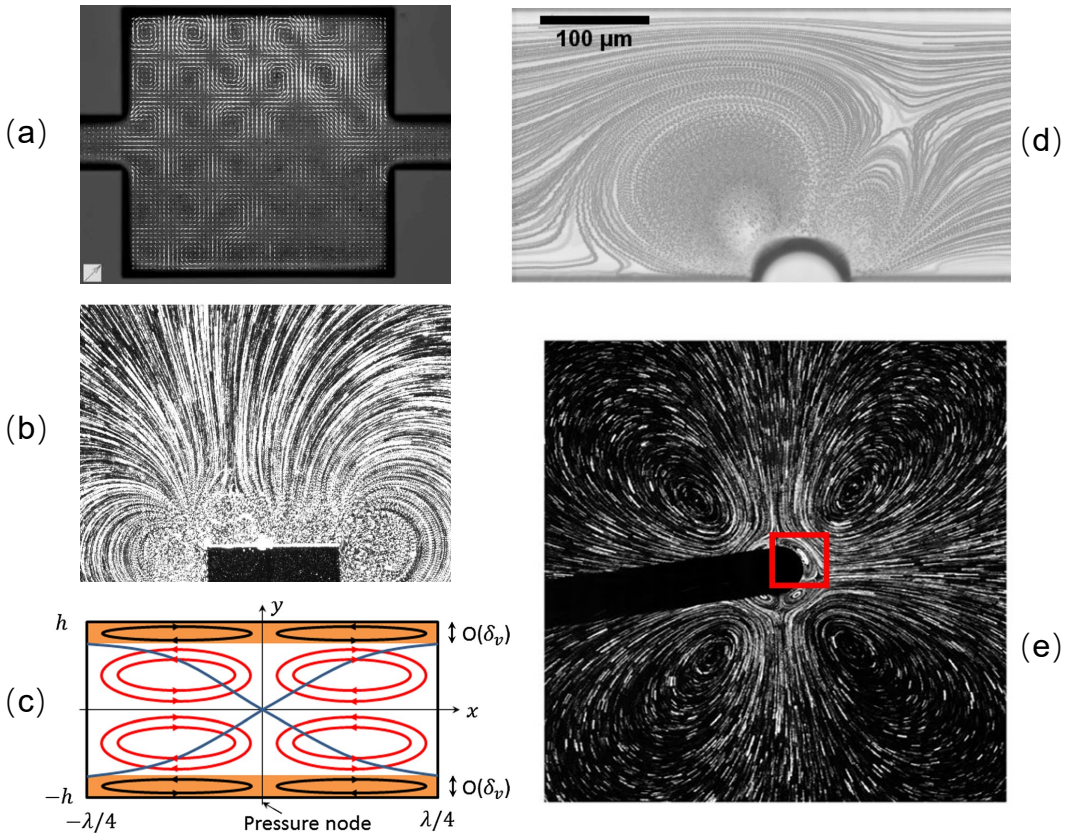

Figure 1.4 – Rayleigh steaming under different acoustic or mechanical forcing and with different geometries: (a) acoustic streaming in a square PDMS microchamber at $f = 2.17\mathrm{MH}z$ BRUUS [2007]; (b) streaming flow around a vibrating metal beam inserted into the water/glycerine solution, $f = 200\mathrm{H}z$ COSTALONGA et collab. [2015]; (c) schematic presentation of a streaming flow in a two-dimensional rectangular channel LEI et collab. [2017]; (d) streaming flow around an acoustically excited bubble in a microchannel at $f = 16.8k\mathrm{H}z$ WANG et collab. [2012]; (e) streaming flow around a vibrating cylinder immersed within a fluid at $f = 60\mathrm{H}z$, the vortex contained by the red square mark refers to the inner streaming within the viscous boundary layer, and the area out of the layer is dominated by the outer streaming or Rayleigh streaming BAHRANI et collab. [2020]

where c means the sound velocity in the fluid. Thus based on Eqn.1.5 combined with Eqn.1.7 and Eqn.1.8, we can get:

$$\frac{1}{c^2}\frac{\partial^2\phi}{\partial t^2} = \nabla^2\phi \tag{1.9}$$

For one-dimensional plane wave, the solution to Eqn.1.9 can be:

$$\phi(x,t) = \mathrm{A}e^{i(\omega x/c-\omega t)} \tag{1.10}$$

where ω means angular velocity; $\omega/c = 2\pi/\lambda$ is known as the wave number, λ is wavelength of the wave.

For the single frequency with appropriate coordinate reference, the expression of $\phi(x,t)$ can be:

$$\phi(x,t) = \mathrm{A}\cos(\omega x/c)\cos(\omega t) \tag{1.11}$$

The velocity and pressure are:

$$u(x,t) = \frac{\partial\phi}{\partial x} = -\mathrm{A}\frac{\omega}{c}\sin(\omega x/c)\cos(\omega t) = \mathrm{V}(x)e^{i\omega t} \tag{1.12}$$

$$p(x,t) = -\rho_0\frac{\partial\phi}{\partial t} = \rho_0\mathrm{A}\omega\cos(\omega x/c)\sin(\omega t) = p(x)e^{i\omega t} \tag{1.13}$$

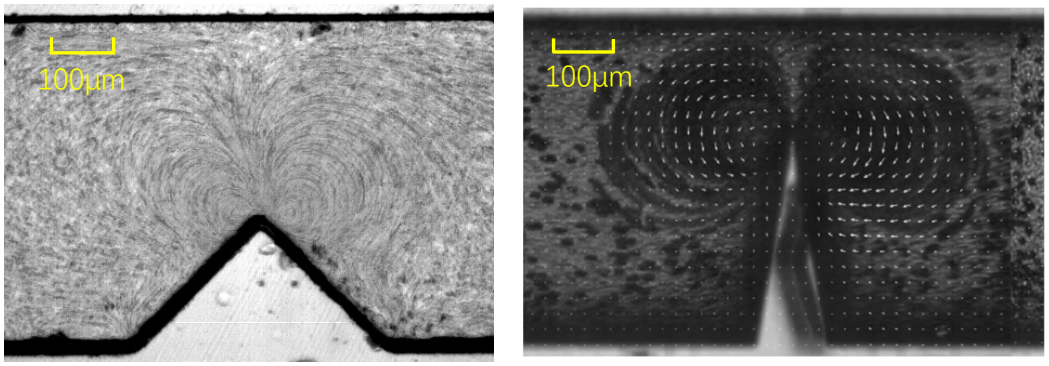

Figure 1.5 – (a and b) Streaming flow near a sharp edge in a microchannel excited by an acoustic field. (a) is captured by Chuanyu ZHANG et al. and (b) is obtained from DOINIKOV et collab. [2020]

Here, we can see that the velocity and pressure in the oscillatory flow can be expressed as a linear combination of the amplitude of $V(x)$ and $p(x)$ and periodic function $e^{i\omega t}$. This will be used in the following part to analyze the streaming phenomenon.

Navier–Stokes equations with dimensionless parameters

In fluid mechanics, Mach number M_a can be used to evaluate the compressibility of the fluid:

$$M_a = U/c \tag{1.14}$$

where U means the local velocity; c refers to the sound speed in a fluid, for water $c = 1482$ m/s at 20 ° C. For the case in which the range of the displacement of the vibration source (from boundary conditions or vibration of transducer material) resides in the scale of µm or lower, the maximum local velocity U is much lower than c for frequency equal to or smaller than the order of MHz. In these cases, $M_a \ll 1$ and the fluid can be treated as incompressible.

Following the Riley's review RILEY [2001], the NS equations for incompressible fluid can be written as:

$$\frac{\partial \boldsymbol{u}'}{\partial t} + (\boldsymbol{u}' \cdot \nabla)\boldsymbol{u}' = -\frac{1}{\rho}\nabla p' + \nu\nabla^2 \boldsymbol{u}' \tag{1.15}$$

$$\nabla \cdot \boldsymbol{u}' = 0 \tag{1.16}$$

in which the dimensionless factors are used as followings:

$$\boldsymbol{x} = \boldsymbol{x}'/a, t = \omega t', \boldsymbol{u} = \boldsymbol{u}'/U_0, \nabla = a\nabla', \xi = a\xi'/U_0 \tag{1.17}$$

where a, U_0 refer to the characteristic length and velocity in the acoustic field respectively. With these dimensionless parameters, Eqn.1.15 can be changed to:

$$\frac{\partial u}{\partial t} + \frac{U_0}{\omega a}(u \cdot \nabla)u = -\frac{1}{\omega \rho a U_0}\nabla p + \frac{U_0}{a^2}\nabla^2 u \tag{1.18}$$

taking the curl of Eqn.1.18 to eliminate the pressure term:

$$\frac{\partial \xi}{\partial t} + \epsilon\nabla \times (u \cdot \nabla)u = \frac{\epsilon}{R}\nabla^2 \xi \tag{1.19}$$

where $\epsilon = U_0/\omega a$ and $R = U_0 a/\nu$. By introducing the stream function: $\boldsymbol{u} = \nabla \times \psi$, Eqn.1.18 becomes:

$$\frac{\partial \nabla^2 \psi}{\partial t} - \epsilon\frac{\partial(\psi, \nabla^2\psi)}{\partial(x, y)} = \frac{\epsilon}{R}\nabla^4 \psi \tag{1.20}$$

Analytical solution of streaming flow

For most studies, perturbation method is used to analyze and solve the streaming phenomenon. And in most situations involving the Rayleigh streaming with relatively high frequency ω, the term ϵ can be treated as a very small parameter, namely $\epsilon = U_0/\omega a \ll 1$. For example, within a simple channel like in Fig.1.4(c), U_0 and a refer to the amplitude of acoustic vibration in terms of velocity and width of the channel (ranging from 200μm to 1mm) respectively. From the previous perspective of application and engineering, transducers activated with frequency ranging from 50kHz to several MHz, associated with the vibration amplitude in terms of spatial scale a_ω at several μm or nm, can provide a relatively more stable and controllable acoustic field into a focus field. In such cases:

$$\epsilon = U_0/\omega a = \pi f a_\omega / 2\pi f a = a_\omega / 2a \ll 1 \tag{1.21}$$

So ϵ is assumed to be a very small parameter in most previous studies; while in this thesis, this assumption is not true within the local area near the tip of the sharp edge structure.

With $\epsilon \ll 1$, it is possible to introduce the perturbation method, and the expressions of the small parameter expansion of velocity field $\boldsymbol{u}(x,y,t)$, vorticity field $\xi(x,y,t)$ and stream function $\psi(x,y,t)$ for a two-dimensional domain are as followings:

$$\boldsymbol{u}(x,y,t) = \boldsymbol{u_0}(x,y,t) + \epsilon \boldsymbol{u_1}(x,y,t) + \epsilon^2 \boldsymbol{u_2}(x,y,t) + ... \tag{1.22}$$

$$\xi(x,y,t0 = \xi_0(x,y,t) + \epsilon\xi_1(x,y,t) + \epsilon^2\xi_2(x,y,t) + ... \tag{1.23}$$

$$\psi(x,y,t) = \psi_0(x,y,t) + \epsilon\psi_1(x,y,t) + \epsilon^2\psi_0(x,y,t) + ... \tag{1.24}$$

substitution of these expansions into the momentum equations above like the stream function equation gives the leading order equation, by scale order analysis:

$$\text{In main area} \quad \frac{\partial \nabla^2 \psi_0}{\partial t} = 0 \tag{1.25}$$

$$\text{In stokes boundary layer} \quad \frac{\partial}{\partial t}\left(\frac{\partial^2 \boldsymbol{\Psi_0}}{\partial \eta^2}\right) = \frac{1}{2}\frac{\partial^4 \boldsymbol{\Psi_0}}{\partial \eta^4} \tag{1.26}$$

where the domain is separated into an area far away from the boundary layer and another one within the boundary layer. And new dimensionless variables are defined: $\psi = (\frac{2\epsilon}{R})^{1/2}\boldsymbol{\Psi}$ and $y = (\frac{2\epsilon}{R})^{1/2}\eta$, and η is the coordinate variable along y direction. With the perturbation method, the leading order equation can be treated without considering the nonlinear convective terms, which make it possible to solve the equation analytically, here we get the analytical solution of ψ_0 within the boundary layer:

$$\boldsymbol{\Psi_0}(x,y,t) = U(x)[\eta - \frac{1}{2}(1-i) \times 1 - e^{-(1+i)\eta}]e^{it} \tag{1.27}$$

Further, to the order O(ϵ) within the boundary layer:

$$\frac{1}{2}\frac{\partial^4 \boldsymbol{\Psi_1}}{\partial \eta^4} - \frac{\partial}{\partial t}\left(\frac{\partial^2 \boldsymbol{\Psi_1}}{\partial \eta^2}\right) = \frac{\partial(\partial^2 \boldsymbol{\Psi_0}/\partial \eta^2, \boldsymbol{\Psi_0})}{\partial x, \eta} \tag{1.28}$$

taking time-average of Eqn.1.28, we get:

$$\frac{1}{2}\frac{\partial^4 \boldsymbol{\Psi_1}}{\partial \eta^4} = < \frac{\partial(\partial^2 \boldsymbol{\Psi_0}/\partial \eta^2, \boldsymbol{\Psi_0})}{\partial x, \eta} > \tag{1.29}$$

Here, the expression in term of velocity u, corresponding to the right term $< u \cdot \nabla > u^*$ is called *Reynolds Stress Force*. Based on Eqn.1.29, the slip velocity can be obtained:

$$u_{slip} = -\frac{3}{8}[(1-i)U^* \frac{dU}{dx} + (1+i)U\frac{dU^*}{dx}] \tag{1.30}$$

where U^* is the complex conjugate of U; u_{slip} is the driving mechanism for the steady streaming in the bulk fluid and is usually used as the value to characterize the streaming.

Simulation Model with perturbation method and direct solving NS equations

The above process above attempts to analytically find out the solution of the streaming field with perturbation theory. With the development of Computational Fluid Dynamics(CFD), more and more studies rely on simulations to analyze the streaming phenomenon in complex geometries for which it is almost impossible to obtain any accurate analytical solutions. For the mathematical model of simulations in most studies, mostly utilizing the above process with a perturbation theory framework, in an incompressible fluid, the physical fields can also be assumed to be a combination of separate fields with very different scale orders. As shown in Eqn.1.12 and Eqn.1.13, in a periodic vibration field, the velocity and pressure field can be treated as spatial functions of amplitude linearly with a periodic term $e^{-i\omega t}$. Here, the velocity and pressure can be:

$$v = v_a e^{-i\omega t} + v_s \tag{1.31}$$

$$p = p_a e^{-i\omega t} + p_s \tag{1.32}$$

where $v_a e^{-i\omega t}$ and $p_a e^{-i\omega t}$ correspond to the oscillatory field and v_s and p_s refer to the steady streaming field.

For an incompressible fluid, the N-S equations are:

$$\frac{\partial \boldsymbol{v}}{\partial t} + (\boldsymbol{v}\cdot\nabla)\boldsymbol{v} = -\frac{1}{\rho}\nabla p + \nu\nabla^2\boldsymbol{v} \tag{1.33}$$

$$\nabla\cdot\boldsymbol{v} = 0 \tag{1.34}$$

Taking Eqn.1.31 and Eqn.1.32 into Eqn.1.33 and Eqn.1.34, we obtain:

$$i\boldsymbol{\omega} v_a + (\boldsymbol{v}_s\cdot\nabla)\boldsymbol{v}_a + (\boldsymbol{v}_a\cdot\nabla)\boldsymbol{v}_s = -\frac{1}{\rho}\nabla p_a + \nu\nabla^2\boldsymbol{v}_a \tag{1.35}$$

$$(\boldsymbol{v}_s\cdot\nabla)\boldsymbol{v}_s + \frac{1}{2}\mathrm{Re}[(\boldsymbol{v}_a\cdot\nabla)\boldsymbol{v}_a^*] = -\frac{1}{\rho}\nabla p_s + \nu\nabla^2\boldsymbol{v}_s \tag{1.36}$$

$$\nabla\cdot\boldsymbol{v}_a = 0 \tag{1.37}$$

$$\nabla\cdot\boldsymbol{v}_s = 0 \tag{1.38}$$

where Eqn.1.35 stands for the unsteady part of the momentum equation (periodic term $e^{-i\omega t}$ has been left out), and Eqn.1.36 is the steady part. Here, $\mathrm{F}_s = \frac{1}{2}\mathrm{Re}[(\boldsymbol{v}_a\cdot\nabla)\boldsymbol{v}_a^*]$ called *Reynolds Stress Force*, as we mention above, is a steady force source by oscillatory motion $v_a e^{-i\omega t}$. $\mathrm{Re}[\cdot]$ means only real part of the expression. As the assumption for perturbation method: $v_a \gg v_s$, $(\boldsymbol{v}_s\cdot\nabla)\boldsymbol{v}_a + (\boldsymbol{v}_a\cdot\nabla)\boldsymbol{v}_s$ can be neglected because of smaller scale order, then:

$$i\omega\boldsymbol{v}_a = -\frac{1}{\rho}\nabla p_a + \nu\nabla^2\boldsymbol{v}_a \tag{1.39}$$

$$(\boldsymbol{v}_s\cdot\nabla)\boldsymbol{v}_s + \mathrm{F}_s = -\frac{1}{\rho}\nabla p_s + \nu\nabla^2\boldsymbol{v}_s \tag{1.40}$$

v_a, amplitude of the oscillatory motion, is solved from Eqn.1.39 combined with Eqn.1.37, similar to the process from Eqn.1.9 to Eqn.1.12 in the last section. After solving out the oscillatory field, F_s can be calculated and then steady streaming velocity field can be obtained by solving Eqn.1.38 with Eqn.1.40. Although the classical perturbation method has been widely applied in the streaming studies, its assumption is invalid in some cases, which will be discussed in the following. Beside the perturbation method, directly solving NS equations (DNS) is another solid method.

Instead of separating the steady motion from the oscillatory parts and solving step by step like Eqn.1.39 and Eqn.1.40, DNS method means solving Eqn.1.35-1.38 simultaneously with periodic boundary conditions $v = v_a e^{i\omega t}$. Then the steady streaming velocity field can emerge by taking the time average of the time-dependent solution. Compared with the perturbation method, DNS takes the coupling between steady v_a and v_s into consideration. In this thesis, the DNS method is adopted to predict the streaming field. The details of this method are presented in the next chapter *"Methodology"*.

Failure of perturbation method

Let's go back to the dimensionless number $\epsilon = U_0/\omega a$ in the last section and put the Eqn.1.19 here again:

$$\frac{\partial \xi}{\partial t} - \epsilon \nabla \times (u \times \xi) = \frac{\epsilon}{R} \nabla^2 \xi \tag{1.41}$$

where $\nabla \times (u \cdot \nabla) u = -\nabla \times (u \times \xi)$. Here it is clear that the scale order of ϵ decides the weight of nonlinear term in the equation, which means that $\nabla \times (u \times \xi) \sim F_s \sim \mathbf{O}(\epsilon)$. However, the basic assumption of the perturbation method is that nonlinear terms in the equation are much smaller than other parts in terms of scale order, namely $\epsilon \ll 1$. In most situations where the frequency ω and characteristic length a are relatively large, such assumption can be satisfied. As shown in

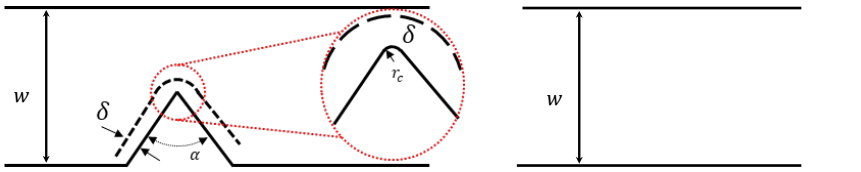

(a) Parallel wall with sharp edge structure (b) Parallel wall without sharp edge structure

Figure 1.6 – Schematic of geometry with and without sharp edge structures

Fig.1.6, for geometries with and without sharp variation of wall, the characteristic length a might be very different. For Fig.1.6(b), the classical channel with two parallel wall structure to study streaming, a is equal to the width of the channel, $a = w \sim 500\mu m$. But for Fig.1.6(a), for most area between two parallel wall, $a \sim \mathbf{O}(w)$, except that near the tip of the sharp edge where $a \sim 2r_c \sim 10\mu m$. Although with the frequency $f \sim MHz$, the assumption $\epsilon \ll 1$ can still be satisfied with amplitude U_0 at MHz, for geometry like Fig.1.6(a) with $f \sim kHz$ and $U_0 \sim 50$ mm/s, at least in the area near the tip, the ϵ is comparable to the unit 1, $\epsilon \sim \boldsymbol{o}(1)$. This means the convective term $\nabla \times (u \times \xi)$, of which the ϵ is the weight factor, can't be neglected during the solving process. Hence very strong streaming can be induced near the tip OVCHINNIKOV et collab. [2014]; ZHANG et collab. [2019] and coupling of oscillatory and steady motion are directly observed i experiments by ZHANG et collab. [2019]. In such a situation, it's reasonable to say that solving the oscillatory motion by neglecting the nonlinear terms in NS equation will bring a considerable error in further simulating the streaming flow.

Formation of streaming near the sharp edge structure: from the perspective of Womersley Number

Sharp variation of geometry not only leads to the invalidation of perturbation method, but also is a indispensable condition for inducing the streaming velocity near the sharp edge. Here we introduce the Womersley Number α , which represents a ratio of transient inertial to viscous force for vibration flow with a certain frequency, to analyze the formation of streaming:

$$\alpha^2 = \frac{\text{transient inertial force}}{\text{viscous force}} = \frac{\rho \omega U}{\mu U a^{-2}} = \frac{a^2}{\nu/\omega} \tag{1.42}$$

$$\alpha = \frac{a}{\sqrt{\nu/\omega}} = \frac{a}{\delta} \tag{1.43}$$

where a is the characteristic length scale, near the tip of sharp edge, $a = 2r_c$, and δ refers to the thickness of boundary layer, shown in the Fig.1.6(a). As we know, formation of streaming comes from the dissipation of acoustic energy within boundary layers (for Rayleigh streaming). When $\alpha \ll 1$, corresponding to a very sharp curvature compared with δ, viscous force dominates the area and much more acoustic energy is dissipated here to generate streaming flow. On the contrary, for area far away from the tip, where $a = w$, $\alpha \gg 1$, transient force dominate the vibration flow.

Viscosity

As discussed above, viscosity of fluid plays an important role in the streaming flow. In many situations, existence of viscosity is the only source of attenuation of acoustic wave, which allows the gradient of flux momentum and drives the streaming flow. One the other hand, viscosity is also the main resistance to the extension of the streaming flow out of viscous boundary layer. So without regard to the specific acoustic field, it is not easy to determine the influence of the variations of the kinematic viscosity coefficient ν on the streaming flow. For the classical problem of streaming study, where standing wave is built up between two parallel wall, as early as the first analytical solutions of the streaming field by RAYLEIGH [1945], the maximum value of the streaming velocity was independent of value of the coefficient of viscosity even though it's origin can be attributed to fluid viscosity. Later, in the study of NYBORG [1958], with regard to the plane wave between parallel walls with no-slip boundary conditions, it was demonstrated that ν could be cancelled out in the final analytical solution and this restated the comments of Rayleigh, the "limiting velocity"(streaming velocity along the viscous boundary layer) is independent of viscosity coefficient ν. The theory developed by Rayleigh and Nyborg has become a classical treatment and a dominant tool for researchers to investigate the streaming flow driven by attenuation within the viscous boundary layer.

However, as pointed out by NYBORG [1953] and LIGHTHILL [1978], the classical treatment might not be valid in situations where the acoustic energy is not attenuated only within the viscous boundary layer; the curvature of surface between fluid and solid becomes great; the local acoustic power is very high and the inertia effect of the streaming flow can't be neglected. When the acoustic field fails to satisfy the assumptions, the influence of the viscosity on the streaming flow has to be considered. Like the Eckart streaming, where propagating acoustic waves induce a streaming flow far from the walls, as shown in Fig.1.3, the fluid viscosity and other properties significantly affect the acoustic attenuation coefficient and then the intensity of the steady streaming flow.

As has been discussed in section 1.1.3, the existence of sharp edges puts the validation of the classical Rayleigh streaming theory into questions. It is reasonable to have a judgement that the influence of viscosity on SEAS might be different from the classical one.

1.2 Micro- and mini-fluidics

In general, microfluidic systems manipulate and control fluids that are geometrically constrained within environments having internal dimensions, or hydrodynamic diameters, at a scale of micrometres ELVIRA et collab. [2013]. The motivation behind the development of microfludic is inspired by its advantages: i) distinct cost advantage in small volumes of precious liquids (like chemical or bio reagents) where minimal volumes are sufficient for analytical purpose; ii) the possibility to carry out accurate manipulation of small particles (like biological cells) and to provide precise management of the reaction or process environment over the local conditions in the microfludic systems; iii) potential way to transform the microfludic system from Lab to industrial applications by using parallel reactors system (numbering up rather than scaling up); iv) safety. More generally, the above advantages are qualified as Process Intensification (PI) technology. PI refers to enhanced mass and heat transfer in the development of high performing process devices with significant benefits.

However, on the other side, the above benefits are usually counteracted by some disadvantages typical from low Reynolds number flows. More specifically, within small dimension and constrained geometries, the flow pattern within a microfluidic is dominated by laminar-plug flow (Reynolds number is generally lower than 10, down to much lower than 1 with some highly viscous fluids). For this reason, mixing enhancement is always troublesome in the microfluidic and is limited by ineffective mass transfer rate, especially along the cross-section direction of the channel. To overcome such problem, additional techniques, like acoustic vibrations, should be introduced into microchannels to make them more competitive.

1.2.1 Application of acoustic in microfluidics

Acoustofluidics, consisting of the actuation of fluids with acoustic waves, usually in particular within microfluidic channels, has been used in various areas. Fig.1.7 illustrates several examples of mechanisms and tasks such as particle manipulation, microswimmers, pumping, etc., applied to sensor technology, among others.

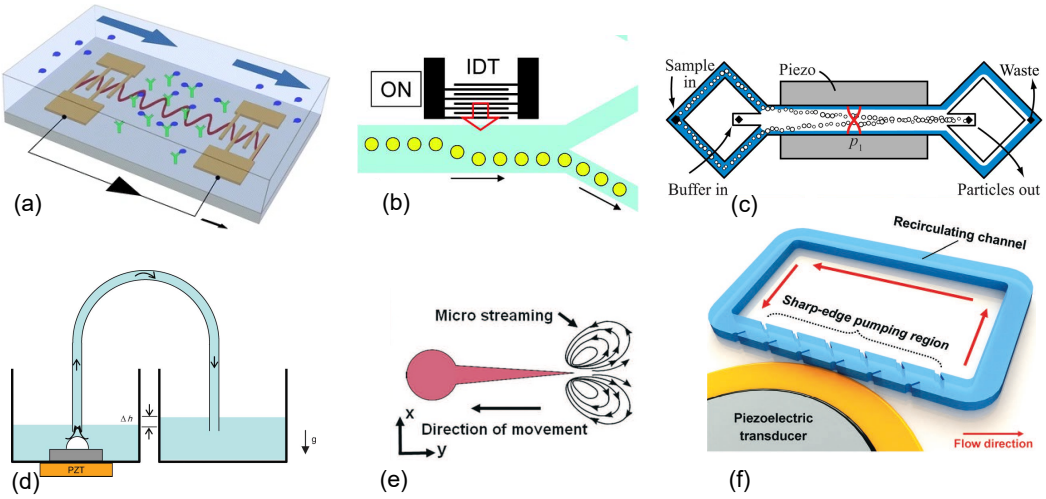

Figure 1.7 – Applications of acoustic techniques in several areas: (a) Biosensor with surface acoustic waves; (b) Particle sorting with streaming flow along the channel wall; (c) Particle sorting by radiation force; (d) Micro-pumping driven by the streaming flow near the bubble; (e) Swimmer driven the streaming near a sharp tail; (f) Circulation flow induced by the SEAS in a closed microchannel.

- Sensor technologies

  Fig.1.7(a) presents a basic surface acoustic wave biosensor which is integrated in a sample flow with Input Interdigitated Transducers (IDTs). Specific analytic molecules can be immobilized on the device from the sample stream. Captured molecules in turn influence the acoustic velocity field and thus generate output signals LÄNGE et collab. [2008] that can be correlated to its concentration within the sample. Based on this principle, quartz crystal microbalances are developed to monitor the growth of the material and biological tissues FRIEND et YEO [2011]. In addition, quartz crystal microbalances are useful to characterize fluid viscosity and density properties.

- Particle manipulation

  For higher acoustic frequency, usually in the ultrasonic range, radiation force and streaming flow simultaneously exist in a acoustofluidic device. Using these two forces to create specific momentum gradients, various strategies have been developed to manipulate particles within a mainstream flowing through a microstructure. As shown in Fig.1.7(b), when IDTs is on, the streaming induced along the upside wall drives the droplets to the lower channel of the branch FRANKE et collab. [2009]. Based on the same principle, particles sorting can also be achieved as shown in Fig.1.7(c), where particles moving along a wall are concentrated on the node part of wave through the radiation force within the acoustic wave field AUGUSTSSON et collab. [2009].

- Process engineering

  More and more acoustic technologies are applied to chemical microreactors, especially to the preparation phase, i.e., the mixing of reactants. The details will be discussed in the following section.

- Other applications

  Recently, the development of acoustics enables more interesting trails in Lab on Chip area. Like in Fig.1.7(d) RYU et collab. [2010] shows a novel kind of pump based on the bubble streaming induced by PZT. The bubble atop the PZT materials is acoustically excited at its resonance frequency. Only the upward flow of vortex streaming enters into a capillary tube. Inspired by the streaming flow around the sharp edge, a sharp-edge swimmer has been designed like in Fig.1.7(e). In the acoustic field, streaming plays as the fluid jet out of the tips of the tails to push the particle following certain direction KAYNAK et collab. [2017]. Another kind of acoustofludic pump is shown in Fig.1.7(f), in a closed loop with inclined sharp edge arrays under the acoustic vibration, certain cycle flow driven by streaming flow on one side can be generated HUANG et collab. [2014].

1.2.2 Mixing process in microchannel

As discussed above, characterized by a typical dimension less than one millimeter, a microchannel in which the dynamics of flow is usually restricted in a low-Reynolds level, faces several challenges, like inducing any mass or heat transport in the direction transverse to the main flow, which is generally strongly diffusion-limited. So mixing is an important aspect in improving the efficiency of various chemical reactions at high enough throughput. Specifically, in a Y type microchannel, two parallel flows, injected separately in a microfluidic channel, will stay separated and mix very slowly with each other, because of the laminar flow conditions that commonly exist in such a submillimeter domain. In most microfluidic systems wherein chemical reactions take place, however, one of the major issues is the time required for the reactants to develop a large enough contact surface with each other and to mix efficiently BENGTSSON et LAURELL [2004]. Therefore, it is difficult to ensure the homogeneity of fluids which is a basic but vital requirement, for many potential application of microchannel. So mixing is an important aspect in improving the ability to deliver sufficient reactants and the yield of many chemical reactions.

Because most microfluidic flows are laminar and thus the mixing predominantly relies on diffusion, chemical reactions upon which most practical applications rely proceed very slowly even though the diffusion distances are smaller than for bench-top-sized reaction vessels. The methods available to mix fluids chaotically at the microscale are typically separated into passive and active mixing.

- Passive mixer

  Here mixing is simply a consequence of the fluid passing through the device. It is ostensibly attractive because such mixers do not require a separate power source and or complexity in design to incorporate extra mechanical or electro-mechanical components. Passive mixers rely on the structure of the channel itself to reduce the diffusion distance between multiple miscible fluids. However, passive mixers can be difficult to fabricate at small scales because of the intricate design usually required to achieve effective performance while avoiding unacceptably high losses.

- Active mixer

  Active mixers usually displace the required complexity from the fluid structure to external sources FRIEND et YEO [2011]. It accelerates mixing by bringing energy from outside the channel into the fluid, for instance with magnetic fields, mechanical motions or acoustic vibrations etc. This type of mixer might achieve very high mixing efficiency within very short residence time or distance. Though, the coupling of such an outside field with the microchannel flow might cause more complexity on the system.

Recently, many attempts and studies focusing on passive or active micromixing can be found. For example, the continuous oscillatory baffles reactor (COBRs) designed by AVILA et collab. [2020] achieves good mixing quality through combining the oscillatory flow (active method) with baffles

(passive method) inside the reactors. Fig.1.8(a) shows a classical passive multi-lamellae mixer. The thickness of each specie diminishes, with compressing solutions from numbers of sources into one channel within a short distance. During such a process, the diffusion distance for mixing is significantly reduced; Another common method relies on the periodic injection from different solutions into one channel like Fig.1.8(b). With this method, each miscible solution is on purpose segmented into small parts, which is surrounded by another part, giving rise to much larger interfaces. Fig.1.8(c) presents another active mixer using bubble-vibration-induced streaming inside a mixing chamber. A bubble with certain size is fixed on one side of chamber. Activated by the PZT material on the bottom, significant streaming vortices around the bubble cause strong advection flow between separate solutions. Fig.1.8(d) describes an continuous mixer. The high-speed side flow squeezes the inlet flow into a very thin stream. The width of the inlet flow can be reduced to a size as small as 50 nm. At such small length scales, molecules from the both side flows rapidly diffuse across the stream, making for fast mixing. Intensification of the mixing in a common Y type microfluidic channel has also been studied, as in Fig.1.8(e). A horse-shoe type structure is designed to fasten the bubble between two solutions. Close to the transducer, strong streaming vortices bring in the advection between two solutions, thus accelerate the mixing process. In summary, passive mixers do not require any external source but they require either the fabrication of highly complicated structures or relatively long channels.

For some mixers which introduce the specific mixing part into the system, as Fig.1.8(b), a drawback of these solutions is that the mixing often is separated from the rest of the system. Therefore, the system might require redesigning and this can increase the dead volume of the system BENGTSSON et LAURELL [2004]. The mixing process with the help of acoustic field can often avoid such problem since the integration between vibration source (piezo-transducer) and the channel system is usually contactless.

Three time parameters in a mixing process

In typical quantitative study of a micromixer, three times are closely related to a micromixing process: i) diffusion time, ii) residence time and iii) micromixing time.

- Diffusion time

  The approximate average time for a small portion of fluid to diffuse over a distance L can be estimated by

  $$t_d = \mathrm{L}^2/\mathrm{D} \tag{1.44}$$

  where D is the mass diffusion coefficient of the liquid, L is the diffusion length. The above equation can be used to predict the order of time-scale of mass diffusion. As it suggests, one can dramatically reduce the mixing time by reducing the diffusion length required for mixing or increasing the contact area between two different liquids while keeping the volume constant.

- Residence time

  The terms "contact time" or "residence time" t_r are used primarily in discussions of continuous flow processes. They represent the average duration that it takes for a fluid element to travel from the reactor inlet to the reactor outlet HILL. For stirred tank reactors or other reactors there should be a distribution of residence times for the different fluid elements. However, for plug flow reactors, like the conditions in this thesis, all fluid elements will have the same residence time. The residence time is an important parameter while evaluating the mixing performance in the chemical reactor. If the time required for local mixing is longer than the actual residence time that a fluid element stays in the mixer, the process cannot provide a complete mixing, and it fails its designed purpose.

  For a microchannel structure, t_r can be determined by the internal reactor volume and the flow rate:

  $$t_r = \mathrm{V}_c/\mathrm{Q}_c \tag{1.45}$$

where V_c is the volume of the microchannel and Q_c refers to the volume flow rate through the system.

- Micromixing time

  The micromixing time t_m is used to characterize the time of local mixing process, at the molecular level. It is usually measured in the mixing process where two parallel chemical reactions (like the Villermaux-Dushman reactions, two neutralization reactions with different kinematic of reaction, discussed later) proceed with very different reaction time. Based on the certain ions concentration in the final solution, the micromixing time can be calculated. A shorter t_m means better local mixing and homogeneous distribution of reactants as fast as the reaction kinetics. Otherwise, if the micromixing time is long, the local concentration of one reactant becomes excessive, which gives opportunity for the undesirable slow reaction go on simultaneously with the fast one. Since this procedure is irreversible, the production of the parasite product thus increases with long t_m. It is clear that the micromixing time is only influenced by the kinematic constants of two competitive reactions and local concentration distribution of those reactants, independently of the specific way in which the mixing process proceeds. So it is an important performance indicator to make direct comparison between various mixers.

Now, a simple comparison can be made between the t_d and t_r: for the microchannel in this thesis, the diffusion length L is equal to the width of the channel, 0.5mm. With $D = 2.39\times10^{-9} m^2/s$, the diffusion time $t_d \approx 104$s, while the residence time is as short as $t_r \approx 2s$. Hence, $t_d \ll t_r$, which means that only by pure diffusion process, the mixing of the studied 0.5*0.05*7 mm microchannel is far from being satisfactory.

Determination of mixing performance

Flow visualization

Generally, the simplest and most common way to evaluate mixing performance in a microstructure is done by direct visualization of the flow. This measurement usually comes with mixing between diluted-dye and transparent streams for which the optical changes can be related to the variations of the dye concentration through Beer-Lambert law. In most situations where the dye concentration is low enough, the Beer-Lambert law gives a linear relation between concentration and grey level, so that one may directly use normalized grey level to quantify concentration. In addition, microscope and high-speed camera are indispensable tools for capturing the instantaneous or steady optical configuration throughout the experiments.

With visualization results, the Mixing Index M can be used to characterize the mixing at specific positions using:

$$M = \sqrt{\frac{\frac{1}{N}\sum_{i=1}^{N}(I_i - I_m)^2}{I_m^2}} \tag{1.46}$$

where I_i is the grey level value of i_{th} pixel; I_m is the average grey value of N pixels which refers to the specific area focused in the mixers. M = 1 means totally segregated fluids while M = 0 represents perfect mixing.

Another way of interpreting and quantifying macromixing performance, instead of measuring for the whole volume, is to make concentration profiling along the channel's cross section or perpendicular to the direction of main throughput. Depicting such concentration profiles in various positions gives a spatial evolution of mixing with detailed information.

Despite its wide application and convenience, the main disadvantage of such measurement resides in the fact that the color configuration is an average of the layers stacked along height path through the fluid. This can result in an overestimate of mixing performance when the state of intertwining lamellae of solution is treated as uniform one from height perspective.

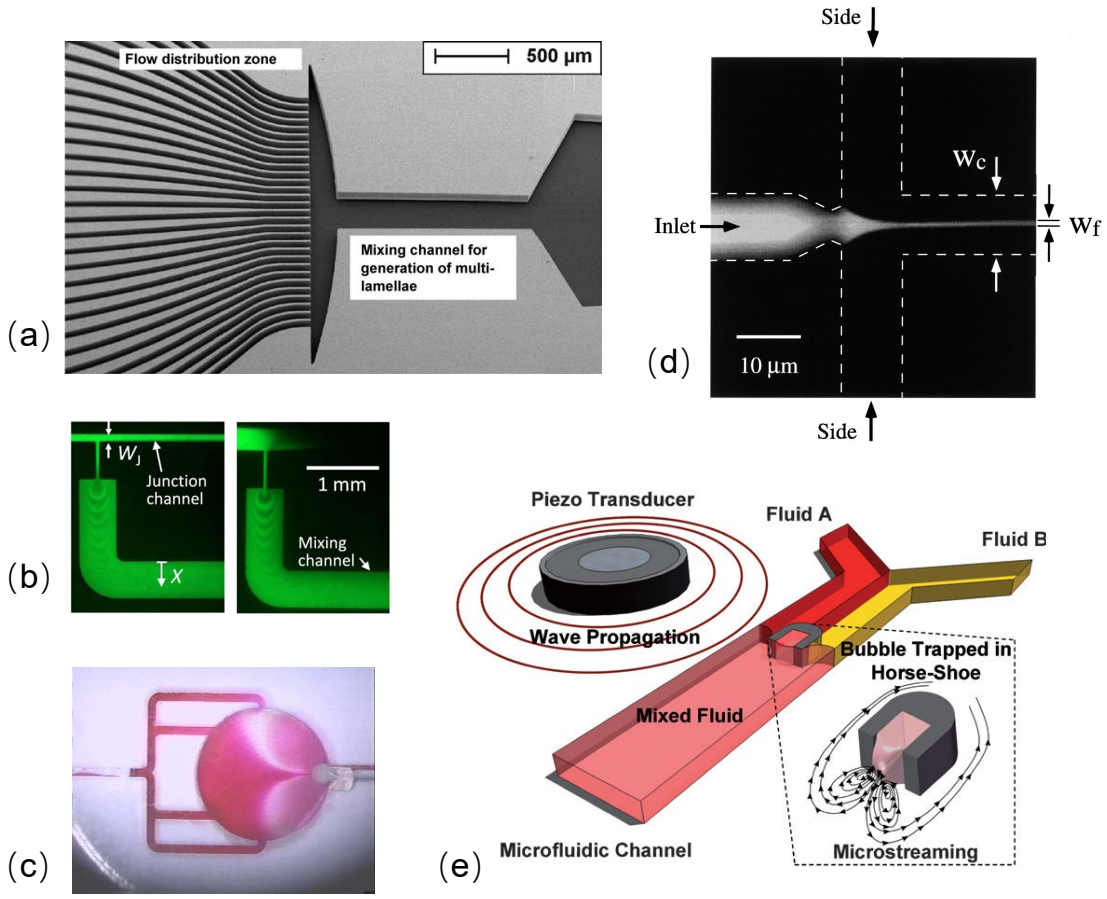

Figure 1.8 – Passive and active mixers in the previous studies(a) Multi-lamina (b)Periodic injection (c) bubble streaming (d) Quenched by Side flow (e) bubble streaming within the Y type mixer.

Micromixing characterization

One of the most frequently applied competitive reactions for characterizing the mixing efficiency is the Villermaux-Dushman reaction FOURNIER et collab. [1996]. This method, initially proposed to characterize micromxing in the traditional stirred reactor now has become an extensive method to evaluate the continuous mixers FALK et COMMENGE [2010]. Micromixing time, a concentration-free feature measured through this method can be used to compare different kinds of mixers. Hence, it has been extensively used to evaluate micromixing performance of micromixers COMMENGE et FALK [2011], or to study other continuous microchannel with mixing functionality through simulations and experiments FONTE et collab. [2020]. This reaction scheme, involving the neutralization of dihydroborate ions (R1, Eqn.1.47) and a redox reaction (R2, Eqn.1.48), is sensitive to mixing at the molecular level through the formation of Iodine (I_2) molecules:

$$H_2BO_3^- + H^+ \rightleftharpoons 3HBO_3 \tag{1.47}$$

$$5I^- + IO_3^- + 6H^+ \rightleftharpoons 3I_2 + 3H_2O \tag{1.48}$$

$$I_2 + I^- \rightleftharpoons I_3^- \tag{1.49}$$

Once the molecular Iodine is generated (due to ineffective mixing), an equilibrium is established between the iodine and the iodide ion that results in the formation of the tri-iodide ion, I_3^-, through R3 (Eqn.1.49).

Reactions R1 and R3 are quasi-instantaneous; while reaction R2 is by several orders of magnitude slower than the two others. Within a perfect mixing process, the product distribution is solely governed by the chemical kinetics and most H^+ are consumed by $H_2BO_3^-$, resulting in no or very small iodine production. On the other hand, a significant amount of iodine occurs under bad mixing conditions, which can be attributed to a local excess of H^+, not only being consumed by reaction R1, but also taking part in the reaction R2 and R3. Under the later condition, tri-iodide appears in the final product and its concentration can characterize the micromixing process. The whole process is thus considered as a chemical probe to assess the micromixing rapidity. The advantage of competitive reaction resides in the possibility to quantify the micromixing time, which allows to make a direct comparison between different types of micromixers based on the same criteria. On the other hand, in some situations, a change of reactant concentrations leads to very high product concentration which results in spectrometer saturation. So it requires the adjustments of the reactants concentrations for each specific experiment.

Details and parameters in the micromixing process will be presented in the next chapter.

1.3 Question to answer in this thesis

1.3.1 Mechanism of Sharp Edge Acoustic Streaming (SEAS)

As discussed above, strong streaming phenomenon observed near a sharp edge cannot be simply formulated and explained by the classic Rayleigh streaming theory, which remains valid only if the local radius of curvature of the walls is always larger than the boundary layer thickness. Moreover, as mentioned in Section 1.1.3, in a confined microchannel, the presence of a sharp edge results in inhomogeneous vibration of fluid. The transmission of acoustic field from solid to liquid is thus complex and multi-physic. Furthermore, the physical mechanism of the SEAS with respect to the sharp edge structure is not fully clear.

In particular, the vibration conditions required to generate significant streaming need more quantitative measurements. The available literature only provides the electrical input into transducers (mainly excitation frequency and input voltage) which is not a direct physical parameter to understand and quantify the generation of streaming. The pioneering study from T.J. Huang's group HUANG et collab. [2013] attributes the induced streaming flow to the mechanical vibrations of the sharp structures induced by a transducer stuck on the microchannel wall. Such a vibration was indeed observed with high-speed imaging, and it raises the question on the adaptation of the sharp edge geometry to the prescribed frequency in order to ensure a resonance condition. In the current thesis, an oscillating flow was prescribed to the whole fluid, which also generates strong streaming around the sharp tip, but without the constraint of operating at a specific frequency. Although OVCHINNIKOV et collab. [2014] suggests that both situations should in principle lead to similar streaming flows, the first-order fluid oscillations should be different between the two situations. Other experimental parameters such as clamping, transducer type and quality can make reproducing challenging. As a result, the physical interpretation of the fluid–wall interaction in a confined mini/micro-fluidic structure under acoustic excitation, as well as its influence on acoustic streaming generation and mass transfer performances is of fundamental scientific interest

Then, although both experiments HUANG et collab. [2013] and simulations NAMA et collab. [2014]; OVCHINNIKOV et collab. [2014] confirm the AS intensity depends on the sharpness of the tip, none of them dissociates the tip angle from the curvature diameter $2r_c$, as shown in Fig.1.6, both of which being a sign of sharpness. The difficulty is that in practice, the micro-lithography techniques make these two quantities related with each other. Therefore, only numerical simulations could help to tackle this challenging question.

Last, while most studies on acoustic streaming generated around obstacles concern situations where $\rho \ll 2r_c$ and that of OVCHINNIKOV et collab. [2014] deals with the opposite situation ($\rho \ll 2r_c$), it is unclear how the crossover between the two situations takes place.

From a theoretical point of view, sharp-edge AS remains a ground for a nonlinear framework in acoustofluidics equations. Indeed nonlinear terms coupling the steady and periodic velocity

fields can become dominant, or at least non-negligible, a feature which in turn makes the classical perturbation theory no longer adapted. This situation is the consequence of that, as mentioned above, the streaming velocity can be locally as strong as the vibration velocity ZHANG et collab. [2019].

1.3.2 Characterizations of SEAS

Features of SEAS include magnitude of streaming velocity, disturbance distance to the main flow, vortices size and shape, as discussed in Section 1.1.2. With different geometrical conditions (tip angles associated with curvature diameters $2r_c$) and different channel throughput, SEAS characteristics change. Questions remain to be answered regarding how SEAS varies with different acoustic intensities and experimental or geometrical conditions.

As the local characteristic length scale is comparable to the Stokes layer, with a constant local geometrical structure, the ratio between them is strongly affected by fluid property, mainly the viscosity ν. The excitation acoustic frequency f also has influence, according to the expression of the Stokes layer thickness: $\delta = \sqrt{\frac{2\nu}{\omega}}$. With a frequency in the audible range, relative small change of ω can lead to a sensible variation of boundary layer thickness, which further influences SEAS. How SEAS varies with different fluid and excitation conditions should also be addressed attentively.

1.3.3 Application: SEAS micromixer

SEAS is a jet-like flow at the transverse direction of the main flow, and it actively brings disturbances into the fluid. This makes SEAS a very promising tool to disturb the flow through the channel. In this thesis, utilizing the SEAS disturbances to improve the mixing process will be investigated. The mixing performances, including both macro- and micro-mixing, as well as involving microchannel from a single sharp edge to a pattern of multiple sharp edges, will be quantified. One main question consists in finding the optimal configuration of multiple edges to achieve efficient SEAS-assisted mixing. Once the best structure is identified, the mixing performance variation with different excitation conditions and throughput will be characterized and compared to those of passive mixers reported in the literature.

In particular, from a micromixer application perspective, evaluation of micromixing performance of SEAS through parallel chemical reactions (mainly based on micromixing time), to the best of our knowledge, is still absent in the literature. Micromixing time allows a direct comparison with other type of micromixers (both passive and active), in terms of mixing performance and energy cost.

Finally, from a methodology point of view, as discussed in Section 1.1.3, the simulations of SEAS with perturbation method can bring in considerable errors, especially under large acoustic intensity. Developing appropriate numerical scheme to resolve the acoustic-hydrodynamic-mass transfer coupling phenomenon is of high reference value for other acoustofluidics researches.

1.4 References

AUGUSTSSON, P., J. PERSSON, S. EKSTRÖM, M. OHLIN et T. LAURELL. 2009, «Decomplexing biofluids using microchip based acoustophoresis», *Lab on a Chip*, vol. 9, nº 6, doi:10.1039/b811027a, p. 810–818, ISSN 14730189. 13

AVILA, M., D. F. FLETCHER, M. POUX, C. XUEREB et J. AUBIN. 2020, «Mixing performance in continuous oscillatory baffled reactors», *Chemical Engineering Science*, vol. 219, doi:10.1016/j.ces.2020.115600, p. 115 600, ISSN 00092509. URL https://doi.org/10.1016/j.ces.2020.115600. 14

BAHRANI, S. A., N. PÉRINET, M. COSTALONGA, L. ROYON et P. BRUNET. 2020, «Vortex elongation in outer streaming flows», *Experiments in Fluids*, vol. 61, nº 3, doi:10.1007/s00348-020-2926-8, ISSN 14321114. URL https://doi.org/10.1007/s00348-020-2926-8. 7

BENGTSSON, M. et T. LAURELL. 2004, «Ultrasonic agitation in microchannels», *Analytical and Bioanalytical Chemistry*, vol. 378, nº 7, doi:10.1007/s00216-003-2334-y, p. 1716–1721, ISSN 16182642. 14, 15

BOLURIAAN, S. et P. MORRIS. 2003, «Acoustic streaming: from Rayleigh to today», *International Journal of Aeroacoustics*, vol. 2, nº 3, doi:10.1260/147547203322986142, p. 255–292, ISSN 1475-472X. URL http://dx.doi.org/10.1260/147547203322986142. 3, 4

BRUNET, P., M. BAUDOIN, O. B. MATAR et F. ZOUESHTIAGH. 2010, «Droplet displacements and oscillations induced by ultrasonic surface acoustic waves: A quantitative study», *Physical Review E - Statistical, Nonlinear, and Soft Matter Physics*, vol. 81, nº 3, doi:10.1103/PhysRevE.81.036315, p. 1–8, ISSN 15393755. 2

BRUNET, P., J. EGGERS et R. D. DEEGAN. 2007, «Vibration-induced climbing of drops», *Physical Review Letters*, vol. 99, nº 14, doi:10.1103/PhysRevLett.99.144501, p. 3–6, ISSN 00319007. 3

BRUUS, H. 2007, «Theoretical Microfluidics (Oxford Master Series in Physics)», cahier de recherche, doi:10.1017/CBO9781107415324.004. URL http://homes.nano.aau.dk/lg/Lab-on-Chip2008{_}files/HenrikBruus{_}Microfluidicslectures.pdf. 5, 7

COMMENGE, J.-M. et L. FALK. 2011, «Villermaux–Dushman protocol for experimental characterization of micromixers», *Chemical Engineering and Processing: Process Intensification*, vol. 50, nº 10, doi:10.1016/J.CEP.2011.06.006, p. 979–990, ISSN 0255-2701. URL https://www.sciencedirect.com/science/article/pii/S0255270111001395?via{%}3Dihub. 17

COSTALONGA, M., P. BRUNET et H. PEERHOSSAINI. 2015, «Low frequency vibration induced streaming in a Hele-Shaw cell», *Physics of Fluids*, vol. 27, nº 1, doi:10.1063/1.4905031, ISSN 10897666. 7

DOINIKOV, A. A., M. S. GERLT, A. PAVLIC et J. DUAL. 2020, «Acoustic streaming produced by sharp - edge structures in microfluidic devices», *Microfluidics and Nanofluidics*, doi:10.1007/s10404-020-02335-5, p. 1–13, ISSN 1613-4990. URL https://doi.org/10.1007/s10404-020-02335-5. 5, 8

DVOŘÁK, V. 1874, «Ueber die Entstehungsweise der Kundt'schen Staubfiguren», *Annalen der Physik*, vol. 227, nº 4, doi:10.1002/andp.18742270413, p. 634–639, ISSN 15213889. URL http://doi.wiley.com/10.1002/andp.18742270413. 3

ELVIRA, K. S., X. C. I SOLVAS, R. C. WOOTTON et A. J. DEMELLO. 2013, «The past, present and potential for microfluidic reactor technology in chemical synthesis», doi:10.1038/nchem.1753. URL http://www.nature.com/articles/nchem.1753. 12

FALK, L. et J. M. COMMENGE. 2010, «Performance comparison of micromixers», *Chemical Engineering Science*, vol. 65, nº 1, doi:10.1016/j.ces.2009.05.045, p. 405–411, ISSN 00092509. URL https://linkinghub.elsevier.com/retrieve/pii/S0009250909003819. 17

FARADAY, M. 1831, «On a Peculiar Class of Acoustical Figures; and on Certain Forms Assumed by Groups of Particles upon Vibrating Elastic Surfaces», *Philosophical Transactions of the Royal Society of London*, vol. 121, nº 0, doi:10.1098/rstl.1831.0018, p. 299–340, ISSN 0261-0523. URL http://rstl.royalsocietypublishing.org/cgi/doi/10.1098/rstl.1831.0018. 2, 3

FONTE, C. P., D. F. FLETCHER, P. GUICHARDON et J. AUBIN. 2020, «Simulation of micromixing in a T-mixer under laminar flow conditions», *Chemical Engineering Science*, vol. 222, doi:10.1016/j.ces.2020.115706, p. 115 706, ISSN 00092509. URL https://linkinghub.elsevier.com/retrieve/pii/S0009250920302384. 17

FOURNIER, M. C., L. FALK et J. VILLERMAUX. 1996, «A new parallel competing reaction system for assessing micromixing efficiency - Experimental approach», *Chemical Engineering Science*, vol. 51, nº 22, doi:10.1016/0009-2509(96)00270-9, p. 5053–5064, ISSN 00092509. URL https://linkinghub.elsevier.com/retrieve/pii/0009250996002709. 17

FRANKE, T., A. R. ABATE, D. A. WEITZ et A. WIXFORTH. 2009, «Surface acoustic wave (SAW) directed droplet flow in microfluidics for PDMS devices», *Lab on a Chip*, vol. 9, nº 18, doi:10.1039/b906819h, p. 2625–2627, ISSN 14730189. 13

FREE, G. et D. GRUCHY. 2017, «Chinese Spouting Bowl in Slow Motion - The Slow Mo Guys», URL https://www.youtube.com/watch?v=Lf42yiZP3og. 2

FRIEND, J. et L. Y. YEO. 2011, «Microscale acoustofluidics: Microfluidics driven via acoustics and ultrasonics», *Reviews of Modern Physics*, vol. 83, nº 2, doi:10.1103/RevModPhys.83.647, p. 647–704, ISSN 00346861. URL https://researchbank.rmit.edu.au/view/rmit:15064/n2006029889.pdf. 2, 13, 14

GEISSLER, F. et F. V. HUNT. 1980, *Origins in Acoustics: The Science of Sound from Antiquity to the Age of Newton*, vol. 36, Yale University Press, ISBN 0300022204, 896 p., doi:10.2307/939759. 2

GLASGOW, I. et N. AUBRY. 2003, «Enhancement of microfluidic mixing using time pulsing», *Lab on a Chip*, vol. 3, nº 2, doi:10.1039/b302569a, p. 114–120, ISSN 14730189. 3

HELMHOLTZ, H. L. 2009, *On the sensations of tone as a physiological basis for the theory of music*, Cambridge University Press, ISBN 9780511701801, 1–824 p., doi:10.1017/CBO9780511701801. URL /core/books/on-the-sensations-of-tone-as-a-physiological-basis-for-the-theory-of-music/6B5630E5D439286A8946CEB9D62BE6EC. 2

HILL, C. G. *An introduction to chemical engineering kinetics & reactor design*, ISBN 0471396095. 15

HUANG, P.-H., N. NAMA, Z. MAO, P. LI, J. RUFO, Y. CHEN, Y. XIE, C.-H. WEI, L. WANG et T. J. HUANG. 2014, «A reliable and programmable acoustofluidic pump powered by oscillating sharp-edge structures», *Lab Chip*, vol. 14, nº 22, doi:10.1039/C4LC00806E, p. 4319–4323, ISSN 1473-0197. URL http://xlink.rsc.org/?DOI=C4LC00806E. 14

HUANG, P. H., L. REN, N. NAMA, S. LI, P. LI, X. YAO, R. A. CUENTO, C. H. WEI, Y. CHEN, Y. XIE, A. A. NAWAZ, Y. G. ALEVY, M. J. HOLTZMAN, J. P. MCCOY, S. J. LEVINE et T. J. HUANG. 2015, «An acoustofluidic sputum liquefier», *Lab on a Chip*, vol. 15, nº 15, doi:10.1039/c5lc00539f, p. 3125–3131, ISSN 14730189. URL http://xlink.rsc.org/?DOI=C5LC00539F. 5

HUANG, P.-H., Y. XIE, D. AHMED, J. RUFO, N. NAMA, Y. CHEN, C. Y. CHAN et T. J. HUANG. 2013, «An acoustofluidic micromixer based on oscillating sidewall sharp-edges», *Lab on a Chip*, vol. 13, nº 19, doi:10.1039/c3lc50568e, p. 3847, ISSN 1473-0197. URL http://xlink.rsc.org/?DOI=c3lc50568e. 18

KAYNAK, M., A. OZCELIK, A. NOURHANI, P. E. LAMMERT, V. H. CRESPI et T. J. HUANG. 2017, «Acoustic actuation of bioinspired microswimmers», *Lab on a Chip*, vol. 17, nº 3, doi:10.1039/c6lc01272h, p. 395–400, ISSN 14730189. URL http://xlink.rsc.org/?DOI=C6LC01272H. 14

LÄNGE, K., B. E. RAPP et M. RAPP. 2008, «Surface acoustic wave biosensors: A review», *Analytical and Bioanalytical Chemistry*, vol. 391, nº 5, doi:10.1007/s00216-008-1911-5, p. 1509–1519, ISSN 16182642. 13

LANGELIER, S. M., D. S. CHANG, R. I. ZEITOUN et M. A. BURNS. 2009, «Acoustically driven programmable liquid motion using resonance cavities», *Proceedings of the National Academy of Sciences of the United States of America*, vol. 106, nº 31, doi:10.1073/pnas.0900043106, p. 12 617–12 622, ISSN 00278424. 3

LEI, J., P. GLYNNE-JONES et M. HILL. 2017, «Comparing methods for the modelling of boundary-driven streaming in acoustofluidic devices», *Microfluidics and Nanofluidics*, vol. 21, nº 2, doi:10.1007/s10404-017-1865-z, p. 1–11, ISSN 16134990. 7

LIGHTHILL, S. I. R. J. 1978, «ACOUSTIC STREAMINGt», *Journal of Sound And Vibration*, vol. 61, nº April, p. 391–418. 3, 12

MITRAGOTRI, S. 2005, «Healing sound: The use of ultrasound in drug delivery and other therapeutic applications», *Nature Reviews Drug Discovery*, vol. 4, nº 3, doi:10.1038/nrd1662, p. 255–260, ISSN 14741776. URL https://www.nature.com/articles/nrd1662. 3

MULLER, P. B. et H. BRUUS. 2015, «Theoretical study of time-dependent, ultrasound-induced acoustic streaming in microchannels», *Physical Review E - Statistical, Nonlinear, and Soft Matter Physics*, vol. 92, nº 6, doi:10.1103/PhysRevE.92.063018, ISSN 15502376. 3

NAMA, N., P. H. HUANG, T. J. HUANG et F. COSTANZO. 2014, «Investigation of acoustic streaming patterns around oscillating sharp edges», *Lab on a Chip*, vol. 14, nº 15, doi:10.1039/c4lc00191e, p. 2824–2836, ISSN 14730189. 5, 18

NOWICKI, A., T. KOWALEWSKI, W. SECOMSKI et J. WÓJCIK. 1998, «Estimation of acoustical streaming: Theoretical model, Doppler measurements and optical visualisation», *European Journal of Ultrasound*, vol. 7, nº 1, doi:10.1016/S0929-8266(98)00020-2, p. 73–81, ISSN 09298266. 6

NYBORG, W. L. 1953, «Acoustic Streaming due to Attenuated Plane Waves», *The Journal of the Acoustical Society of America*, vol. 25, nº 1, doi:10.1121/1.1907010, p. 68–75, ISSN 0001-4966. URL http://asa.scitation.org/doi/10.1121/1.1907010. 12

NYBORG, W. L. 1958, «Acoustic Streaming near a Boundary», *The Journal of the Acoustical Society of America Acoustical Society of America Cavitation Microstreaming The Journal of the Acoustical Society of America*, vol. 30, nº 54, doi:10.1121/1.1907611. 3, 12

OBERTI, S., A. NEILD et T. WAH NG. 2009, «Microfluidic mixing under low frequency vibration», *Lab on a Chip*, vol. 9, nº 10, doi:10.1039/b819739c, p. 1435–1438, ISSN 14730189. 3

OVCHINNIKOV, M., J. ZHOU et S. YALAMANCHILI. 2014, «Acoustic streaming of a sharp edge», *The Journal of the Acoustical Society of America*, vol. 136, nº 1, doi:10.1121/1.4881919, p. 22–29, ISSN 0001-4966. URL http://asa.scitation.org/doi/10.1121/1.4881919. 5, 11, 18

PETKOVIC-DURAN, K., R. MANASSEH, Y. ZHU et A. OOI. 2009, «Chaotic micromixing in open wells using audio-frequency acoustic microstreaming», *BioTechniques*, vol. 47, nº 4, doi:10.2144/000113242, p. 827–834, ISSN 07366205. 3

RAYLEIGH, J. W. S. 2013, *The Theory of Sound, Volume One.*, Dover Publications, ISBN 9780486140438, 985 p.. URL http://cds.cern.ch/record/105679. 2

RAYLEIGH, L. 1945, *Theory of Sound*, vol. 1, Dover Publications, New York, ISBN 978-1-62198-641-6,978-0-486-66016-5. 2, 12

RENAUDIN, A., E. GALOPIN, V. THOMY, C. DRUON et F. ZOUESHTIAGH. 2007, «Creeping, walking and jumping drop», *Phys. Fluids*, vol. 19, doi:10.1063/1.2775412, p. 91 111. URL https://doi.org/10.1063/1.2775412. 2

RILEY, N. 2001, «Steady treaming», *Annual Review of Fluid Mechanics*, vol. 33, p. 43–65. 8

RYU, K., S. K. CHUNG et S. K. CHO. 2010, «Micropumping by an Acoustically Excited Oscillating Bubble for Automated Implantable Microfluidic Devices», *Journal of Laboratory Automation*, vol. 15, nº 3, doi:10.1016/j.jala.2010.01.012, p. 163–171, ISSN 15402452. URL http://dx.doi.org/10.1016/j.jala.2010.01.012. 14

SCHLICHTING, H. 1932, «Über die Stabilität der Couetteströmung», *Annalen der Physik*, vol. 406, nº 8, doi:10.1002/andp.19324060804, p. 905–936, ISSN 00033804. URL http://doi.wiley.com/10.1002/andp.19324060804. 3

SCHUFLE, J. A. 1981, «Answer: Chinese Brass Water-Spouting Bowl», *Isis*, vol. 72, nº 1, doi:10.1086/352653, p. 86–88, ISSN 0021-1753. 2

STOKES, G. G. 2010, «On the Theories of the Internal Friction of Fluids in Motion, and of the Equilibrium and Motion of Elastic Solids», dans *Mathematical and Physical Papers vol.1*, Cambridge University Press, p. 75–129, doi:10.1017/cbo9780511702242.005. URL /core/books/mathematical-and-physical-papers. 4

VAINSHTEIN, P. et M. SHAPIRO. 2008, «Aerodynamic focusing in a channel with oscillating walls», *Journal of Aerosol Science*, vol. 39, nº 11, doi:10.1016/j.jaerosci.2008.07.001, p. 929–939, ISSN 00218502. 3

WANG, C., S. V. JALIKOP et S. HILGENFELDT. 2012, «Efficient manipulation of microparticles in bubble streaming flows», *Biomicrofluidics*, vol. 6, nº 1, doi:10.1063/1.3654949, p. 012 801, ISSN 1932-1058. URL http://aip.scitation.org/doi/10.1063/1.3654949. 7

WHITEHILL, J., A. NEILD, T. W. NG, S. MARTYN et J. CHONG. 2011, «Droplet spreading using low frequency vibration», *Applied Physics Letters*, vol. 98, nº 13, doi:10.1063/1.3574001, p. 2012–2015, ISSN 00036951. 3

WIKLUND, M., R. GREEN et M. OHLIN. 2012, «Acoustofluidics 14: Applications of acoustic streaming in microfluidic devices», *Lab on a Chip*, vol. 12, nº 14, doi:10.1039/c2lc40203c, p. 2438, ISSN 1473-0197. URL http://xlink.rsc.org/?DOI=c2lc40203c. 4

ZACHARIAS, J. et C. D. OHL. 2013, «Fluid dynamics, cavitation, and tip-to-tissue interaction of longitudinal and torsional ultrasound modes during phacoemulsification», *Journal of Cataract and Refractive Surgery*, vol. 39, nº 4, doi:10.1016/j.jcrs.2012.10.050, p. 611–616, ISSN 08863350. URL http://www.ncbi.nlm.nih.gov/pubmed/23395353https://linkinghub.elsevier.com/retrieve/pii/S0886335012018433. 4, 5

ZHANG, C., X. GUO, P. BRUNET, M. COSTALONGA et L. ROYON. 2019, «Acoustic streaming near a sharp structure and its mixing performance characterization», *Microfluidics and Nanofluidics*, vol. 23, nº 9, doi:10.1007/s10404-019-2271-5, p. 104, ISSN 1613-4982. URL http://link.springer.com/10.1007/s10404-019-2271-5. 11, 19

Chapter 2

Methodology

2.1 Experimental characterization

2.1.1 Prototype preparation

The Y-shaped Polydimethylsiloxane (PDMS) channel is designed by 2D photo-lithography. First, a mould made of SU8 negative photoresist was fabricated: a 50 microns-thick SU8 liquid layer was spin-coated on a silicon wafer. After a soft baking at 65°C, the resist was exposed to UV through a photomask. The resist was then immersed in a developer bath and then hard-baked at 95°C. Then, PDMS (Sylgard 184) was thoroughly mixed with 10% in mass of curing agent, degassed in a vacuum chamber, and poured on the SU8 mould in order to constitute a 2.5 mm thick layer of PDMS mixture on top of the wafer. The whole was put in a stove at 65°C during 4 hours.

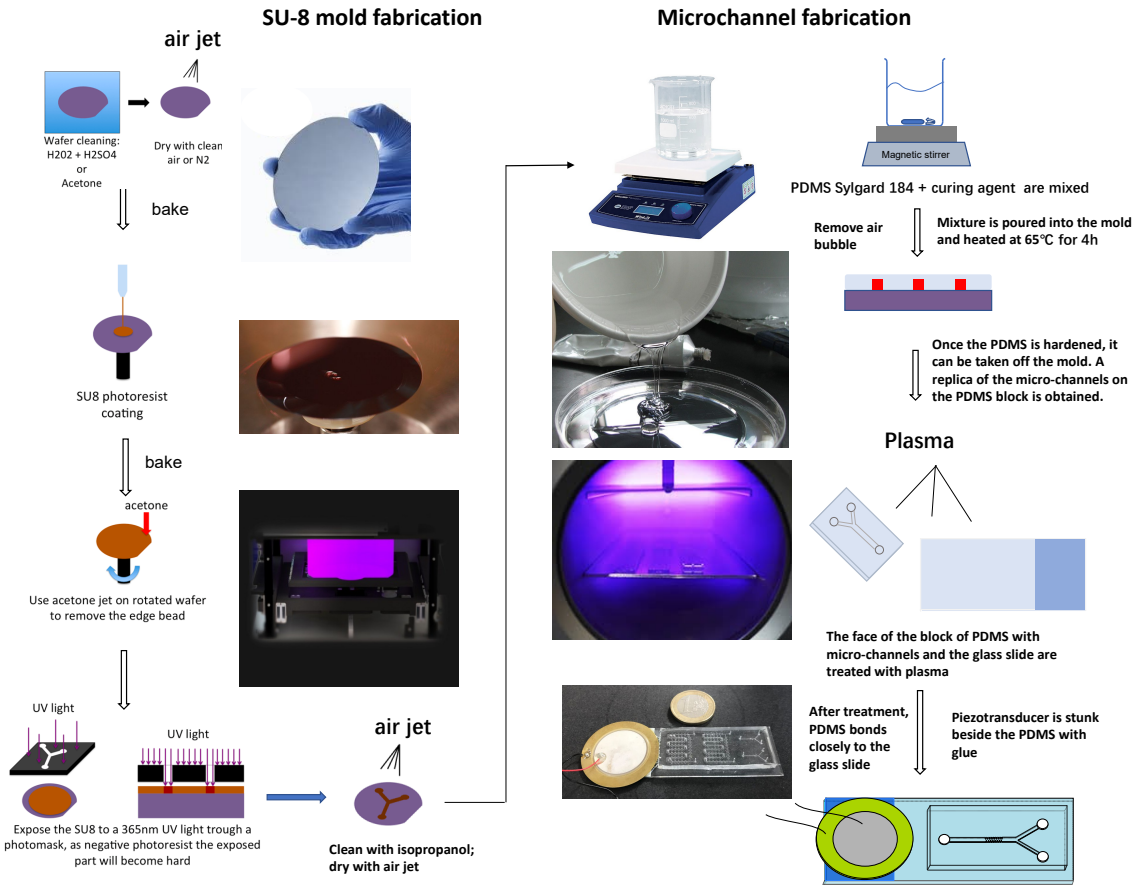

Figure 2.1 – Microfluidic chip preparation process: from SU-8 mold fabrication to the adhesion of PDMS cured microchannel on glass slide

The PDMS microchannel was then sealed and stuck on a glass microscope slide after a 1 min oxygen plasma treatment of both sides. The microchannel of a height of 50 µm was then formed between the PDMS and the glass slide. The plasma treatment enables the microchannel to withstand the pressure from inlets without leakage. Key geometrical dimensions of the Y-mixer are detailed in Fig.2.2. Sharp edges with different angles α (30°, 60°, 80° and 90°), as shown in Fig.2.3, were fabricated from various moulds. Then, all channels were sealed similarly on glass slides, and rapid cure epoxy adhesive was used to permanently glue the transducers on glass slides. It turned out that the best acoustic coupling was obtained this way. The radii of curvatures of the different tips were measured by visualization through a 120X microscope with five repeated measurements of each angle. According to our measurement of the curvature diameter $2r_c$ of the sharp edge, its value ranges from 2.8 µm to 10.3 µm, which is shown in Fig.2.3 and Table 2.1. These values are all smaller than the viscous boundary layer thickness $\delta = \sqrt{2\nu/\omega} = 11.5$ µm, with ν the kinematic

viscosity of the fluid, and ω the angular acoustic frequency $\omega = 2\pi \cdot f$ and $f = 2.5$ kHz.

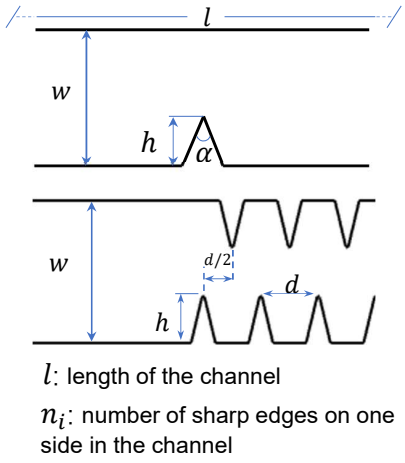

Parameter	Channel with single sharp edge	Channel with multiple sharp edges
w	$500\mu m$	$500\mu m$
l	$7mm$	$7mm$
h	$180\mu m$	$180\mu m$
α	30°/60°/80°/90°	30°
d	-	$100\mu m/200\mu m/300\mu m$
n_i	1	24/12/8

Figure 2.2 – Sharp-edge geometries in different steps of the study

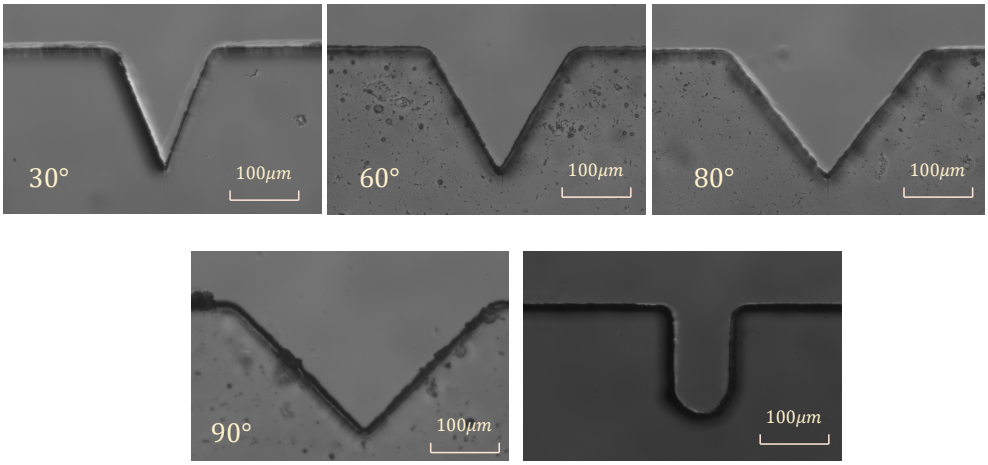

Figure 2.3 – Microscopic view of different sharp edge structures

2.1.2 Experimental setup

Fig.2.4 shows our experimental setup as well as the microchannel geometry. In this thesis, two types of microchannels are fabricated: one is Y-type channel with a single sharp edge on one side; the other is Y-type channel with multiple sharp edges on both sides. The setup around the Y-shaped microchannel (left in Fig.2.4) is composed of a syringe pump (Newtown Company & Co) allowing the injection of fluid from two syringes, under well-controlled flow rate through the channel and via the two inlets. Meanwhile, the fluid flows out via the outlet and enters into a effluent receiver (not shown in Fig.2.4). Three valves are fixed on the two inlet pipes and one outlet pipe. A function generator (Model 33220A Arbitrary waveform generator, Agilent) with a home-made adjustable power amplifier provides input to a piezoelectric transducer (Model ABT-455-RC, RS Components). The voltages imposed on the transducer change from 0V to 60V. The transducer is glued on a standard glass microscope slide (width*length*thickness: 26 mm * 76 mm * 1 mm) through which the visualization is made using a binocular microscope together with a fast camera

tip angle α(°)	30	60	80	90
curvature diameter (μm)	2.8±0.3	5.8±0.4	7.1±0.4	10.3±0.6

Table 2.1 – Curvature diameter corresponding to different tip angles of the sharp edges

(MotionBLITZ Cube4, Mikrotron). The piezoelectric transducer (diameter 35 mm and thickness 0.51 mm, RS PCB Mount Magnetic Buzzer, 85 dB) delivers acoustic vibrations to the glass slide and to the whole channel stuck onto it, at various resonance frequencies from about 0.2 kHz up to 40 kHz, especially in range of 0.2 kHz to 3.5 kHz. The coupling of transducer with glass slide is complicated at audible frequency. In experiment, we chose to operate at these resonance peaks f, namely that at $f = 2.5$ kHz, for which strongest vibration is observed, then $f = 1.2$ kHz, $f = 800$ Hz .... It turns out that the best operating conditions in terms of streaming flow were obtained at these frequencies.

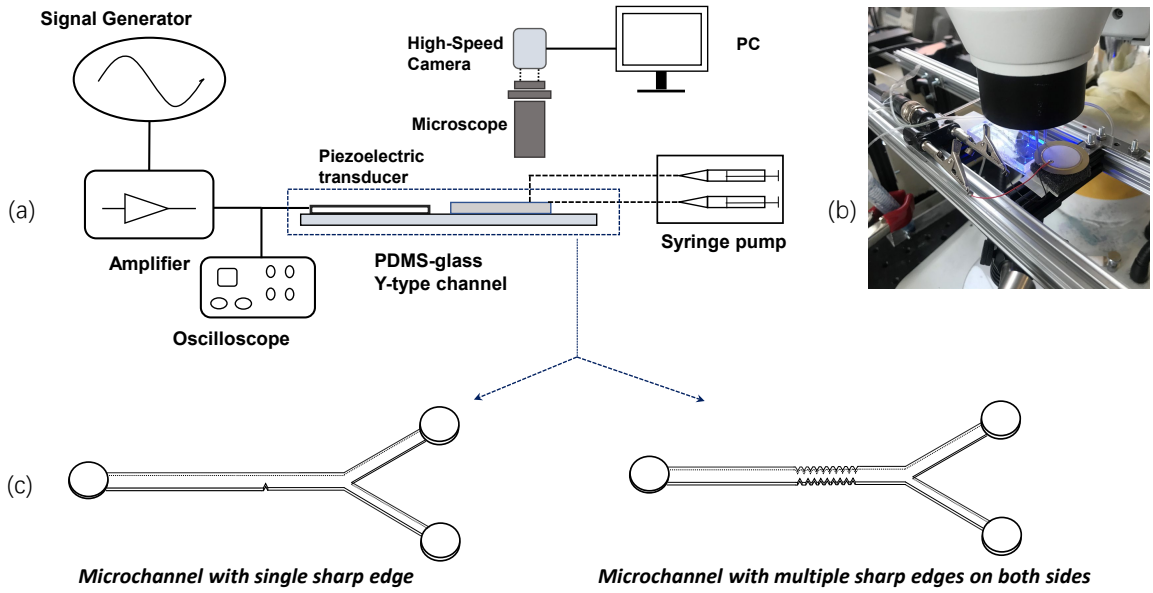

Figure 2.4 – Schematic of experimental setup (a) and its photo (b) with single or multiple sharp-edge channels in (c)

For the experiment without flowrate in the channel, the valves fixed on the inlet tubes and outlet tube are closed to prevent the disturbances from outside. When throughput is needed, two syringe pumps provide equal flow rate Q_s through the two PDMS microchannel inlets. It should be noted that hereafter the channel throughput Q_c is defined as the flow rate in the main channel. It is the sum of the two single inlet flow rates provided by each syringe (Q_s), the latter being always kept equal during the study.

The transducers are excited with periodic sinusoidal signal. After amplification, the available range of peak-to-peak voltage is between 0 V and 60 V. It is important to notice that the speed of sound (c) in water is 1430 m/s and that in glass is 4540 m/s, so the wavelengths of vibration ($\lambda = c/f$) like at 2.5 kHz are respectively 0.57 m and 1.82 m. These values are far greater than the scales of the channel, whose width is 0.5 mm and length is 25 mm. The acoustic wave, in term of phase is therefore expected to be uniform in the whole channel. It's worth noting that the vibration coupling of the transducer and glass slide is very complex. Measurement of different vibration amplitudes is shown in Section 2.1.3.

Streaming velocity visualization

To visualize the flow, the fluid was seeded with fluorescent particles (green polystyrene microspheres, diameter 4.9 µm and 1 µm, Thermo Fisher Scientific). Due to the limited sensitivity of the high-speed camera, the best contrast and image quality were obtained by direct lighting with white light, hence with the diffused light instead of the fluorescence-emitted light. To enhance the contrast, a cold-light beam shined from the bottom of the glass slide. The depth of field of the microscope lens was about 10 microns, five-times smaller than the channel depth (50 microns). Hence, after careful focal adjustments (based on finding the position that shows the maximal transverse velocity for a given flow rate), we obtained high fidelity pictures with clear focus.

Macromixing observation

Two fluids are fed into the two inlets for visualization purpose. The one is Methylene Blue dye (Fisher BioReagents) diluted into deionized water. The other one is pure deionized water. The concentration of Methylene Blue was adjusted so that the images kept unsaturated in terms of grey scale at the strongest concentration.

Micromixing evaluation

The micromixing evaluation follows the Iodide-Iodate (or Villermaux-Dushman) protocol FOURNIER et collab. [1996], involving two competing parallel reactions. Two reactants are prepared: one is with sulfuric acid and the other solution contains I^-, IO_3^- and $HBO_3{}^-$ with well controlled concentrations.

Precautions are necessary in the choice of reactant concentrations with which the Absorbance Unit (AU) given by the spectrophotometry under all operation conditions should fall in the range $0.1 < AU < 3$. This is to guarantee the linearity in the use of Beer-Lambert law to determine the molar concentration of tri-iodide yield. To this end, we adopt a trial-and-error approach to find the best concentration choice, as shown in Table 2.2. Secondly, a micro-cuvette (Hellma, QS105, 50 µL) is necessary since the flow rate is as low as several µL/min.

	$[H^+]$	[KI]	$[KIO_3]$	[NaOH]	$[H_3BO_3]$
C [mol/L]	0.03	0.016	0.003	0.045	0.045

Table 2.2 – Concentration set used to characterize micromixing

2.1.3 Measurement process and data treatment

Measurement of vibration

Generally, vibration field on the glass slide and in the microchannel varies significantly according to factors like sticking style of transducers, position of transducers and structure of channel, etc. This makes the vibration adjustment the most tricky and time-consuming part of the thesis experience. To our best knowledge, no study has been done to accurately investigate the vibration of glass-slide with fluid-filled microchannel at audible frequency. So this brings in a great challenge to make a comparison between different structures or among various glass slides if uniform vibration field can't be ensured. In many papers of T.J. Huang's group HUANG et collab. [2013]; NAMA et collab. [2016], they have presented the vibrating state of the tip of the sharp edge during acoustic excitation and they treated the displacement of the tip as a parameter to characterize the amplitude of vibration field in the channel. However, in our experiment, though with similar setup, we consistently failed to observe the relative motion of the tip to other part of the wall in our experiment.

Chip vibration

We first attempted to use a laser vibrometer to quantify the chip vibration in three dimensions. The measurement was done with a vibrometer (OFV-5000 Modular Vibrometer, Polytec), on an optical table. For frequency of 3 kHz and input amplitudes, the vibration of the chip is measured. As shown in Fig.2.5, for the position on the x-y surface of chip, the displacement and velocity at 60 V (maximum voltage in this thesis) are 0.5 $\times 10^{-8}$ m ~ 3.5 $\times 10^{-7}$ m and 1~7 mm/s. For the other two surfaces, its vibration velocities are even smaller. Considering the magnitude order of SEAS streaming velocity, 7~60 mm/s, it seems that the vibration of surface of the chip is not the cause of the streaming inside the channel or at least it cannot be the direct vibration parameter to analyse the streaming. As discussed by DUAL et MÖLLER [2012], the coupling of piezoelectric materials and chip is usually very complex, vibration of the surface of the chip, though it proves that the chip has been excited by the piezotransducer stuck on it, it fails to help us further investigate the streaming inside the channel. Instead, the focus should be *fluid vibration* inside of the microchannel, or at least the stronger of the two vibrations.

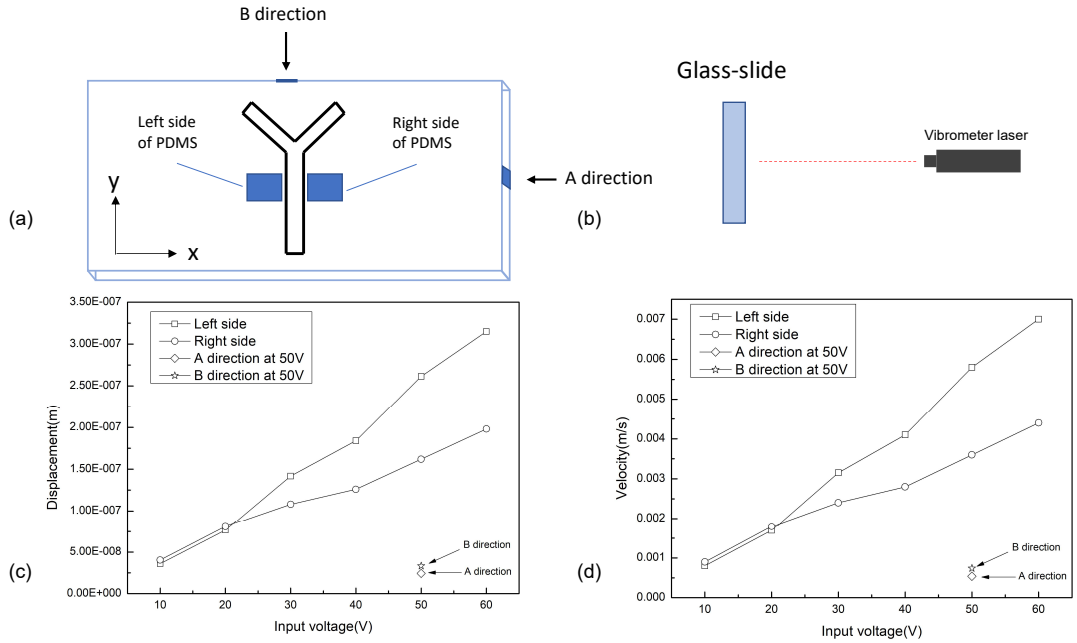

Figure 2.5 – Measurement of vibration and displacement and velocity amplitude on the surface of glass slide at 3 kHz. (a) position of measurement: two positions beside the channel (blue area) and A, B direction perpendicular to two sides of the glass slide; (b) Doppler laser vibrometer is used to measure the vibration; (c)(d) variations of vibration displacement and velocity with input voltages

Fluid vibration

To calibrate the vibration field, in this thesis, we try to use image analysis instead of trying to directly control the vibration field. As shown in the zoom-in picture in Fig.2.6(a), with acoustic excitation, the particles suspending in the fluid have the almost constant displacement (2A) in the area far away from the tip. Note that the direction of the vibration is parallel to the wall. As sinusoidal signal is added on the piezotransducer, we have:

$$2\mathrm{A} = \int_{\frac{n}{f}}^{\frac{1}{2f}+\frac{n}{f}} v_a \sin(2\pi f t)\, dt \tag{2.1}$$

then v_a can be obtained by

$$v_a = 2\mathrm{A} \cdot \pi f \tag{2.2}$$

Based on this method, amplitude of the vibration field can be determined. Fig.2.6(c) shows the variations of the v_a with input voltage, and in the most range of input voltage except value larger than 50 V, their relation is linear. In addition, because of the piezo hysteresis effect, different change trend of the applied electric field may correspond to different displacement curve of the piezotransducer material. For Fig.2.6(c), these data is measured with increasing voltage instead of decreasing input value. This measure process is kept for all experimentations developed in this thesis. However, as mentioned above, vibration field on the glass-slide can't be controlled currently, so relation like Fig.2.6(c) had to be calibrated for every structure studied.

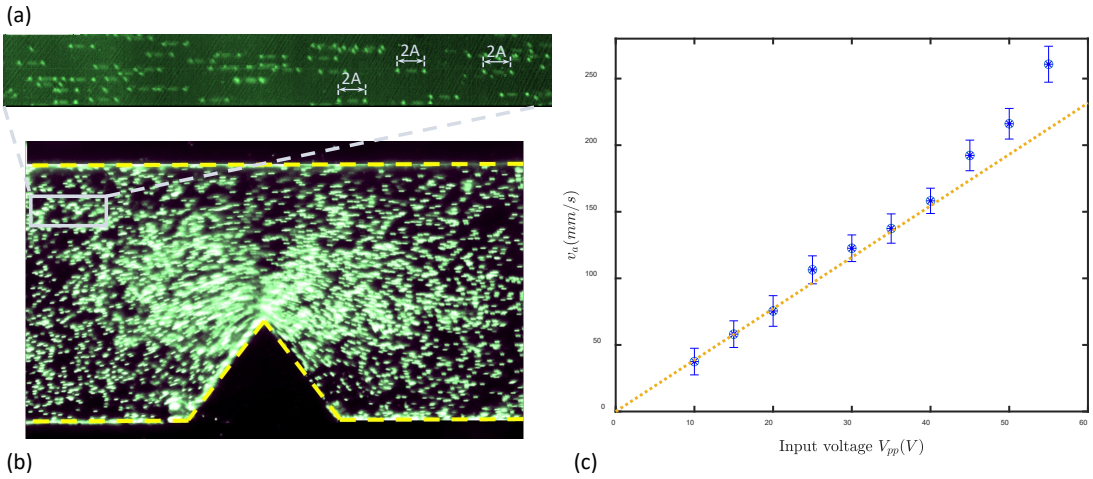

Figure 2.6 – Measurement of acoustic vibration amplitude in fluid by direct visualization. (a) Zoom-in picture showing the displacement of particles in the fluid, stack of four images, corresponding to the real time: one period $1/f$, exposure time 50 µs and fps = 10 000; (b) Streaming motion induced near the sharp edge structure and (c) Variation of vibration velocity with input voltage

Measurement of streaming velocity

Since the streaming velocity near the tip can be of comparable magnitude to the vibration velocity, which is different from most previous studies SQUIRES et QUAKE [2005], another challenge is to observe and measure these two velocities separately. The following methods are used: first, to detect the motion of the particles during one vibration period and compute the streaming velocity, the frame rate of the camera is set to as high as 25 kHz and the exposure time as short as 25 µs. Under this condition, any individual particle appears as a small sphere of a few pixels because the exposure time is much smaller than the vibration period ($1/f = 400$µs). As the schematic shown in Fig.2.7, a total of ten pictures are captured for every vibrating cycle, making the visualization of the acoustic vibration possible. To obtain the streaming velocity, we choose sequential images with a time interval of one acoustic period to "hide" the vibration velocity, just like the red particles in the Fig.2.7.

During the experiment, the pictures are continuously synchronized with the camera to the computer. The vibration of particles has been recorded as videos as supplementary materials of ZHANG et collab. [2019]. Images are processed with open source software ImageJ SCHNEIDER et collab. [2012]. For vibration velocity, the particles' displacements are directly measured from the captured images, as shown in Fig.2.6. For the streaming field, the relative displacement of particles at a given time phase of the vibration period and at given locations, allows the determination of the velocity field. Successive frames are converted into an array of displacement vectors for each particle by the software PIVlab THIELICKE et STAMHUIS [2014]. Second, summing the intensity of the images of a number of frames allows clear visualization of trajectories and then the location, form and sizes of vortices.

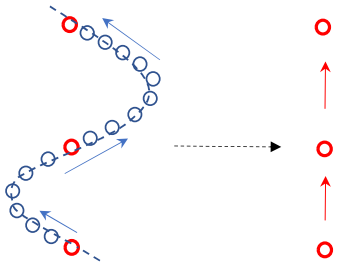

Figure 2.7 – Schematic of measuring the streaming velocity

2.1.4 Mixing characterization

Macromixing evaluation

By observing the variations of the concentration of the blue dye across the channel width and measuring the mixing extent along flow direction, we assess the effect of acoustic excitation on the mixing process. To qualify the macromixing performance, two parameters are introduced in this thesis: one is the normalized concentration to describe the concentration profile along the width of the channel, as shown in Fig.2.8(a), which is to reflect the concentration profile at a specific position and another is the Mixing Index to present the mixing extent following throughput direction, as in Fig.2.8(b). Mixing Index has beed defined in Eqn.1.46. The normalized concentration is obtained by:

$$C_n = ln\frac{I_0}{I} / ln\frac{I_0}{I_b} \tag{2.3}$$

where C_n stands for the normalized concentration; I_0 is the gray value of pure water; I_b is the gray value of the unmixed blue dye liquid; I is the gray value of pixels.

Micromixing assessment and comparison

As mentioned in *Introduction*, measurement of micromixing parameters is based on the parallel competitive reactions. In this thesis, Iodide-Iodate reaction is used, known as Villermaux-Dushman method. As shown in the Fig.2.9, two solutions are injected into the channel, like the process of the macro-mixing above. Once the two solutions contact with each other, chemical reaction starts to proceed in the mixing area. The final solution out from the outlet is collected in the high-precision ultra micro-cuvette (Hellma, QS105 model, 50 µL, light path 10 mm). Each test is under steady-state condition. Furthermore the sample is collected as close as possible from the channel outlet. Details of the chemical reactions appear in Appendix D.

Then the determination of micromixing parameters: Segregation Index outlined below and Micromixing time in the microchannel can be separated into several steps:

a) Measuring the concentration of the I_3^- in the final solution;

b) Calculation of Segregation Index based on the concentrations of reactants in the initial solutions before mixing and concentration of the I_3^- in the final solution after mixing;

c) Building up the relation between Segregation Index X_S and micromxing time t_m through Model of Interaction by Exchange with the Mean (IEM).

Measuring concentration of I_3^-

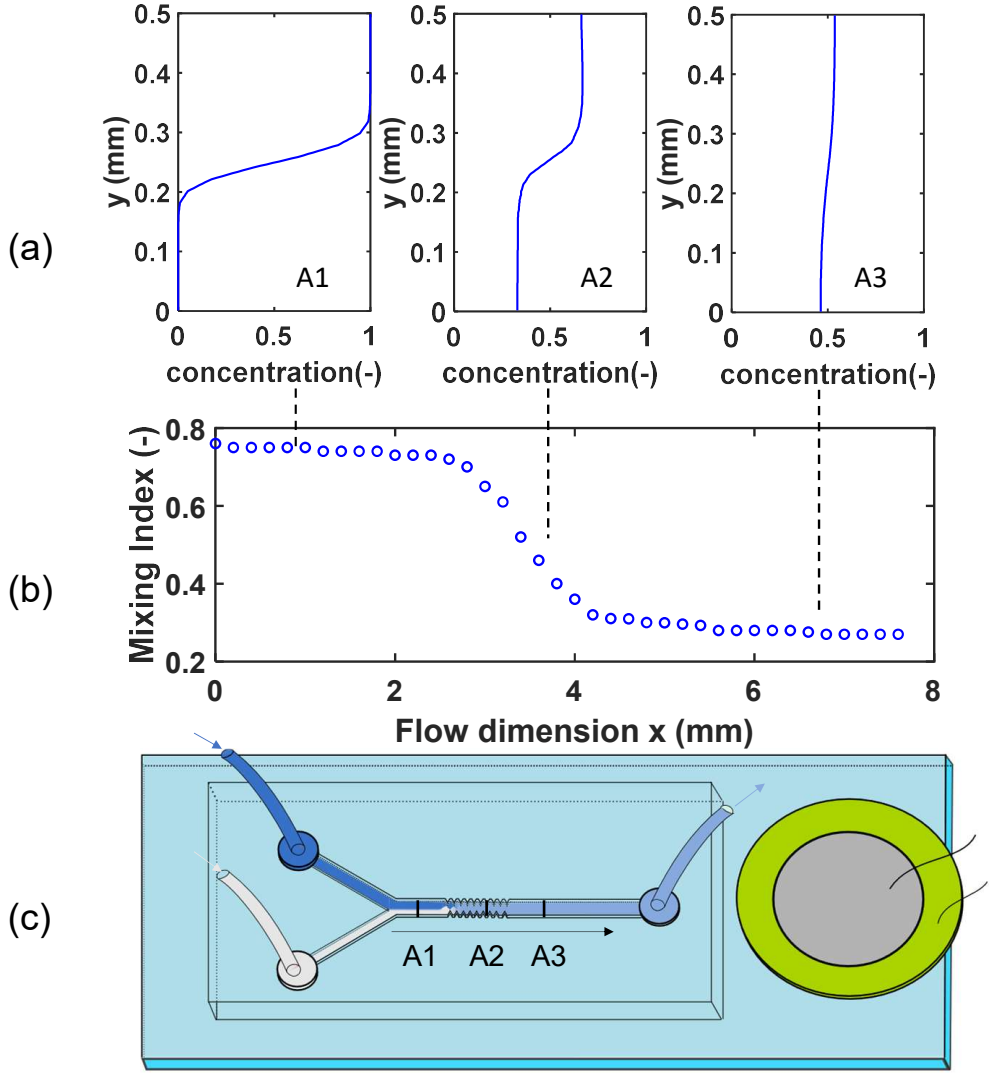

Figure 2.8 – Macromixing performance visualisation in the microchannel: (a) concentration profile along width (like in A1 A2 A3 position); (b) Mixing Index along throughput direction (like along A direction)

A spectrophotometer (Jenway 7310) is used to obtain the Absorbance A during the 353 nm light travels through the final solution in the cuvette. Then concentration of the I_3^- in the final solution can be quantified based on the Beer-Lambert Law, which relates the attenuation of light to the properties of materials through which the light is travelling. To determine its concentration from the Absorbance Unit given by spectrophotometer, we use Eqn.2.4:

$$C_{I_3^-} = AU / \epsilon_{353nm} l \tag{2.4}$$

where AU is the Absorbance Unit (-) through the cuvette, ϵ_{353nm} means the molar attenuation coefficient of tri-iodide ions at its peak absorptivity wave-length at 353 nm, $\epsilon_{353nm} = 26047$ L/(mol·cm), l denotes the optical path length which is $l = 10$ mm in our case.

Calculation of Segregation Index

The Segregation Index (X_S), which characterizes the ratio of consumption of acid ion H^+ in two reactions, is defined as:

$$X_S = \frac{Y}{Y_{ST}} \tag{2.5}$$

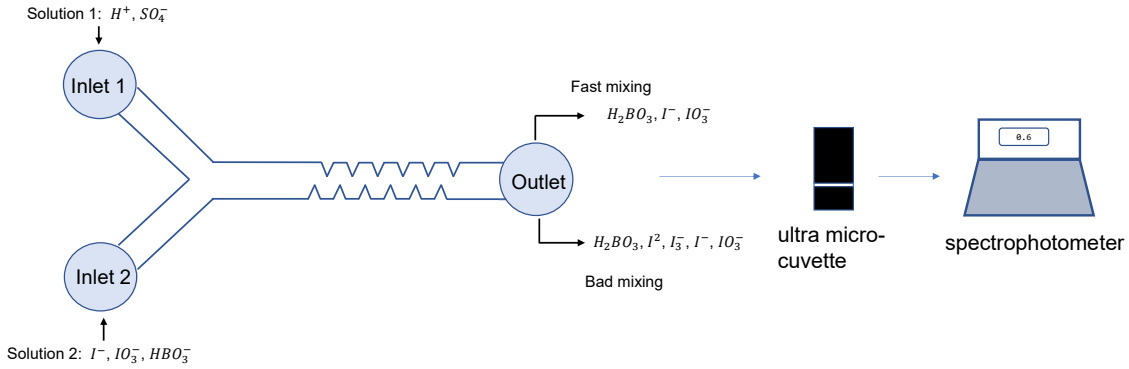

Figure 2.9 – Schematic of Iodide-Iodate reactions used to micromixing characterization of SEAS micromixer

Calculation of Y and Y_{ST} from the concentration of reactants as well as that of the tri-iodide yield follows Eqn.2.6 and 2.7 GUO et collab. [2013]. More specifically, Y is the ratio of acid ion H^+ consumed by reactions R2 (Eqn.1.48) and R3 (Eqn.1.49) and its initial concentration in the mixture. C represents the concentration of ions and Q_1, Q_2 stand for flow rates of different solutions, in this study $Q_1 = Q_2$. Y_{ST} is the higher limit of Y in the total segregation case, also based on the initial boric acid and iodate ions concentrations. Details of calculation are given in Appendix D.

$$Y = \frac{2(M_{I_2} + M_{I_3^-})}{M_{H^+,0}} = \frac{2(C_{I_2} + C_{I_3^-})(Q_1 + Q_2)}{2C_{H_2SO_4}Q_2} \tag{2.6}$$

$$Y_{ST} = \frac{6M_{IO_3^-,0}/M_{H_2BO_3^-,0}}{6M_{IO_3^-,0}/M_{H_2BO_3^-,0} + 1} = \frac{6C_{IO_3^-,0}Q_1}{(6C_{IO_3^-,0} + C_{H_2BO_3^-,0})Q_1} \tag{2.7}$$

Micromixing time determination

In this thesis, IEM model is used to describe the relation between X_S and t_m. Interaction by Exchange with the Mean (IEM) model allows the estimation of the micromixing time GUO et collab. [2013]; VILLERMAUX et FALK [1994], and makes them independent of the concentration choice of reactants. The comparison of mixing evaluation results is thus possible. One pre-requisite of using IEM model is that the residence time of the two solutions from the initial contact and along flow direction being the same. Our sharp edge Y-mixer satisfies this requirement. Besides, another assumption in this model is that exchange of ions between two solutions occurs at a same constant in term of micromixing time t_m, which is generally true for microchannel continuous mixers.

Details of determination of the kinetics for each reaction, IEM model, relation between X_S and t_m refer to Appendix D. The general procedure, as shown in Fig.2.10, is to use a presumed t_m and known initial concentrations of ions, to resolve three differential equations numerically based on second order Runge-Kutta method. For each step, concentrations and their corresponding mean values, kinetic data are updated by the results from the previous step. The iteration process moves forward step by step until the concentration of H^+ in the solution decreases under a critically low value (10^{-9} mol/L in this study). After this, the H^+ is considered to approach zero and the reactions terminate. The final concentration $C_{I_3^-}$ allows to identify corresponding X_S value for the given t_m. An algorithm has been built in Matlab to link Segregation Index with micromixing time in a large range.

Special attention should be paid to the iteration time step h. On the one hand, the step h should be small enough to avoid unrealistic negative concentrations due to global consumption of ions in the reactions; on the other hand, too small time step requires heavier computing loads with more iterations. In this study, the h is kept constant as $10^{-8}s$.

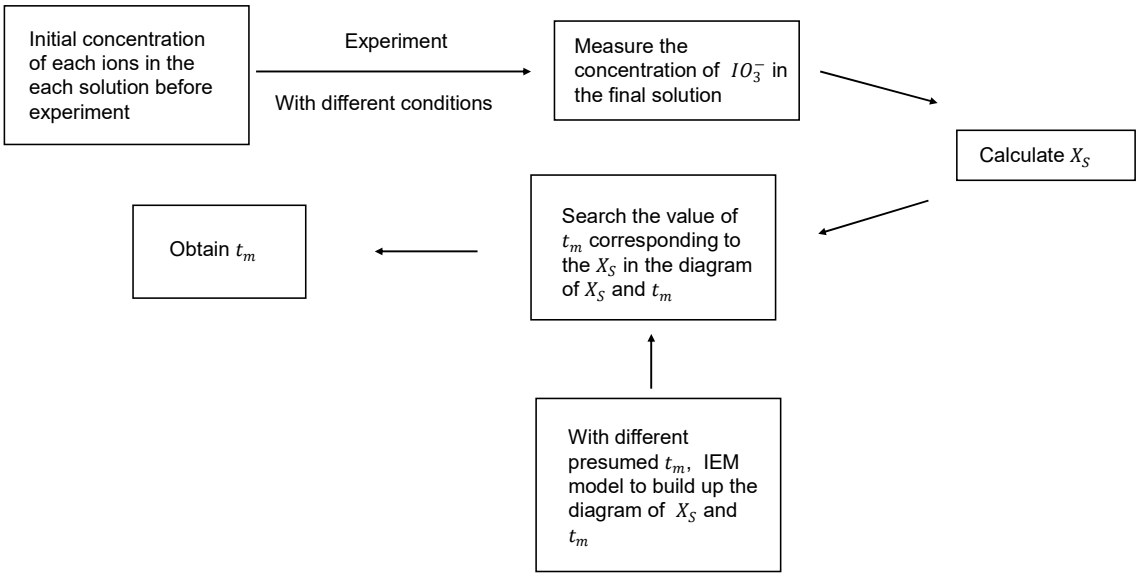

Figure 2.10 – Steps for determining X_S and t_m with the help of IEM model

Energy dissipation rate

In order to facilitate the comparison with other mixers in terms of energy dispassion, energy E_{ac} and power P_{ac} of the vibration field are calculated. Here, the energy dissipation rate only refers to the energy consumed by the fluid inside the channel.

Acoustic energy imposed to a fluid under excitation can be expressed according to v_ω in an acoustic period T:

$$E_{ac} = \frac{1}{T}\int_0^T \int_V \frac{1}{2}\rho {v_\omega}^2 dV dT \tag{2.8}$$

where V is the volume of the channel.

Acoustic power (or acoustic dissipation rate) is time-dependent and can be expressed as:

$$P_{ac} = \int \partial_t (\frac{1}{2}\rho v_\omega^2) dV \tag{2.9}$$

In this thesis, the peak value of P_{ac} during an acoustic period is used.

With the viscous boundary layer and throughput in the microchannel, another term of energy dissipation is related to pressure drop, which is an important parameter, especially for passive mixers. Simulation is done to the part of channel without connectors, as shown in Fig.2.11 to obtain the pressure losses with respect to flowrate Q_c. The energy dissipation rate per unit mass (W/kg) ε_p by pressure drop can be defined as in COMMENGE et FALK [2011]:

$$\varepsilon_p = \frac{Q_c \cdot \Delta P}{\rho \cdot V} \tag{2.10}$$

where Q_c is the throughput; ΔP is the pressure drop of the part of channel concerned; V refers to the volume of the part concerned.

In the case of SEAS mixers, the energy dissipation includes both passive (pressure drop) and active mechanisms (acoustic field). The energy dissipation rate (W/kg) thus includes active and passive parts:

$$\varepsilon = \varepsilon_p + \varepsilon_a = \frac{Q_c \Delta P}{\rho V} + \pi f {v_a}^2 sin(4\pi f t) \tag{2.11}$$

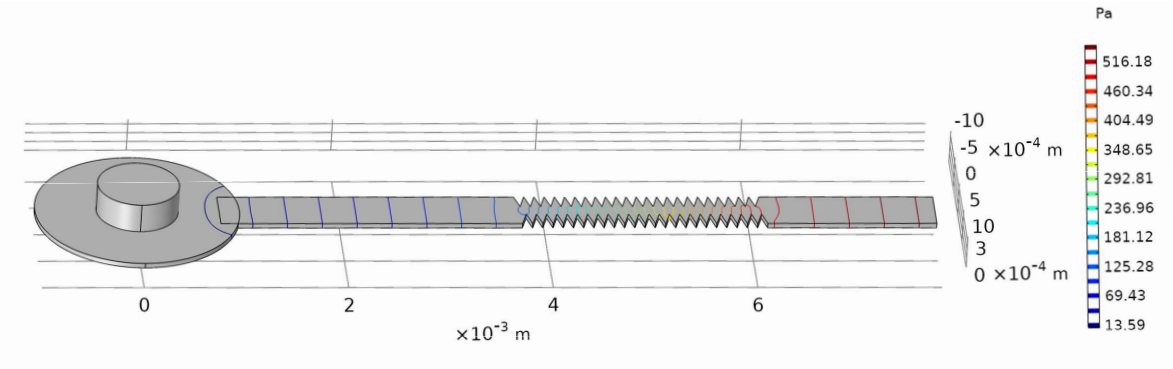

Figure 2.11 – 3D Model in COMSOL to simulate the pressure drop according to channel throughput

2.2 Numerical investigation

While the streaming phenomena at ultrasonic frequency on a chip can be modelled in good agreement with experimental observations BRUUS [2012]; LEI et collab. [2017], the real challenge of the simulation at kHz is how to quantitatively describe the vibration field on the chip. Incorporating the entire chip, including the solid structures surrounding the channel, into the model might be a more sound however also very difficult solution WIKLUND et collab. [2012]. To avoid this, vibration field of fluid is directly determined by the displacement of fluorescent particles in the stacked experimental images, as mentioned above. The results of such measurement are treated as the boundary conditions in this thesis.

As a commonly used numerical scheme, the Perturbation Theory is generally adapted to address acoustofluidics problems in the framework of "weak disturbance". With limited computing load during Computational Fluid Dynamics (CFD), PT is a very powerful tool to reduce the N-S equation, which potentially include non-linear terms that couple the acoustic and streaming velocity fields, into a simpler one where only the non-linear term involving the acoustic velocity within the VBL remains significant. Therefore, PT provides a convenient method to bring out the physical fundamental core of the acoustic streaming problems while retaining relatively simple mathematical formulation BRUUS [2012]; LIGHTHILL [1978]; NYBORG [1953]; OVCHINNIKOV et collab. [2014]; RILEY [1998]; SADHAL [2012].

Although being particularly useful in qualitative interpretation of the origin of acoustic streaming near sharp edges, the classical Perturbation Theory (PT) fails to accurately predict the magnitude of the streaming velocity. The main reason lies in the particularity of sharp edge streaming for which the streaming velocity v_s can be of the same order of magnitude as the vibration velocity v_a ZHANG et collab. [2019], which is not the case for classic Rayleigh streaming. More specifically, the momentum equation Eqn.2.12 can be separated into two parts: oscillatory part (Eqn.2.13) and steady part (Eqn.2.14). PT method simplifies the coupling of v_a and v_s by neglecting the convective terms in Eqn.2.13, $(\mathbf{v}_s \cdot \nabla)\mathbf{v}_a + (\mathbf{v}_a \cdot \nabla)\mathbf{v}_s$. As a consequence, PT method may give inaccurate resolution of the streaming velocity and the coupling terms in the context of sharp edge streaming are to be considered.

$$\begin{aligned}&\frac{\partial \mathbf{v}_\omega}{\partial t} + \{[\mathbf{v}_s + \mathrm{Re}(\mathbf{v}_a e^{i\omega t})] \cdot \nabla\}[\mathbf{v}_s + \mathrm{Re}(\mathbf{v}_a e^{i\omega t})] \\ &= -\frac{1}{\rho}\nabla[p_s + \mathrm{Re}(p_a e^{i\omega t})] + \nu\nabla^2[\mathbf{v}_s + \mathrm{Re}(\mathbf{v}_a e^{i\omega t})]\end{aligned} \tag{2.12}$$

$$i\omega v_a + (\mathbf{v}_s \cdot \nabla)\mathbf{v}_a + (\mathbf{v}_a \cdot \nabla)\mathbf{v}_s = -\frac{1}{\rho}\nabla p_a + \nu\nabla^2\mathbf{v}_a \tag{2.13}$$

$$(\mathbf{v}_s \cdot \nabla)\mathbf{v}_s + \frac{1}{2}\mathrm{Re}[(\mathbf{v}_a \cdot \nabla)\mathbf{v}_a^*] = -\frac{1}{\rho}\nabla p_s + \nu\nabla^2\mathbf{v}_s \tag{2.14}$$

An alternative simulation method consists of directly solving Navier-Stokes equations with pe-

riodic boundary conditions, using DNS (Direct Numerical Simulation) ZHANG et collab. [2020]. With this technique, the time-dependent variable $v = Re(v_a e^{i\omega t}) + v_s$ at a given time-step can be obtained through directly solving Eqn.2.12 in a 2D domain. The steady velocity field can be obtained by taking temporal mean of transient solutions starting form $t = 0$.

$$\bar{v} = v_s + v_0 = \frac{\int_0^t v dt}{t} \tag{2.15}$$

where v_0 is the steady velocity field corresponding to channel throughput.

Although OVCHINNIKOV et collab. [2014] points out the limitation of PT with respect to DNS method, PT remains a powerful framework to analyze the underlying physics of the streaming fields near the sharp tip, especially when the vibration amplitude within the liquid is small enough so that the acoustic Reynolds number $Re_a = \frac{A\omega h}{\nu}$ remains of the order of one.

Based on the above methodology, simulations of the velocity field can be proceeded as the first step. Then, species transport (macromixing) can be included by adding the classical mass transport equation Eqn.2.16 in a second step with species concentration boundary conditions as shown in Fig.2.12 (b).

$$-D_i \Delta C_i + \boldsymbol{v} \cdot \nabla C_i = 0 \tag{2.16}$$

where D_i is the diffusion constant of the i_{th} species. C_i refers to the molar concentration of the i_{th} species. Physically, the equation represents equal value of diffusive part $D_i \Delta C_i$ with convective part $v \cdot \nabla C_i$ in a steady-state source-less diffusion-convection phenomenon.

It is worth noting that in this step, we use the mean steady velocity $\bar{v}$ from the hydrodynamic solution as **v** in the convective term. In other words, the periodic acoustic oscillation velocity is considered to have no influence on mixing. First, this assertion is based on our experimental visualization to a smooth channel, showing no mixing enhancement effect without acoustic streaming even with acoustic ON. Indeed, the first order vibration, as it mainly follows the longitudinal direction of the mixing channel hence in parallel to the main flow, does not increases the transverse advection of the two species.

Specifically, two solutions with $C_1 = 1$ and $C_2 = 0$ allow to directly obtain dimensionless concentration between 1 to 0 (mixing degree). Then macromixing process between two miscible fluids intensified by streaming phenomenon in the micro channel with sharp edges array can be simulated.

2.2.1 Implementation of governing equations in COMSOL Multiphysics

In this thesis, the simulation studies are conducted based on the Finite Element Method (FEM). The equations are implemented and solved in the commercial software COMSOL Multiphysics 5.2.

DNS method

As we mentioned previously, DNS method refers to directly solving Navier-Stokes equations with periodic boundary conditions. In COMSOL Multiphysics, the NS equations included in the Laminar model are:

$$\rho \boldsymbol{u}_t + \rho(\boldsymbol{u} \cdot \nabla)\boldsymbol{u} = \nabla \cdot [-p\mathbf{I} + \mathbf{K}] + \mathbf{F} \tag{2.17}$$

$$\mathbf{K} = \mu(\nabla \boldsymbol{u} + (\nabla \boldsymbol{u})^{\mathrm{T}}) \tag{2.18}$$

$$\rho \nabla \cdot (\boldsymbol{u}) = 0 \tag{2.19}$$

together with an Ordinary Differential Equation (ODE) which is solved simultaneously:

$$\frac{\partial \boldsymbol{uint}}{\partial t} = \boldsymbol{u} \tag{2.20}$$

weak form	weak expression in COMSOL
$\int_\Omega(\rho\frac{\partial \boldsymbol{u}}{\partial t}\cdot\boldsymbol{\psi_1})$	spf.rho*(-ut*test(u)-vt*test(v))
$-\int_\Omega((\nabla\cdot[-p\mathbf{I}+\mathbf{K}])\cdot\boldsymbol{\psi_1})$	(p-spf.K_stress_tensorxx)*test(ux) -spf.K_stress_tensorxy*test(uy) -spf.K_stress_tensoryx*test(vx) +(p-spf.K_stress_tensoryy)*test(vy)
$\int_\Omega(\mathbf{F}\cdot\boldsymbol{\psi_1})$	spf.Fx*test(u)+spf.Fy*test(v)
$\int_\Omega((\rho(\boldsymbol{u}\cdot\nabla)\boldsymbol{u})\cdot\boldsymbol{\psi_1})$	spf.rho*(-(d(u,x)*u+d(u,y)*v)*test(u) -(d(v,x)*u+d(v,y)*v)*test(v))
$\int_\Omega((\rho\nabla\cdot(\boldsymbol{u}))\cdot\boldsymbol{\psi_2})$	-(spf.rho*spf.divu)*test(p)

Table 2.3 – Weak expressions of Eqn.2.17 and Eqn.2.19 in COMSOL Multiphysics software

where $\boldsymbol{u}$, ρ, $\mathbf{I}$,$\mathbf{K}$ and $\boldsymbol{uint}$ refer to the velocity, density, unity tensor, viscous stress tensor and integral of velocity respectively. For FEM, the equations are implemented in terms of weak form. The weak expressions for domain ω of Eqn.2.17 and Eqn.2.19 in COMSOL are listed in Table 2.3. The spf.x refers to the x variable of this Laminar flow(single phase flow) model in COMSOL. Here, the Ψ_1 and Ψ_2 are the basis functions in the weak form and in COMSOL, Ψ_1 and Ψ_2 are denoted as text($\boldsymbol{u}$) and text(p).

PT method

The simulation of streaming flow by the perturbation method is based on the study by MULLER et collab. [2012]. It consists of two steps to resolve the acoustic streaming: i) acoustic field and ii) streaming field.

Acoustic Field

To resolve the acoustic field in the frequency domain, the model of *Thermoviscous Acoustics* in COMSOL is used. At the frequency of several kHz, variation of temperature is negligible. The equations implemented in COMSOL are:

$$i\omega\rho_t+\nabla\cdot(\rho_0\boldsymbol{u}_t)=0 \tag{2.21}$$

$$i\omega\rho_0\boldsymbol{u}_t=\nabla\cdot[-p_t\mathbf{I}+\mu(\nabla\boldsymbol{u}_t+(\nabla u_t)^{\mathrm{T}})-(\frac{2}{3}\mu-\mu_{\mathrm{B}})(\nabla\cdot\boldsymbol{u}_t)\mathbf{I}] \tag{2.22}$$

$$\rho_t=\rho_0(\beta_{\mathrm{T}}p_t-\alpha_p\mathrm{T}_t) \tag{2.23}$$

As fluid with vibration at kHz can be treated as incompressible one, ρ_t is 0 in the equations. In COMSOL, Eqn.2.21 and Eqn.2.22 have to be expressed in weak form, as listed in Table 2.4. In the table, ta.x refers to the x variable of thermoviscous acoustics (ta) model in COMSOL.

Streaming flow

The equations governing the streaming flow consist of the steady NS equations and the force source from the acoustic field:

$$\rho(\boldsymbol{u_2}\cdot\nabla)\boldsymbol{u_2}=\nabla\cdot[-p_2\mathbf{I}+\mathbf{K}]+\mathbf{F} \tag{2.24}$$

$$\mathbf{K}=\mu(\nabla\boldsymbol{u_2}+(\nabla\boldsymbol{u_2})^{\mathrm{T}}) \tag{2.25}$$

$$\rho\nabla\cdot(\boldsymbol{u_2})=0 \tag{2.26}$$

Their weak forms are listed in Table 2.3. In addition to this, for equations of streaming flow, the force source $\mathbf{F}$ includes averaged force term by the acoustic first-order velocity field (Reynolds stress force) and radiation force. The magnitude order of the latter is much smaller at the frequencies in this thesis so only Reynolds stress force are considered.

$$\mathbf{F}=<\rho_1\partial_t\boldsymbol{u}>+\rho_0<(\boldsymbol{u}\cdot\nabla)\boldsymbol{u}> \tag{2.27}$$

weak form	weak expression
$\int_\Omega (i\omega\rho_t + \nabla\cdot(\rho_0 \boldsymbol{u}_t)\cdot \boldsymbol{\Psi_2}$	-(ta.rhot+ta.rho0*ta.divu+ta.u$_t x * d(ta.rho0, x)$ +ta.u$_t y * d(ta.rho0, y)) * test(p1) * (1/(ta.omega * i))$
$\int_\Omega (-i\omega\rho_0 \boldsymbol{u}_t + \nabla\cdot[-p_t\mathbf{I} + \mu(\nabla \boldsymbol{u}_t + (\nabla u_t)^{\mathrm{T}}) - (\frac{2}{3}\mu - \mu_B)(\nabla\cdot \boldsymbol{u}_t)\mathbf{I}]) \cdot \boldsymbol{\Psi_1}$	(-ta.rho0*ta.utx*test(u1)-ta.rho0*ta.uty*test(v1) -ta.T_stress_tensorxx*ta.gradtestuxx -ta.T_stress_tensorxy*ta.gradtestuxy -ta.T_stress_tensorxz*ta.gradtestuxz -ta.T_stress_tensoryx*ta.gradtestuyx -ta.T_stress_tensoryy*ta.gradtestuyy -ta.T_stress_tensoryz*ta.gradtestuyz -ta.T_stress_tensorzx*ta.gradtestuzx -ta.T_stress_tensorzy*ta.gradtestuzy -ta.T_stress_tensorzz*ta.gradtestuzz)*1/(ta.omega*i)

Table 2.4 – Weak expressions of Eqn.2.21 and Eqn.2.22 in COMSOL Multiphysics software

weak form	weak expression
$\int_\Omega \mathbf{F}\cdot\Psi_1$	(ta.rho0*0.5*(real(conj(u1)*d(u1,x))+real(conj(v1)*d(u1,y))))*test(u2) +(ta.rho0*0.5*(real(conj(u1)*d(v1,x))+real(conj(v1)*d(v1,y))))*test(v2)

Table 2.5 – Weak form of force source in the Perturbation method

where $< A(t)B(t) >= \frac{1}{2}Re[A(0)^* B(0)]$, asterisk representing complex conjugation. At the frequencies in this thesis, $\rho_1 \approx 0$, the latter term actually dominates the force source. The weak form of **F** is given by Table 2.5.

2.2.2 Boundary conditions (DNS method)

Boundary conditions for hydrodynamic simulation

Only the channel section with sharp-edge patterns is taken into account in the simulation. As shown in Fig.2.12, for one port of the channel, a periodic velocity boundary condition is given: $v_b = Re(v_{ab}e^{i\omega t}) + v_{0b}$, with v_{ab} being the acoustic vibration velocity v_a at boundary, and v_{0b} being the boundary velocity corresponding to channel throughput (cf Fig.2.12 (a)). The values of v_a measured in the area far away from the sharp edge structure, as described in Fig.2.6(c) are prescribed as v_{ab}. On the other port of the channel, $p = 0$ is set as the boundary condition. Other lateral sides are set as no-slip wall. With this boundary conditions, vibration field through the microchannel from left to right side is simulated. For v_{ob}, similar to the measurement of v_{ab} in Section 2.1.3, particle's displacements d_p based on the two consecutive images are obtained with ImageJ SCHNEIDER et collab. [2012], then at different throughput, $v_{ob} = d_p$·fps. fps is the frame rate of the camera, which is 100Hz during v_{ob} measurement. For simulation cases without throughput, $v_{ob} = 0$.

Boundary conditions for species transport

To simulate the mixing of two separated miscible fluids, the left side is divided into two area, one with dimensionless concentration $C_1 = 1$, another one with dimensionless concentration $C_2 = 0$. For the right port as the outlet for hydrodynamic part and other boundaries, variation of concentrations perpendicular to boundary is set as 0, $n\cdot\nabla C_i = 0$, as shown in Fig.2.12(b).

2.2.3 Steps of simulation

The procedure of the calculation based on PT consists of two steps: i) Solving the wave equation Eqn.2.13 to determine the vibration velocity field in the geometry structure, with first-order

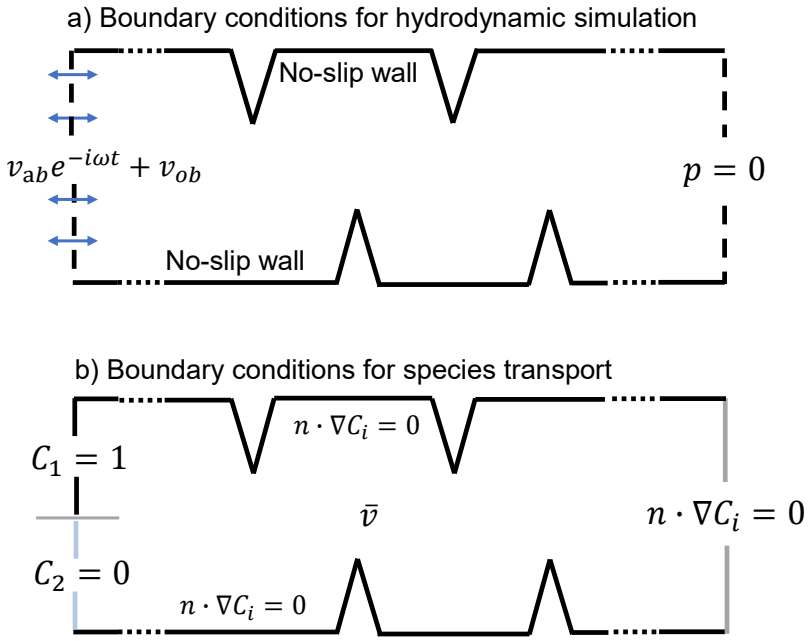

Figure 2.12 – Boundary conditions of simulations

time-periodic terms, and ii) Solving the streaming equation Eqn.2.14, in which the force term in Eqn.2.14 can be determined by the results of the previous step. The second-order terms are steady ones, from which the streaming velocity v_s is deduced. In COMSOL, basic steps to implement Perturbation Method are:

1. Module "Thermoviscous Acoustics, Frequency Domain"for solving the acoustic vibration velocity field; for the boundary conditions, the left and right boundaries are set with the acoustic velocity oscillating at the prescribed value of amplitude in the normal direction, and to be in phase with each other. Other boundaries are set as no-slip walls.

2. Module "Laminar flow" for solving the streaming velocity field with $\mathbf{F}_s = -\frac{\rho}{2}\langle \mathrm{Re}[(\mathbf{v}_a \cdot \nabla)\mathbf{v}_a^*]\rangle$ as the "Volume Force" inserted into the model; The left and right sides of the domain are set as inlet and outlet at given incoming velocity, and are taken equal to zero with no throughput in the channel. The other boundaries are set to be no-slip walls.

The detailed description of DNS has been given in Section 2.2.1. Implementing DNS in COMSOL includes the following steps:

1. Module "Laminar Flow" for direct solving the N-S equations with periodic velocity boundary conditions; Time-independent solver is adopted.

2. Module "Domain ODEs and DAEs" for calculating the time average values of the velocity field in step 1; Then the velocity at steady state $\bar{v}$ is available by time averaging v on an integer number of acoustic periods.

3. Then $\bar{v}$ is set as the background velocity field in 'Transport of Diluted Species' module. Steady solver is adopted.

2.2.4 Mesh and grid independence study

The mesh grid is built with triangle elements, with the maximum element size being 0.014 mm, and the minimum one being 0.0002 mm. Smooth transition is performed with a maximum ele-

ment growth rate of 1.1. Close to the sharp edge, the mesh is refined by inflation layers to better account for the strong velocity gradients inside the VBL. The number of the layers is 3 and the layer stretching factor is 1.2.

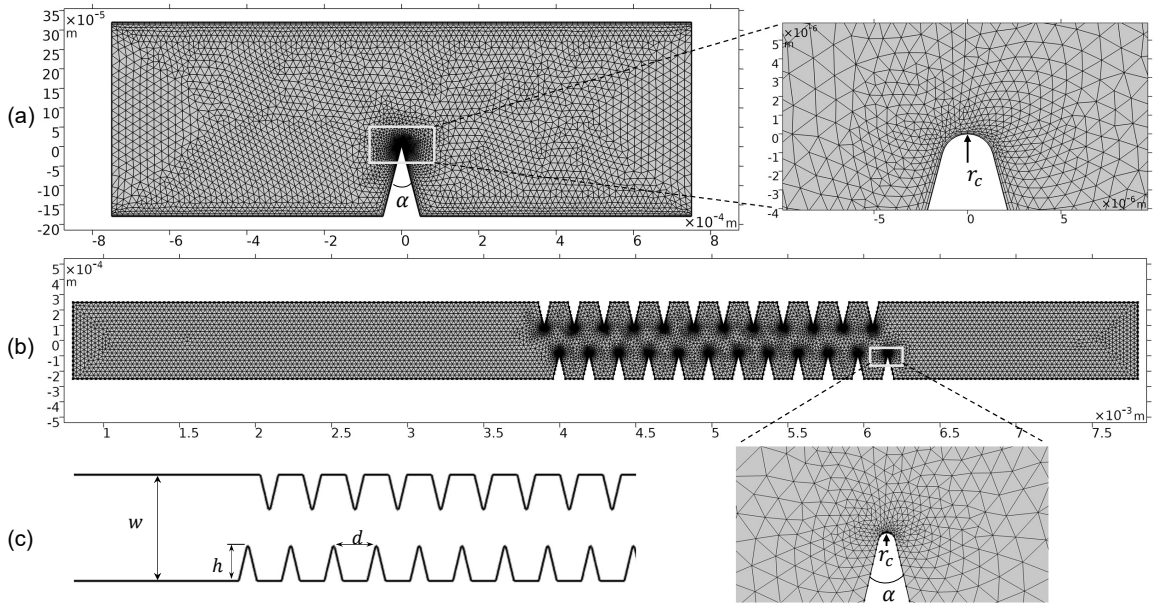

Figure 2.13 – Meshes used in the numerical study, single sharp edge and multiple sharp edges

The mesh independence is assessed by comparing the results from the chosen mesh with those obtained in a refined mesh, which is generated by increasing the number of cells by 30%. Comparing the two meshes, the obtained streaming velocity value differs by less than 1%. The current mesh is thus considered as being a satisfactory balance in terms of accuracy, reliability and computing time.

2.2.5 Time to reach steady streaming field and time step

For the PT method, the two-steps procedure belongs to a steady computation process which can be done almost instantaneously by computer. However, for DNS method, the streaming flow appears after a transient state, and thus needs some time to be fully developed and to reach its steady state. As shown in Fig.2.14(a), the streaming velocity v_{sm} (v_{sm} refers to the maximum value of the streaming velocity field, which is obtained by the time average of the total velocity from the beginning of the simulation to a given time) grows with the number time-steps until reaching a steady state. The corresponding time duration is roughly 12 ms, hence 30 acoustic cycles under the acoustic frequency of 2500 Hz (period of 400 μs).

The value of the time-step is also essential to meet the CFL (Courant-Friedrichs-Lewy) stability condition. The Courant number, given by CFL = $v_a \Delta t / \Delta x$, should be kept lower than 1 to guarantee the numerical iteration stable MULLER et BRUUS [2015]. As shown in Fig.2.14, we test four time-steps from 1 µs to 120 µs, or from $1/400^{th}$ to $3/10^{th}$ of an acoustic period. Only $\Delta t_4 = 120\mu s$ gives a CFL higher than unit but $\Delta t_3 = 80\mu s$ is not fine enough to give a satisfactory maximum streaming velocity v_{sm}, see Fig.2.14(a) and a reliable streaming distribution along the y direction $v_{sy}(y)$, see Fig.2.14(b). We thus choose $\Delta t_2 = 8\mu s$ as a compromise since it gives the same results as $\Delta t_1 = 1\mu s$ but with a shorter computing time. With the chosen time step of 8 µs and a total of 30 acoustic cycles, the DNS computing cost is about 25 mn per case study on an Intel i5-7500 CPU and 16G RAM.

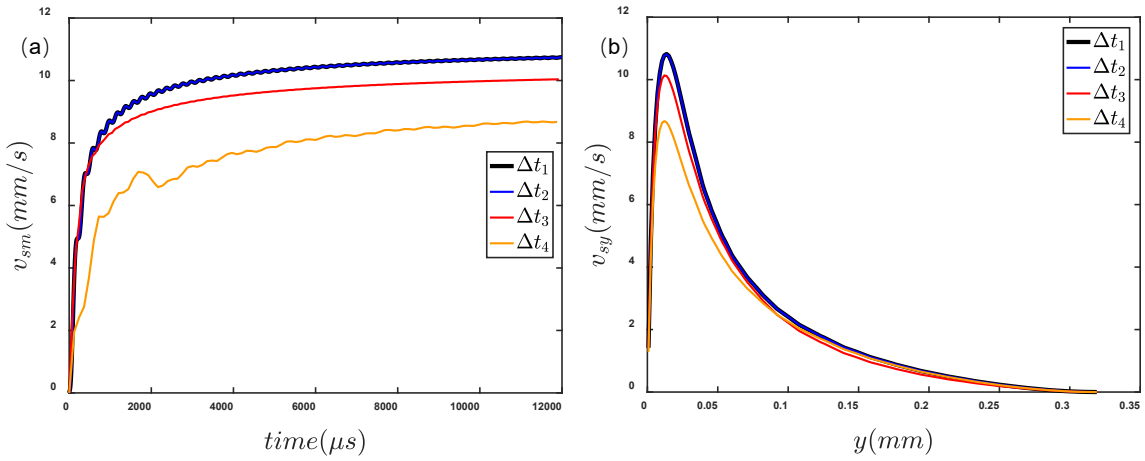

Figure 2.14 – Variation of streaming velocity with numerical iteration time (a), and the steady y-direction streaming velocity at different time steps (b). Time steps $\Delta t_1 = 1\mu s$, $\Delta t_2 = 8\mu s$, $\Delta t_3 = 80\mu s$, $\Delta t_4 = 120\mu s$, correspond to $1/400^{th}$, $1/50^{th}$,$1/5^{th}$ and $1/3.33^{rd}$ of an acoustic period. The whole duration of the simulation equals 30 acoustic periods.

2.3 References

BRUUS, H. 2012, «Acoustofluidics 2: Perturbation theory and ultrasound resonance modes», *Lab Chip*, vol. 12, nº 1, doi:10.1039/C1LC20770A, p. 20–28, ISSN 1473-0197. URL http://xlink.rsc.org/?DOI=C1LC20770A. 36

COMMENGE, J.-M. et L. FALK. 2011, «Villermaux–Dushman protocol for experimental characterization of micromixers», *Chemical Engineering and Processing: Process Intensification*, vol. 50, nº 10, doi:10.1016/J.CEP.2011.06.006, p. 979–990, ISSN 0255-2701. URL https://www.sciencedirect.com/science/article/pii/S0255270111001395?via{%}3Dihub. 35

DUAL, J. et D. MÖLLER. 2012, «Acoustofluidics 4: Piezoelectricity and application in the excitation of acoustic fields for ultrasonic particle manipulation», *Lab on a Chip*, vol. 12, nº 3, doi:10.1039/c1lc20913b, p. 506, ISSN 1473-0197. URL http://xlink.rsc.org/?DOI=c1lc20913b. 30

FOURNIER, M. C., L. FALK et J. VILLERMAUX. 1996, «A new parallel competing reaction system for assessing micromixing efficiency - Experimental approach», *Chemical Engineering Science*, vol. 51, nº 22, doi:10.1016/0009-2509(96)00270-9, p. 5053–5064, ISSN 00092509. URL https://linkinghub.elsevier.com/retrieve/pii/0009250996002709. 29

GUO, X., Y. FAN et L. LUO. 2013, «Mixing performance assessment of a multi-channel mini heat exchanger reactor with arborescent distributor and collector», *Chemical Engineering Journal*, vol. 227, nº 0, doi:10.1016/j.cej.2012.08.068, p. 116–127, ISSN 13858947. 34

HUANG, P. H., Y. XIE, D. AHMED, J. RUFO, N. NAMA, Y. CHEN, C. Y. CHAN et T. J. HUANG. 2013, «An acoustofluidic micromixer based on oscillating sidewall sharp-edges», *Lab on a Chip*, vol. 13, nº 19, doi:10.1039/c3lc50568e, p. 3847–3852, ISSN 14730189. 29

LEI, J., P. GLYNNE-JONES et M. HILL. 2017, «Comparing methods for the modelling of boundary-driven streaming in acoustofluidic devices», *Microfluidics and Nanofluidics*, vol. 21, nº 2, doi:10.1007/s10404-017-1865-z, p. 1–11, ISSN 16134990. 36

LIGHTHILL, S. I. R. J. 1978, «ACOUSTIC STREAMINGt», *Journal of Sound And Vibration*, vol. 61, nº April, p. 391–418. 36

MULLER, P. B., R. BARNKOB, M. J. H. JENSEN et H. BRUUS. 2012, «A numerical study of microparticle acoustophoresis driven by acoustic radiation forces and streaming-induced drag forces», *Lab on a Chip*, vol. 12, nº 22, doi:10.1039/c2lc40612h, p. 4617–4627, ISSN 14730189. 38

MULLER, P. B. et H. BRUUS. 2015, «Theoretical study of time-dependent, ultrasound-induced acoustic streaming in microchannels», *Physical Review E - Statistical, Nonlinear, and Soft Matter Physics*, vol. 92, nº 6, doi:10.1103/PhysRevE.92.063018, ISSN 15502376. 41

NAMA, N., P. H. HUANG, T. J. HUANG et F. COSTANZO. 2016, «Investigation of micromixing by acoustically oscillated sharp-edges», *Biomicrofluidics*, vol. 10, nº 2, doi:10.1063/1.4946875, ISSN 19321058. URL http://dx.doi.org/10.1063/1.4946875. 29

NYBORG, W. L. 1953, «Acoustic Streaming due to Attenuated Plane Waves», *The Journal of the Acoustical Society of America*, vol. 25, nº 1, doi:10.1121/1.1907010, p. 68–75, ISSN 0001-4966. URL http://asa.scitation.org/doi/10.1121/1.1907010. 36

OVCHINNIKOV, M., J. ZHOU et S. YALAMANCHILI. 2014, «Acoustic streaming of a sharp edge», *The Journal of the Acoustical Society of America*, vol. 136, nº 1, doi:10.1121/1.4881919, p. 22–29, ISSN 0001-4966. URL http://asa.scitation.org/doi/10.1121/1.4881919. 36, 37

RILEY, N. 1998, «Acoustic streaming», *Theoretical and Computational Fluid Dynamics*, vol. 10, nº 1-4, doi:10.1007/s001620050068, p. 349–356, ISSN 09354964. URL http://link.springer.com/10.1007/s001620050068. 36

SADHAL, S. S. 2012, «Acoustofluidics 13: Analysis of acoustic streaming by perturbation methods», *Lab on a Chip*, vol. 12, nº 13, doi:10.1039/c2lc40202e, p. 2292, ISSN 1473-0197. URL http://xlink.rsc.org/?DOI=c2lc40202e. 36

SCHNEIDER, C., W. RASBAND et K. ELICEIRI. 2012, «ImageJ», *Nature methods*, vol. 9, nº 7, p. 671–675. 31, 39

SQUIRES, T. M. et S. R. QUAKE. 2005, «Microfluidics: Fluid physics at the nanoliter scale», *Reviews of Modern Physics*, vol. 77, nº 3, doi:10.1103/RevModPhys.77.977, p. 977–1026, ISSN 00346861. URL https://link.aps.org/doi/10.1103/RevModPhys.77.977. 31

THIELICKE, W. et E. J. STAMHUIS. 2014, «PIVlab – Towards User-friendly, Affordable and Accurate Digital Particle Image Velocimetry in MATLAB», *Journal of Open Research Software*, doi:10.5334/jors.bl, ISSN 2049-9647. 31

VILLERMAUX, J. et L. FALK. 1994, «A generalized mixing model for initial contacting of reactive fluids», *Chemical Engineering Science*, vol. 49, nº 24, doi:10.1016/0009-2509(94)00303-3, p. 5127–5140, ISSN 00092509. 34

WIKLUND, M., R. GREEN et M. OHLIN. 2012, «Acoustofluidics 14: Applications of acoustic streaming in microfluidic devices», *Lab on a Chip*, vol. 12, nº 14, doi:10.1039/c2lc40203c, p. 2438, ISSN 1473-0197. URL http://xlink.rsc.org/?DOI=c2lc40203c. 36

ZHANG, C., X. GUO, P. BRUNET, M. COSTALONGA et L. ROYON. 2019, «Acoustic streaming near a sharp structure and its mixing performance characterization», *Microfluidics and Nanofluidics*, vol. 23, nº 9, doi:10.1007/s10404-019-2271-5, p. 104, ISSN 1613-4982. URL http://link.springer.com/10.1007/s10404-019-2271-5. 31, 36

ZHANG, C., X. GUO, L. ROYON et P. BRUNET. 2020, «Unveiling of the mechanisms of acoustic streaming induced by sharp edges», cahier de recherche. 37

Chapter 3

Results and Discussions

In this chapter, the experimental and simulation results of the sharp edge acoustic streaming (SEAS) are presented. They address different aspects of SEAS, from fundamental aspects (physical origin, fluid viscosity sensibility), to mixing application. Besides, the development of DNS gives critical comparison with the current analytical theory. These results are separated into four sections and to be read in combination with four journal papers in Appendix A, B, C and D.

3.1 Unveiling the mechanism of SEAS phenomenon by DNS

Acoustic waves can generate steady streaming within a fluid owing to the generation of viscous boundary layers near walls, of typical thickness $\delta = \sqrt{2\nu/\omega}$. In microchannels, generally, the acoustic wavelength λ is adjusted to twice the channel width w to ensure a resonance condition, which implies the use of MHz transducers to induce the surface acoustic wave on the base material. However, SEAS is an intense streaming flow generated by acoustic waves of a few kHz (hence with $\lambda \gg w$), owing to the presence of sharp-tipped structures of curvature radius at the tip r_c smaller than δ. The study in this section quantitatively investigates this SEAS via direct resolution of the full Navier-Stokes equations in COMSOL. Detailed simulation process has been described in *Chapter1: Methodology* as well as in a paper under revision with "Physics Review E" https://arxiv.org/abs/2003.01208 in Appendix A.

The influence of VBL δ, curvature radius r_c and fluid viscosity ν on the acoustic streaming performance is quantified. Our results suggest choices of operating conditions and geometrical parameters, via dimensionless quantities r_c/δ and δ/w and provide guidelines on how to obtain strong, optimal sharp-edge acoustic streaming. In absence of an established analytical model to describe SEAS mechanism, our numerical scheme and results put a step forward to understand the fundamentals of SEAS.

Main results in this section include:

1. With the presence of the sharp edge structure, the amplitude and direction of the vibration of the fluid particle near the tip changes a lot than that in far-away area. Homogeneity of acoustic vibration field in an area much smaller than the wavelength is broken by the sharp edge structure. As shown in Fig.3.1(a), the acoustic field takes place in the whole channel. Far from the walls, fluid particles oscillate with fixed amplitude A and orientation ruled by that of the nearest wall. As previously stated, while for $\lambda \gg (w, l)$ no streaming force can develop within the microchannel, the presence of a tip induces a sharp spatial gradient in the orientation of vibrations, see Fig.3.1(c), where the aforementioned centrifugal effect clearly appears in the vicinity of the tip.

2. v_{sm}, which is the maximum velocity along y direction from the tip, is introduced to characterize the intensity of the SEAS. Simulation comparison, in term of v_{sm}, between Perturbation Theory (PT)and fully Direct-solving NS (DNS) equation has been done, with different acoustic intensities. It shows that results by DNS are closer to the experimental studies. As discussed in *Introduction*, the particular geometry feature of sharp edge structure makes the perturbation theory less accurate.

3. Parameter $\theta = \Delta v_{sm}/\Delta v_a^2$ that is independent of acoustic intensity, is used to characterize the influence of geometry structure on the streaming intensity, with constant frequency.

4. Dimensionless factor r_c/δ is interpreted as the geometrical origin of the SEAS. These results reveal a decrease of θ with $2r_c$, and this decrease becomes more significant within the range $2r_c > \delta$, see Fig.3.3. Hence, the conversion of acoustic power into streaming flow is less efficient when r_c becomes large. In Fig.3.3, results from simulations using the PT method for the two extreme values of α are put, again in the aim to illustrate the gap between both methods. It confirms that PT systematically over-estimates the magnitude of the streaming flow, by a factor of roughly 1.2. Once $2r_c$ is increased larger than δ, θ significantly decreases, which is common for all tip angles (Fig.3.3). This is in accordance with the spreading and

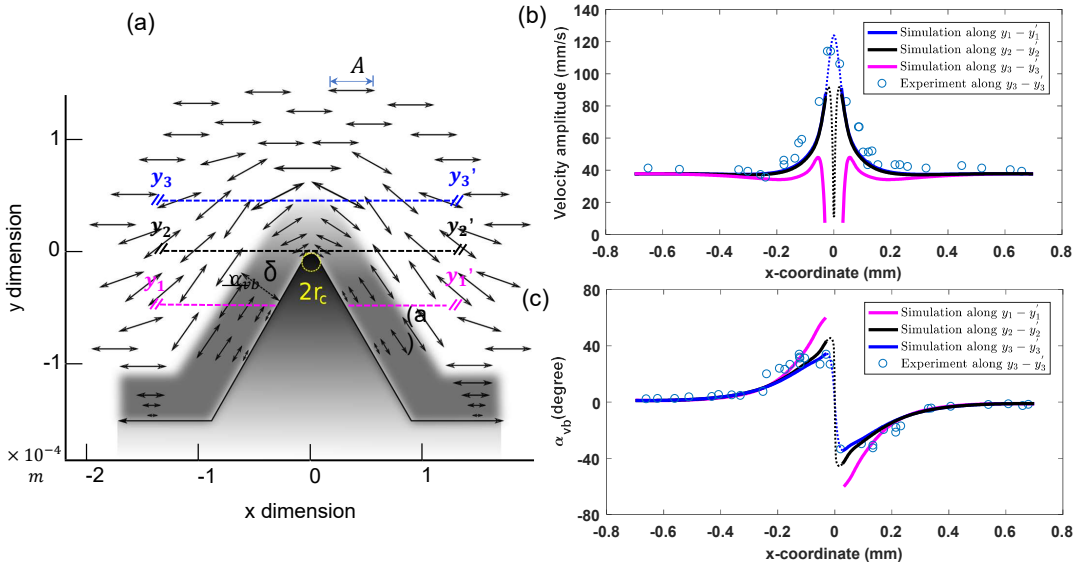

Figure 3.1 – Acoustic vibration and streaming flow around the sharp edge structure: (a) Sketch of the acoustic vibrations of fluid particles near the sharp edge, δ is the acoustic boundary layer, the segment $y_1 - y_1'$ is located 0.05 mm below the tip; $y_2 - y_2'$ intersects the tip; $y_3 - y_3'$ is located 0.01 mm above the tip, (b) Amplitude of the vibration velocity recorded along $y_1 - y_1'$, $y_2 - y_2'$ and $y_3 - y_3'$. Circles stand for experiments recorded along $y_3 - y_3'$, (c) Orientation of the vibration velocity $\alpha_{vb} = \arctan[v_{ay}/v_{ax}]$ along $y_1 - y_1'$, $y_2 - y_2'$ and $y_3 - y_3'$. Circles stand for experiments recorded along $y_3 - y_3'$. Parameters: $\alpha = 60°$, $2r_c$=5.8 µm, f=2500 Hz, v_a=37.8 mm/s, δ=11.5 µm.

weakening contour observed in Fig.3.2(g-h). When the tip is no longer sharp, the magnitude of AS weakens as we should retrieve the classic Rayleigh-Schlichting streaming.

5. Viscosity of the fluid has a significant influence on the intensity of streaming flow. When $r_c/\delta \ll 1$ is satisfied, streaming flow obviously decays with increasing viscosity. In addition, when $r_c/\delta \gg 1$, streaming flow shows no variation with larger viscosity, which is consistent with the previous studies at MHz.

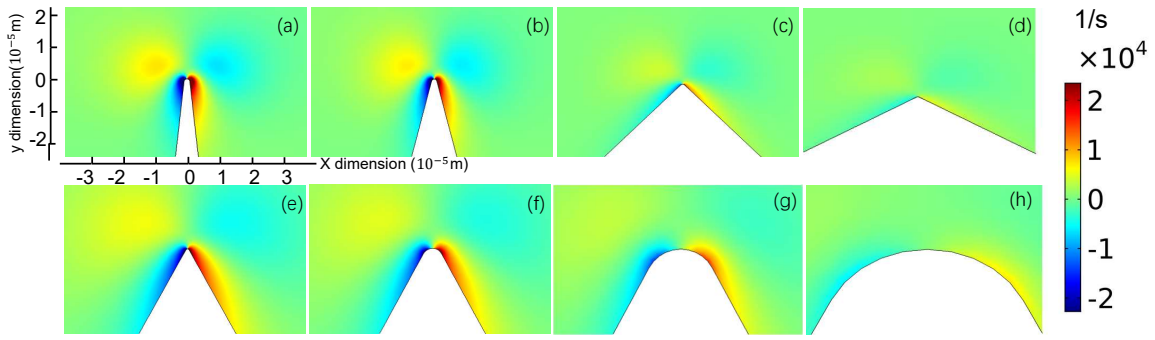

Figure 3.2 – Vorticity maps of the streaming flow near the tip under different geometrical conditions. Red color (positive vorticity) and blue color (negative vorticity) respectively correspond to flows in anticlockwise and clockwise directions. Vibration amplitude $v_a = 101.7mm/s$. For all maps, $f = 2500$ Hz and liquid is water, so that $\delta \simeq 11.3$ µm. Figs.(a)-(d) have the same curvature diameter $2r_c = 2.8\mu m$ but different tip angles α, (a) α = 12°; (b) α = 30°; (c) α = 90°; (d) α = 120°. Figs.(e)-(h) have the same tip angle (α = 60°) but different curvature diameters (e) $2r_c = 1.0$ µm; (f) $2r_c = 6$ µm; (g) $2r_c = 20$ µm; (h) $2r_c = 50$ µm.

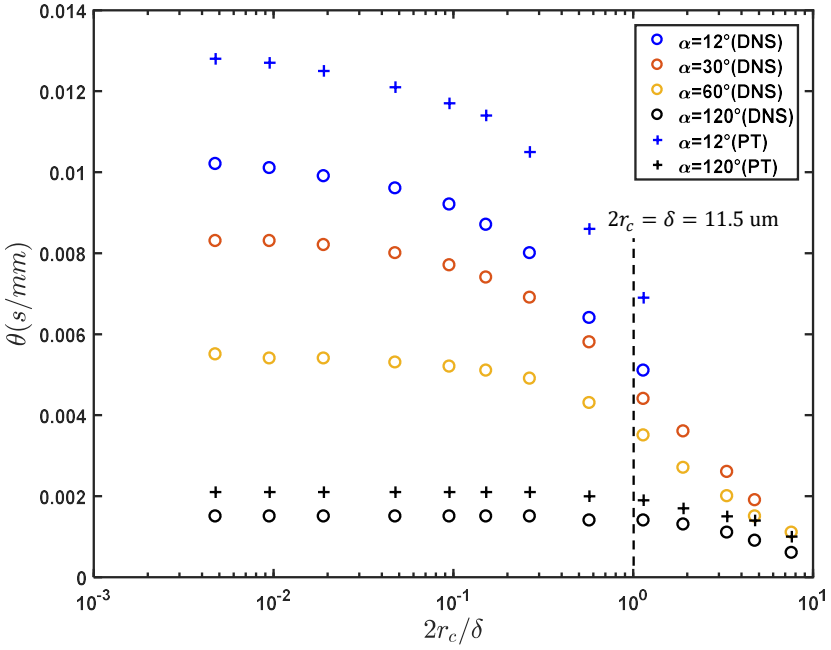

Figure 3.3 – Coefficient θ, based on the maximal value of streaming velocity, versus ratio between curvature diameter $2r_c$ and boundary layer thickness δ, for four different tip angles α. $\theta = \Delta v_{sm}/\Delta(v_a^2)$, fitting efficiency of the momentum conversion from acoustic to streaming flows. DNS results should be considered as reliable and PT simulation appears to over-estimate the result according to the two extreme cases (α = 12° and α = 120°).

3.2 Hydrodynamic interpretation by direct visualization

After investigating the mechanism of SEAS close to the tip, it becomes clear that the geometrical features of the sharp edge play an important role in the generation of acoustic streaming. Qualitatively, the nonlinear term, inertial term $(v \cdot \nabla)v$ in the NS equations becomes very significant near the tip area. And stronger streaming is usually accompanied by sharper structure. For SEAS, the degree of *sharpness* is characterized by tip angle α and curvature diameter $2r_c$, as shown in Fig.1.6(a) in Section 1.1.3. Strong curvature leads to bent trajectories on the time-periodic acoustic flow, which provides favorable condition for stronger streaming generation.

In this section, we experimentally investigate the influence of the sharp structure and vibration velocity on the streaming flow. The geometry of the sharp structure is shown in Fig.2.3. The vibration velocities are characterized by directly visualizing the displacement of tracing particles and the generated acoustic streaming is observed using particle image velocimetry, under various operating conditions. In addition, by measuring the concentration of a fluorescence dye, we evaluate the mixing performance for different values of tip angle, vibration amplitude and flow rate through the microchannel. The followings have been investigated in this section:

Comparison between small r_c which is comparable to the thickness of boundary layer and edge with big r_c, the results show that under low-frequency (2.5 kHz) acoustic condition, intense streaming is only observed near the edge with small r_c, which further confirms that local curvature diameter is a key parameter in the mechanism of SEAS. As shown in Fig.3.4(a), a clear streaming in an extended region appears near the tip when acoustic excitation. The streaming image in Fig.3.4(c) is obtained by superposition of time sequential individual particle trajectories. Two streaming vortices are observed on both sides of the sharp edge. In the case of a round, smooth structure with big enough curvature, as shown in Fig.3.4(d), the acoustic streaming is not observed. While this is not strictly a parametric study on curvature diameter, the result is in accordance with OVCHINNIKOV et collab. [2014] framework demonstrating that this type of streaming should be generated with sharp structures.

Coupling of vibration and streaming motion has also been presented in the experiments. In the left sub-figure in Fig.3.4(c), the particle vibration by taking six images within one vibration period is shown. This allows the quantification of the acoustic vibration amplitude A. On its right, the trajectory of one particle during 10 periods is followed. This picture shows that near the tip, the streaming velocity v_s (in the direction of the sharp tip, shown as vertical) has a magnitude comparable to the vibration velocity v_ω (in the direction of the fluid channel, shown as horizontal). There is a coupling between these two motions.

Streaming around different tip angle α and $2r_c$ are measured. Being consistent with the above analysis, sharpest tip corresponds to the strongest streaming flow, which is characterized by maximum velocity v_{sm} along Y direction from the tip. Same as the simulation results, the linear relation of v_{sm} with v_a^2 can be observed in the experiment.

Further, with and without the throughput Q_c, vortex sizes of SEAS around single sharp edge are measured under different geometry features and acoustic intensity v_a to present the disturbance of the streaming flow into the other area of the microchannel and the main flow. SEAS, though strong near the tip area, decreases quickly in the area far away from the tip. This means that SEAS is sensitive to the throughput. Influence of the Q_c on the vortex size is also investigated in this section. For example, Fig.3.5 shows the variation of vortex size at both downstream and upstream of a 30° tip, under different flow rates. As the flow rate increases from null to 1 µL/min, the vortices size reduces drastically from 0.42 to 0.29 (upstream) and 0.26 (downstream). The vortices continue to shrink after 4 µL/min and they totally disappear when the flow rate is higher than 16 µL/min. In most cases, the upstream vortex is smaller than the downstream one, i.e., between 4 µL/min and 16 µL/min. However, results suggest that there is a threshold of flow rate around 2 µL/min under which the upstream vortex is even larger than the downstream one. A possible underlying reason is that the main stream velocity is lower than the upstream longitudinal AS velocity coming from the counter-flow direction. In such a situation, part of the fluid of the upstream vortex still flows back to the sharp edge, enhancing the vortex development. Otherwise, the fluid goes away with the

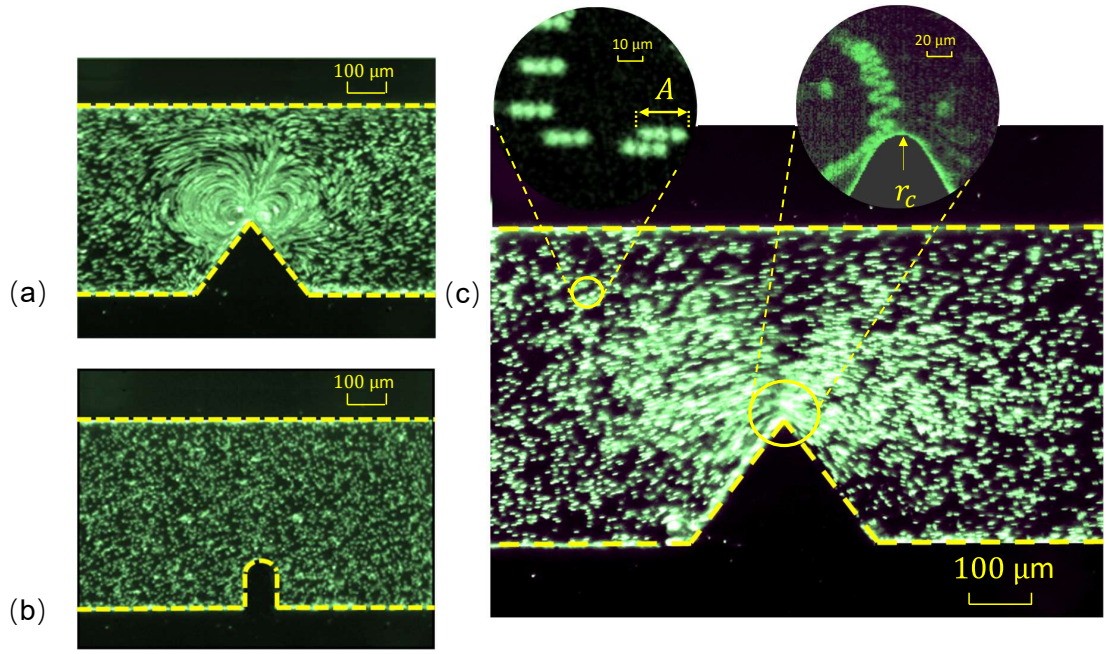

Figure 3.4 – (a) the streamline of the acoustic excited particles movement under a stack of 100 images equivalent to a duration of 100 ms, V_a = 37.8 mm/s, f = 2.5 kHz; (b) round-edge with a curvature of 100 µ m under acoustic excitation but with no acoustic streaming, V_a = 37.8 mm/s, f = 2.5 kHz; (c) the mechanism of acoustic streaming explained by high-speed visualization of acoustic vibrations within the fluid, from particle trajectories over a few periods, the velocity measured is 101.7 mm/s.

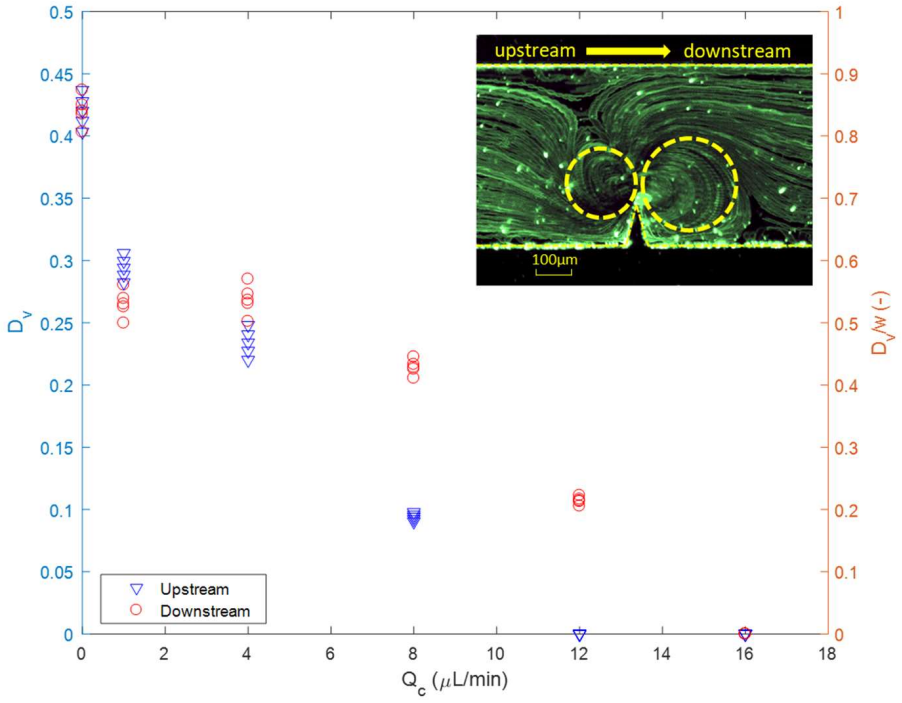

Figure 3.5 – Upstream and downstream vortex size (D_v and D_v/w) at different flowrates. Condition: α=30°, v_a = 70.5 mm/s and f = 2.5 kHz

main flow, thus reducing the vortices size. At higher throughput, comparatively, the downstream vortex varies relatively more slowly with flow rate and is subjected to less influence from main flow, presumably because the vortex is squeezed into the low-pressure area formed by the sharp structure. Although there still exists the upstream vortex at large throughput, it plays little role on the main flow.

Mixing enhancement through SEAS with single sharp edge has been investigated. Mixing Index significantly drops after sharp edge structure, especially under small throughput.

The results are referred to a paper in Appendix. B appeared in "Microfluidics and Nanofluidics" https://doi.org/10.1007/s10404-019-2271-5.

3.3 Coupling Influence of Frequency and Viscosity on SEAS

As discussed in the Section 3.1, geometrical features play an important role in the SEAS. However, for the acoustic frequency f and viscosity ν, as important parameters in acoustic field, their influences on the SEAS are still not very clear. In this section, Experiments are conducted with Particle Image Velocimetry to quantify this streaming flow through the influence of liquid viscosity ν, from 1 mm^2/s to 30 mm^2/s, and acoustic frequency f from 500 Hz to 3500 Hz. Both quantities supposedly influence the thickness of the viscous boundary layer $\delta = (\mu/\pi f)^{1/2}$.

The configuration of the streaming velocity field is presented by the velocity map with PIV. For all situations, the streaming flow appears as a main central jet from the tip, generating two lateral vortices beside the tip and outside the boundary layer. The profiles of the streaming velocity along the y direction from the tip have been plotted. The maximal velocity $V_{s\,max}$ (being equivalent to the v_{sm} of last section) of the profile is located at the distance δ from the tip. Then the position changes with both ν and f. Similar to the above section, this value is used to the characterized the intensity of streaming velocity field. Fig.3.6(a-d) present typical streaming velocity fields obtained from the PIV treatment. The streaming flow appears as a main central jet from the tip, which is symmetric with respect to the y axis (x=0). It clearly appears that the flow intensity decreases with an increasing viscosity. The jet induces the formation of two symmetric vortices beside the sharp edge. In terms of location, the eddies are very near to the tip for the lowest viscosity, and for more viscous liquids they are pushed away and more aside from the tip. Let us also remark that at higher viscosity (Fig.3.6(c and d)), the flow in the VBL along the lateral walls becomes relatively more significant.

The empirical relations with $V_{s\,max}$ with f and ν has been introduced. For example, in the seek for an empirical law quantifying the dependence on f, we tried to plot V_s versus other combinations of V_a^2 and f^β, with β being a real exponent, predicted to equal -0.1 from OVCHINNIKOV et collab. [2014]'s theory, Fig.3.7 shows the two most successful attempts: Fig.3.7(a): the plot of V_s versus $V_a^2 \times f$ shows a good collapse of data for the three lowest frequency values (500, 800 and 1250 Hz). But the rescaling does not fit with the two other data sets corresponding to the highest frequencies (2500 and 3500 Hz). Fig.3.7(b): the plot of V_s versus $V_a^2 \times f^{-1/2}$ shows a fair collapse of data for all frequencies, though it is more convincing at higher acoustic amplitude.

Detailed results can be found in our paper appeared in "Micromachines" in Appendix.C https://doi.org/10.3390/mi11060607.

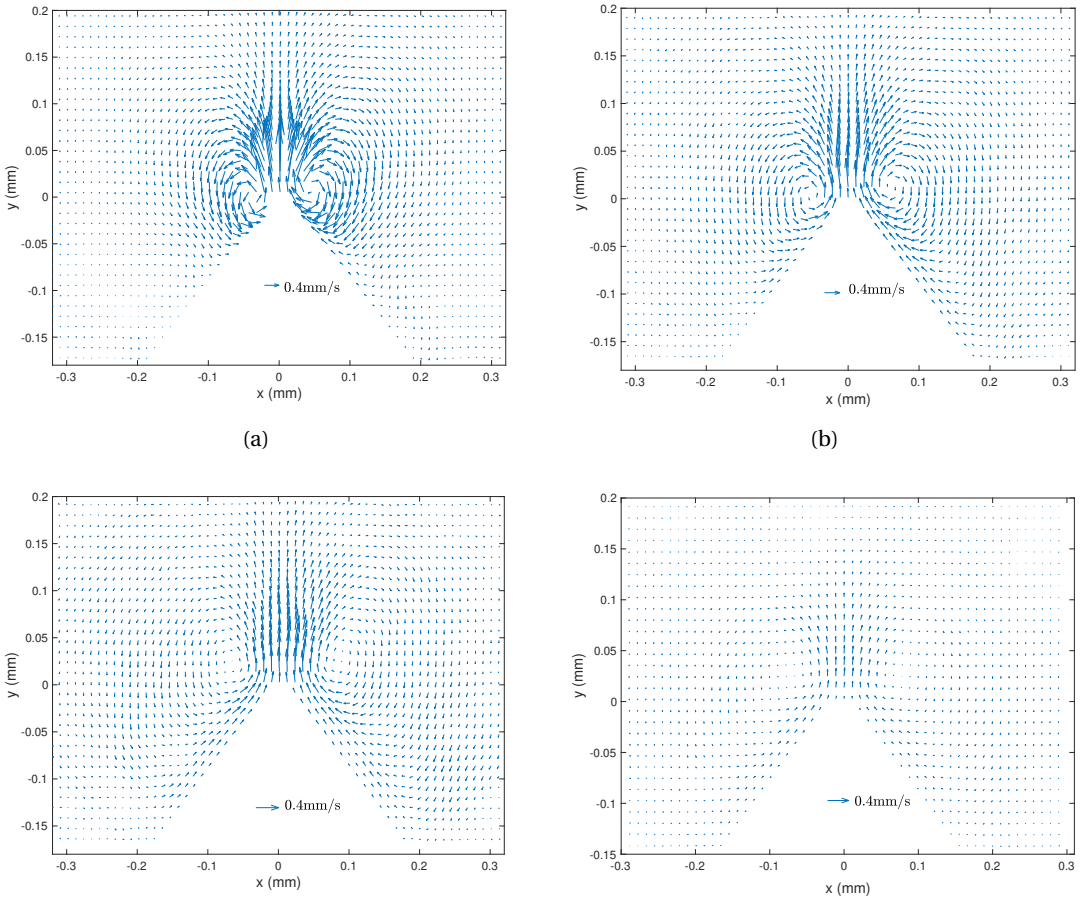

Figure 3.6 – Streaming velocity field $V_s(x, y)$ from PIV measurements, with different liquid viscosities. f = 2500 Hz and V_a = 35 mm/s. (a) ν = 1.158 mm^2/s, (b) ν = 4.32 mm^2/s, (c) ν = 13.75 mm^2/s, (d) ν = 29.44 mm^2/s. Scales are the same for the four cases.

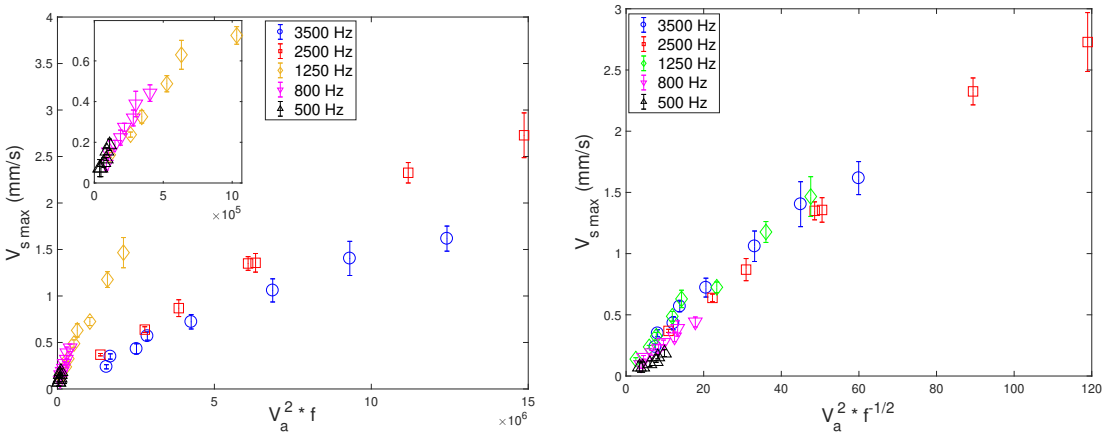

Figure 3.7 – Attempts of data re-scaling for $V_{s\,max}$ (a) versus $V_a^2 \times f$ (insert shows data in the lowest range of V_a^2 and, (b) versus $V_a^2 \times f^{-1/2}$ showing a fair collapse of data.

3.4 SEAS and mixing enhancement in microchannel with multiple sharp edges

Based on the results of above sections, it is reasonable to assert that significant disturbance can be caused by SEAS in the microchannel. Without AS disturbance and due to low Re (from 0.002 to 0.012), molecular exchange between two fluids is dominantly achieved through slow diffusion. However, when SEAS is actuated, the generated vortices can strengthen the mixing process through enlarged interface between fluids. Phenomenologically similar as the Rayleigh streaming, but with strong local Reynolds stress enhancement near the tip, the sharp-edge acoustic streaming is viewed as a promising one since it enables strong streaming disturbance to the flow with low energy input and low-cost transducers and amplifiers. Microchannel SEAS mixer with multiple sharp edges can achieve effective mixing but requires optimal coupling between acoustic streaming and main flow, which is the focus of this section. In this section, three Sharp-Edge Acoustic Streaming (SEAS) micromixers with multiple sharp edge patterns actuated by piezoelectric transducers are investigated to evaluate their mixing performance. To this end, Direct Numerical Simulations (DNS) are used to resolve the multi-physics phenomena involving acoustics, fluid dynamics and additionally mass transfer. Besides, macromixing experiments with Methylene blue dye are carried out to validate the numerical results. Further, experiments with Iodide-Iodate reactions are conducted to evaluate the micromixing performances.

Main findings in this section include:

The mechanism of the mixing process intensified by the SEAS has been clarified. The influence of the sharp edge pattern i.e., the spacing between individual structures, channel throughput as well as acoustic intensity are studied. Shown in Fig.3.8 are numerical dye concentration contours of the three SEAS mixers under the same operating condition (acoustic amplitude v_a=130 mm/s, channel throughput Q_c=8 µL/min). Additional quantified concentration evolution curves across the channel width at five critical longitudinal positions are also illustrated. C_{in} and C_{out} are respectively inlet and outlet of the channel. With the same upstream tracer distribution and two separated fluids, S2 achieves the best mixing result at the downstream while S1 corresponds to the worst mixing(Fig.3.8). Qualitative concentration evolution curves in Fig.3.8 clearly confirm the different performances of the three mixers. With the same inlet C_{in}, a disturbed concentration distribution C_1 can be shown due to the strong advection at the entrance just before the first sharp-edge. Here S1 seems to have stronger disturbance than S2 and S3. Moving on with the main flow, S2 shows higher mixing performance in the whole range between C_2 and the outlet. This is probably due to a large number of effective vortices for mixing enhancement. The performance of S3 is between those of S1 and S2, presumably as the number of sharp edges is limited, but generates effective vortices too. As a matter of comparison, S1 shows the most segregated fluid at the outlet C_{out}, even though it gets a small advantage at the first sharp edge.

Segregation Index (X_S) and micromixing time (t_m) of the optimal channel S2 have been measured under different Q_c conditions. Fig.3.9 shows the values of X_S (left axis) and t_m (right axis) as a function of vibration amplitude v_a, of SEAS mixer S2 at three different flow-rates Q_c. Firstly, as acoustic intensity v_a increases, X_S and t_m drop sharply, which means the achievement of better micromixing performance at the molecular scale. In comparison to the lowest acoustic streaming at v_a=40 mm/s, Segregation Index sharply decreases from 0.06 down to 0.01 under the strongest acoustic intensity (v_a=150 mm/s), confirming the achievement of good micromixing. Micromixing time based on IEM decreases by a factor of 10: from 0.3 s under mild forcing (v_a=40 mm/s, at 10 V) to 0.04 s under strong acoustic vibration (v_a=150 mm/s at 40 V). This is in agreement with the SEAS mixing enhancement mechanism, according to which strong interactive vortices under high acoustic vibration enable to achieve effective mixing.

Another influential factor is the flow-rate Q_c, which is inversely proportional to the residence time. The latter can also be described as the time during which the fluid is *actively* perturbed by acoustic streaming. As shown in Fig.3.9, a lower channel throughput Q_c corresponds to lower X_S and shorter t_m, thus better micromixing. This results are in accordance with our previous section,

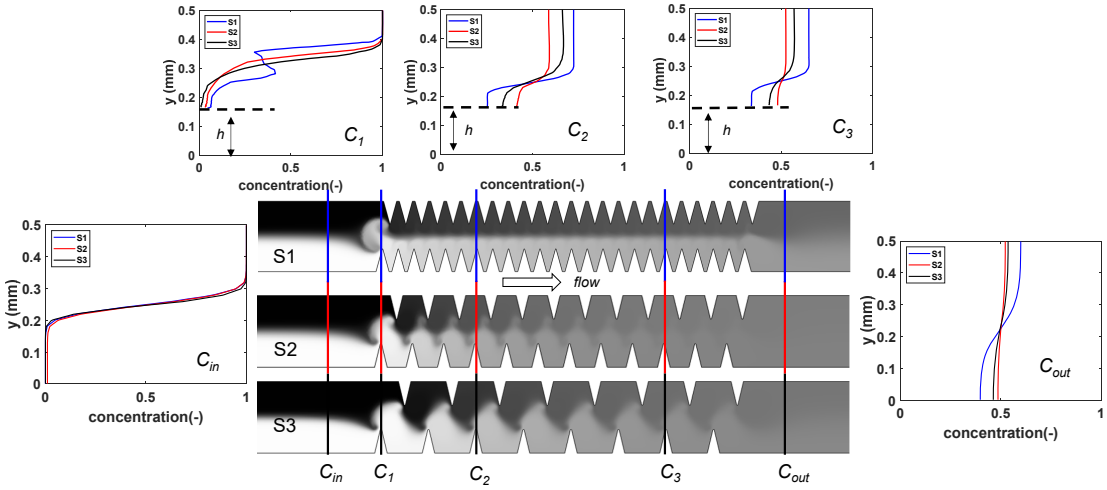

Figure 3.8 – Comparison of mixing performance of three micromixers S1/S2/S3. Numerical simulation under conditions v_a=120 mm/s and Q_c= 8 µL/min for the three mixers. The colour evolution shows S2 to be the optimal sharp edge structure for best mixing application. Concentration curves from C_{in} to C_{out} quantitatively confirms the performance order from S2>S3>S1, with an identical inlet condition C_{in}.

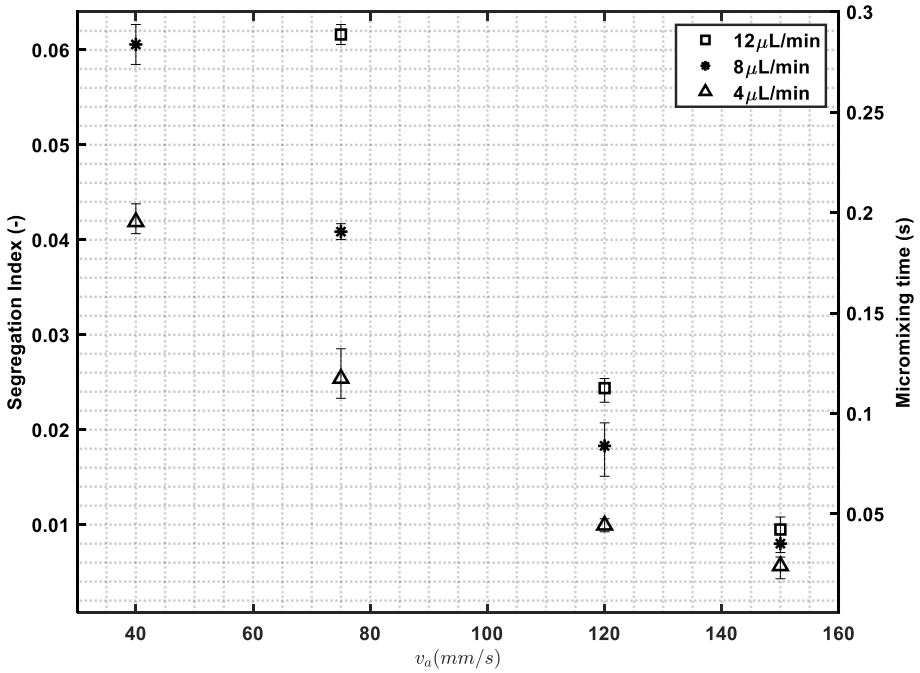

Figure 3.9 – Micromixing performance of SEAS mixer under different flowrate and acoustic intensities. Segregation Index and Micromixing time are shown respectively at the left- and right-axis. Acoustic intensity is controlled by input voltage to the piezoelectric actuator, for a range of 10 V, 20 V, 30 V and 40 V, corresponding to acoustic vibration magnitude of v_a from 40-150 mm/s. Uncertainties are shown by repeated tests for each condition.

according to which the vortex formed by acoustic streaming near a single sharp edge is strongly influenced by the throughput. As Q_c gets higher, the disturbance from the streaming flow into the main one decays, resulting in worse mixing performance. Similarly, the differences of values of X_S and t_m with different throughput are significant. Under weak acoustic field and high throughput, the mixing improvement becomes weak or even negligible.

Finally, a comparison with literature on passive mixers confirms the equivalent micromixing performance of SEAS mixer in terms of Reynolds number and energy dissipation rate.

The above results are part of a manuscript in Appendix.D which is under review at "Chemical Engineering Journal".

3.5 References

OVCHINNIKOV, M., J. ZHOU et S. YALAMANCHILI. 2014, «Acoustic streaming of a sharp edge», *The Journal of the Acoustical Society of America*, vol. 136, nº 1, doi:10.1121/1.4881919, p. 22–29, ISSN 0001-4966. URL http://asa.scitation.org/doi/10.1121/1.4881919. 49, 51

Chapter 4

Conclusions and Perspectives

In this thesis, motivated by the streaming phenomenon near sharp edges, experiments and simulations are conducted to investigate the mechanism of the SEAS and its corresponding application on the mass transfer in a microchannel. Both fundamental interpretation and application work are done. These works have partially answered the questions raised at the beginning of the manuscript and they are summarized in this section.

Besides concluding works done, a general perspective is also given. Future works consist of both fundamental investigations and various speculative applications once we are fully capable to design a SEAS device with perfectly predictable streaming performance.

4.1 Conclusions

The main conclusions of this thesis are highlighted as follows:

1. For the first-order acoustic velocity field, it turns out that both the orientation of the oscillation and its amplitude are *tuned* by the sharp structure to give a strongly localized perturbation to the fluid. This effect, which significantly contributes to the streaming efficiency, depends on the sharp edge structure.

2. For the influence of the tip sharpness, results in Section 3.1 reveals that the two parameters r_c and α are crucial for the generation of acoustic streaming. Sharper the tip (smaller the r_c and α), the stronger streaming field. Results in the Section 3.1 shows that the streaming flow does not gain much in strength when r_c is lowered below $\delta/2$, while streaming magnitude decays significantly with the increase of r_c when$r_c > \delta/2$. The crossover between the SEAS and classical Rayleigh streaming regimes has been investigated by tuning the value of $2r_c/\delta$.

3. Compared with the perturbation theory method (PT), direct solving the Navier-Stokes equations (DNS) presents better predictions of the SEAS. Although requiring higher computation capability and hiding the physical mechanism, the DNS method is proved to provide more reliable solutions and can be a basis to develop more specific analytical analysis of SEAS.

4. Being different from classic Rayleigh streaming, an increase of viscosity leads to globally weaken streaming velocity and outer vorticity. At constant ν_a, a decrease of frequency tends to increase the streaming velocity. Our results, although unexplained by the current theoretical state of the art, suggests the empirical law: $V_s \sim V_a^2 f^{-1/2}$. Furthermore, the lower the frequency f is, the more spread out the streaming vortices are.

5. The streaming flow far from the tip follows an exponential decrease over a certain length scale (for example roughly 130 µm for the angle of 60°, and tip height h = 180 µm). Induced by streaming jet from the tip, symmetrical counter-rotating vortices appear when flow rate is zero. Meanwhile these vortices are sensitive to the throughput and upstream/downstream symmetry is broken as the flow rate is turned on. The perturbation distance by streaming is compressed into a small area as soon as large throughput, like 12 µL/min enters the channel. In addition, not very intuitively, the disturbance extent is crucial for the mixing application, but not the vortex size itself.

6. For microchannel with single sharp edge, perhaps not implausibly, stronger streaming (with sharper tip and under larger vibration magnitude) helps achieve better mixing. Performance of multiple SEAS micromixers doesn't simply scale up the performance of single sharp edge and also depends on the interaction among sharp edges as well as the entrance effect. Comparing different sharp edge patterns, a sufficient number of highly disturbed zigzag flow makes the S2 with d = 0.2 mm best in mixing performance.

7. As an active enhancement device, SEAS mixer corresponds to much smaller micromixing time t_m than the previous mixers, especially passive ones and it shows better performance

at low Re (small flow rate). With respect to the energy dissipation rate, even if the maximum value during the periodic vibration is taken, the energy cost by SEAS mixer can still be comparable to the passive mixers. Considering its disturbance to the fluid, the potential application in chemical or biological fluids mixing is quite promising.

4.2 Perspectives

The current manuscript opens new perspectives in the research on SEAS and development of new acoustofluidic device based on SEAS principle.

4.2.1 Fundamentals of SEAS

From the fundamental point of view, an interesting but tricky work is to investigate the vibration transmission from the source (piezoelectric) to the fluid inside microchannel. From experimentation, as already shown in our vibration measurement, there is a difference between chip vibration and fluid oscillation. The tricky side lies in the double knowledge of acoustic and fluid mechanics, both complex physics branches. A detailed mapping of vibration will be a powerful tool to address this issue.

In addition, using broad-band vibration sources, like natural vibration, flow induced vibration (low frequency), or vibration harvesting, can be an interesting perspective. The search of an optimal structure capable to reach high SEAS but without energy consuming excitation actuator will be appealing. Since we already have a COMSOL scheme who works well, this can be realized in the very near future.

4.2.2 Numerical schemes of SEAS

Regarding the numerical method, a more efficient model or analytical scheme is desirable to precisely represent the physical mechanism of SEAS with NS equations. This also will help to reduce the calculation workload of simulation with FEM, like in COMSOL Multiphysics. After all, the transient solution of Navier-Stokes equations with a higher frequency might require significant amount of calculation time, which should be further multiplied by the number of cases (structure, flow rate, acoustic conditions) to simulate.

4.2.3 Fabrication of SEAS device

Fabrication of acoustofluidic devices has been one of the main challenges throughout this study and requires clean room facilities. Recently, Tsinghua and MIT researchers WANG et collab. [2018] developed an interesting simple technique to expand the prototype capacity of tubular device within the lab. They used thermoforming method to reshape commercial available fluoropolymer tubes into patterned tubular micromixers. This method can be a promising alternative to achieve rapid prototyping with relatively precise flow structure.

4.2.4 Application of SEAS

From an applications point of view, coupling SEAS with heat transfer with the aim of enhancing convection can be a good opportunity. This can be shown as a acoustic driven heat pump similar to the study of magnetic ferrofluid to realize self pumping cooling by CHAUDHARY et collab. [2017].

Further, another important opportunity is to use natural vibration sources on a lower and larger frequency band. The current thesis has paved the numerical protocol as well as some analytical conclusions according to which achieving low frequency SEAS is possible. This will help achieve an vibration energy recovery based process intensification.

4.3 References

CHAUDHARY, V., Z. WANG, A. RAY, I. SRIDHAR et R. V. RAMANUJAN. 2017, «Self pumping magnetic cooling», *Journal of Physics D: Applied Physics*, doi:10.1088/1361-6463/aa4f92, p. aa4f92, ISSN 1361-6463. URL http://dx.doi.org/10.1088/1361-6463/aa4f92. 59

WANG, K., H. ZHANG, Y. SHEN, A. ADAMO et K. F. JENSEN. 2018, «Thermoformed fluoropolymer tubing for in-line mixing», *Reaction Chemistry and Engineering*, vol. 3, nº 5, doi:10.1039/c8re00112j, p. 707–713, ISSN 20589883. URL https://pubs.rsc.org/en/content/articlehtml/2018/re/c8re00112jhttps://pubs.rsc.org/en/content/articlelanding/2018/re/c8re00112j. 59

Appendix A

Paper under revision with Physics Review E

Unveiling of the mechanisms of acoustic streaming induced by sharp edges

Chuanyu Zhang, Xiaofeng Guo, and Laurent Royon
Université de Paris, LIED, UMR 8236, CNRS, F-75013, Paris, France.[*]

Philippe Brunet
Université de Paris, MSC, UMR 7057, CNRS, F-75013, Paris, France.[†]

(Dated: July 31, 2020)

Abstract

Acoustic waves can generate steady streaming within a fluid owing to the generation of viscous boundary layers near walls, of typical thickness δ. In microchannels, the acoustic wavelength λ is adjusted to twice the channel width w to ensure a resonance condition, which implies the use of MHz transducers. Recently though, intense acoustic streaming was generated by acoustic waves of a few kHz (hence with $\lambda \gg w$), owing to the presence of sharp-tipped structures of curvature radius at the tip r_c smaller than δ. The present study quantitatively investigates this sharp-edge acoustic streaming via the direct resolution of the full Navier-Stokes equation, using Finite Element Method. The influence of δ, r_c and viscosity ν on the acoustic streaming performance are quantified. Our results suggest choices of operating conditions and geometrical parameters, in particular the dimensionless tip radius of curvature r_c/δ, but also liquid viscosity.

Keywords: Acoustic Streaming; Microfluidics; Acoustofluidics; Boundary layers

I. INTRODUCTION

Acoustic streaming (AS) is a time-averaged steady flow generated by an acoustic field in a fluid, due to second-order nonlinear effects originating from the coupling between acoustics and hydrodynamics. The phenomenon has attracted researcher's attention for almost two centuries, since as early as 1831 when Faraday [1] first observed steady patterns of light particles on vibrating plates. More recently, AS has been proven to be a useful and non-invasive solution in various applied situations [2], like mixing under low-Reynolds number laminar flow conditions [3], particles manipulation and sorting [4–9], particles patterning [10, 11] or heat transfer [12, 13].

Acoustic streaming originates from the dissipation of acoustic energy within a fluid, which creates a time-averaged effective forcing [2, 14–22]. Meanwhile, depending on where in the fluid acoustic attenuation is mainly prevalent, AS can be induced either by viscous bulk fluid attenuation - denoted as Eckart streaming [15, 17]), or by boundary layer attenuation - denoted as Rayleigh-Schlichting streaming [2, 18–22]). For the latter, the development of an unsteady viscous boundary layer (VBL) along walls can lead to non-zero time-averaged Reynolds stress within this layer [19]. Rayleigh's theory [18, 19, 22] describes that the intense vorticity generated within the VBL appears as an array of eddies pairs (called inner vortices) aligned along the channel walls [7, 23, 24]. This stress extends its influence beyond the VBL of thickness $\delta = \left(\frac{2\nu}{\omega}\right)^{\frac{1}{2}}$ from the wall, where ν is the liquid kinematic viscosity and ω is the angular frequency of the wave, and induces larger-scale eddies of typical width $\lambda/2$ [23, 25] in the fluid bulk.

To achieve AS in microfluidics geometries, the channel width w and the wavelength are generally adjusted to ensure a resonance condition, typically obtained when $w \simeq \lambda/2$ [26]. Given that the sound velocity in water and in most liquids is between 1000 and 1800 m/s,the wave frequency f shall then be of the order of a few MHz. Therefore, while typical cost-effective transducers and associated amplifiers are generally in a range of a few kHz to a few tens of kHz, they should in principle fail to generate AS in microchannels, as the acoustic field would then be homogeneous in space. Although a few studies could circumvent this limitation by tuning the excitation of immersed bubbles [27], with micropillars [28] or flexural waves on a flexible wall [13], by prescribing a wavy channel geometry [29–31], or by tuning streaming modes within the transducer plane [32], the majority of them were carried

Quantity	Abbreviation
Kinematic viscosity	ν
Acoustic wavelength	λ
Viscous boundary layer thickness	δ
Tip angle of sharp edge	α
Height of the sharp edge	h
Radius of curvature of the tip	r_c
Width of the microchannel	w
Acoustic angular frequency	ω
Acoustic frequency	f
Streaming velocity	$\mathbf{v}_s$
Acoustic vibration velocity	$\mathbf{v}_\omega$
Amplitude of acoustic vibration velocity	$\mathbf{v}_a$
Spatial amplitude of acoustic vibration	A
Orientation angle of the vibration velocity	α_{vb}
Maximum streaming velocity	v_{sm}
Maximum streaming velocity along the y-axis	$v_{sm}^{'}$
Fitting coefficient relating v_{sm} and v_a^2	θ
Fitting coefficient relating $v_{sm}^{'}$ and v_a^2	$\theta^{'}$

Table I: Definition of the main physical quantities

out under ideal geometries such as infinite or semi-infinite domains. Still, remaining issues concern the influence of geometry, for instance the presence of obstacles or non-straight profiles like constrictions, or a situation of confinement when δ can be comparable to one of the channel dimensions [25].

Recent studies have shown that intense AS could be generated via the coupling between acoustic waves and sharp structures [33–36]. One of the particularities and main advantages of "sharp-edge AS" is that it is generated at relatively low frequency, typically in the kHz range. Meanwhile, the order of magnitude of the steady streaming velocity can even be comparable to the vibration velocity, hence up to several hundreds of mm/s [37]. Benefiting from this strong disturbance within the fluid, various applications using sharp structures streaming have been developed in microfluidics: mixing processes [35, 38], bio-particle control [39, 40], as well as various on-chip devices [34, 41].

However up to now, the underlying mechanisms of this streaming are not yet fully clear [42]. First, the pioneering study from T.J. Huang's group [33] attributes the induced streaming flow to the mechanical vibrations of the sharp structures induced by a transducer stuck on the microchannel wall. Such a vibration was indeed observed with high-speed imaging, and it raises the question on the adaptation of the sharp edge geometry to the prescribed frequency in order to ensure a resonance condition. In Zhang *et al.*'s study [37], an oscillating flow was prescribed to the whole fluid, which also generates strong streaming around the sharp tip, but without the constraint of operating at a specific frequency. Although Ovchinnikov *et al'*s study [42] suggests that both situations should in principle lead to similar streaming flows, the first-order fluid oscillations in both situations should be different from each other. A very recent study proposed more complete analytical expressions for the streaming flow, as well as detailed flow profiles from numerics and experiments at much higher frequency [43]. The same authors evidenced that sharp-edged structures are also suitable for particle clustering via acoustic radiation pressure [44].

Second, although both experiments [33, 37] and simulations [35, 42] confirm the AS intensity depends on the sharpness of the tip, none of them dissociates the tip angle α from the curvature diameter $2r_c$, as shown in Fig.1(a) and (d), both of which being a sign of sharpness. The difficulty is that in practice, the micro-lithography techniques make these two quantities related to each other [37]. Therefore, only numerical simulations could help to tackle this challenging question. Third, while most studies on acoustic streaming generated around obstacles concern situations where $\delta \ll 2r_c$ and those by Ovchinnikov *et al.* [42] and by Doinikov *et al.* [43] address the opposite situation ($\delta \gg 2r_c$), it is unclear how the crossover between the two situations takes place. Very recently published experimental results showed that the dependence on viscosity and frequency can be more complex than

expected even if $\delta \gg 2r_c$ [45], possibly as a consequence of a constrained geometry as δ can be of the same order as the channel depth d.

Finally, from a theoretical point of view, sharp-edge AS remains a ground for a nonlinear framework in acoustofluidics equations. Indeed nonlinear terms coupling both the steady and periodic velocity fields can become dominant, or at least non-negligible, a feature which in turn is susceptible to make the classical perturbation theory no longer adapted. This situation is the consequence of that, as mentioned above, the streaming velocity can be locally as strong as the vibration velocity [37].

Motivated by these unsolved questions, and in the aim to propose quantitative predictions, the current study aims to address the AS flow under different operating conditions (vibration amplitude A, sound frequency f), fluid properties (kinematic viscosity ν) and geometries (tip sharpness quantified by both r_c and α). This parametric study is made possible by directly solving the full Navier-Stokes equation using Finite Elements Method. Results from the DNS (Direct Numerical Simulation) are first validated by recent experiments, and then compared with those from simulations using classical Perturbation Theory (hereafter denoted as PT). This comparison points out the necessity to treat and include all non-linear terms in the numerical model. In a more applied purpose, this study aims to provide a framework for designing the optimal geometrical structure which would provide the strongest possible AS flow field for a given acoustic forcing.

II. THEORETICAL MODEL

A. Equations of motion

The fundamental equations governing acoustic streaming have been previously presented in various theoretical studies [2, 14, 16, 20, 21, 46, 47], which we summarize thereafter. Bold and normal font style respectively represent vectorial and scalar quantities. Without external body forces nor heat sources and for an isotropic homogeneous fluid, the mass and momentum conservation equations governing the flow are:

$$\frac{\partial \rho}{\partial t} + \nabla \cdot (\rho \mathbf{v}) = 0 \tag{1}$$

$$\rho \frac{\partial \mathbf{v}}{\partial t} + \rho(\mathbf{v} \cdot \nabla)\mathbf{v} = \nabla \cdot \overline{\overline{\sigma}} \tag{2}$$

where ρ is the liquid density and $\mathbf{v}$ the velocity field. The Cauchy stress tensor $\overline{\overline{\sigma}}$ is the sum of the viscosity (μ) term $\overline{\overline{\tau}}$ and pressure term $-p\overline{\overline{I}}$. As in our situation, $\lambda \gg w$, and that the Mach number $Ma = v_a/c \ll 1$, the fluid can be treated as being incompressible, leading to $\overline{\overline{\sigma}} = -p\overline{\overline{I}} + \mu(\nabla\mathbf{v} + \nabla\mathbf{v}^{\intercal})$. Then, Eqs. (1) and (2) can be reduced to:

$$\nabla \cdot \mathbf{v} = 0 \tag{3}$$

$$\rho\frac{\partial \mathbf{v}}{\partial t} + \rho(\mathbf{v}\cdot\nabla)\mathbf{v} + \frac{\mathbf{1}}{\rho}\nabla\mathbf{p} = \mu\nabla^2\mathbf{v} \tag{4}$$

To analyse the AS flow, the Perturbation Theory (PT) constitutes a common framework [2, 14, 16, 20, 21, 46, 47]. The velocity and pressure fields are decomposed into an unperturbed state, oscillating and steady streaming parts, hereafter denoted with subscripts 0, ω and s, respectively:

$$\mathbf{v} = \mathbf{v}_0 + \mathbf{v}_\omega + \mathbf{v}_s,\ \mathbf{v}_\omega = Re(\mathbf{v}_a e^{i\omega t}) \tag{5a}$$

$$p = p_0 + p_\omega + p_s,\ p_\omega = Re(p_a e^{i\omega t}) \tag{5b}$$

where $\mathbf{v}_0 = \mathbf{0}$ is the unperturbed bulk flow considered to be null in this study, $\mathbf{v}_\omega$ is the acoustic (oscillating) part of the velocity field; $\mathbf{v_a}$ is the complex amplitude of the vibration velocity, $\mathbf{v_s}$ is the steady streaming velocity; similarly, p_ω, p_a are the pressure and complex amplitude of the acoustic pressure field, p_0 is the gauge atmospheric pressure and p_s is the steady pressure field associated to the streaming flow. The classical PT assumes $\|\mathbf{v}_s\| \ll \|\mathbf{v}_a\|$ and $p_s \ll p_\omega$, i.e. that the streaming flow velocity is of considerably lower magnitude than the driving acoustic velocity [2, 15, 35, 36, 42, 43, 46–49]. Given the strong AS which is generated near sharp edges, we dismiss these simplifying assumptions.

By injecting the decomposition of Eq. (5) into Eqs. (3) and (4), and after a bit of algebra, the momentum equation leads to time-dependent (Eq. 6) and steady (Eq. 7) parts:

$$i\omega\mathbf{v}_a + (\mathbf{v}_s\cdot\nabla)\mathbf{v}_a + (\mathbf{v}_a\cdot\nabla)\mathbf{v}_s = -\frac{1}{\rho}\nabla p_a + \nu\nabla^2\mathbf{v}_a \tag{6}$$

$$(\mathbf{v}_s\cdot\nabla)\mathbf{v}_s + \frac{1}{2} < Re[(\mathbf{v}_a\cdot\nabla)\mathbf{v}_a^*] >= -\frac{1}{\rho}\nabla p_s + \nu\nabla^2\mathbf{v}_s \tag{7}$$

Equations (6) and (7) both contain non-linear terms in velocity, coupling the unsteady and steady components. By time-averaging Eq. (7), one then sets a body force $\mathbf{F_s}$ to account for the non-linear effects of vibration motions [15, 42]:

$$(\mathbf{v}_s \cdot \nabla)\mathbf{v}_s = \frac{1}{\rho}(\mathbf{F}_s - \nabla p_s) + \nu\nabla^2\mathbf{v}_s \tag{8}$$

where the body force is:

$$\mathbf{F}_s = -\frac{\rho}{2}\left\langle Re[(\mathbf{v}_a \cdot \nabla)\mathbf{v}_a^*]\right\rangle \tag{9}$$

here the operator $< . >$ stands for a time-averaging over one period of acoustic oscillation $1/f$.

In the PT framework, the non-linear terms at the left-hand side of eq. (6), coupling $\mathbf{v}_a$ and $\mathbf{v}_s$, are commonly neglected. Also in Eqs. (7) and (8), $(\mathbf{v}_s\cdot\nabla)\mathbf{v}_s$ is considered as a negligible, fourth-order term in most previous studies of acoustic streaming [2, 15, 42, 43, 46–48]. As stated above, in the case of sharp-edge streaming, ignoring these terms should deviate the modelled results from reality. The primary reason is, as previously mentioned, $\mathbf{v}_s$ can be of the same order as $\mathbf{v}_a$. It implies that the convection of the acoustic field by the streaming one becomes significant, as it was directly revealed by our previous experimental results, see inset of Figure 5 in [37], especially in the upper range of acoustic velocity. The second reason lies in the boundary layer. Under usual situations where δ is much thinner than any other lengths of the problem - in particular, much smaller than the radius of curvature of the boundary walls, the resolution is carried out by solving separately the streaming flow within the steady VBL [20, 47, 48] and that outside of the VBL. It consists of prescribing a distribution of slip velocities along walls, previously derived from the calculation within the VBL, to the fluid bulk. In the case of sharp edges when $r_c < \delta$, the direct numerical resolution in the whole domain, and especially within the VBL, becomes necessary. Ovchinnikov *et al.*'s study [42] was dedicated to this situation, and our study is partly inspired by their approach. As our study aims to investigate streaming flows in an extended range of amplitude, we choose to keep these terms in our simulations.

B. Qualitative view of the streaming force

Let us now briefly examine the term $\mathbf{F}_s$ of Eq. (9). We assume that $\mathbf{v}_a = [v_{ax}\, v_{ay}\, 0]$ is a vector remaining in the (xy) plane, which is true far from the upper and lower walls. Let us then calculate $\mathbf{v}_a$ in this plane:

$$(\mathbf{v}_a \cdot \nabla)\mathbf{v}_a = \begin{pmatrix} v_{ax}\dfrac{\partial v_{ax}}{\partial x} + v_{ay}\dfrac{\partial v_{ax}}{\partial y} \\ v_{ax}\dfrac{\partial v_{ay}}{\partial x} + v_{ay}\dfrac{\partial v_{ay}}{\partial y} \\ 0 \end{pmatrix}$$

Results from our previously reported direct high-speed visualization [37] showed that, near sharp edges, the acoustic velocity field in fluid is aligned in parallel to the nearest wall. Furthermore, the no-slip boundary condition sets $\mathbf{v}_a$=$\mathbf{0}$ along walls so that the amplitude of acoustic oscillations decreases to zero approaching the wall. This velocity gradient is the origin of shear stress within the VBL.

In summary, gradients of acoustic velocity should originate from at least two effects: (i) the no-slip boundary condition which creates variation of acoustic velocity amplitude from $v_a = 0$ at the wall to $v_a \simeq A\omega$ at a distance to the wall farther than δ, here A is the spatial amplitude of the acoustic vibration, and (ii) the orientation of $\mathbf{v}_a$ bending by an angle of $\pi - \alpha$ over a distance of $2r_c$.

Along a straight horizontal wall, v_{ay} is null and v_{ax} is invariant with x. Therefore, only v_{ax} and $\frac{\partial v_{ax}}{\partial y}$ take non-zero values, which implies that $\mathbf{F}_s$ is null along a straight wall. This can easily be generalised along any straight wall of arbitrary orientation. However, the streaming force $\mathbf{F}_s$ is non zero where there is a steep change of orientation of $\mathbf{v}_a$, typically achieved near a sharp tip. This non-zero force is the origin of a centrifugal-like effect emphasised in previous studies [37, 42].

Let us finally remark that we deliberately choose to keep dimensional quantities in this study. First, our study aims for a quantitative comparison with previous experiments, which is made easier with dimensional quantities. Second, our problem involves four length scales which must be decoupled from each other. More specifically, the acoustic wavelength (λ), the channel width (w), the VBL thickness (δ) and the tip radius of curvature (r_c), must fulfil the condition: $\lambda \gg w \gg \delta \gg r_c$. This condition would lead to complex formulations for dimensionless equations. Thirdly, the COMSOL software we use for our simulations,

naturally handles dimensional quantities.

III. DESCRIPTION OF THE NUMERICAL SCHEME

Most of the numerical results presented in this paper are based on the direct solving of the Navier-Stokes equation (DNS). We also present a few results obtained from the Perturbation Theory (PT) inspired from Ovchinnikov *et al.*'s study [42]; so that the efficiency of the two methods can be compared under different conditions. Both PT and DNS simulations are conducted with Finite Element Method (FEM) using COMSOL Multiphysics [50]. Details of the simulation implementation scheme are described in Appendices A to E.

A. Domain of study

The geometry of the microchannel with a single sharp tip are detailed in Figure 1. Length and width of the channel are respectively $l = 1.5$ mm and $w = 0.5$ mm. A symmetrical sharp structure with a tip angle α and a curvature diameter $2r_c$ is located on one side of the channel. While both α and $2r_c$ are taken at different values for different simulation cases, the height of the sharp structure is kept constant: h=0.18 mm.

It worth noting that the simulations are conducted in the framework of a bidimensional (2D) geometry. Precisely, the channel is considered infinitely deep. This choice is justified by two main reasons. First, all previous experiments of sharp-edge streaming including ours, are conducted with water and f equal to a few kHz, yielding δ between 8 and 15 μm, while the channel depth d is equal or larger than 50 μm. Second, the cross-sectional depth/width aspect ratio is roughly 1/10. As a consequence, the streaming develops essentially within the (xy) plane.

Near the sharp edge, the mesh is refined (Fig. 1) since velocity gradients - thus the streaming force, are expected to be locally concentrated near the tip, since the mesh step is locally much smaller than r_c. The mesh refining also allows to accurately account for the sharp geometry of the tip. Furthermore, a similar mesh refinement is also imposed within the VBL of both channel and sharp-edge walls. This is essential to finely simulate the effect of viscous shear stress from which AS originates.

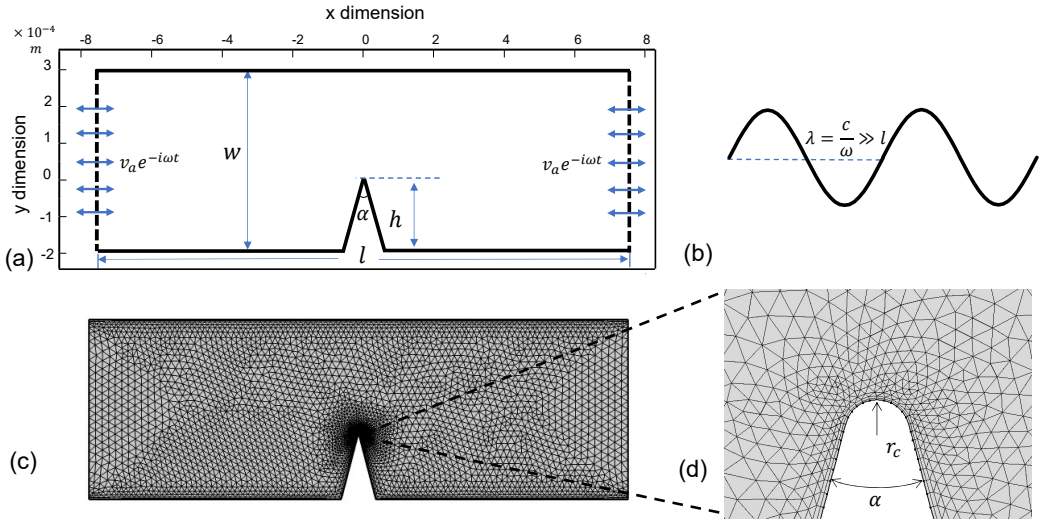

Figure 1: Geometry of the domain of study, sketched in the top-left inset, together with the acoustic wave parameters in the top-right inset. The mesh for the computation is shown in the bottom figure, with a magnified view around the sharp edge tip on the right.

B. Boundary conditions

DNS is different from the PT method as it directly computes the fluid motion equations (6-8) for the acoustic oscillations (time-periodic) and for the steady streaming. Periodic boundary conditions are set at left and right ends of the channel. The left end (here set as the inlet) is attributed a periodic velocity $v_x = v_a sin(2\pi ft)$ along the horizontal direction and $v_y = 0$ along the vertical one. For the right end (outlet), a condition of pressure fixed at p_0 is assigned.

Since the fluid remains incompressible, and the length scale of the domain is much smaller than the acoustic wavelength ($l \ll \lambda$), the above conditions result in an in-phase periodic velocity for the right and left borders, as shown in Fig. 1. These conditions are supported by experimental observations of oscillations of fluid particles within the whole channel, while the sharp-edged tip remains static in the laboratory frame [37]. A no-slip condition is prescribed on all other channel boundaries including along the sharp edge itself.

For the time-dependent simulations, each acoustic period is discretized into 50 time steps, for an overall duration of 30 acoustic periods. It turns out that this duration is sufficient to allow the full establishment of a quasi-steady acoustic streaming, once the flow is averaged

over an acoustic period. Moreover, the choice of 50 time steps per acoustic period is validated by comparing the streaming results from 4 different time steps. This validation process is documented in Appendix D and shown in Fig. 12.

IV. RESULTS AND DISCUSSIONS

A. Validation of the numerical scheme

The comparison between previous experimental results [37] and present DNS ones, ensures the validation of our numerical scheme. Figures 2 and 3 intend to illustrate the mechanism of acoustic streaming, by showing both typical acoustic and steady velocity fields. Figure 2(a) presents a qualitative sketch and Figures 2(b-c) show typical amplitude and orientation of the acoustic velocity field from both experiments and numerical simulations.

1. Acoustic velocity

As shown in Figure 2(a) and Figures 3(a-d), the acoustic field takes place in the whole channel. Far from the walls, fluid particles oscillate with fixed amplitude A and with orientation roughly imposed by that of the nearest wall. As previously stated, while for $\lambda \gg (w, l)$ no streaming force can develop within the microchannel, the presence of a tip induces a sharp spatial gradient in the orientation of vibrations, see Fig. 2(c), where the aforementioned centrifugal effect clearly appears in the vicinity of the tip. This effect induces a locally strong streaming jet shooting from the tip, as shown in Fig. 3(b).

Careful high-speed Particle Image Velocimetry (PIV) measurements of the acoustic flow reveal that oscillations close to the tip are stronger than elsewhere in the channel, roughly by a factor of two to three. The exact value of this factor is found to depend on both α and v_a, and presumably on the height h.

Figures 2(b) and (c) respectively show the amplitude of the acoustic velocity v_a and the vibration orientation, quantified by the angle α_{vb}, obtained from both experiments and simulations. Approaching x=0, the velocity v_a sharply increases from its value far from the tip (38.5 mm/s), to reach its maximum value at $x = 0$ (here roughly 120 mm/s) and then sharply decreases back to its value at infinity, see Fig. 2(b). The values of the velocity amplitude v_a and angle α_{vb} are respectively symmetrical and antisymmetrical about $x = 0$, along

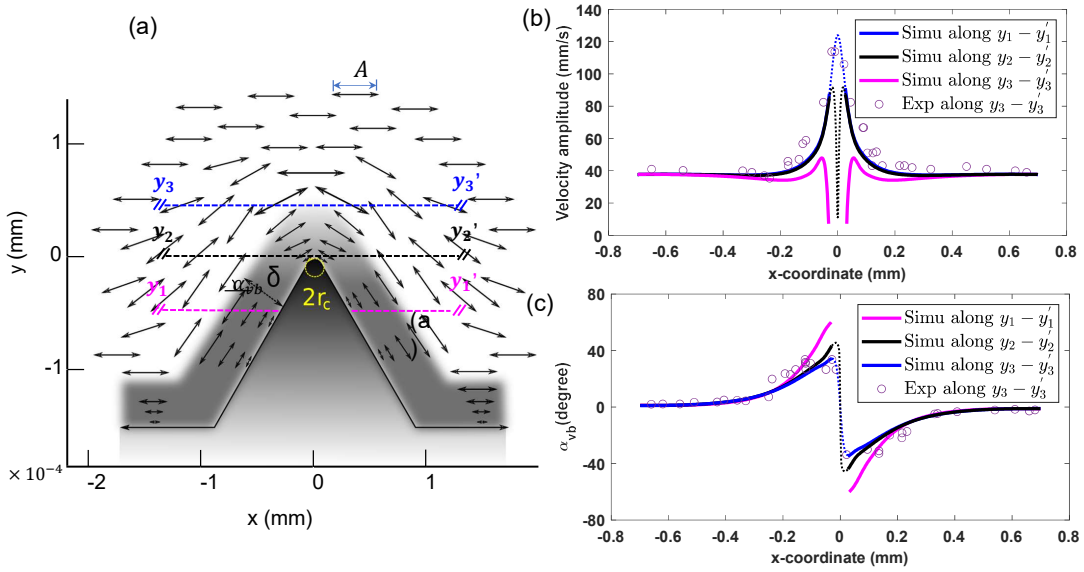

Figure 2: Acoustic vibration and streaming flow around the sharp edge structure: (a) Sketch of the acoustic vibrations of fluid particles near the sharp edge, δ is the acoustic boundary layer, the segment $y_1 - y_1'$ is located 0.05 mm below the tip; $y_2 - y_2'$ intersects the tip; $y_3 - y_3'$ is located 0.01 mm above the tip, (b) Amplitude of the vibration velocity recorded along $y_1 - y_1'$, $y_2 - y_2'$ and $y_3 - y_3'$. Circles stand for experiments recorded along $y_3 - y_3'$, (c) Orientation of the vibration velocity $\alpha_{vb} = \arctan[v_{ay}/v_{ax}]$ along $y_1 - y_1'$, $y_2 - y_2'$ and $y_3 - y_3'$. Circles stand for experiments recorded along $y_3 - y_3'$. Parameters: $\alpha = 60°$, $2r_c$=5.8 μm, f=2500 Hz, v_a=37.8 mm/s, δ=11.5 μm.

the vertical direction from the tip. For both quantities, the influence of the sharp structure is significant mainly within the region from x=-0.2 mm to 0.2 mm, hence comparable to the height of the structure h=0.18 mm.

As shown in Figure 2(c), the orientation angle α_{vb} of $\mathbf{v}_a$ varies along the x direction. The evolution of $\alpha_{vb}(x)$ depends much on the distance from the tip y. If $y = 0.01$ mm (line $[y_3 - y_3']$), hence roughly equal to δ, α_{vb} increases from 0 far enough from the tip, up to roughly 32°. Then it sharply decreases down to its corresponding negative value, roughly -32°, continuously and slowly increases back to zero far away from the tip. This profile is in very good agreement with our previous measurements obtained from high-speed imaging [37] and extracted at the same distance y from the tip. In Fig. 2(c), we also plot $\alpha_{vb}(x)$

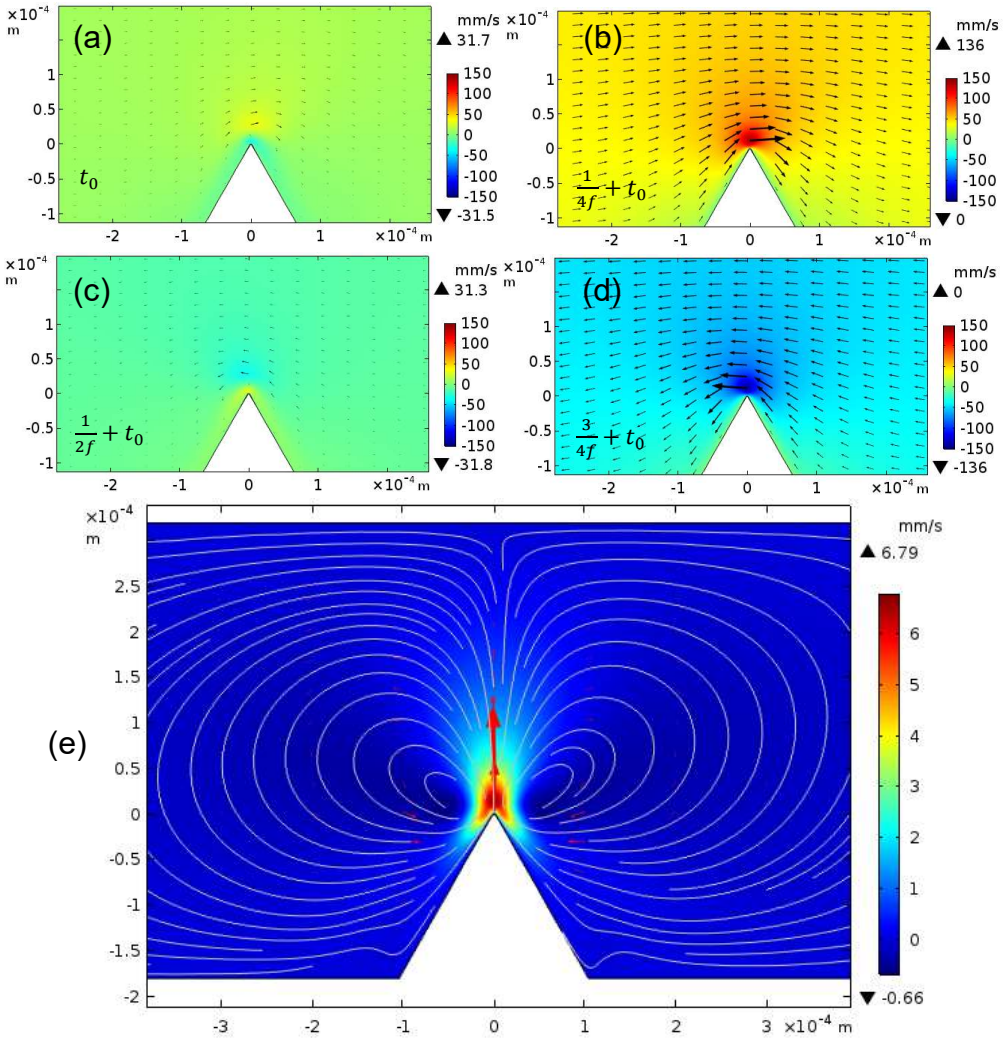

Figure 3: Acoustic vibration and streaming flow around the sharp edge : (a-d) Successive velocity fields at different time (or phase) during an acoustic period, (e) Magnitude and streamlines of the streaming flow, from a time-average during several acoustic periods. Parameters: $\alpha = 60°$, $2r_c$=5.8 μm, f=2500 Hz, v_a=37.8 mm/s, δ=11.5 μm.

along the line $[y_2 - y_2']$, which corresponds to $y = 0$, hence intersecting the edge right at the tip. The overall profile of $\alpha_{vb}(x)$ resembles the previous one, except near the tip where the maximal and minimal values have larger absolute values, around 40° and -40° respectively. Finally, the values extracted from a line $[y_1 - y_1']$ lower than the tip, show the same trend

for $\alpha_{vb}(x)$, with maximal and minimal values very close to that of the wall, i.e. $(\pi/2 - \alpha/2)$ and $(\alpha/2 - \pi/2)$.

At this stage and at a qualitative level, we can conclude that the value of α sets the amplitude of the jump in the orientation of $\mathbf{v}_a$, whereas the value of r_c sets the sharpness of the spatial variation of orientation. Both of them should play crucial influence on the magnitude of acoustic perturbation within the fluid.

2. Streaming velocity

Figure 3(e) shows the steady streaming velocity and corresponding streamlines. We observe perfectly symmetrical streaming vortices in the vicinity of the sharp tip. This clearly shows how focused the driving streaming force is, in particular in the vicinity of the sharp tip, and confirms previous findings [42]. Thereafter, we denote the maximal value, evaluated within the whole streaming flow, as v_{sm}. In sharp-edge streaming, the velocity is found to be maximal along the y axis, hence at x=0, and directed toward the y direction. We shall see that this is no longer the case when r_c is large enough with respect to δ.

Figure 4 shows the streaming velocity $v_{sy}(x = 0, y)$ along the y direction, with the frame origin ($x = 0$ and $y = 0$) taken at the tip. For a reason of symmetry, $v_{sy}(x = 0, y)$ is oriented along y so that only the y component of v_s is plotted. Results from DNS are in very good agreement with experiments extracted from our previous study [37]. In addition, the numerical study further allows to access velocity within the thin VBL, which was hardly possible in experiments, due to limitations of the visualization technique. Within the VBL range $y \leq \delta$, the streaming velocity sharply increases with y to its maximum value v_{sm} obtained near $y \simeq \delta$. Beyond this point, the streaming velocity decreases along the y direction and vanishes to zero at a distance from the tip roughly equal to $w - h$, here $\simeq 0.3$ mm.

We also define $v_{sm}^{'}$ as the maximal streaming velocity determined only on the y axis. Let us here point out that for most situations investigated in this study, namely the situation of sharp edge where $2r_c < \delta$, v_{sm} is found to be along the y axis (at x=0 and $y \simeq \delta$ like in Fig. 4), and then $v_{sm} = v_{sm}^{'}$. However, when r_c is significantly larger than δ, the maximal velocity is found out of the y axis, typically in the periphery of the two eddies of the VBL, making v_{sm} different from $v_{sm}^{'}$. This is illustrated by the two insets of Fig. 4. In the latter

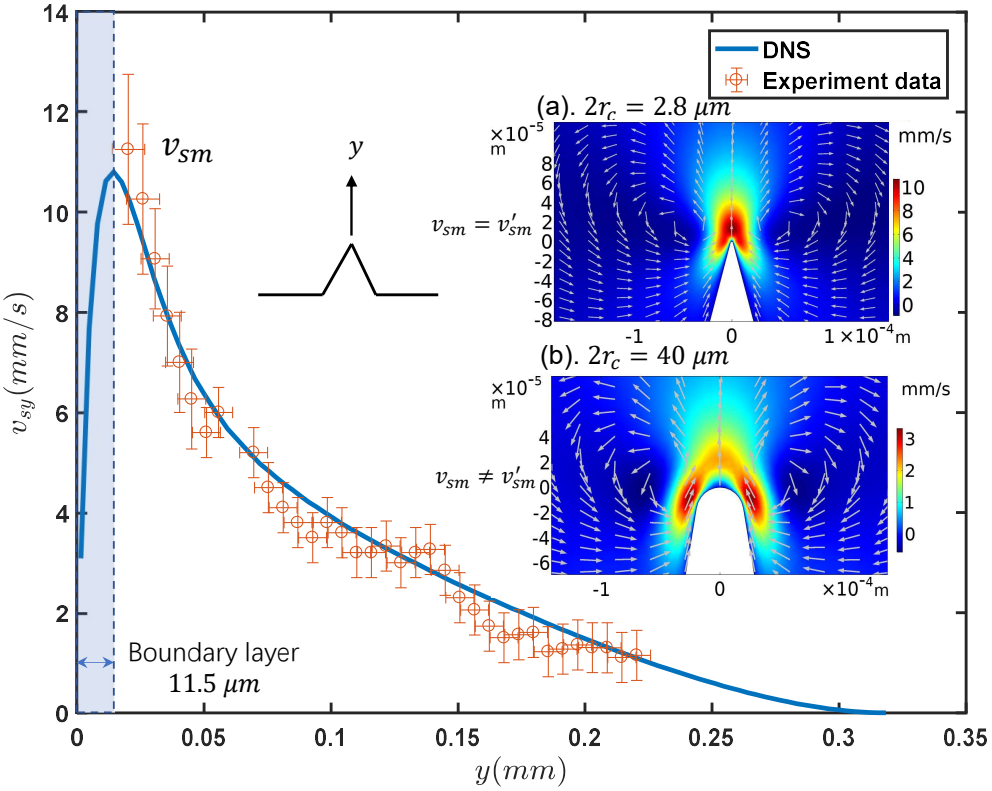

Figure 4: Streaming velocity along the y-direction: comparison between experiments and simulations. Conditions are: $\alpha = 30°$, $2r_c$=2.8 μm, v_a = 37.8 mm/s. Due to the finite size of PIV particles, the flow could not be solved within the boundary layer with a thickness of 11.5 μm. The two inserted maps show the magnitude of the streaming velocity field (reddish color standing for larger velocity) and its direction (arrows) in respectively two situations: sharp edge situation (upper map) where the maximal velocity v_{sm} is located on the y axis and round edge one (lower map) where v_{sm} is located besides the y axis and hence different from v'_{sm}.

situation, these two values shall be treated separately. Let us finally remark that the ratio r_c/δ rules the crossover between sharp-edge and classical Rayleigh streaming.

3. DNS versus PT

Based on the above analyses, we extract v_{sm} as a relevant quantity to characterise the streaming velocity field, under the combination of different operating parameters. Other quantities like the size of streaming vortices and the area influenced by the streaming flow are directly related to v_{sm} [37]. In order to better quantify the situations where $r_c > \delta$, and in particular to understand and quantify the crossover between sharp-edge and smooth-edge configurations, we also systematically extract v'_{sm}, hence restricting the area to the y axis.

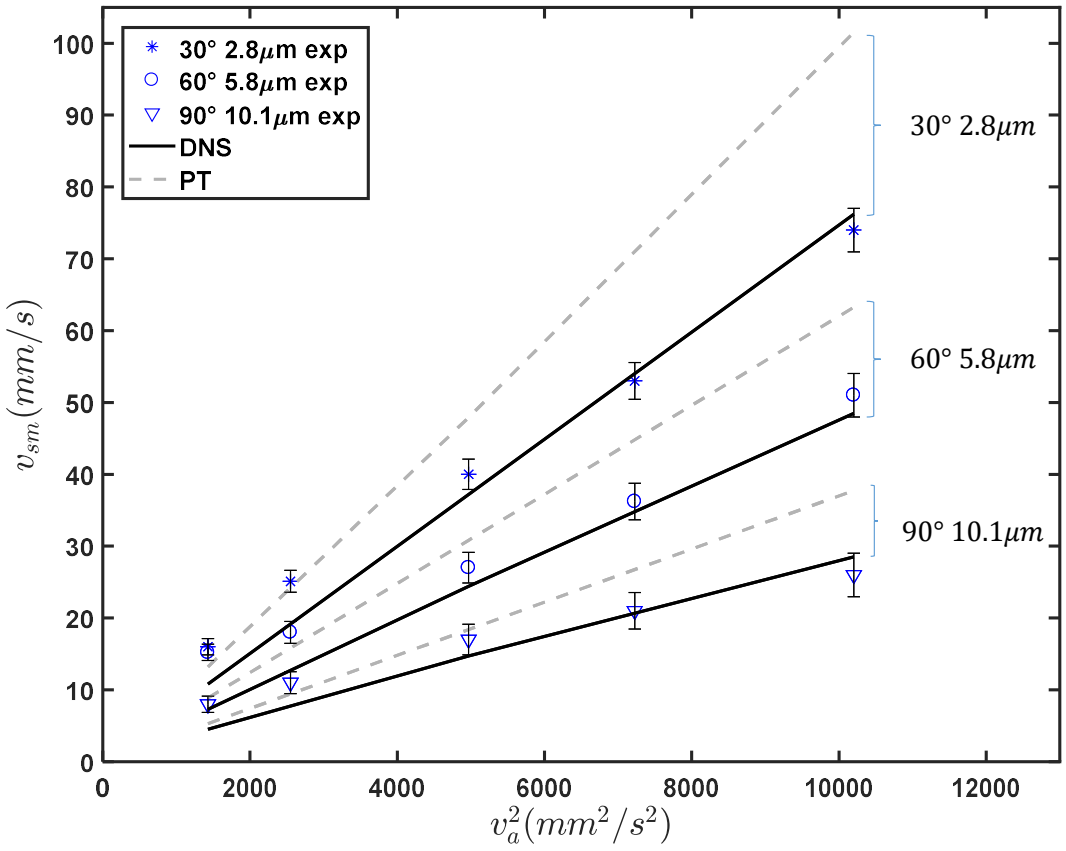

, for different sets of values for angle α and radius of curvature r_c. Results are extracted from experiments (symbols), PT simulation (dashed lines) and DNS (plain lines).

Figure 5: Maximum streaming velocity versus square of acoustic vibration v_a^2

First, we quantitatively investigate the influence of the forcing on v_{sm}. Figure 5 shows

a quadratic dependence between v_{sm} and the acoustic velocity amplitude v_a. Experimental results with water are taken from [37] and from three sets of values of α and r_c. Results from DNS and PT simulation are shown respectively as plain and dashed lines for the three sets of parameters. At low enough acoustic amplitude, both the PT and DNS simulations give satisfactory agreement with experiments.

However, at larger acoustic velocity, results of DNS are in better agreement with experiments than those from PT. The latter tends to over-estimate the streaming velocity by roughly 20 % under strong acoustic vibration.

The above results suggest that DNS provides a better prediction of the streaming velocity around the tip and it can be considered as a reliable method to predict the streaming flows generated by sharp structures.

B. Quantitative results

1. Vorticity maps

Figure 6 show vorticity maps of the streaming flow, calculated by DNS with different tip angle α and curvature diameter $2r_c$. The acoustic forcing velocity is taken relatively strong, at $v_a = 101.7mm/s$, corresponding to the right uttermost points in Figure 5. It reveals that intense vorticity is localised near the tip, within the VBL, and takes values of opposite signs in the regions to the left and right of the tip. The inner vortices in turn induce outer vortices of opposite sign and of larger size, further away from the tip (see in particular subfigs (a-b)). These outer vortices correspond to the ensemble of streamlines shown in Fig. 3-(b). For all cases, the extrema of vorticity roughly remain at the same locations: very close to the tip and in either side of it.

Subfigures (a-d) in Fig. 6 illustrate the comparative influence on vorticity maps of the different angle α - ranging from acute ($\alpha = 12°$) to obtuse ($\alpha = 120°$), while keeping r_c constant. More intense vorticity appears for sharper structures (see subfigs (a-b)) while its magnitude decreases as α increases (see subfigs (c-d)). Subfigures (e-h) illustrate the influence of the value of r_c, while keeping α constant. Two distinct behavior emerge: within the range $2r_c > \delta$ (g-h), increasing r_c leads to more spread and weaker vortices, while in the range $2r_c < \delta$ (e-f) the vorticity does not vary significantly with r_c.

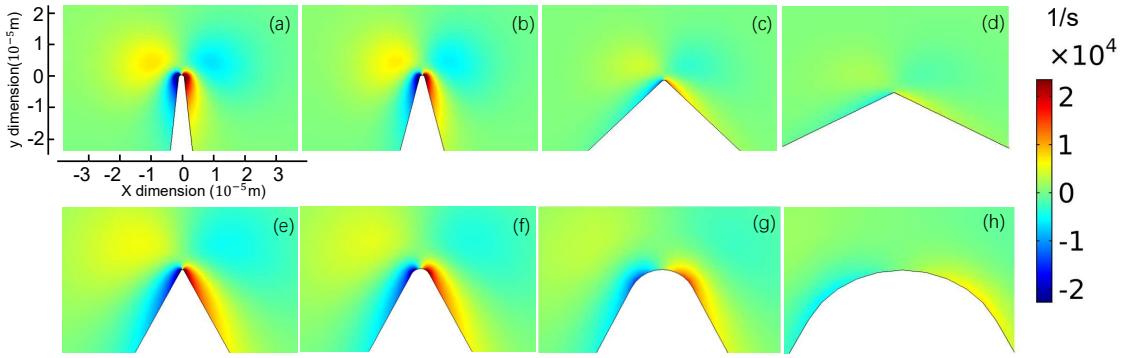

Figure 6: Vorticity maps of the streaming flow in the region close to the tip, under different geometrical conditions. Red color (positive vorticity) and blue color (negative vorticity) respectively correspond to flows in anticlockwise and clockwise directions. For all maps, the vibration velocity v_a =101.7 mm/s, f = 2500 Hz and liquid is water, so that $\delta \simeq$ 11.3 μm. Figs.(a-d) correspond to the same curvature diameter $2r_c = 2.8\mu m$ but different tip angles α : (a) $\alpha = 12°$; (b) $\alpha = 30°$; (c) $\alpha = 90°$; (d) $\alpha = 120°$. Figs.(e-h) correspond to the same tip angle ($\alpha = 60°$) but different curvature diameters : (e) $2r_c$ = 1.0 μm; (f) $2r_c$ = 6 μm; (g) $2r_c$ = 20 μm; (h) $2r_c$ = 50 μm.

Based on these results, we can conclude that the curvature diameter and tip angle have qualitatively different influences on streaming vorticity, both inside and outside the VBL. Smaller and sharper structure provides stronger streaming force and flow.

2. Streaming velocity magnitude per acoustic power

We now aim to define a simple fitting parameter to quantify the efficiency of the response of streaming flow in regards to the prescribed vibration. The analyses in Ovchinnikov *et al.* [42] end up to a general expression for the streaming velocity in cylindrical coordinate (r, ϕ) as:

$$v_s(r) = \frac{v_a^2}{\nu} \frac{\delta^{2n-1}}{a^{2n-2}} H_\alpha(\frac{r}{\delta}) \tag{10}$$

where n is a coefficient that depends on α, $n = \frac{\pi}{2\pi-\alpha}$; a is a length scale close to that of the sharp-edge height h. The function $H_\alpha(\frac{r}{\delta})$ contains the radial profile of the streaming

flow. Quantitatively, we mainly focus on the characteristic (and maximal) value of $v_s(r)$ at $r = \delta$ and $\phi = 0$, so what follows we shall just consider the constant prefactor $\frac{1}{\nu}\frac{\delta^{2n-1}}{a^{2n-2}}$ that relates v_s to v_a^2. Let us note that this equation, supposedly valid in the range $r_c < \delta$, does not contain any dependence on r_c.

The results presented in Figure 5 confirm that for a given combination of geometry, acoustic frequency and liquid viscosity - and actually for most experimental conditions, v_{sm} varies quadratically with the amplitude of vibration velocity v_a. Therefore, we define the fitting parameter $\theta = \frac{\Delta v_{\mathrm{sm}}}{\Delta(v_a^2)}$ as a measurement of the efficiency of the momentum conversion from acoustic to streaming flows. In the following, we shall consider θ to quantify the influence of the different varying parameters, namely α, r_c and ν. Similarly, we define $\theta' = \frac{\Delta v'_{\mathrm{sm}}}{\Delta(v_a^2)}$.

3. Influence of tip angle

In this first series of results, we quantify the strength of the streaming flow for different values of angle α, from 12° to 180°, keeping all other quantities constant. In particular, as illustrated in the vorticity maps of Figures 6-(a-d), r_c can be kept constant for different α, except of course for $\alpha = 180°$ that corresponds to case of a flat, straight wall. Figure 7 shows v_{sm} versus v_a^2 for different values of α. As previously stated, the more acute the angle, the stronger the streaming flow for a given v_a. Besides, a flat wall with $\alpha = 180°$ does not generate any streaming flow even for high v_a.

Since the vast majority of cases exhibited a robust quadratic dependence between v_{sm} and v_a, we extracted θ for each value of α. The results are shown in Figure 8, where θ is plotted versus $(180 - \alpha)$.

Keeping all other parameters constant, here, $2r_c = 2.8$ μm, $f = 2500$ Hz and liquid properties being those of water ($\delta = 11.5$ μm), θ achieves its highest value with the sharpest angle, $\alpha = 12°$. The maximal efficiency of the momentum conversion is slightly below 10^{-2} s/mm. When α reaches 90°, θ drops to roughly $3{\times}10^{-3}$ s/mm, and it vanishes to zero when α approaches 180°. Thus the dependence of θ with $\pi - \alpha$ is strongly non-linear.

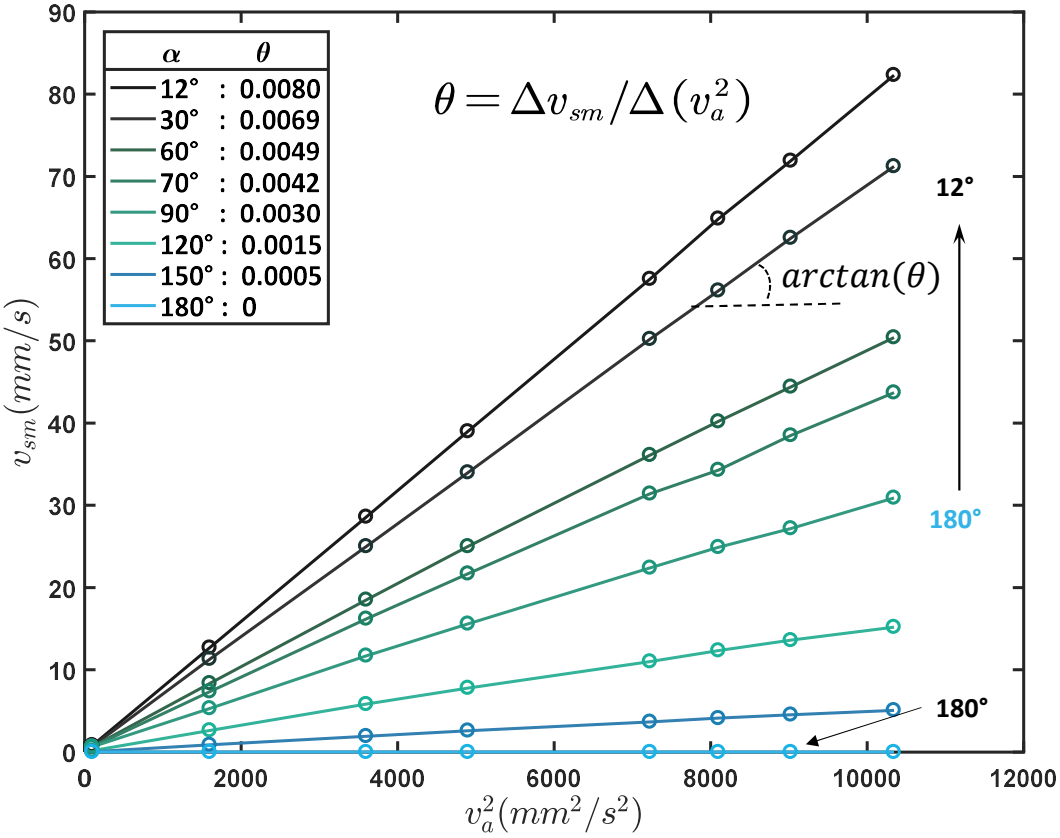

Figure 7: Maximum velocity versus square of the vibration velocity v_a^2, with different tip angles. The coefficient θ is extracted from a linear fit, which holds very well within the whole range of v_a. Other conditions are: $2r_c = 2.8$ μm, $f = 2500$ Hz.

4. Influence of tip curvature

We now investigate the influence of r_c on θ, for a series of four values of α, from 12° to 120°. As previously, simulations were carried out under the same liquid viscosity (water, ν=10^{-6} m^2/s) and frequency $f = 2500$ Hz, so that δ was kept constant at 11.5 μm and only r_c was varied. Figure 9 shows the dependence of θ versus $2r_c/\delta$.

These results reveal a decrease of θ with r_c, and this decrease becomes more significant within the range $2r_c > \delta$, see Figure 9. Let us note that in Figure 9, we also put results from simulations using the PT method for the two extreme values of α, again in the aim to illustrate the gap between both methods. This confirms that PT systematically over-

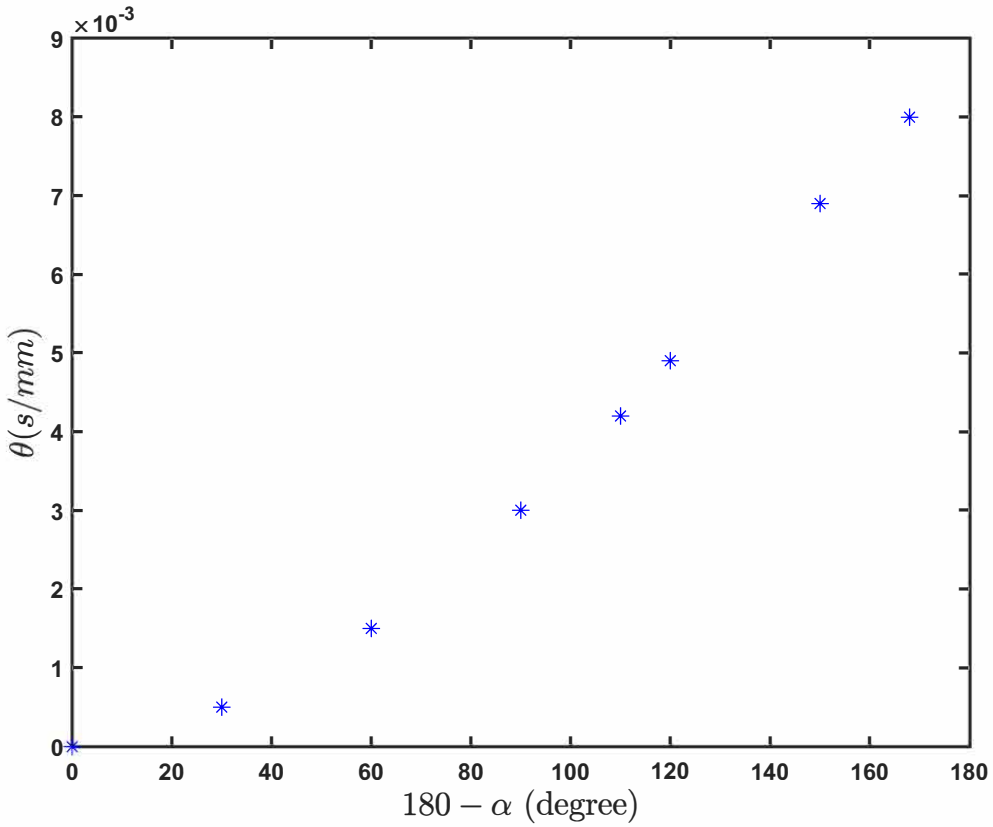

Figure 8: Coefficient $\theta = \Delta v_{sm}/\Delta(v_a^2)$ (efficiency of the momentum conversion from acoustic to streaming flows) versus the supplementary of the tip angle $180 - \alpha$. Other conditions are: $2r_c$=2.8μm (except for $\alpha = 180°$ where r_c is infinite), f=2500 Hz.

estimates the magnitude of the streaming flow, by a factor of roughly 1.2.

This constitutes a quantitative confirmation of what was suggested in the vorticity maps of Figures 6(a-d). Also, the influence of r_c is more pronounced when the tip angle is more acute.

Once $2r_c$ is increased and become larger than δ, θ significantly decreases, which is observed for all tip angles (Fig.9). This is in accordance with the spreading and weakening contour observed in Figure 6-(g-h). Hence in the range $2r_c > \delta$, the conversion of acoustic power into streaming flow is less efficient, which again emphasizes that the sharpness of the structure is determinant for the generation of intense streaming. In other words, when the tip is no longer sharp, the magnitude of AS weakens as we should retrieve the classical Rayleigh-

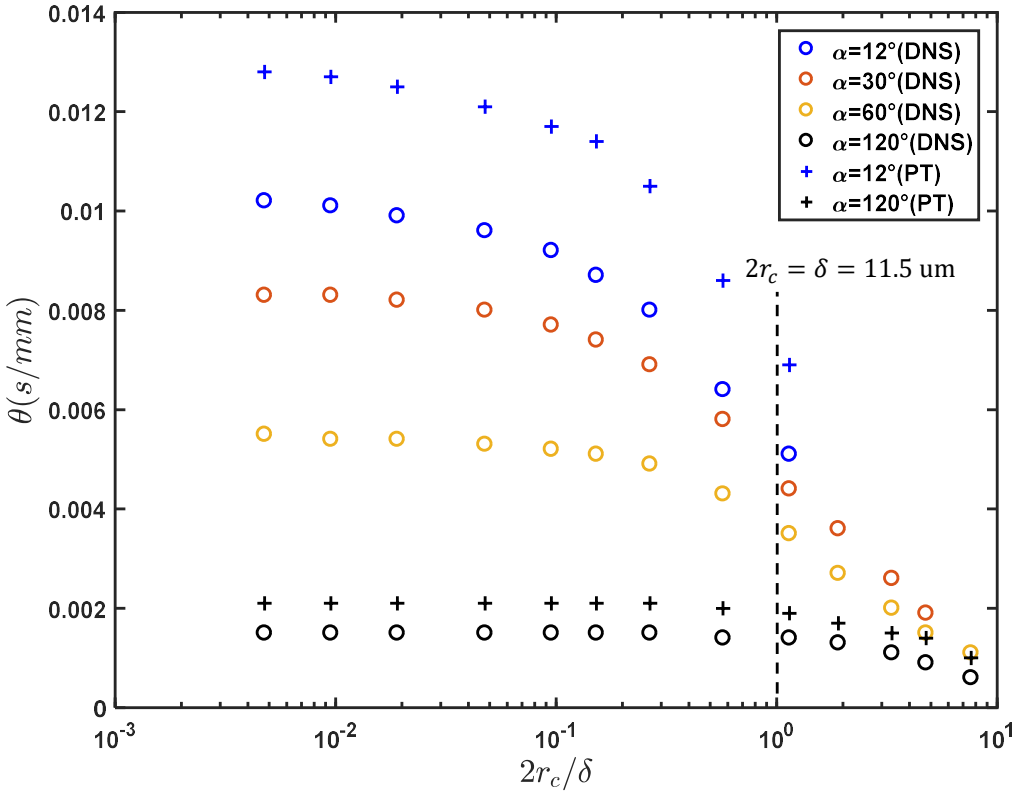

Figure 9: Coefficient $\theta = \Delta v_{sm}/\Delta(v_a^2)$ (efficiency of the momentum conversion from acoustic to streaming flows) based on the maximal value of streaming velocity, versus ratio between curvature diameter $2r_c$ and boundary layer thickness δ, for four different tip angles α. DNS results should be considered as reliable and PT simulation appears to over-estimate the result according to the two extreme cases ($\alpha = 12°$ and $\alpha = 120°$).

Schlichting streaming. Let us mention that the analytical prediction of Doinikov et al.'s study (eq. (27) of [43]) suggests a power law dependence on r_0 of the streaming velocity. However, it is hard to directly compare it with our results, since the values of r_0/δ in this latter study can be very different from those used here.

5. *Influence of viscosity*

One of the remarkable and non-intuitive features of Rayleigh-Schlichting streaming is its independence on viscosity, providing that the typical size of the container is much larger than

the thickness of the VBL, δ [14, 20]. This classical result, which expresses that streaming is both spawned and hindered by viscosity, can be retrieved by simple scaling arguments [48, 51], though it is no longer true in confined geometries [51]. Here in the case of sharp-edge streaming, we show that, despite δ can remain small compared to the channel size, viscosity has a strong influence on the sharp-edge induced streaming. As previously, we extracted θ as a fitting parameter that relates vsm with v_a^2 over a large range of v_a, for different values of ν and keeping r_c and α at fixed values.

Figure 10 shows a strong decrease of θ with kinematic viscosity ν in Log-Log axes. We span a large range of values for ν, from that of water (10^{-6} m^2/s) to a 1000-times more viscous liquid, with a corresponding $\delta \simeq 357$ μm, which in practice would correspond for instance to pure glycerin. In particular for $2r_c = 6$ μm, together with $f = 2500$ Hz and constant $\alpha = 30°$, we remain in a sharp-edge streaming situation since $2r_c < \delta$. The decrease can be well fitted by a power-law, with an exponent of -0.867 giving the best fit, see Fig. 10.

We now change the value of $2r_c$ from 6 μm to 25 and 50 μm. The cases investigated with $2r_c$= 25 and 50 μm reveal that the decrease of θ with viscosity is much less pronounced for higher values of $2r_c/\delta$, hence in the lower viscosity range. Actually, for these two values, the evolution of θ shows a crossover from sharp-edge streaming to classical Rayleigh-Schlichting streaming. Therefore if $2r_c > \delta$, it turns out that the dependence of θ on viscosity is not captured by a power law. Let us note that, while we ran our simulations up to ν=10^{-3} m^2/s, the relationship between v_{sm} and v_a^2 is no longer purely linear within this high-viscosity range. Therefore, the value of θ could not be extracted for the highest values of ν.

Conversely, the value of θ is independent on r_c in the high viscosity range, i.e. when $2r_c/\delta < 1$: this is a trademark of sharp-edge streaming.

Equation (10) taken from Ovchinnikov *et al.*'s study [42] predicts a decrease of θ with ν via a power-law of negative exponent, as $\theta \sim \nu^{\left(n-\frac{3}{2}\right)}$. For the chosen angle $\theta = 30°$, $n \simeq 0.54$, yielding an exponent $\left(n - \frac{3}{2}\right)$ of -0.96, close to but different from the value of -0.867 found empirically. The corresponding analytical prediction of Doinikov *et al.*'s study [43] propose an exponent of -1.

Let us here give more details on an apparent contradiction between the results of Figure 9 and those of Figure 10, concerning the dependence of θ with ν. The results of Figure 9 were obtained by varying r_c while keeping ν, ω constant (and thus δ at 11.5 μm). Conversely, the results of Fig 10 were obtained by varying ν, while keeping r_c constant for the same set

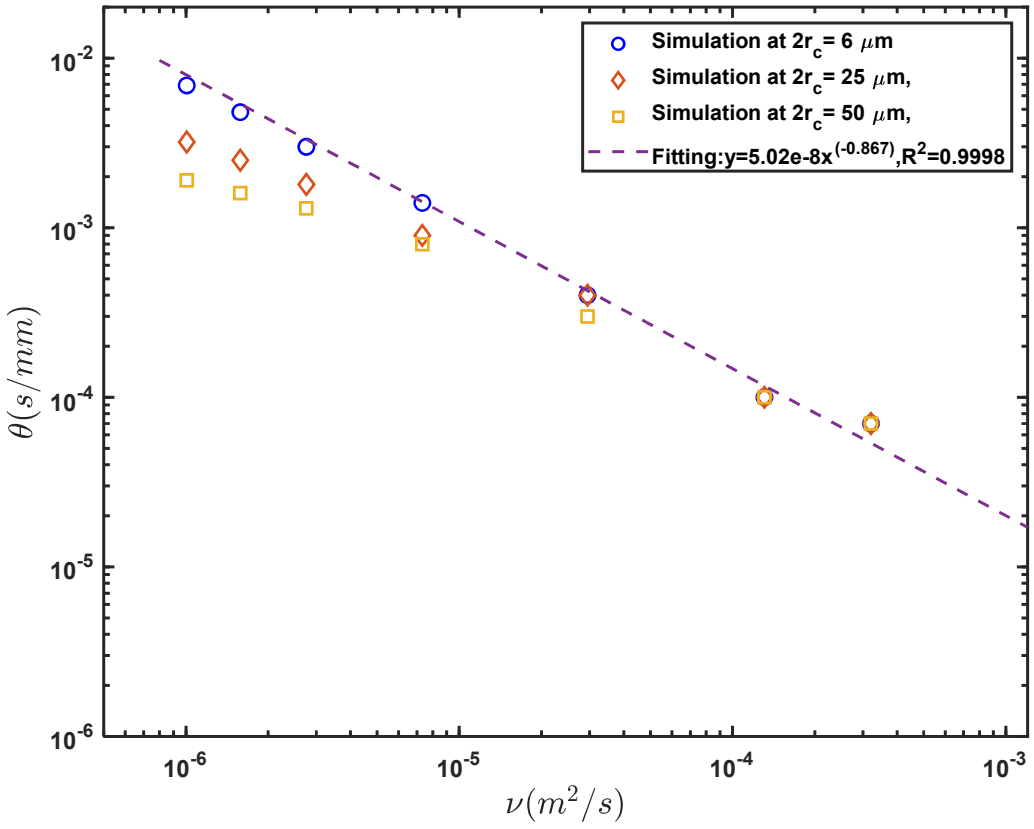

Figure 10: Coefficient $\theta = \Delta v_{sm}/\Delta(v_a^2)$ (efficiency of the momentum conversion from acoustic to streaming flows), versus kinematic viscosity ν. Other parameters are: $\alpha = 30°$, $f = 2500$ Hz. The fitting power-law curve is based on the results for $2r_c = 6\mu m$. For $\nu >$ $5{\times}10^{-5}$ m^2/s, the data points coincide with each others, showing that θ is almost independent on r_c.

of data. Hence, the apparent paradox of the influence of ν on θ comes from that :

- the decrease of θ with r_c/δ in Figure 9 is attributed to that the streaming is weaker when r_c increases, in particular when it becomes of the same order as, or larger than, δ : in this latter condition, the tip is no longer considered as sharp with respect to δ. Conversely in a situation of sharp edge streaming, the streaming flow is almost independent on r_c, as shown in the left region of the plot.

- the decrease of θ with ν is effective only in the situation of sharp edge streaming, where

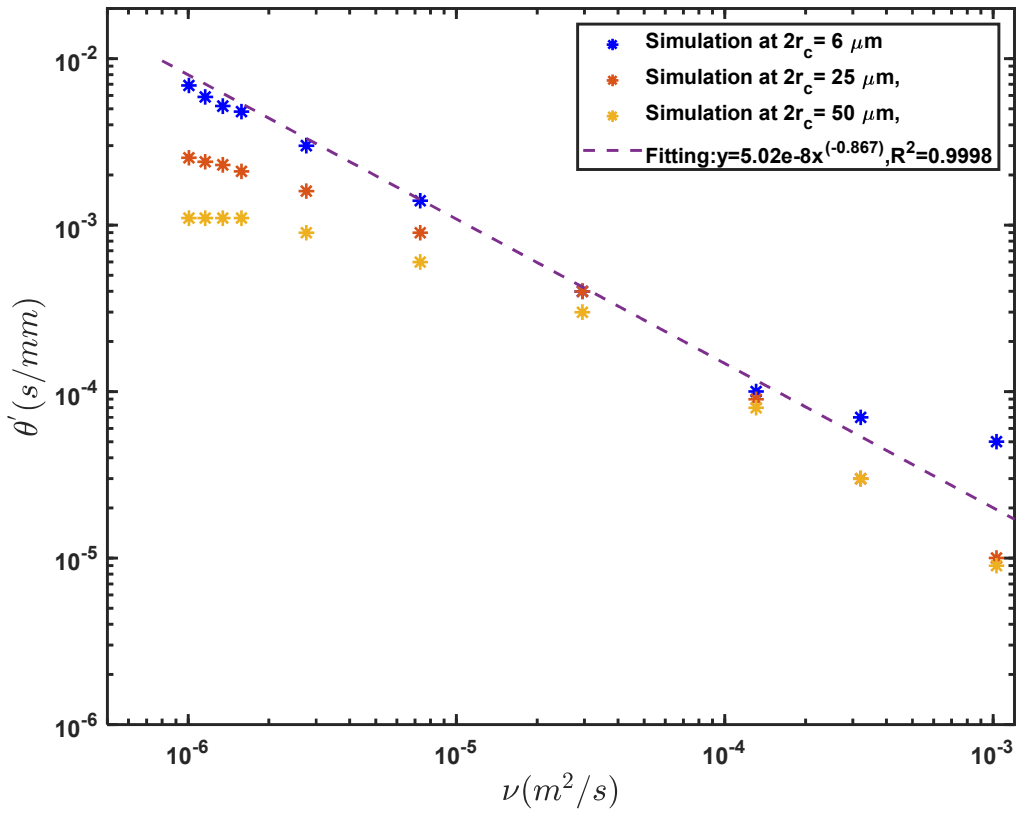

Figure 11: Coefficient θ' versus kinematic viscosity ν. $\theta' = \Delta v'_{sm}/\Delta(v_a^2)$, fitting efficiency from of the momentum conversion from acoustic to streaming flows. Other parameters are: $\alpha = 30°$, $f = 2500$ Hz. The fitting power-law curve is based on the simulation when $2r_c$=6 μm.

r_c is significantly smaller than δ. If this latter condition is true for water, it will of course remain true for more viscous liquids, as for the results in Figure 10.

The dependence of θ' with ν also shows a global decrease, see Figure 11. But the main difference with θ, is that within the range where r_c/δ is large enough hence, the edge is not sharp), the value of θ' is independent on ν. It is clearly evidenced for $r_c = 50$ μm in the low viscosity range. The distinction between θ and θ' is mostly significant where $r_c/\delta > 1$, which corresponds to situations depicted in the vorticity maps of Figs. 6-(g,h). In these situations, the maximum of streaming velocity is not localized along the y axis, and ressembles classical

Rayleigh streaming. In any case, the behavior of v'_{sm} follows a quadratic increase with v_a, so that θ' remains well defined. More surprisingly, beyond ν=10^{-4} m^2/s, the decrease of θ' with ν deviates from a power law. Also, θ' remains dependent on r_c in the whole range of ν investigated.

V. DISCUSSIONS AND CONCLUSION

Let us now recall and summarize the main results. Motivated by experimental results on the generation of intense acoustic streaming near sharp edges [33–37, 42, 45], the results of our DNS simulations allow a characterization of the streaming flow both outside and inside the VBL, here of typical thickness $\delta = 11.5$ μm for water at $f = 2500$ Hz. This constitutes a significant step forward with respect to the state of the art, since it is experimentally hard to access the flow details within the VBL [37]. Furthermore, few studies employed the DNS method so far [43], and our study provided results of better precision than the classical PT, especially at high forcing. In particular, providing $2r_c$ is smaller than δ (which is the case of sharp-edge streaming), the maximum of streaming velocity is found near the apex of the sharp tip, at a distance of roughly $y = \delta$, inducing regions of strong and concentrated vorticity aside and within the VBL, as well as larger outer vortices, which ensure efficient mixing across the whole channel [33, 35–37].

Furthermore, we gained better understanding of the first-order acoustic velocity field. It turns out that both the orientation of the oscillations and their amplitude are influenced by the sharp structure, which leads to a strong and sharply localized perturbation to the fluid. Namely, the norm of $\mathbf{v}_a(x, y)$ is maximal near the tip, precisely around the location of the maximum of streaming velocity ($x = 0, y = \delta$). Surprisingly, this velocity v_a is found twice to three times larger than that far away from the tip. Let us note that this confirms recent experiments [37]. This effect, which significantly contributes to the streaming efficiency, depends on the sharp edge structure. Though, it remains to be explained and quantified in more details.

Our study also focuses on the influence of the tip sharpness, and reveals that the two parameters r_c and α are crucial for the generation of acoustic streaming. While their respective influences were difficult to dismantle in experiments, our numerical results provided a better understanding. Since the acoustic flow direction (angle α_{vb}) follows that of the walls,

the sudden change of oscillation orientation beside the tip leads to such a centrifugal effect. Along a typical length as short as $2r_c$, the orientation jumps from $\alpha_{vb} = \pi/2 - \alpha/2$ for $x \ll r_c$ to $\alpha_{vb} = \alpha/2 - \pi/2$ for $x \gg r_c$, hence an overall rotation of $\Delta\alpha_{vb} = \pi - \alpha$. This *gradient* generates strong values for the effective streaming force F_s.

One of the remaining challenging issue, is the detailed determination of the radial and azimuthal flow profile. In this aspect, the study by Doinikov *et al.* constitutes a step forward, and offer results complementary to ours. This latter study revealed in particular the occurrence of secondary vortices along the sharp edge, when the angle of the wedge α is large enough. the origin of these secondary vortices remain unclear, and could be specific to situations of higher frequencies. Very recent experiments [45] also emphasized the non trivial influence of f and ν when δ is no longer small compared to channel depth and width.

Let us briefly comment on Eq. (8). Due to relatively local strong values for $\mathbf{v}_s$, i.e. comparable in magnitude to $\mathbf{v}_a$, the non-linear term $(\mathbf{v}_s \cdot \nabla)\mathbf{v}_s$ should in principle be significant. The physical meaning of this term can be viewed as the self-advection of the streaming flow, which in practice leads to vortex elongation in Rayleigh-Schlichting streaming [52]. However, this is somewhat contradictory with the robust quadratic relationship found between v_{sm} and v_a, regarding Eq. (8). To explain this apparent contradiction, we retain two possible hypotheses:

i) although the magnitude of $\mathbf{v}_s$ can locally be relatively large, the term $(\mathbf{v}_s \cdot \nabla)\mathbf{v}_s$ could be negligible, especially in the region around the maximum v_{sm}.

ii) the term $(\mathbf{v}_s \cdot \nabla)\mathbf{v}_s$ could be irrotational, so that it can be exactly compensated by the pressure gradient term ∇p_s.

To check these two assumptions, we plotted the maps of the norms of both quantities $(\mathbf{v}_s \cdot \nabla)\mathbf{v}_s$ and $\nu\nabla^2\mathbf{v}_s$. The results are shown in Fig. 13, for a typical value of v_a in the intermediate range. It turns out that the first assumption is the right one, as it shows that the magnitude of $\|\nu\nabla^2\mathbf{v}_s\|$ overcomes that of $\|(\mathbf{v}_s \cdot \nabla)\mathbf{v}_s\|$ by a factor of roughly 70. Therefore, the non linear term $(\mathbf{v}_s \cdot \nabla)\mathbf{v}_s$ can be considered as negligible in Eq. (8), which explains the extension of the quadratic behavior between v_{sm} and v_a in sharp-edge streaming. Furthermore, it underlines that the differences between PT and DNS simulation results, and the fact that DNS matches better experiments of sharp-edge streaming should be explained by the importance of the other non-linear terms $(\mathbf{v}_a \cdot \nabla)\mathbf{v}_s$ and $(\mathbf{v}_s \cdot \nabla)\mathbf{v}_a$ in Eq. (6).

In the seek for optimal operating conditions of sharp edge AS, the efficiency of conver-

sion from acoustic vibrations to streaming flow is quantified by θ. In particular, while the fabrication of sharp tips requires in practice careful and expensive techniques, especially for r_c as small as a few microns, Fig. 9 shows that the streaming flow does not gain much in strength when r_c is lowered below $\delta/2$. The precise identification of the influence of r_c and α was made possible thanks to the DNS simulations.

The role of viscosity was also investigated. The power-law decrease of θ with ν, predicted by Ovchinnikov *et al.* [42] was confirmed by our simulations, although the exponent was found weaker than the predicted one. We also confirmed the independence of θ on r_c in the range $2r_c < \delta$, and we investigated the crossover between the sharp edge AS and classical Rayleigh streaming regimes by tuning the value of $2r_c/\delta$. In particular, we recover the independence of θ on ν if $2r_c/\delta \gg 1$ (as in classical Rayleigh streaming).

Also, our simulations showed that the quadratic relationship $v_{sm} \sim v_a^2$ fails at high enough viscosity. This has to be considered as a geometrical constraint, since with higher range of v_a, the size of the outer vortices is comparable to that of the channel width w. For high enough v_a, the streaming can then be limited by the size of the microfluidic channel.

Let us also suggest a quantitative criterion of efficiency in the context of (macro-)mixing under a typical imposed flow-rate Q through the channel. Previous experiments quantifying both the maximal streaming velocity and mixing efficiency revealed that a satisfying mixing rate could be obtained if the averaged flow velocity, here $< V >= \frac{Q}{w \cdot d}$, was comparable to the maximal streaming velocity [37]. For the width $w = 500$ μm and depth $d = 50$ μm used in these experiments, and a middle-range value of $Q = 10$ μl/mn, it yields: $< V > \simeq$ 6.7 mm/s. Therefore in practice, the velocity set point $v_{sm} =< V >$ shall be related to specific conditions on both the tip geometry and liquid viscosity, both ruling the value of θ, also to take into account the maximal v_a that the transducer can generate. It is worth noting though, that micro-mixing at the molecular scale also depends on the form of vortices generated by AS and one of our upcoming study addresses this issue using Iodate-Iodide reaction as a chemical probe [53, 54].

To sum up, the FEM-based DNS method gives very satisfactory agreement with experimental results and it over-performs the classical PT model. The latter does not consider the non-linear terms in the streaming force calculation and tends to over-estimate the streaming velocity. In this sense, our study shows that, providing the right boundary conditions are prescribed and all non-linear terms are kept in the calculation, AS streaming can be suc-

cessfully studied in a quantitative way, with minimal inexpensive computing material, i.e. without computer cluster nor MP - and a FEM commercial software. In this sense, we can finally state that the assumption of a 2D flow is necessary to carry out DNS simulations by keeping a reasonable computational cost, which would be very expensive for simulations under an equivalent 3D geometry. Still, we checked that the flow remained 2D, even by prescribing a 3D geometry similar to that of the experimentally studied channel, under a few typical situations. This is presumably due to the high width/depth ratio in our channel geometry.

APPENDICES

A. Perturbation Theory and its implementation

The Perturbation Theory is generally well adapted to address acoustofluidics problems in the framework of "weak disturbances". With limited access to Computational Fluid Dynamics (CFD), PT is a very powerful tool to reduce the N-S equation, which potentially includes non-linear terms that couple the acoustic and streaming velocity fields, into a simpler one. Therefore, PT provides an convenient method to bring out the physical fundamental core of the acoustic streaming problems while retaining relatively simple mathematical formulation [15, 16, 21, 42, 46, 47].

For the present study, v_a and v_s are governed by both Eq. (6) and Eq. (7), which set respectively the oscillating and steady terms in the velocity field. The PT assumes $v_a \gg v_s$ so that the inertial terms in the Eq. (6), $(\mathbf{v}_s \cdot \nabla)\mathbf{v}_a$ and $(\mathbf{v}_a \cdot \nabla)\mathbf{v}_s$, can be neglected. Without these terms, Eq. (6) and Eq. (7) can then be solved separately to obtain v_a and v_s.

The procedure of the calculation based on PT can be proceeded following two steps : i) Solving the wave equation Eq. (6) to determine the vibration velocity field in the geometry structure, with first-order time-periodic terms, and ii) Solving the streaming equation Eq. (7), in which the force term in Eq. (9) can be determined by the results of the previous step. The second-order terms are steady ones, from which the streaming velocity v_s is deduced.

Although Ovchinnikov *et al.* [42] pointeed out the limitation of PT with respect to DNS method, PT remains a powerful framework to analyze the underlying physics of the

streaming fields near the sharp tip, especially when the vibration amplitude within the liquid is small enough so that the acoustic Reynolds number $Re_a = \frac{A\omega h}{\nu}$ remains of the order of one or lower.

In COMSOL, basic steps to implement Perturbation Theory are:

1. Module "Thermoviscous Acoustics, Frequency Domain"for solving the acoustic vibration velocity field;

2. Module "Laminar flow" for solving the streaming velocity field with $\mathbf{F}_s = -\frac{\rho}{2}\left\langle Re[(\mathbf{v}_a \cdot \nabla)\mathbf{v}_a^*]\right\rangle$ as the "Volume Force" inserted into the model;

3. Boundary conditions: to solve the vibration velocity, the left and right boundaries (labelled as 1 and 6) are set with the acoustic velocity oscillating at the prescribed value of amplitude in the normal direction, and to be in phase with each other Other boundaries are set as no-slip walls.

   For the second-order streaming velocity, the left and right sides of the domain are set as inlet and outlet at given incoming velocity, here taken equal to zero. The other boundaries are set to be no-slip walls.

B. Direct Numerical Simulation implementation

The detailed description of DNS has been given in Section II. Implementing DNS is COMSOL includes the following steps:

1. Module "Laminar Flow" for direct solving the N-S equations with periodic velocity boundary conditions;

2. Module "Domain ODEs and DAEs" for calculating the time average values of the velocity field in step 1;

3. Boundary conditions: the acoustic velocity (in form of a sinusoidal function of time) is set as the left boundary condition and the right boundary condition is set as a pressure p_0. Other boundaries are set as no-slip walls.

C. Mesh and grid independence study

The mesh grid is built with triangle elements, with the maximum element size being 0.014 mm, and the minimum one being 0.0002 mm. Smooth transition is performed with a maximum element growth rate of 1.1. Close to the sharp edge, the mesh is refined by inflation layers to better account for the strong velocity gradients inside the VBL. The number of the layers is 3 and the layer stretching factor is 1.2.

The mesh independence is assessed by comparing the results from the chosen mesh with those obtained in a refined mesh, which is generated by increasing the number of cells by 30%. Comparing the two meshes, the obtained streaming velocity value differs by less than 1%. The current mesh is thus considered as being as satisfactory balance between both in terms of accuracy, reliability and computing time.

D. Time to reach steady streaming field and time step

For the PT method, the two-steps procedure consists in a readily computation process. For the DNS however, the streaming flow appears after a transient state, and thus needs some time to be fully developed and reach its steady state. As shown in Figure 12 (a), the streaming velocity v_{sm} (the time average of the total velocity from the beginning of the simulation to a given time) grows with the number time-steps until reaching a steady state. The corresponding time duration is roughly 12 ms, hence 30 acoustic cycles under the acoustic frequency of 2500 Hz (period of 400 μs).

The value of the time-step is also essential to meet the CFL (Courant-Friedrichs-Lewy) stability condition. The Courant number, given by $CFL = v_a \Delta t / \Delta x$, should be kept lower than 1 to guarantee the numerical iteration stable [55]. As shown in Figure 12, we test four time-steps from 1 μs to 120 μs, or from $1/400^{th}$ to $3/10^{th}$ of an acoustic period. Only $\Delta t_4 = 120\mu s$ gives a CFL higher than unit but $\Delta t_3 = 80\mu s$ is not fine enough to give a satisfactory maximum streaming velocity v_{sm}, see Fig. 12-(a) and a reliable streaming distribution along the y direction $v_{sy}(y)$, see Fig. 12-(b). We thus choose $\Delta t_2 = 8\mu s$ as a compromise since it gives the same results as $\Delta t_1 = 1\mu s$ but with a shorter computing time.

With the chosen time step of 8 μs and a total of 30 acoustic cycles, the DNS computing cost is about 25 mn per case study on an Intel i5-7500 CPU and 16 GB of RAM.

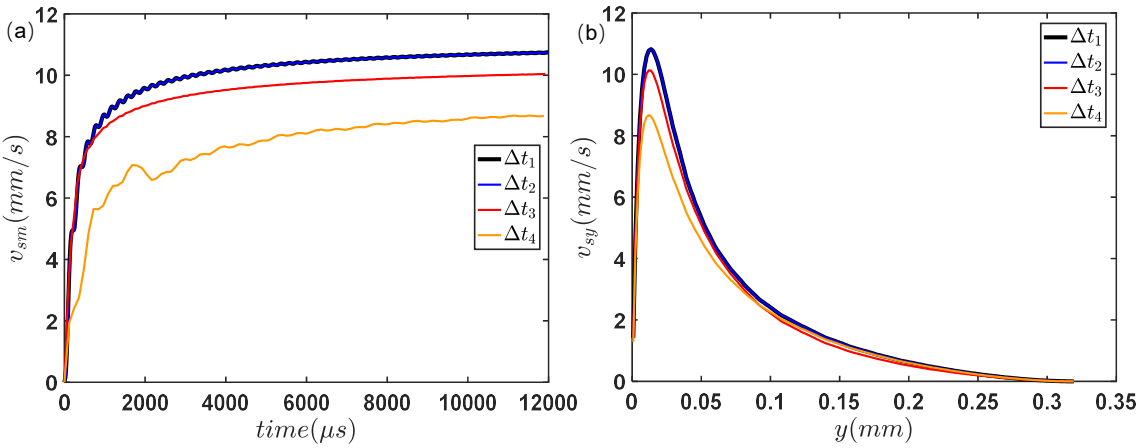

Figure 12: Variation of streaming velocity with numerical iteration time (a), and the steady y-direction streaming velocity at different time steps (b). Time steps $\Delta t_1 = 1\mu s$, $\Delta t_2 = 8\mu s$, $\Delta t_3 = 80\mu s$, $\Delta t_4 = 120\mu s$, correspond to $1/400^{th}$, $1/50^{th}$,$1/5^{th}$ and $1/3.33^{rd}$ of an acoustic period. The whole duration of the simulation equals 30 acoustic periods.

E. Convective versus viscous terms

Equation (7) suggests that the quadratic dependence of v_{sm} with v_a should be right only if the term $(\mathbf{v}_s \cdot \nabla)\mathbf{v}_s$ is negligible compared to the other ones. Therefore, we compared the relative magnitude of $\|\nu\nabla^2\mathbf{v}_s\|$ and $\|(\mathbf{v}_s \cdot \nabla)\mathbf{v}_s\|$, in the form of colormaps shown in Figure 13. The chosen $v_a = 70.5$ mm/s corresponds to a value in the median range of investigation, but this remains true even for the largest investigated v_a, i.e. 107 mm/s. This confirms that although $\mathbf{v}_s$ can be comparable to $\mathbf{v}_a$ in magnitude, the term $(\mathbf{v}_s \cdot \nabla)\mathbf{v}_s$ remains small compared to the others of Equation (7).

---

* chuanyu.dream@gmail.com

† philippe.brunet@univ-paris-diderot.fr

[1] M. Faraday, Philosophical Transactions of the Royal Society of London **121**, 299 (1831).

[2] J. Friend and L. Y. Yeo, Reviews of Modern Physics **83**, 647 (2011).

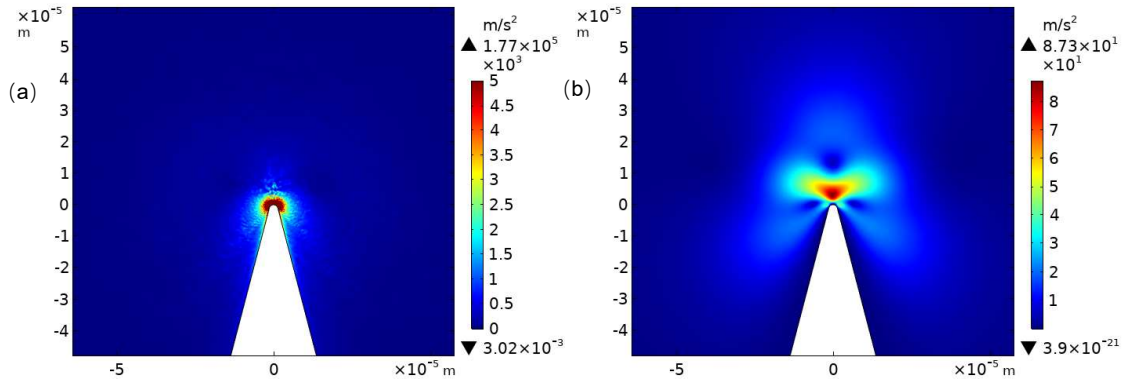

Figure 13: Intensity map of $\|\nu\nabla^2\mathbf{v}_s\|$ (a) and $\|(\mathbf{v}_s\cdot\nabla)\mathbf{v}_s\|$ (b) at $v_a = 70.5mm/s$. The left term has a maximum of 1.77 $\times 10^5 m/s^2$, which is roughly 2000 times stronger than the right one (87.3 m/s^2). Close to the tip, the ratio is about 70. $(\mathbf{v}_s\cdot\nabla)\mathbf{v}_s$ can thus be considered as negligible in Eq.7

[3] K. Sritharan, C. J. Strobl, M. F. Schneider, and A. Wixforth, Applied Physics Letters **88**, 054102 (2006).

[4] T. Franke, S. Braunmuller, L. Schmid, A. Wixforth, and D. A. Weitz, Lab on a Chip **10**, 789 (2010).

[5] A. Lenshof, C. Magnusson, and T. Laurell, Lab on a Chip **12**, 1210 (2012).

[6] S. S. Sadhal, Lab on a Chip **12**, 2600 (2012).

[7] P. B. Muller, M. Rossi, A. G. Marin, R. Barnkop, P. Augustsson, T. Laurell, C. J. Kahler, and H. Bruus, Physical Review E **88**, 023006 (2013).

[8] N. R. Skov, P. Sehgal, B. J. Kirby, and H. Bruus, Physical Review Applied **12**, 044028 (2019).

[9] W. Qiu, J. T. Karlsen, H. Bruus, and P. Augustsson, Physical Review Applied **11**, 024018 (2019).

[10] G. A. Voth, B. Bigger, M. R. Buckley, W. Losert, M. P. Brenner, H. A. Stone, and J. P. Gollub, Physical Review Letters **88**, 234301 (2002).

[11] G. Vuillermet, P.-Y. Gires, F. Casset, and C. Poulain, Physical Review Letters **116**, 184501 (2016).

[12] M. Legay, B. Simony, P. Boldo, N. Gondrexon, S. Le Person, and A. Bontemps, Ultrasonics Sonochemistry **19**, 1194 (2012).

[13] B. G. Loh, S. Hyun, P. I. Ro, and C. Kleinstreuer, Journal of Acoustical Society of America **111**, 875 (2002).

[14] P. J. Westervelt, The Journal of the Acoustical Society of America **25**, 60 (1953).

[15] W. L. Nyborg, The Journal of the Acoustical Society of America **25**, 68 (1953).

[16] S. J. Lighthill, Journal of Sound And Vibration **61**, 391 (1978).

[17] C. Eckart, Physical Review **73**, 68 (1948).

[18] L. Rayleigh, Philosophical Transactions of the Royal Society of London **175**, 1 (1884).

[19] H. Schlichting and K. Gersten, *Boundary-Layer Theory* (Springer Nature, 2017).

[20] W. L. Nyborg, The Journal of the Acoustical Society of America **30**, 329 (1958).

[21] N. Riley, *Theoretical and Computational Fluid Dynamics*, Vol. 10 (Springer US, Boston, MA, 1998) pp. 349–356.

[22] L. Rayleigh, *The Theory of Sound, Volume One.* (Dover Publications, 2013) p. 985.

[23] E. N. Da Costa Andrade, Proceedings of the Royal Society A **134**, 445 (1931).

[24] J. M. Valverde, Contemporary Physics **56**, 338 (2015).

[25] M. F. Hamilton, Y. A. Ilinskii, and E. Zabolotskaya, Journal of Acoustical Society of America **113**, 153 (2002).

[26] M. Wiklund, R. Green, and M. Ohlin, Lab on a Chip **12**, 2438 (2012).

[27] D. Ahmed, X. Mao, B. K. Juluri, and T. J. Huang, Microfluidics and Nanofluidics **7**, 727 (2009).

[28] X. Lu, K. Zhao, H. Peng, H. Li, and W. Liu, Physical Review Applied **11**, 1 (2019).

[29] J. Lei, M. Hill, C. P. de León Albarrán, and P. Glynne-Jones, Microfluidics and Nanofluidics **22**, 140 (2018).

[30] S. Subbotin, V. Kozlov, and M. Shiryaeva, Phys. Fluids **31**, 103604 (2019).

[31] E. A. Jannesar and H. Hamzehpour, arXiv (2019), 1909.03251v1 [physics.flu-dyn].

[32] J. Lei, M. Hill, and P. Glynne-Jones, Physical Review Applied **8**, 014018 (2017).

[33] P. H. Huang, Y. Xie, D. Ahmed, J. Rufo, N. Nama, Y. Chen, C. Y. Chan, and T. J. Huang, Lab on a Chip **13**, 3847 (2013).

[34] P. H. Huang, N. Nama, Z. Mao, P. Li, J. Rufo, Y. Chen, Y. Xie, C. H. Wei, L. Wang, and T. J. Huang, Lab on a Chip **14**, 4319 (2014).

[35] N. Nama, P. H. Huang, T. J. Huang, and F. Costanzo, Lab on a Chip **14**, 2824 (2014).

[36] N. Nama, P. H. Huang, T. J. Huang, and F. Costanzo, Biomicrofluidics **10**, 024124 (2016).

[37] C. Zhang, X. Guo, P. Brunet, M. Costalonga, and L. Royon, Microfluidics and Nanofluidics **23**, 104 (2019).

[38] P. H. Huang, C. Y. Chan, P. Li, Y. Wang, N. Nama, H. Bachman, and T. J. Huang, Lab on a Chip **18**, 1411 (2018).

[39] I. Leibacher, P. Hahn, and J. Dual, Microfluidics and Nanofluidics **19**, 923 (2015).

[40] Z. Cao and C. Lu, Analytical Chemistry **88**, 1965 (2016).

[41] H. Bachman, P. H. Huang, S. Zhao, S. Yang, P. Zhang, H. Fu, and T. J. Huang, Lab on a Chip **18**, 433 (2018).

[42] M. Ovchinnikov, J. Zhou, and S. Yalamanchili, The Journal of the Acoustical Society of America **136**, 22 (2014).

[43] A. A. Doinikov, M. S. Gerlt, A. Pavlic, and J. Dual, Microfluidics and Nanofluidics **24**, 32 (2020).

[44] A. A. Doinikov, M. S. Gerlt, and J. Dual, Physical Review Letters **124**, 154501 (2020).

[45] C. Zhang, X. Guo, L. Royon, and P. Brunet, Micromachines **11**, 607 (2020).

[46] H. Bruus, Lab on a Chip **12**, 20 (2012).

[47] S. Sadhal, Lab on a Chip **12**, 2292 (2012).

[48] S. Boluriaan and P. Morris, International Journal of Aeroacoustics **2**, 255 (2003).

[49] J. Lei, P. Glynne-Jones, and M. Hill, Microfluidics and Nanofluidics **21**, 23 (2017).

[50] *COMSOL Multiphysics® v. 5.3*, www.comsol.com, COMSOL AB, Stockholm, Sweden.

[51] M. Costalonga, P. Brunet, and H. Peerhossaini, Physics of Fluids **27**, 013101 (2015).

[52] S. A. Bahrani, N. Périnet, M. Costalonga, L. Royon, and P. Brunet, arXiv **2001**, 01131 (2020).

[53] X. Guo, Y. Fan, and L. Luo, Chemical Engineering Journal **227**, 116 (2013).

[54] C. Zhang, P. Brunet, L. Royon, and X. Guo, Submitted (2020).

[55] P. B. Muller and H. Bruus, Physical Review E - Statistical, Nonlinear, and Soft Matter Physics **92** (2015).

Appendix B

Paper appeared in Microfluidics and Nanofluidics

Microfluidics and Nanofluidics (2019) 23:104
https://doi.org/10.1007/s10404-019-2271-5

RESEARCH PAPER

Acoustic streaming near a sharp structure and its mixing performance characterization

Chuanyu Zhang[1] · Xiaofeng Guo[1,3] · Philippe Brunet[2] · Maxime Costalonga[4] · Laurent Royon[1,2]

Received: 27 April 2019 / Accepted: 25 July 2019

Abstract
Acoustic streaming can be generated in microchannels by low-frequency acoustic transducer in the vicinity of sharp structures. Close to the tip, the strong curvature induces bent trajectories on the time-periodic acoustic flow, locally enhancing the streaming-generating force. In this study, we investigate the influence of the sharp structure and vibration velocity on the streaming flow. The vibration velocities are characterized by directly visualizing the displacement of tracing particles and the generated acoustic streaming is observed using particle image velocimetry, under various operating conditions. By measuring the concentration of a fluorescence dye, we evaluate the mixing performance for different values of tip angle, vibration amplitude, and flow rate through the microchannel. Our results confirm that intense streaming is generated under low-frequency (2.5 kHz) acoustic condition when the local curvature of the boundary is close to or smaller than the viscous boundary-layer thickness. It is shown that the sharpest the edge tip, the largest the vortices size and the spatial extent of the induced streaming, therefore greatly enhancing the mixing between two miscible liquids. The mixing index, linearly characterizing the mixing degree between 1 (totally separated) and 0 (perfectly mixed), jumps from 0.73 (without acoustic excitation) to 0.38 (with acoustic excitation), resulting in a highly mixed homogeneous fluid just after the sharp edge. This emphasizes the promising potential of acoustic streaming to enhance mass transfer inside microchannels which is usually limited by the laminar flow conditions.

Keywords Acoustic streaming · Sharp structure · Mixing performance · Fluorescence flow visualization

1 Introduction

Increasing interests in milli- or micro-fluidic devices represent both advantages and challenges. Their advantages in efficiency and compactness make them attractive for a large range of industrial (Whitesides 2006), biological, and pharmaceutical (Elvira et al. 2013) applications. However, due to geometry and pressure drop constraints, the flow regime in most micro-fluidic devices is laminar. Consequently, transport phenomena are generally considered as a challenge. Acoustic Streaming (AS) has gained interest in recent years due to its ability to generate flows even at very low Reynolds number, therefore making it advantageous in various applications (Gopinath and Mills 1994; Boluriaan and Morris 2003; Whitesides 2006; Lee and Loh 2007; Legay et al. 2012; Huang et al. 2013b, 2018b; Elvira et al. 2013).

Physically, the AS phenomenon is generated in a quiescent fluid subjected to a periodical acoustic or mechanical vibration field. A net mean flow originates from the dissipation of the vibration energy by viscosity of the fluid; the

Electronic supplementary material The online version of this article (https://doi.org/10.1007/s10404-019-2271-5) contains supplementary material, which is available to authorized users.

✉ Xiaofeng Guo
xiaofeng.guo@esiee.fr

✉ Philippe Brunet
philippe.brunet@univ-paris-diderot.fr

[1] Univ Paris Diderot, Sorbonne Paris Cité, LIED, UMR 8236, CNRS, 75013 Paris, France

[2] Univ Paris Diderot, Sorbonne Paris Cité, MSC, UMR 7057, CNRS, 75013 Paris, France

[3] ESIEE Paris, Department SEN, Université Paris Est, 2 Boulevard Blaise Pascal, Cité Descartes, 93162 Noisy Le Grand, France

[4] Massachusetts Institute of Technology, 77 Massachusetts Avenue, Cambridge, MA 02139, USA

Published online: 07 August 2019

latter can be either Newtonian or non-Newtonian. Theoretically, the phenomenon can be modeled by the time-averaged non-linear term of the Navier–Stokes (NS) equation coupled with vibration perturbation. The first AS phenomenon was observed as early as 150 years ago, but continuous research efforts have been done until today due to the diversity of mechanisms and applications (Faraday 1831; Eckart 1948; Nyborg 1953; Stuart 1966; Lighthill 1978; Boluriaan and Morris 2003).

Recently, the observation of intense flow and vortices generated by acoustic fields within sawtooth-shaped microchannels have brought a renewal of interest to boundary-driven streaming flows in micro-fluidics (Huang et al. 2013a, b, 2018a, b; Nama et al. 2014a, b; Ovchinnikov et al. 2014; Tobias et al. 2015). Huang et al. (2013a) first try to apply such type of streaming into mixing enhancement. (Ovchinnikov et al. 2014) conducted theoretical and experimental works to fundamentally investigate such a phenomenon. In their validation experiments, the sharp edge (tip of a needle) provides a 461 Hz mechanical vibration, i.e., the actuation inside the liquid. They pointed out that such streaming velocities can be of several orders of magnitude higher than Rayleigh streaming velocities under similar amplitudes of vibration. They attributed the origin of this new type of streaming to the centrifugal force around the sharp vibrating structure. For instance, in eye surgery process, the jets coming from ultrasonically vibrating needles can reach a speed of as high as 2 m/s (Zacharias and Ohl 2013). In addition to high streaming velocity, another significant characteristic of such streaming is its relatively low acoustic frequency (Huang et al. 2013a; Ovchinnikov et al. 2014) and energy input, which can be particularly adapted to transfer enhancement in micro-fluidics geometries. In the realm of acoustic excitations on microchannels, the vast majority of solutions (Bruus 2012) uses waves of a few MHz or higher frequency, so that the acoustic wavelength in water ($\lambda_c = c/f$, with $c = 1430$ m/s) is of the order of the largest dimension of the channel, namely around half a millimeter or so. The most common setups use two transducers facing each other or a transducer and a reflector (Wiklund et al. 2012; Barnkob et al. 2012; Lei et al. 2013), to generate a resonance condition when the channel width is equal to the half of λ_c. The counterpart of this technique is the necessity to use expensive devices like high-frequency transducers or amplifiers. On the contrary, the use of sharp structures is adapted to low-frequency acoustic waves, even below the ultrasound range, typically of a few kHz, allowing the use of low-cost transducers and amplifiers. While the acoustic wavelength, of several tens of cm, is then much larger than the channel dimensions, the sharp structures induce a local intensification of the acoustic actuation to the fluid.

With the advantages of high streaming velocity and low excitation frequency, the sharp-edge acoustic streaming could potentially efficiently improve processes such as mixing, particle selection, heat transfer, etc. Studies, especially those from Huang's group, reported the characterization of sharp-edge streaming flow and its application in mixing (Huang et al. 2013b, 2018b; Nama et al. 2014a), bioparticle and liquid-drop control (Leibacher et al. 2015; Cao and Lu 2016; Ozcelik et al. 2016), as well as various on-chip devices (Huang et al. 2014, 2015a, b; Bachman et al. 2018; Zhao et al. 2019).

Although experiments and simulations on acoustic streaming in sawtooth-shaped microchannel have been done in the aforementioned studies (Huang et al. 2013b; Ovchinnikov et al. 2014), several issues remain to be investigated. In particular, the vibration conditions required to generate significant streaming need more quantitative measurements. The available literature only provides the electrical input into transducers (mainly excitation frequency and input voltage) which is not a direct physical parameter to understand the generation of streaming. Other experimental variables such as clamping, transducer type, and quality can make reproducing challenging. As a result, the physical interpretation of the fluid–wall interaction in a confined mini/micro-fluidic structure under acoustic excitation, as well as its influence on acoustic streaming generation and mass transfer performances is of both fundamental scientific interest and applicational significance.

In this study, we investigate the streaming flow properties and mixing efficiency of acoustic streaming generated in Y-shaped microchannels with sharp-edged structures. We design an experimental setup that allows to visualize streaming vortices by high-speed imaging and to investigate the key influencing parameters such as acoustic amplitudes, sharp-edge angle, as well as flow rate. A visualization based on fluorescence dye concentration tracking is used to assess the mixing performance of the Y-mixer. The paper is organized as follows: Sect. 2 summarizes the AS theory near sharp edges; Sect. 3 presents the experimental setup and the typical flow visualization; then, Sects. 4 and 5 present experimental results, respectively, on the flow properties and mixing performances, and finally, Sect. 6 concludes on the main findings as well as some perspectives.

2 Theoretical background

The usual framework of AS studies describes the velocity and pressure fields via a decomposition into a first-order time-periodic component and a second-order steady component, with the acoustic vibration velocity (and the subsequent induced periodic flow) being of much larger magnitude than the steady (streaming) flow response (Lighthill 1978; Rayleigh 2013).

In the time-dependent acoustic vibration field, velocity and pressure are denoted as follows:

$$V_1 = \mathrm{Re}\left(V_\omega e^{i\omega t}\right)$$
$$p_1 = \mathrm{Re}\left(p_\omega e^{i\omega t}\right), \quad (1)$$

where V_ω,p_ω are the velocity and pressure variation amplitudes due to the acoustic excitation; V_1, p_1 are, respectively, the first-order acoustic velocity and pressure at time t. *Re* means the real part of the complex terms.

The total velocity and pressure fields comprise thus two components:

$$V = V_1 + V_0$$
$$p = p_1 + p_0, \quad (2)$$

where V and p are the total velocity and pressure of fluid; V_0, p_0 are the steady-flow velocity and pressure.

The sharp-edge AS in this study uses acoustic wavelength ($\lambda_c = c/f$, in the order of ~ m) much higher than the characteristic flow dimensions (the height of the sharp edge or width of the channel, < 1 mm). Both acoustic and streaming velocities are much lower than the sound speed ($c = 1430$ m/s in water), the flow in the present study can be treated as incompressible flow. Inserting Eq. 2 into the incompressible Navier–Stokes and continuity equations leads to two relationships with time-dependent terms in Eqs. 3 and 4:

$$i\omega V_\omega = -\frac{1}{\rho}\nabla p_\omega + \nu\nabla^2 V_\omega \quad (3)$$

$$\nabla \cdot V_\omega = 0. \quad (4)$$

Averaging these two equations over a period yields to the following:

$$\left(V_0 \cdot \nabla\right)V_0 = -\frac{1}{\rho}\nabla p_0 - F_s + \nu\nabla^2 V_0 \quad (5)$$

$$\nabla \cdot V_0 = 0. \quad (6)$$

Here, $F_s = \frac{1}{2}\mathrm{Re}\left[\left(V_\omega \cdot \nabla\right)V_\omega^T\right]$ is the time-averaged inertia term due to the first-order acoustic field, and is treated as a steady-force term in the second-order steady equation.

Applying a spatial derivative to the first-order acoustic equations (Eqs. 3 and 4), we further reduce them to their equivalent form Eq. 7, which is the classical wave equation for the acoustic field:

$$\nabla^2 p_\omega = 0. \quad (7)$$

From the form of F_s, it is clear that a homogeneous acoustic field cannot generate any streaming flow, as the effective force would be null. However, the sharp tip structures with strong local curvature on the channel walls induce strong heterogeneity in the acoustic oscillating flow in the fluid. As sketched in Fig. 1, at a given time, the vibration of the fluid

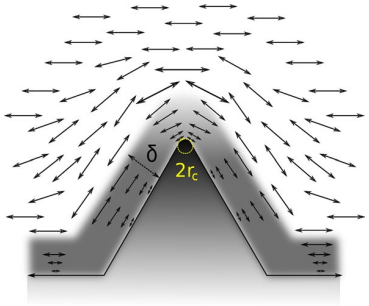

Fig. 1 Sketch of acoustic oscillating flow around a tip edge

is uniformly distributed except for the local zone around the sharp edge, the latter being the source of AS. More specifically, close to the tip, both the orientation of the acoustic field and the vibration amplitude provide favorable condition of an intense F_s very near the tip. Far from the tip, the force is null or negligible. Therefore, the non-uniformity of the acoustic field caused by the sharp structure makes acoustic streaming at relatively low frequencies (several kHz) possible. This is furtherly confirmed by our direct observation presented later in Fig. 5 as well as in the Supplementary video (Supplementary material 1).

With acoustic frequencies of the order of kHz and low-viscosity liquids like water, the dissipation length is much larger than the system size, and hence, most of the dissipation is due to the viscous friction at the solid–liquid interfaces. This friction is located in a viscous boundary layer of width δ. (Ovchinnikov et al. 2014) point out that the streaming only appears in the situation where the radius of curvature of the walls is smaller than δ, meaning that streaming is generated by the sharp, local gradient of velocity near the tip. Therefore, we operated with sharp tips with curvature radius of a few microns, fabricated with photolithography techniques.

As shown in Fig. 2, while no particle motion can be observed in the absence of acoustic field (Fig. 2b), a clear streaming in an extended region appears near the tip when acoustic excitation is prescribed via the transducer stuck on the glass slide (Fig. 2c). The streaming image in Fig. 2c is obtained by superposition of time sequential individual particle trajectories. Two streaming vortices are observed on both sides of the sharp edge. In the case of a round, smooth structure with big enough curvature, as shown in Fig. 2d, the acoustic streaming is not observed. While this is not strictly a parametric study on curvature diameter, the result is in accordance with Ovchinnikov et al.'s framework, demonstrating that this type of streaming should be generated with sharp structures.

Since we can briefly describe that the fluid is jetted from the tip, the resulting vortices and the strong directional

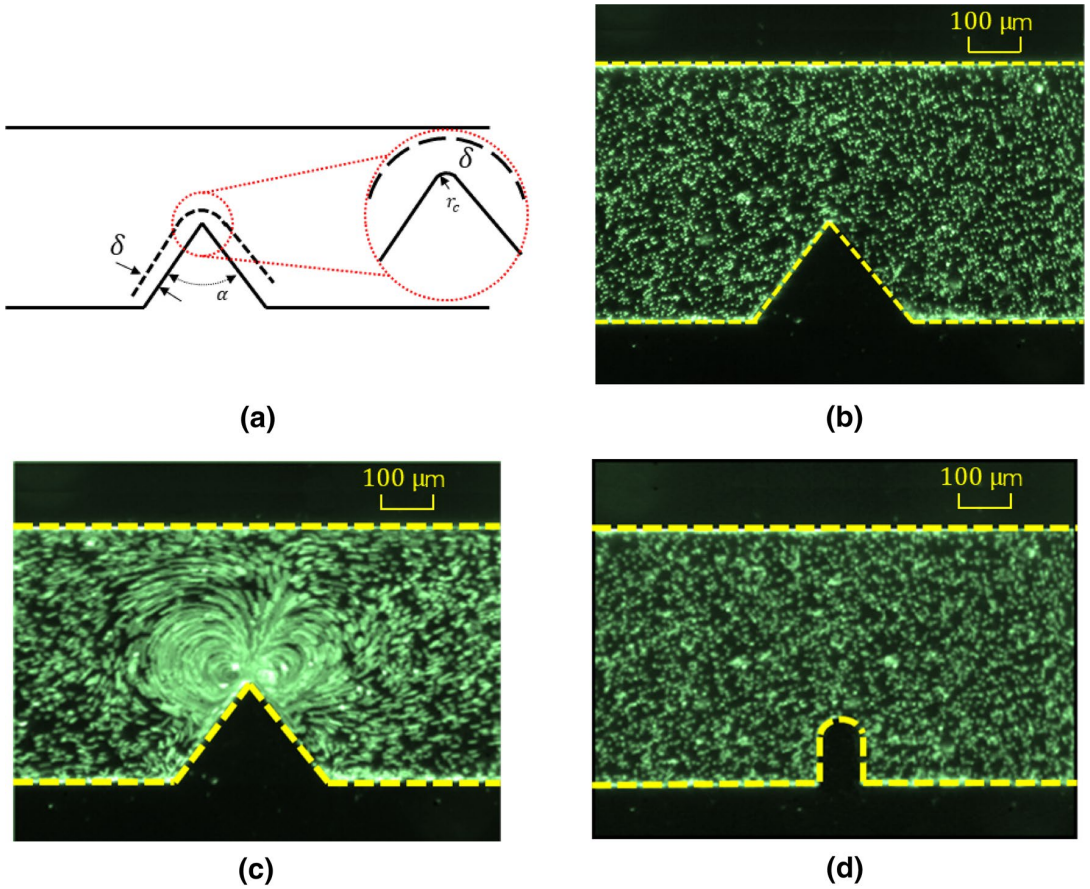

Fig. 2 Mechanism of acoustic streaming under zero flow rate. **a** Acoustic streaming condition, sharp-edge curvature should be lower than the acoustic boundary layer $2\ r_c < \delta$; **b** fluorescent particles distribution around a sharp-edge ($\alpha = 60°$) without acoustic field; **c** the streamline of the acoustic excited particles movement under a stack of 100 images equivalent to a duration of 100 ms, $V_\omega = 37.8$ mm/s, $f = 2.5$ kHz; **d** round edge with a curvature of 100 µm under acoustic excitation but with no acoustic streaming, $V_\omega = 37.8$ mm/s, $f = 2.5$ kHz

flow will actively bring disturbance into the flow along the channel. The ensemble of the phenomena is potentially applicable in a large number of engineering process, such as mixing, heat transfer enhancement, etc.

3 Experiment and post-processing

Figure 3 shows our experimental setup as well as the microchannel geometry. The setup around the Y-shaped microchannel (shown in Fig. 3a) is composed of a syringe pump

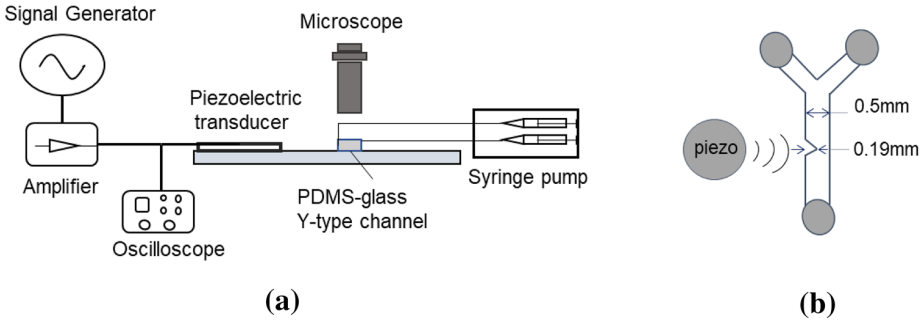

Fig. 3 Sketch of the experimental setup. **a** Fluid circulation and visualization system; **b** Y-type micro-channel with a sharp edge

(Newtown Company & Co) allowing the injection of fluid from two syringes, under well-controlled flow rate through the channel and via the two inlets. A function generator (Model 33220A Arbitrary waveform generator, Agilent) with a home-made adjustable power amplification provides input to a piezoelectric transducer (Model ABT-455-RC, RS Components). The transducer is glued on a standard glass microscope slide (width × length × thickness: 26 mm × 76 mm × 1 mm) through which the visualization is made using a binocular microscope together with a fast camera (MotionBLITZ Cube4, Mikrotron). The piezoelectric transducer (diameter 35 mm and thickness 0.51 mm) delivers acoustic vibrations to the glass slide and to the whole channel stuck onto it, at various resonance frequencies from about 1 kHz up to 40 kHz. We chose to operate at one of these resonance peaks f, namely that at $f = 2.5$ kHz. It turns out that the best operating conditions in terms of streaming flow were obtained at this frequency.

The Y-shaped Polydimethylsiloxane (PDMS) channel is designed by 2D photolithography. First, a mold made of SU8 negative photoresist was fabricated: a 50 µm-thick SU8 liquid layer was spin-coated on a silicon wafer. After a soft baking at 65 °C, the resist was exposed to UV through a photomask. The resist was then immersed in a developer bath and then hard-baked at 95 °C. Then, PDMS (Sylgard 184) was thoroughly mixed with 10% in mass of curing agent, degassed in a vacuum chamber, and poured on the SU8 mold to constitute a 2.5-mm-thick layer of PDMS mixture on top of the wafer. The whole is put in a stove at 65 °C during 4 h.

The PDMS is then sealed and stuck on a glass microscope slide after a 1-min oxygen plasma treatment of both sides. The microchannel of a height of 50 µm is then formed between the PDMS and the glass slide. The plasma treatment enables the microchannel to withstand the pressure from inlets without leakage. Key geometrical dimensions of the Y-mixer are detailed in Fig. 3b. Sharp edges with different angles α (30°, 60°, 80°, and 90°) were fabricated from various molds. Hence, all channels were sealed on a similar glass slide, and rapid cure epoxy resist was used to permanently glue the transducers on each glass slide. It turns out that the best acoustic coupling was obtained this way. The radius of curvature of the different tips was measured with a 120X microscope with five repetition measurements of each angle. According to our measurement of the curvature diameter $2r_c$ of the sharp edge, its value ranges from 2.8 to 10.3 µm, which are shown in Fig. 4 and Table 1. These values are all smaller than the viscous boundary layer thickness 11.5 µm, determined by $\delta = \sqrt{2\upsilon/\omega}$ (Boluriaan and Morris 2003), with υ the kinematic viscosity of the fluid, and ω the angular frequency.

Two syringe pumps provide equal flow rate Q_s through the two PDMS microchannel inlets. It should be noted that hereafter the channel throughput Q_c is defined as the flow rate in the main channel. It is the sum of the two single inlet flow rates provided by each syringe (Q_s).

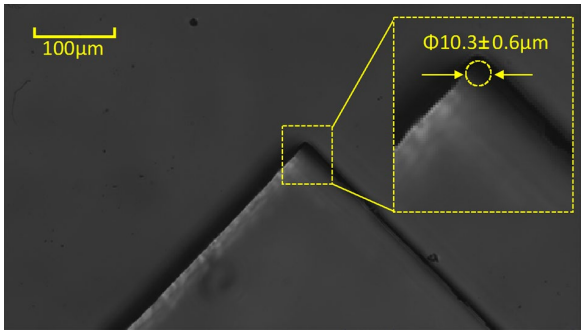

Fig. 4 Measurement of the curvature diameter under a ×120 microscope, here $\alpha = 90°$

Table 1 Curvature diameter corresponding to different tip angles of the sharp edges

Sharp edge angle α (°)	30	60	80	90
Curvature diameter $2r_c$, (µm)	2.8 ± 0.3	5.8 ± 0.4	7.1 ± 0.4	10.3 ± 0.6

The transducers are excited with periodic sinusoidal signal. The available range of peak-to-peak voltage is between 0 and 30 V (up to ± 15 V). It is important to notice that the speed of sound (c) in water is 1430 m/s and that in glass is 4540 m/s, so the wavelengths of vibration ($\lambda = c/f$) at 2.5 kHz are, respectively, 0.57 m and 1.82 m. These values are far greater than the scales of the channel, whose width is 0.5 mm and length is 25 mm. The amplitude of the acoustic wave is, therefore, expected to be uniform in the whole channel.

To visualize the flow, the fluid is seeded with fluorescent particles (green polystyrene microspheres, diameter 4.9 m, Thermo Scientific). However, due to the limited sensitivity of the high-speed camera, the best contrast and image quality is obtained by direct lighting with white light, hence with the diffused light instead of the fluorescence-emitted light. To enhance the contrast, a cold-light beam shines from the bottom of the glass slide. The depth of field of the microscope lens is about 10 µm, five times smaller than the channel depth (50 µm). Hence, after careful focal adjustments (based on finding the position that shows the maximal transverse velocity for a given flow rate), we obtain high fidelity pictures with clear focus, as shown in Fig. 2b–d.

Since the streaming velocity near the tip can be of comparable magnitude to the vibration velocity, which is different from most previous studies (Squires and Quake 2005) and will be discussed later (Sect. 4.3.2), another challenge is to observe and measure these two velocities separately. The

following methods are used: first, to detect the motion of the particles during one vibration period and compute the streaming velocity, the frame rate of the camera is set to as high as 25 kHz and the exposure time as short as 25 µs. Under this condition, any individual particle appears as a small sphere of a few pixels, because the exposure time is much smaller than the vibration period ($1/f = 400$ µs). A total of ten pictures are captured for every vibrating cycle, making the visualization of the acoustic vibration possible. To obtain the streaming velocity, we choose sequential images with a time interval of one acoustic period to "hide" the vibrational velocity. Then, to measure the acoustic vibration velocity V_ω, the frame rate of the camera is reduced to 2.5 kHz with an exposure time extended to 400 µs. Under this condition, particles in these pictures appear as threads of fixed length that corresponds to the amplitude of its acoustic-driven motion (Fig. 5). Results are shown in supplementary video. During the experiment, the pictures are continuously synchronized with the camera to the computer.

The obtained images are then treated with open-source software ImageJ (Schneider et al. 2012). For vibration velocity, the particles' displacements are directly measured from the captured images, and the results as well as the uncertainties are discussed in detail in Sect. 4.2. For the streaming field, the relative displacement of particles at a given phase of the vibration period and at given locations allows the determination of the velocity field. Successive frames are converted into an array of displacement vectors for each particle by the software PIVlab (Thielicke and Stamhuis 2014). Second, summing the intensity of the images of a number of frames allows clear visualization of trajectories and then the location, form, and sizes of vortices.

Besides, COMSOL Multiphysics © simulation is used as a control study to verify the reliability of the PIV result in terms of velocity characterization. The control study is done without acoustic excitation using a standard laminar flow model. The results are shown to be highly close (See Supplementary material 2).

4 Results and discussion

4.1 From acoustic vibration to AS

The direct visualization of fluid motion responding to the acoustic forcing is shown in Fig. 5a and the supplementary video. The main image Fig. 5 is obtained from acquisitions with high-speed imaging (1.25 kfps) of particle trajectories over a few vibration periods. No apparent motion of the microchannel walls could be evidenced from these visualizations. Hence, the analysis of individual traces left by particles gives both the amplitude of the acoustic wave in the fluid and the orientation of this field V_ω. Besides the main image, two magnified details are shown on top of it. On the left of Fig. 5, we show the particle vibration by taking six images within one vibration period. This allows the quantification of the acoustic vibration amplitude 2A. On its right, the trajectory of one particle during ten periods is followed. This picture shows that near the tip, the streaming velocity V_0 (in the direction of the sharp tip, shown as vertical) has a magnitude comparable to the vibration velocity V_ω (in the direction of the fluid channel, shown as horizontal). Similar to the idealized sketch of the amplitude and direction of this first-order flow in Fig. 1, far enough from the viscous boundary layer, the amplitude is found constant and the fluid displacement is parallel to the channel walls where the oscillating fluid movement is possible. However, due to the no-slip boundary condition along the wall, the viscous shear develops within the layer of thickness δ along the walls and this amplitude vanishes within this boundary layer. Furthermore, the orientation of the acoustic fluid motion has to locally match that of the walls. Consequently, the acoustic velocity field V_ω is subjected to sharp variation of orientation around the tip. Furthermore, the acoustic amplitude is higher near the tip than elsewhere in the channel, as shown in Fig. 5. As emphasized in (Ovchinnikov et al. 2014), this leads to an intense streaming force F_s very near the tip, while this force is null or negligible far from the tip. Therefore, the non-uniformity of the acoustic field caused by the sharp structure makes acoustic streaming at relatively low frequencies (several kHz) possible.

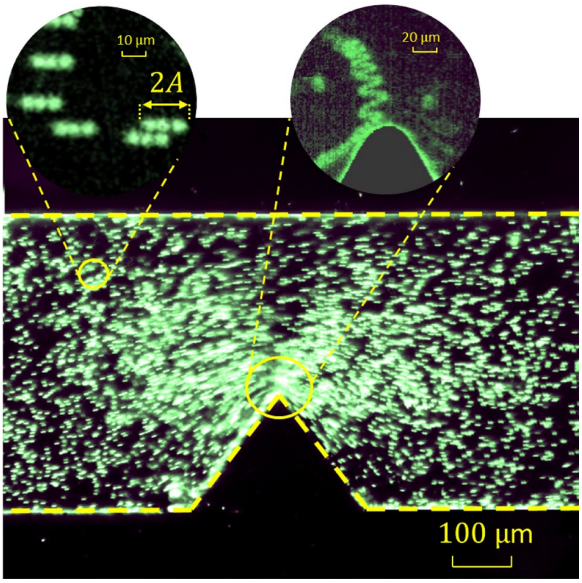

Fig. 5 The mechanism of acoustic streaming explained by high-speed visualization of acoustic vibrations within the fluid, from particle trajectories over a few periods; the velocity measured is 101.7 mm/s (see Supplementary video for dynamic visualization effect)

4.2 Acoustic vibration speed

As the transmission from electrical transducer power to the solid glass then to the fluid is rather complex (Uchida et al. 1995), we here only experimentally characterize the resulted vibration. Therefore, the vibration amplitude and velocity induced by the transducer are measured directly on the glass slide and indirectly in the fluid, the former by a laser vibrometer, and the second by particle visualization. Their comparison allows us to identify the relative oscillation velocity on the fluid–solid interface, where the acoustic streaming develops.

On one hand, a laser vibrometer (OFV-505 model, Polytec) is used to directly measure the vibration on the glass slide—near the location of the channels and after the PDMS bonding. Within the uncertainties of measurements, the relationship between the prescribed voltage and the local vibration velocity $V_{\omega,\text{glass}}$ is found to be linear. We measured for instance $V_{\omega,\text{glass}} = 2.2$ mm/s, 4.4 mm/s, and 6.9 mm/s corresponding, respectively, to input peak-to-peak voltages U_{pp} of 10, 20, and 30 V, at 2.5 kHz. In terms of acoustic amplitude A_{glass}, such that $V_{\omega,\text{glass}} = A_{\text{glass}}\omega$, and as $f = 2.5$kHz, it corresponds to displacement of the order of 1 micron or smaller on the glass.

On the other hand, acoustic fluid displacement 2A is extracted from high-speed imaging, as already shown in Fig. 5. Figure 6 shows the linear relation between induced vibration velocity of the particles inside the liquid and the peak-to-peak voltage of the piezo-transducer, which is consistent with (Franke et al. 2003). The error of measuring the vibration velocity mainly comes from the pixel resolution and uncertainties of 2A are within 1 pixel (representing 0.75 µm) which corresponds to ± 6.1 mm/s. For instance, our results show values of the particles acoustic vibration velocity $V_\omega = 37.8$ mm/s, 50.5 mm/s, 70.5 mm/s, 85 mm/s, and 101.7 mm/s at 2.5 kHz and corresponding to a peak-to-peak voltage U_{pp} of 10 V, 15 V, 20 V, 25 V, and 30 V, which will be the main experimental conditions of the present study. For higher vibration amplitudes with transducer inputs between 30 and 60 V, the vibration velocities are also shown in Fig. 6. However, due to experimental limitations (mainly exposure time of the fast camera in case of very high streaming velocity), our experimental conditions are only limited to under 30 V.

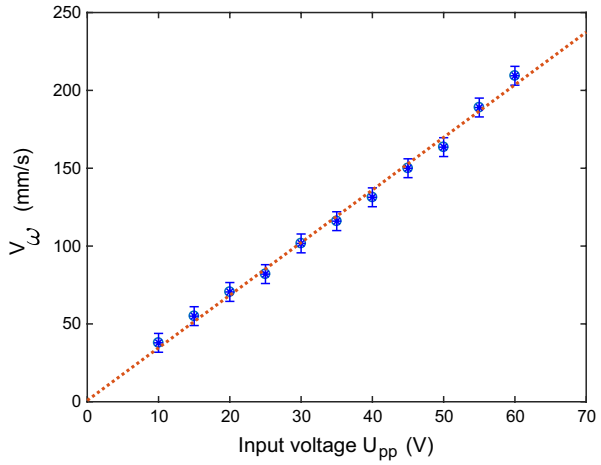

Fig. 6 Acoustic vibration velocity measured by particle visualization at different input peak-to-peak voltage of the piezo-transducer. The calibration is given by the linear fit $V_\omega = aU_{\text{pp}}, a = 3.38\,\text{mm}/(\text{s}\cdot\text{V})$

Since only the relative fluid–wall vibration accounts for the acoustic streaming phenomenon, and considering the measured solid vibration is lower than the tenth of the liquid vibration, hereafter, we use the particles visualization-based vibration speed as the reference, i.e., V_ω. The following discussions are all based on this reference (Fig. 6).

4.3 Flow visualization

In this section, we keep the piezoelectric transducer input to 2.5 kHz and use three different vibration velocities: $V_\omega =$ 37.8 mm/s, 70.5 mm/s, and 101.7 mm/s. Different tip angles α are used: 30°, 60°, 80°, and 90°, so as to different channel flow rates $Q_c = 0$, 1, 4, 8, 12, 16 µL/min. We focus our following discussions on how the acoustic streaming disturbs the main flow.

4.3.1 General characteristic of the flow

Acoustic perturbation to the fluid can be clearly observed from the velocity field given by the PIV. As shown in Fig. 7a, under an acoustic vibration of $V_\omega = 37.8$ mm/s at 2.5 kHz, the fluid around the sharp edge is jetted from the tip through the transverse direction of the microchannel. Since no throughput is imposed in that case, two symmetrical vortices appear besides the sharp edge. Outside of the region near the sharp edge (shown in the red square in the upper right corner of Fig. 5a), however, no fluid disturbance is observed, confirming that AS originates from the geometrical singularity of the tip. As already discussed in Fig. 2d, for the "round" structure with $2r_c = 100\ \mu\text{m} \gg \delta$, there is no evident streaming appearing around the structure. This confirms the hypothesis given by the perturbation theory (Ovchinnikov et al. 2014), that only when the tip curvature is narrower than the acoustic boundary layer, that the acoustic streaming could appear.

Indeed, considering $F_s = \frac{1}{2}Re\left[\left(V_\omega \cdot \nabla\right)V_\omega^{\text{T}}\right]$, it is clear that the stress is stronger in areas where the spatial variations of V_ω are sharper. Hence, the streaming vortices around the sharp structure can be attributed to the periodical curved motion of the fluid around the tip. The streaming force F_s generates a jet from the tip, perpendicular to the channel

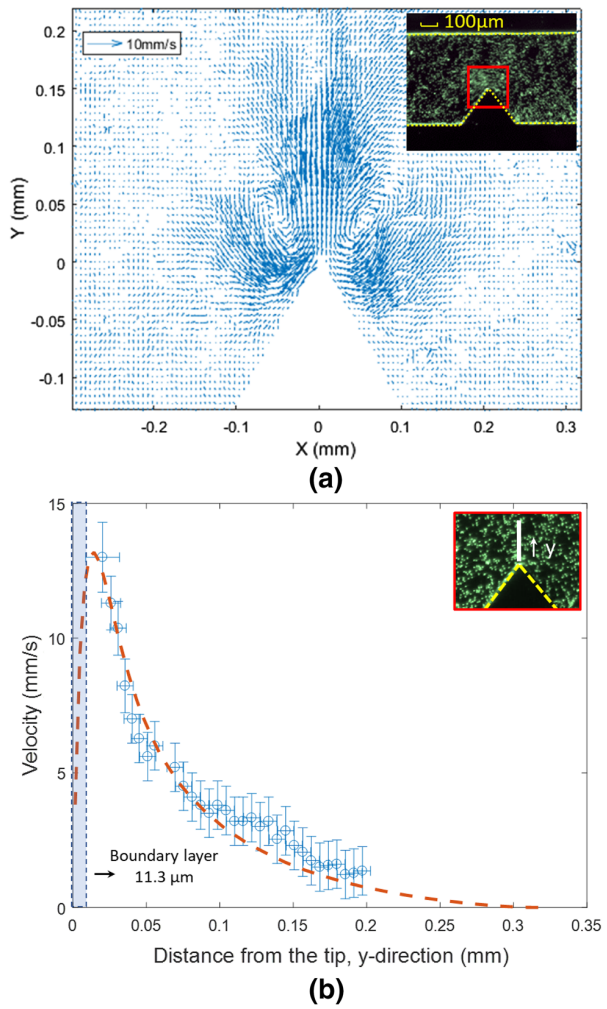

Fig. 7 Acoustic streaming velocity field, at $V_\omega = 37.8\,\mathrm{mm/s}$ and $f = 2.5\,\mathrm{kHz}$. **a** Velocity field obtained from PIV and **b** velocity distribution along the transverse direction from the tip. The acoustic streaming is obtained from a tip with $\alpha = 60°$, $Q_c = 0$. The red line shows qualitatively the velocity evolution profile which is in accordance with the simulation results by (Ovchinnikov et al. 2014)

longitudinal direction, which in turn induces the aforementioned vortices' pair.

In Fig. 5b, we trace the velocity distribution along the y-direction (following the thick white line shown in the upper right corner, $y = 0$ is taken at the tip) based on the PIV results. It clearly shows a rapid increase of the AS velocity from zero to a maximum value in a distance as short as 0.025 mm. After the peak, the AS velocity reduces gradually as its momentum transfer to the main fluid in the channel. The sharp decrease of the streaming velocity is consistent with Ovchinnikov's estimation (Ovchinnikov et al. 2014), the force is localized within a distance of less than δ from the tip; therefore the velocity along y-direction decreases

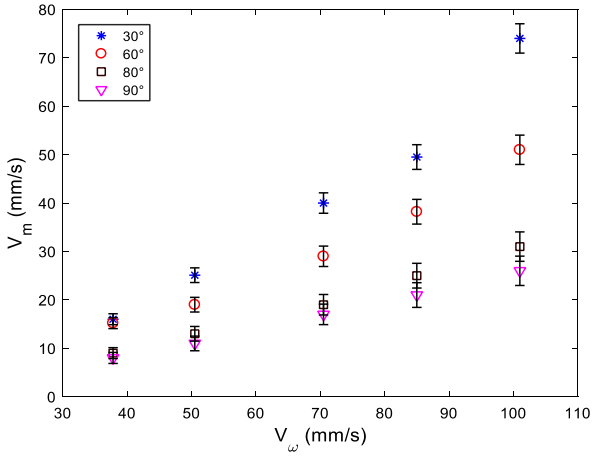

Fig. 8 Maximum streaming velocity versus acoustic velocity, generated near sharp tips of different angles, under no-flow condition ($Q_c = 0$)

locally and rapidly after reaching the maximum value. Under the above condition, the peak value (maximum AS velocity) is $V_m = 15.4$ mm/s and it depends significantly on the excitation amplitude, sharp-edge angle, etc. It should be noted that uncertainties of streaming velocity mainly come from two aspects: the first is the coupling of the acoustic vibration with the streaming, which primarily concerns the maximal velocity value V_m, and the second lies in the pixel resolution. For the first, the error of V_m is proportional to the streaming velocity and is estimated to be $\pm 3\%$ of V_ω. For the second, the pixel resolution (1 pixel = 0.75 μm) during two sequential images of a time slaps of 400 μs results in an error of ± 0.9 mm/s.

4.3.2 Maximum acoustic-induced streaming velocity

As a signature of the acoustic streaming intensity, we extract from each velocity field the transverse component V_m of the maximum velocity along the tip axis, as shown in Fig. 5b.

Figure 8 illustrates the influence of acoustic velocity V_ω and tip angles α of the sharp edge on the maximum AS velocity V_m. Sharper edges and stronger acoustic excitation lead to higher maximal velocity. Under our test conditions, the highest maximum AS velocity is 73 mm/s and it appears at $V_\omega = 101.7$ mm/s (peak-to-peak voltage of 30 V) with the sharpest edge angle 30° (with $2r_c = 2.8$ microns). This confirms that the two velocities are in the same order of magnitude, with a ratio of $V_\omega/V_m = 1.2$. Under lower acoustic excitation, the AS effect is lower and the ratio becomes $V_\omega/V_m = 1.7$ ($V_\omega = 37.8$ mm/s, $V_m = 20$ mm/s, for the 30° sharp edge). The fact that V_ω and V_m are not linearly related is consistent with Ovchinnikov et al.'s theory (Ovchinnikov et al. 2014). However, the framework of their work

is $V_\omega \gg V_m$, and hence, a quantitative agreement with our results should not be expected. Furthermore, higher streaming velocities are found for structures with sharper tip and smaller angle. This is consistent with that sharper tips lead to stronger Rayleigh stress near the tip, for the same vibration velocity and confirms previously observed trends (Nama et al. 2014b).

Let us note that the above conclusion is based on results $Q_c = 0$. When $Q_c > 0$, the streaming vortex is strongly influenced and a detailed visualization on the vortex shapes is necessary.

4.4 Vortex shape, size, and flow disturbance

From Fig. 9a, which illustrates the particle trajectories at $Q_c = 0$, it is clear that the acoustic streaming originates from the sharp edge and induces two counter-rotating symmetrical vortices. These vortices have significant spatial extension: the disturbance can extend even to the other side of the channel, where streams initially flowing in the centerline are dragged to the side of the sharp edge. Furthermore, when $Q_c > 0$, the symmetry of the two vortices is broken (Fig. 9b–d). Due to longitudinal convection of momentum, both vortices on the upstream and downstream side shrink at moderate-flow rate, generally not in a perfectly symmetric way. With the presence of unidirectional main stream, the vortices on the downstream are less impacted than the upstream ones (Fig. 9c, d). For instance, at a flow rate of 12 µL/min, the vortex downstream can still exist, while the upstream one completely disappeared. Therefore, the influence of acoustic vibration on the flow, and in particular the relative importance of the traverse streaming velocity component, vanishes at very high flow rates. Let us underline that the maximal throughput flow rate (12 µL/min) corresponds to an averaged longitudinal velocity of about 1 cm/s which, except very near the tip, is generally much larger than the transverse component of the streaming velocity.

To quantify the disturbance of the streaming flow to the main flow Q_c, vortex size and disturbance distance are measured. For each experimental condition, five repeated

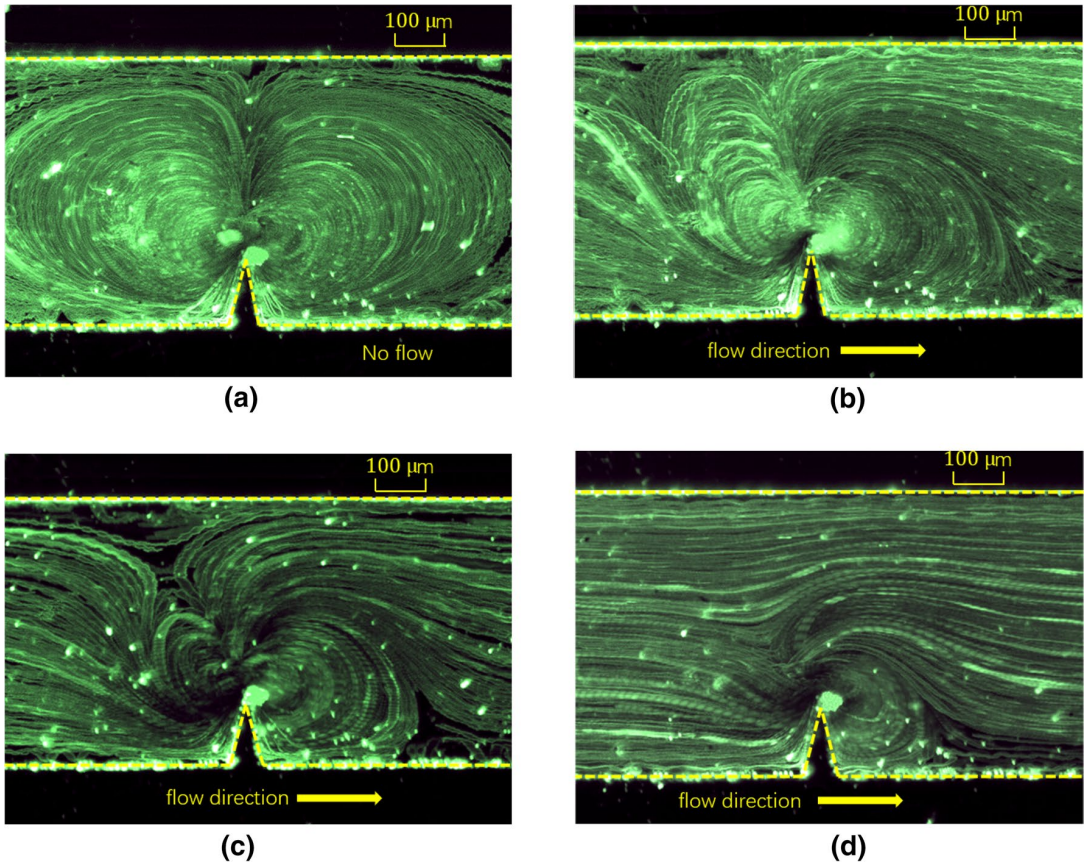

Fig. 9 Flow visualization near the sharp tip, using particle trajectories at different channel throughputs, experimental conditions: $\alpha = 30°$, $V_a = 101.7$ mm/s and $f = 2.5$ kHz. The flow direction is from left to right. Flowrate: **a** $Q_c = 0$, **b** $Q_c = 4$ L/min, **c** $Q_c = 8$ L/min, and **d** $Q_c = 12$L/min

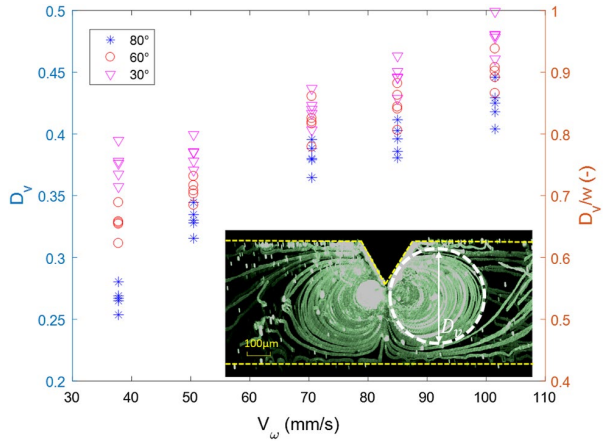

Fig. 10 Vortex size D_v and its relative value to the channel width D_v/w, versus acoustic vibration velocity, at zero flowrate around different sharp edge angles and acoustic stimulations. Condition: with $= 30°, 60°, 80°$ $Q_c = 0$, $V_\omega = 37.8, 70.5$ and 101.7 mm/s, and $f = 2.5$ kHz; $w = 0.5$ mm means the total width of the channel

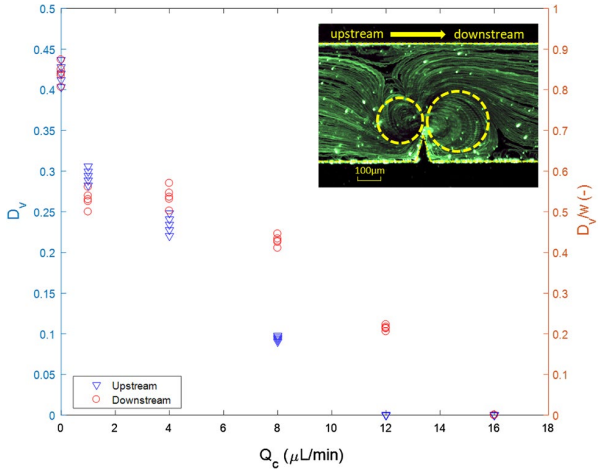

Fig. 11 Upstream and downstream vortex size (D_v and D_v/w) at different flow rates. Condition: $\alpha = 30°$, $V_\omega = 70.5$ mm/s, and $f = 2.5$ kHz

measurements are conducted with the acoustic excitation. In addition, for each measurement, 1000 images (5 s) are stacked to assure that the vortex reaches a steady size and uncertainties mainly come from the pixel resolution and particle density near the interface area.

Figure 10 shows, for the case $Q_c = 0$, how the vortex size varies with different acoustic velocity V_ω and tip angle α. The vortex size, D_v, is defined as the diameter of vortices appearing, respectively, at the upstream and downstream side of the sharp edge. For the particles outside the circle, their motions are only driven by inertia force of the main flow instead of the acoustic streaming. Hence, D_v characterizes the maximum area influenced by the streaming. As the two vortices are symmetrical, we do not distinguish the upstream and the downstream vortex size.

The vortex size takes larger values for stronger vibration velocities, and for a sharper tip angle (smaller diameter than curvature): this is consistent with the similar trends observed for the maximal streaming velocity. At $V_\omega = 101.7$ mm/s and $\alpha = 30°$, the vortex size can reach 0.48 mm. As V_ω increases, the acoustic streaming spreads over the whole channel width (D_v/w approaches 1) for almost all tip angles tested. In such a situation, the vortex size is limited by the microchannel width. On the other hand, with low acoustic excitation, only sharp edge with smaller angle can help to achieve big vortices: at $V_\omega = 37.8$ mm/s, the value of D_v/w can reach 0.76 for the 30° tip but only 0.27 for the 80° one.

Figure 11 shows the variation of vortex size at both downstream and upstream of a 30° tip, under different flow rates. As the flow rate increases from null to 1 μL/min, the vortices size reduces drastically from 0.42 to 0.29 (upstream) and 0.26 (downstream). The vortices continue to shrink after 4 μL/min and they totally disappear when the flow rate is higher than 16 μL/min. In most cases, the upstream vortex is smaller than the downstream one, i.e., between 4 and 16 μL/min. However, results suggest that there is a threshold of flow rate around 2 μL/min under which the upstream vortex is even larger than the downstream one. A possible underlying reason is that the main stream velocity is lower than the upstream longitudinal AS velocity coming from the counter-flow direction. In such a situation, part of the fluid of the upstream vortex still flows back to the sharp edge, enhancing the vortex development. Otherwise, the fluid goes away with the main flow, thus reducing the vortices size. At higher throughput, comparatively, the downstream vortex varies relatively more slowly with flow rate and is subjected to less influence from main flow, presumably because the vortex is squeezed into the low-pressure area formed by the sharp structure. Although there still exists the upstream vortex at large throughput, it plays little role on the main flow.

From the point of view of transverse mass transfer in the channel, we introduce the disturbance extension D_{dis} to quantify the perturbation of the streaming on the main flow. The identification of D_{dis} requires the definition of a critical streamline, as shown in the sub-Fig. 12. The critical streamline (Wang et al. 2012) separates an active perturbation zone (between the tip and the critical line, most of the fluid pass by the tip and then jetted out) and a passive zone (out of the critical line, only a distortion of the main flow is witnessed). As illustrated in Fig. 12, the flow remains laminar in the passive zone while highly perturbed in the active one. The D_{dis} is defined as the distance from the tip to the tangential limit of the critical streamline.

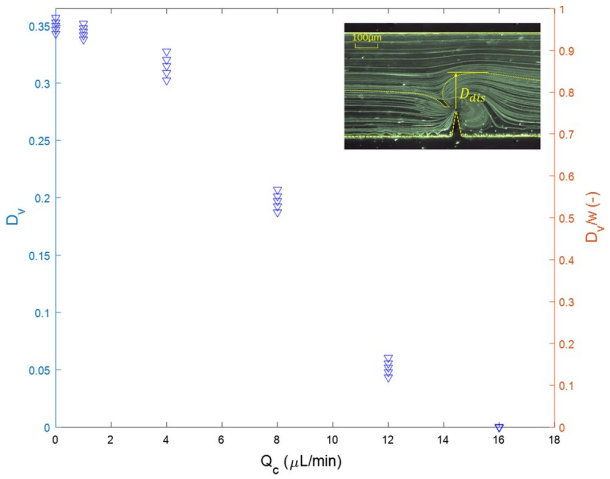

Fig. 12 Disturbance extension D_{dis} as a function of channel throughput. Conditions: $\alpha = 30°$, $V_\omega = 70.5$ mm/s, and $f = 2.5$ kHz

Relative value is also defined for the disturbance extension with respect to the transverse distance from the tip, noted as RD_{dis}:

$$RD_{\mathrm{dis}} = \frac{D_{\mathrm{dis}}}{w - h_{\mathrm{v}}}, \tag{8}$$

where $w = 0.5$ mm is the channel width, and $h_{\mathrm{v}} = 0.18$ mm represents the tip height.

As shown in Fig. 12, despite that the upstream vortex may disappear, the disturbance extension might not be zero. At high flow rates like 12 μL/min, the perturbation could reach 14% of the channel ($RD_{\mathrm{dis}} = 0.14$). To sum up, the flow perturbation is closely coupled with the flow rate and the disappearance of vortices does not mean no acoustic streaming occurs. Channel throughput should be considered as a critical parameter that is coupled with acoustic streaming. Particularly, at high flowrate, vortices are either easily flushed or are fully shadowed in the main stream.

5 Mixing performance

From the above analyses, we expect that the acoustic streaming brings active disturbance into the channel flow, especially at low flow rate and high vibration velocity. To confirm this, we performed mixing experiments using two miscible fluids. One is deionized water and the other is deionized water filled with fluorescent blue dye (Methylene Blue, Fisher Scientific S.A.S.). By observing the variations of the concentration of the blue dye across the channel width and measuring the mixing extent along flow direction, we assess the effect of acoustic excitation on the mixing process.

As a reference, the same flow condition but without acoustic excitation is used for comparison. Besides, several flow rate scenarios are tested based on identical single inlet flow rates Q_{s}, which equals $\frac{1}{2}Q_{\mathrm{c}}$. The following discussions are based on Q_{s}.

Figure 13 shows how the normalized concentration (in Eq. 9, based on Beer–Lambert law) across the transverse direction of the channel evolves at different locations. One location A1 before and two locations A2–A3 after the sharp edge are sampled. We observe that at A1 ahead of the sharp edge, the two fluids begin to mix with each other driven by the upstream vortex. At the sharp edge position, the mixing process is furtherly improved by the intense jet. After the sharp edge, the mixing process is no longer influenced by the acoustic streaming and, therefore, only mass diffusion contributes to mixing, as shown between A2 and A3 in Fig. 13.

The enhancement of the mixing process around the sharp edge can be divided into two steps: (i) the upstream vortex pushes some (high-concentration) fluid against the main flow, directly making it into contact with the other stream; (ii) the fluid jetted by the sharp structure as well as the downstream vortex furtherly disrupt the mixing interfaces. To quantify the mixing, we introduce the mixing index M along the flow direction (Eqs. 9 and 10):

$$C_n = \ln \frac{I_0}{I} \Big/ \frac{I_0}{I_b}; \quad C_n \in [0, 1] \tag{9}$$

$$M = \sqrt{\frac{\frac{1}{N}\sum_{i=1}^{N}\left(I_i - I_{\mathrm{m}}\right)^2}{I_{\mathrm{m}}^2}}, \quad M \in [0, 1], \tag{10}$$

where C_n stands for the normalized concentration; I_0 is the gray value of pure water; I_{b} is the gray value of the unmixed blue dye liquid; I is the gray value of pixels. In Eq. 10, I_i is the gray value of i_{th} pixel; I_{m} is the average gray value of N pixels. In this study, I_{m} is the average gray value of pixels across the width of the channel at certain pixel position along flow direction.

Errors of the Mixing Index in this study are mainly caused by dye deposition near the channel border both on the glass slide and on the PDMS. For every experimental condition, five repeated measures under the same experiment setup are conducted and the maximum error for Mixing Index is 0.02.

As shown in Fig. 14, without acoustic excitation and as a result of the sole diffusion, the mixing index slowly decreases. At $V_\omega = 70.5$ mm/s, the mixing index decreases from 0.8 to 0.6 while crossing the sharp structure and at $V_\omega = 101.7$ mm/s, it furtherly decreases from 0.78 to 0.4. Therefore, the stronger the acoustic excitation, the higher the mixing index obtained. It is obvious that the mixing process within the vicinity regions ahead and after the sharp structure is accelerated by the upstream and downstream vortices

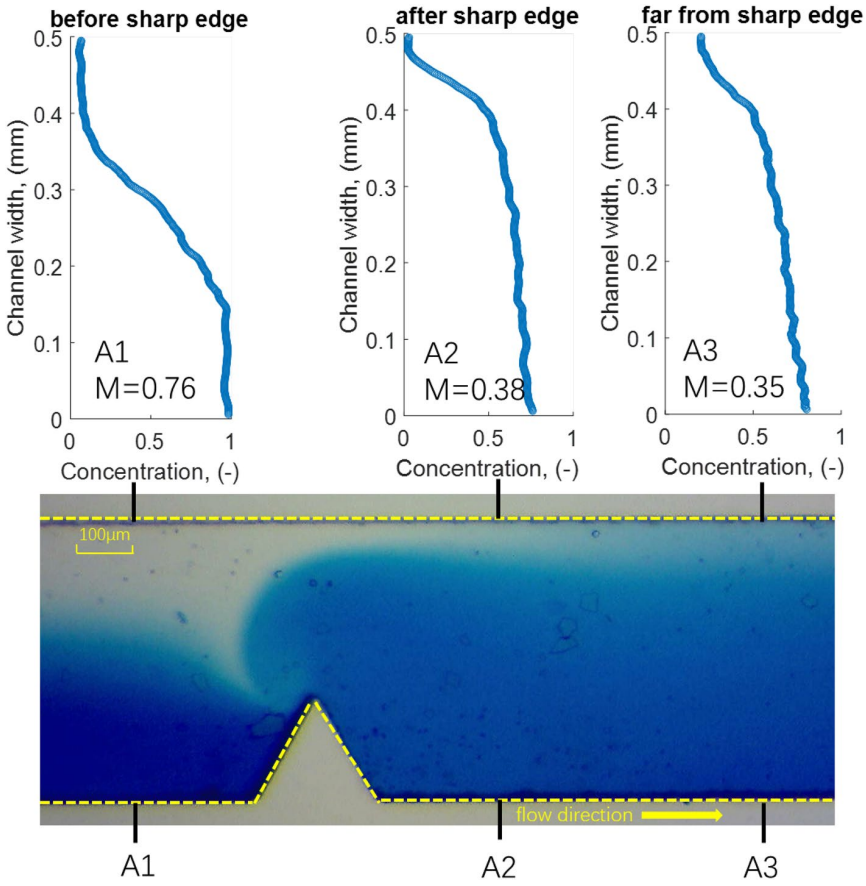

Fig. 13 Concentration field across the microchannel section in the nearby area before and after the sharp edge. *X*-axis is the normalized concentration C_n (values 0 and 1 represent two different fluids, 0.5 means complete mixing); *Y*-axis is channel width. Conditions: $\alpha = 30°$, $V_\omega = 70.5$ mm/s, $f = 2.5$ kHz and $Q_s = 0.5$ μL/min

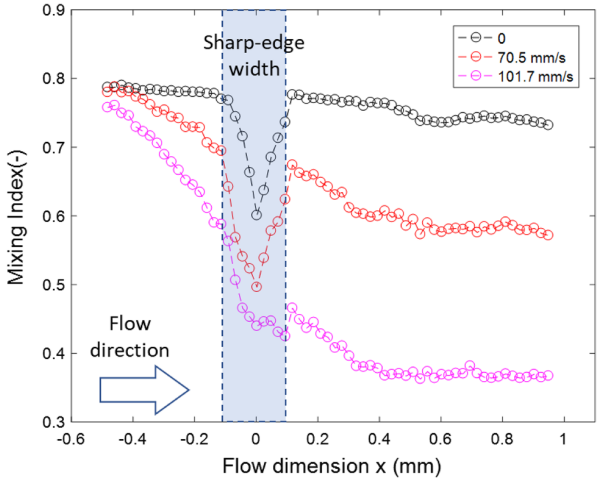

Fig. 14 Mixing index at different acoustic excitation amplitudes. Conditions: $\alpha = 30°$, $Q_s = 2$ μL/min, and $f = 2.5$ kHz

discussed above. Actually, diffusive mixing happens before the sharp edge, so the mixing index does not start from 1 in the figures.

It should be noted that the width of the channel can influence the calculation of the Mixing Index, so the values within the shadow (beside the sharp edge) in Fig. 14 cannot be reliable criteria of the mixing. Only values before and after sharp edge are directly comparable.

Figure 15 shows the mixing index as a function of different tip angles. Sharper angles clearly allow better mixing degree at the outlet, since the mixing index drops from 0.7 to 0.52 for the 30° tip but only to 0.65 for the 80° one. This is consistent with the stronger streaming effect, in terms of vortex diameter and disturbance extent, with sharper tips.

The influence of the flow rate Q_s on the mixing performance is shown in Fig. 16. When the inlet flow rate increases from 0.5 to 1.5 μL/min, the mixing index at the outlet turns from 0.38 to 0.6, thus reducing the mixing degree. In case of even higher flow rate at the same acoustic condition, the mixing continues to degrade. For example, with a flow rate of Q_s=4 μL/min, the mixing index is only achieved to 0.68. Above 1.5 μL/min, the effect of acoustic streaming on the mixing performance can be considered negligible. The short fluid residence time in the channel (Guo et al. 2018) in cases of high flow rate seriously weakens the mixing efficiency at the outlet. To sum up, with low flow rate, one single acoustically excited sharp edge can

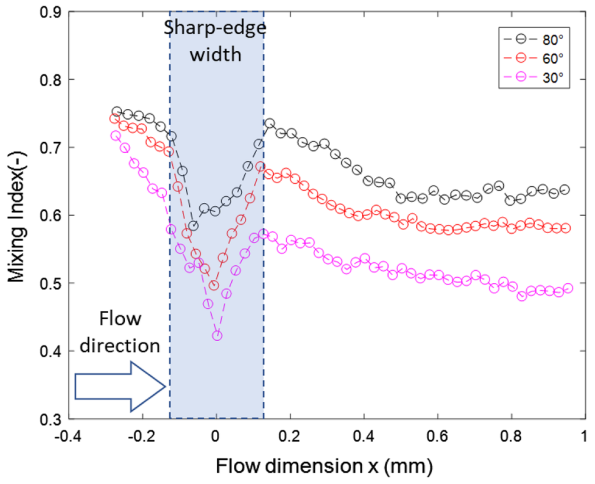

Fig. 15 Mixing index at different tip angles of the sharp edges. Conditions: $V_\omega = 70.5$ mm/s and $f = 2.5$ kHz, $Q_s = 2$ µL/min

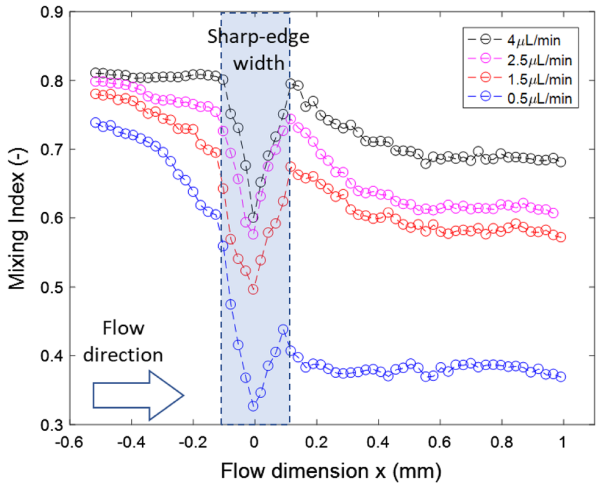

Fig. 16 Mixing index at different flow rates; the values shown being those for each individual inlet. Conditions: $\alpha = 30°$, $V_\omega = 70.5$ mm/s, and $f = 2.5$ kHz

be enough to accomplish a homogeneous mixing; however, under larger flow rates (particularly above $Q_s = 1.5$ µL/min for the current study), the disturbance brought by a single sharp edge is limited and several additional similar structures should be introduced along the microchannel to achieve good mixing performance.

6 Conclusions and perspectives

The main outcome of this study is to investigate the mechanism of AS by direct particle visualization and demonstrate the potentiality for mixing enhancement in microchannels via acoustic streaming around sharp structures. Phenomenologically similar as the Rayleigh streaming, but with strong local Reynolds stress enhancement near the tip, the sharp-edge acoustic streaming is viewed as a promising one, since it enables strong streaming disturbance to the flow with low energy input and low-cost transducers and amplifiers. Indeed, within flat channels, no streaming would be generated at such frequency and amplitude. We use particle visualization and PIV treatment to characterize the AS conditions of appearance, spatial structure, magnitude, and its disturbance level relative to the main stream. The flow characteristics under different experimental conditions (tip angle, vibration amplitude/velocity, and flow rate) are quantitatively investigated.

Our mains conclusions are the following.

First, regarding the AS phenomenon, our study confirms the perturbation theory about the boundary layer condition. Sharp edges, whose curvature radius (1.3–5.2 µm in this work) is smaller than the viscous boundary layer (11.3 m in this work), can achieve strong acoustic streaming flow. Conversely, a round-edge structure with a curvature diameter of 100 µm, is shown to be inefficient for generating acoustic streaming and mixing.

Second, sharper edges and higher vibration amplitude give stronger streaming flows. Under our test conditions, the highest maximum streaming velocity is 75 mm/s and it is obtained for $V_\omega = 101.7$ mm/s with the sharpest edge angle 30°. Meanwhile, the corresponding vortex can almost cover the whole channel until reaching the opposite channel wall. In terms of shapes of vortices, we observe symmetrical counter-rotating vortices when flow rate is zero, and the upstream/downstream symmetry is broken as the flow rate is turned on. In the latter case, the upstream vortex disappears as Q_c is set beyond a relatively low value, while the downstream one remains within a larger range of Q_c. The perturbation distance can also be as large as the channel width under low flow rate and with the sharpest tip, even for moderate vibration magnitude.

Finally, perhaps not implausibly, stronger streaming (with sharper tip and under larger vibration magnitude) helps to achieve better mixing. Significant mixing improvement is witnessed with the fluorescent dye measurement: a mixing index of 0.38 (mostly mixed) when AS is generated, compared to 0.73 when acoustic excitation is off, for the case of 2 µL/min, 30° tip and under a vibration amplitude of 70.5 mm/s. In terms of flowrate, mixing enhancement by streaming is obviously weakened at flow

rates above 1.5 μL/min. In addition, not very intuitively, the disturbance extent is crucial for the mixing application, but not the vortex size itself.

In further studies, the sharp-edge structure could be redesigned in an asymmetrical way, so that the downstream vortices could be restricted while improving the upstream one, the latter being favorable to the mixing efficiency. Another ongoing work is the evaluation of heat transfer (Guo et al. 2014), residence time distribution (Guo et al. 2018), and micromixing performance using chemical iodide–iodate reactions (Guo et al. 2013; Dong et al. 2017). In particular, sharp edges structures are already available in a large number of thermo-fluidic devices, whose performance could potentially benefit from AS generation. Examples include the micropin fins for efficient heat sink design (Chiu et al. 2017; Ambreen and Kim 2018), or ratchet-like microchannel Knudsen pumping thanks to thermal transpiration (Chen et al. 2016; Wang et al. 2019), etc. In summary, AS generated by acoustic fields near sharp structures would also be a heat transfer enhancement that uses both passive and active techniques.

Acknowledgements The authors would like to acknowledge the scholarship support from the CSC (China Scholarship Council). Eric Falcon is acknowledged for his help in the measurement of the vibration velocity with the laser vibrometer. They would like to thank the MSC and LIED lab members for their daily support and discussion.

References

Ambreen T, Kim M-H (2018) Effect of fin shape on the thermal performance of nanofluid-cooled micro pin-fin heat sinks. Int J Heat Mass Transf 126:245–256. https://doi.org/10.1016/J.IJHEATMASSTRANSFER.2018.05.164

Bachman H, Huang P-H, Zhao S et al (2018) Acoustofluidic devices controlled by cell phones. Lab Chip 18:433–441. https://doi.org/10.1039/C7LC01222E

Barnkob R, Augustsson P, Laurell T, Bruus H (2012) Acoustic radiation- and streaming-induced microparticle velocities determined by microparticle image velocimetry in an ultrasound symmetry plane. Phys Rev E Stat Nonlinear Soft Matter Phys 86:056307. https://doi.org/10.1103/PhysRevE.86.056307

Boluriaan S, Morris P (2003) Acoustic streaming: from Rayleigh to today. Int J Aeroacoustics 2:255–292. https://doi.org/10.1260/147547203322986142

Bruus H (2012) Acoustofluidics 2: perturbation theory and ultrasound resonance modes. Lab Chip 12:20–28. https://doi.org/10.1039/c1lc20770a

Cao Z, Lu C (2016) A microfluidic device with integrated sonication and immunoprecipitation for sensitive epigenetic assays. Anal Chem 88:1965–1972. https://doi.org/10.1021/acs.analchem.5b04707

Chen J, Stefanov SK, Baldas L, Colin S (2016) Analysis of flow induced by temperature fields in ratchet-like microchannels by Direct Simulation Monte Carlo. Int J Heat Mass Transf 99:672–680. https://doi.org/10.1016/J.IJHEATMASSTRANSFER.2016.04.023

Chiu H-C, Hsieh R-H, Wang K et al (2017) The heat transfer characteristics of liquid cooling heat sink with micro pin fins. Int Commun Heat Mass Transf 86:174–180. https://doi.org/10.1016/J.ICHEATMASSTRANSFER.2017.05.027

Dong Z, Zhao S, Zhang Y et al (2017) Mixing and residence time distribution in ultrasonic microreactors. AIChE J 63:1404–1418. https://doi.org/10.1002/aic.15493

Eckart C (1948) Vortices and streams caused by sound waves. Phys Rev 73:68–76. https://doi.org/10.1103/PhysRev.73.68

Elvira KS, I Solvas XC, Wootton RCR, Demello AJ (2013) The past, present and potential for microfluidic reactor technology in chemical synthesis. Nat Chem 5:905–915

Faraday M (1831) On a peculiar class of acoustical figures; and on certain forms assumed by groups of particles upon vibrating elastic surfaces. Philos Trans R Soc Lond 121:299–340. https://doi.org/10.1098/rstl.1831.0018

Franke K, Ross-Messemer M, Menck A et al (2003) The highly sensitive optical measurement of absolute SAW amplitudes for power flow analysis. IEEE Trans Ultrason Ferroelectr Freq Control 50:77–80. https://doi.org/10.1109/TUFFC.2003.1176527

Gopinath A, Mills AF (1994) Convective heat transfer due to acoustic streaming across the ends of a Kundt tube. J Heat Transfer 116:47–53. https://doi.org/10.1115/1.2910882

Guo X, Fan Y, Luo L (2013) Mixing performance assessment of a multi-channel mini heat exchanger reactor with arborescent distributor and collector. Chem Eng J 227:116–127. https://doi.org/10.1016/j.cej.2012.08.068

Guo X, Fan Y, Luo L (2014) Multi-channel heat exchanger-reactor using arborescent distributors: a characterization study of fluid distribution, heat exchange performance and exothermic reaction. Energy 69:728–741. https://doi.org/10.1016/j.energy.2014.03.069

Guo X, Fan Y, Luo L (2018) Residence time distribution on flow characterisation of multichannel systems: modelling and experimentation. Exp Therm Fluid Sci 99:407–419. https://doi.org/10.1016/j.expthermflusci.2018.08.016

Huang P-H, Xie Y, Ahmed D et al (2013a) An acoustofluidic micromixer based on oscillating sidewall sharp-edges. Lab Chip 13:3847. https://doi.org/10.1039/c3lc50568e

Huang PH, Xie Y, Ahmed D et al (2013b) An acoustofluidic micromixer based on oscillating sidewall sharp-edges. Lab Chip 13:3847–3852. https://doi.org/10.1039/c3lc50568e

Huang P-H, Nama N, Mao Z et al (2014) A reliable and programmable acoustofluidic pump powered by oscillating sharp-edge structures. Lab Chip 14:4319–4323. https://doi.org/10.1039/C4LC00806E

Huang P-H, Chan CY, Li P et al (2015a) A spatiotemporally controllable chemical gradient generator via acoustically oscillating sharp-edge structures. Lab Chip 15:4166–4176. https://doi.org/10.1039/C5LC00868A

Huang PH, Ren L, Nama N et al (2015b) An acoustofluidic sputum liquefier. Lab Chip 15:3125–3131. https://doi.org/10.1039/c5lc00539f

Huang P-H, Chan CY, Li P et al (2018a) A sharp-edge-based acoustofluidic chemical signal generator. Lab Chip 18:1411–1421. https://doi.org/10.1039/C8LC00193F

Huang PH, Chan CY, Li P et al (2018b) A sharp-edge-based acoustofluidic chemical signal generator. Lab Chip 18:1411–1421. https://doi.org/10.1039/c8lc00193f

Lee Dong-Ryul, Loh Byoung-Gook (2007) Smart cooling technology utilizing acoustic streaming. IEEE Trans Compon Packag Technol 30:691–699. https://doi.org/10.1109/tcapt.2007.901756

Legay M, Simony B, Boldo P et al (2012) Improvement of heat transfer by means of ultrasound: application to a double-tube heat exchanger. Ultrason Sonochem 19:1194–1200. https://doi.org/10.1016/J.ULTSONCH.2012.04.001

Lei J, Glynne-Jones P, Hill M (2013) Acoustic streaming in the transducer plane in ultrasonic particle manipulation devices. Lab Chip 13:2133. https://doi.org/10.1039/c3lc00010a

Leibacher I, Hahn P, Dual J (2015) Acoustophoretic cell and particle trapping on microfluidic sharp edges. Microfluid Nanofluidics 19:923–933. https://doi.org/10.1007/s10404-015-1621-1

Lighthill SIRJ (1978) ACOUSTIC STREAMINGt. J Sound Vib 61:391–418

Nama N, Huang P-H, Huang TJ, Costanzo F (2014a) Investigation of acoustic streaming patterns around oscillating sharp edges. Lab Chip 14:2824–2836. https://doi.org/10.1039/C4LC00191E

Nama N, Huang PH, Huang TJ, Costanzo F (2014b) Investigation of acoustic streaming patterns around oscillating sharp edges. Lab Chip 14:2824–2836. https://doi.org/10.1039/c4lc00191e

Nyborg WL (1953) Acoustic streaming due to attenuated plane waves. J Acoust Soc Am 25:68–75. https://doi.org/10.1121/1.1907010

Ovchinnikov M, Zhou J, Yalamanchili S (2014) Acoustic streaming of a sharp edge. J Acoust Soc Am 136:22–29. https://doi.org/10.1121/1.4881919

Ozcelik A, Nama N, Huang P-H et al (2016) Acoustofluidic rotational manipulation of cells and organisms using oscillating solid structures. Small 12:5120–5125. https://doi.org/10.1002/smll.201601760

Rayleigh JWS (2013) The theory of sound, vol One. Dover Publications, New York

Schneider C, Rasband W, Eliceiri K (2012) ImageJ. Nat Methods 9:671–675

Squires TM, Quake SR (2005) Microfluidics: fluid physics at the nanoliter scale. Rev Mod Phys 77:977–1026. https://doi.org/10.1103/RevModPhys.77.977

Stuart JT (1966) Double boundary layers in oscillatory viscous flow. J Fluid Mech 24:673. https://doi.org/10.1017/S0022112066000910

Thielicke W, Stamhuis EJ (2014) PIVlab—towards user-friendly, affordable and accurate digital particle image velocimetry in MATLAB. J Open Res Softw. https://doi.org/10.5334/jors.bl

Tobias J, Karlsen JT, Bruus H (2015) Forces acting on a small particle in an acoustical field in a thermoviscous fluid Forces acting on a small particle in an acoustical field in a thermoviscous fluid. Phys Rev E. https://doi.org/10.1103/physreve.92.043010

Uchida T, Suzuki T, Shiokawa S (1995) Investigation of acoustic streaming excited by surface acoustic waves. In: IEEE ultrasonics symposium. proceedings. An international symposium. IEEE, pp 1081–1084

Wang C, Jalikop SV, Hilgenfeldt S (2012) Efficient manipulation of microparticles in bubble streaming flows. Biomicrofluidics 6:012801. https://doi.org/10.1063/1.3654949

Wang X, Zhang Z, Zhang W et al (2019) Numerical simulation of thermal edge flow in ratchet-like periodically patterned microchannels. Int J Heat Mass Transf 135:1023–1038. https://doi.org/10.1016/J.IJHEATMASSTRANSFER.2019.02.006

Whitesides GM (2006) The origins and the future of microfluidics. Nature 442:368–373. https://doi.org/10.1038/nature05058

Wiklund M, Green R, Ohlin M (2012) Acoustofluidics 14: applications of acoustic streaming in microfluidic devices. Lab Chip 12:2438. https://doi.org/10.1039/c2lc40203c

Zacharias J, Ohl C-D (2013) Fluid dynamics, cavitation, and tip-to-tissue interaction of longitudinal and torsional ultrasound modes during phacoemulsification. J Cataract Refract Surg 39:611–616. https://doi.org/10.1016/j.jcrs.2012.10.050

Zhao S, He W, Ma Z et al (2019) On-chip stool liquefaction via acoustofluidics. Lab Chip 19:941–947. https://doi.org/10.1039/C8LC01310A

Appendix C

Paper appeared in Micromachines

micromachines

MDPI

Article

Acoustic Streaming Generated by Sharp Edges: The Coupled Influences of Liquid Viscosity and Acoustic Frequency

Chuanyu Zhang [1,*], Xiaofeng Guo [1,2], Laurent Royon [1] and Philippe Brunet [3,*]

1 Laboratoire Interdisciplinaire des Energies de Demain, Université de Paris; UMR 8236 CNRS, F-75013 Paris, France; xiaofeng.guo@esiee.fr (X.G.); laurent.royon@univ-paris-diderot.fr (L.R.)
2 ESIEE Paris, Université Gustave Eiffel; F-93162 Noisy le Grand, France
3 Laboratoire Matière et Systèmes Complexes, Université de Paris; UMR 7057 CNRS, F-75013 Paris, France
* Correspondence: chuanyu.dream@gmail.com (C.Z.); philippe.brunet@univ-paris-diderot.fr (P.B.); Tel.: +33-157276272 (P.B.)

Received: 11 May 2020; Accepted: 21 June 2020; Published: 22 June 2020

Abstract: Acoustic streaming can be generated around sharp structures, even when the acoustic wavelength is much larger than the vessel size. This sharp-edge streaming can be relatively intense, owing to the strongly focused inertial effect experienced by the acoustic flow near the tip. We conducted experiments with particle image velocimetry to quantify this streaming flow through the influence of liquid viscosity ν, from 1 mm^2/s to 30 mm^2/s, and acoustic frequency f from 500 Hz to 3500 Hz. Both quantities supposedly influence the thickness of the viscous boundary layer $\delta = \left(\frac{\nu}{\pi f}\right)^{1/2}$. For all situations, the streaming flow appears as a main central jet from the tip, generating two lateral vortices beside the tip and outside the boundary layer. As a characteristic streaming velocity, the maximal velocity is located at a distance of δ from the tip, and it increases as the square of the acoustic velocity. We then provide empirical scaling laws to quantify the influence of ν and f on the streaming velocity. Globally, the streaming velocity is dramatically weakened by a higher viscosity, whereas the flow pattern and the disturbance distance remain similar regardless of viscosity. Besides viscosity, the frequency also strongly influences the maximal streaming velocity.

Keywords: acoustofluidics; microfluidics; acoustic streaming; sharp edge; particle image velocimetry

1. Introduction

Acoustic streaming (AS) denotes the steady flow generated by an acoustic field in a fluid. Mathematically, it can be explained by the nonlinear coupling between acoustic wave and hydrodynamic momentum conservation equations. Physically, the underlying mechanism of AS comes from the dissipation of acoustic energy within the fluid, which induces spatial gradient of momentum, and in turn creates a time-averaged effective forcing [1–10].

The phenomenon has attracted researcher's attention since Faraday's observations in 1831 [11], who reported that light particles on vibrating plates spontaneously form steady clusters. More recently and especially in the context of microfluidics, AS has been proven to be a suitable technique for fluid and particle handling in various situations [4]. We wish to point out the studies on fluid mixing at a low-Reynolds number [12], particle manipulation and sorting [13–18], particle patterning [19,20] and heat transfer [21,22], among others.

Amongst different sorts of acoustic streaming, the one relevant in microfluidics situations usually involves viscous stress along walls or obstacles, generated by no-slip conditions and resulting in the presence of a viscous boundary layer (VBL). It is referred to *Rayleigh–Schlichting*

streaming [4,6–10], and is different from that induced by acoustic attenuation in the bulk of fluid. The bulk acoustic streaming is denoted as *Eckart streaming* [2,5] and becomes significant only with high frequencies (>MHz) or with very viscous liquids, so that the attenuation length is smaller than—or of the same order as—the vessel size [23–25]. In Rayleigh–Schlichting streaming, a non-zero, time-averaged vorticity is generated inside the unsteady VBL [7] of typical thickness $\delta = \left(\frac{2\nu}{\omega}\right)^{\frac{1}{2}}$, where ν is the kinematic viscosity and $\omega = 2\pi f$ the acoustic angular frequency. This vorticity appears in the form of an array of eddies pairs [6,7,10], denoted as inner vortices, along the channel walls [16,26,27]. This vorticity extends its influence beyond the VBL and in turn induces larger-scale eddies of width $\lambda/2$ [26,28] in the fluid bulk, where $\lambda = \frac{c_s}{f}$ is the acoustic wavelength and c_s the speed of sound. Rayleigh–Schlichting streaming is generally treated within the incompressibility framework.

Traditional acoustic streaming in microchannels is achieved by adjusting the channel width w and the wavelength λ to ensure a resonance condition, typically obtained when $w \simeq \lambda/2$ [29]. However, recent studies evidenced that relatively intense streaming could be generated by designing microchannels with sharp structures along the walls [30–36] excited by acoustic waves. The sharp structures can be easily prototyped by the facilities offered by microfabrication in clean rooms; e.g., with photolithography. One of the main advantages of "sharp-edge streaming" is that it can be generated at relatively low frequencies, typically in a range between a few hundred Hz and several kHz (but it is observed for much higher frequencies as well [34]). Within this low frequency range, numerous performant and stable piezoelectric transducers are available at low cost, and can be supplied with inexpensive amplifiers. Other advantages of operating at relatively low frequency include: efficient acoustic coupling between the transducer and the solid in contact, and negligible acoustic dissipation within the liquid. Finally, previous experiments reported that near the tip of the sharp edge, the streaming velocity can be very strong [30–32,37], and can even be comparable to the vibration velocity, hence up to several hundreds of mm/s [35,36] at a typical distance δ from the tip. Benefiting from these strong disturbances within the fluid inside a microchannel, various applications using sharp structures streaming have been developed: mixing processes [32,38], bio-particle control [39,40] and various on-chip devices [31,41].

The present study aims to investigate the influence of both liquid kinematic viscosity ν and acoustic frequency f on the streaming flow magnitude and pattern. The focus of this study is based on the fact that one of the key parameters of sharp-edge streaming is the thickness of the VBL, which depends on both f and ν. Actually, three main dimensionless numbers involve δ: the ratio of the tip diameter and δ, $d^* = \frac{2r_c}{\delta}$, the ratio with respect to the channel depth p, $p^* = \frac{p}{\delta}$ and the ratio between the channel width w and δ, $w^* = \frac{w}{\delta}$. Sharp-edge streaming is defined by the *sharpness* condition $d^* < 1$ [37], and almost no streaming could be noticed, even at relatively high forcing when $d^* \gg 1$ [35,36]. In the typical framework with water and f of a few kHz (let us say between 2500 and 6000 Hz as in previous studies), δ ranges between 7.3 and 11.3 µm, so that the two other ratios $w^*, p^* \gg 1$, for microfluidic channels, are typically thicker than 50 µm.

Additionally, quantifying the influence of viscosity distinguishes sharp edge acoustic streaming from classical ones. In classical Rayleigh–Schlichting streaming, the flow is found to be independent on viscosity providing that the VBL thickness δ is much thinner than the vessel size [8,9,42]. For sharp-edge streaming in microchannels or in wider vessels, it is found that this independence on viscosity is lost even if δ remains thin compared to the channel width w or depth p [37]. Ovchinnikov et al.'s perturbative theory predicts a decrease of the typical streaming velocity V_s with ν, though with a subtle dependence on the sharp-edge geometry. With a viscous enough liquid and/or a low enough frequency, the dimensionless lengths p^* or w^* can fall into the order of one. Under this condition, an overlap between geometrical confinement and the intrinsic nature of sharp-edge streaming makes it more complex to determine the influence of ν and f on the flow. On this latter point, Equation (22) from [37] predicted a typical streaming velocity in cylindrical coordinate (r, ϕ) as:

$$V_s(r) = \frac{V_a^2}{\nu} \frac{\delta^{2n-1}}{h^{2n-2}} H_\alpha\left(\frac{r}{\delta}\right) \quad (1)$$

where V_a is the amplitude of the acoustic velocity, n is a coefficient that depends on α as $n = \frac{\pi}{2\pi-\alpha}$; h is the length scale of the sharp-edge height. The function $H_\alpha(\frac{r}{\delta})$ contains the radial profile of the streaming flow. It is worth noticing that Equation (1), supposedly valid in the range $r_c < \delta$, does not exhibit any dependence on r_c.

The present study intends to quantify the coupled role of viscosity and excitation frequency in both the streaming flow pattern and magnitude. The paper is organised as follows: Section 2 described the experimental setup and visualisation method. Then in Sections 3 and 4 the results at different viscosities and different frequencies are presented respectively. Finally, Section 5 summarises the main results and conclusions. The main physical quantities are defined in Table 1.

Table 1. Definition of the main physical quantities.

Quantity	Abbreviation
Kinematic viscosity	ν
Viscous boundary layer thickness	δ
Tip angle of sharp edge	α
Height of the sharp edge	h
Radius of curvature of the tip	r_c
Width of the microchannel	w
Depth of the microchannel	p
Acoustic frequency	f
Acoustic angular frequency	ω
Amplitude of acoustic displacement	$\mathbf{A}$
Amplitude of acoustic velocity	$\mathbf{V}_a$
Amplitude of acoustic velocity far from the tip	V_a
Streaming velocity	$\mathbf{V}_s$
Maximum streaming velocity	V_{smax}
Fitting coefficient relating V_{smax} and V_a^2	θ

2. Experimental Setup

2.1. Microchannel and Acoustic Wave

The experimental setup is sketched in Figure 1, and presented in more detail in [35]. It is built around a Y-shaped polydimethylsiloxane (PDMS) microchannel devised by standard photolithography techniques: starting from a SU8 resist-made mould of thickness 50 µm made on a silicon wafer, a mixture of PDMS (Sylgard 184) with 10% in mass of curing agent is poured on the SU8 mould and forms a 2.5-mm-thick layer on top of the wafer. After a baking at 65 °C for 4 h, the PDMS mixture is then sealed and attached to a glass coverslip after a 1 mn O_2 plasma treatment of both faces. A PDMS microchannel of depth p = 50 µm is then obtained. The width w is equal to 500 µm. Its geometrical dimensions are detailed in Figure 2a. Sharp edges with different angles (30°, 60°, 80° and 90°) could be fabricated from various moulds, and previous studies evidenced that a sharper tip and more acute angle would lead to stronger streaming under the same forcing amplitude [30–32,35,36]. For the present study, since the focus is on the influence of ν and f, we operated with the same angle of α = 60°, with a corresponding tip diameter of $2r_c$ = 5.8 ± 0.4 µm.

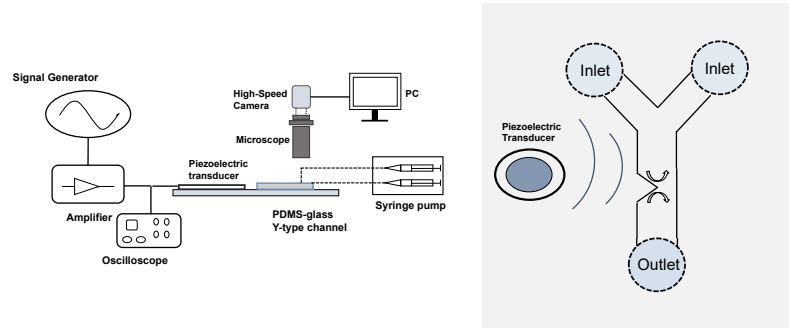

Figure 1. Left—Sketch of the experimental setup. A piezoelectric transducer is glued on a glass microscope slide, which is used as a coverslip for a PDMS microchannel with one or several sharp-edge structures. The transducer is supplied with a function generator and a home-made amplifier, adjusted by the peak-to-peak voltage monitored with an oscilloscope. The fluid seeded with fluorescent particles is brought by a syringe pump through two inlets. The flow inside the microchannel is visualised by a high-speed camera connected to a binocular microscope. Right —The piezo-transducer generates an acoustic wave within the Y-shaped channel. In the vicinity of the sharp-edge structure, the acoustic wave generates a streaming flow.

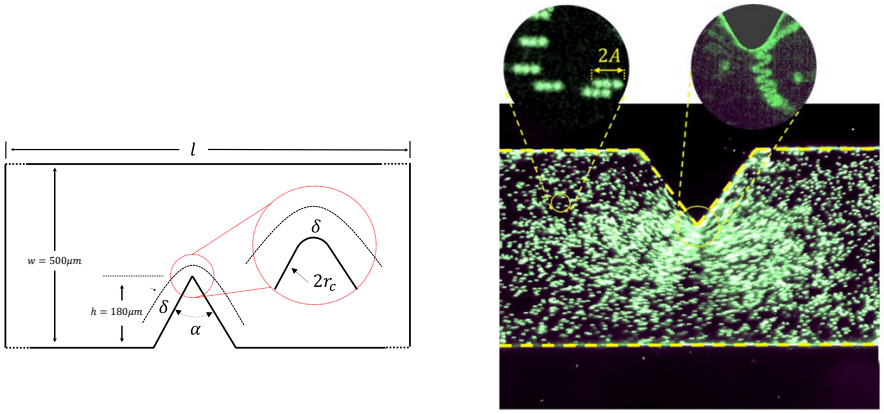

(**a**) (**b**)

Figure 2. (**a**) Geometry of the microchannel and sharp-edge. (**b**) Trajectories of individual particles (diameter 4.9 μm), over several periods, for the left-hand-side zoom-in image. The frame per second (fps) equals $4f$ = 10,000 fps; for the right-hand-side one, the fps equals $10f$ = 25,000 fps; the two images have the same exposure time $1/(10f) = 1/25{,}000$ s. Far from the tip, the flow is oscillating at frequency f and amplitude A, as testified by the segment described by each particle. Close to the tip, the trajectories of the particles show a superposition of oscillations with higher amplitude due to the sharp edge and advection due to the intense streaming flow.

The microchannel is fed with liquid seeded with fluorescent and reflective particles (green polystyrene microspheres, Thermo Scientific, Boston, MA, USA) of diameter 1 μm (The particle diameter has to be much smaller than δ to get the inner streaming flow, but to measure the amplitude of acoustic vibration velocity and get a qualitative image of the flow (see Figure 2b), larger particles of diameter 4.9 μm were more adapted) by a syringe pump (Newtown Company and Co, Newtown Blvd, Cebu). The acoustic wave is ensured by a piezoelectric transducer (Model ABT-455-RC, RS Components) glued on an upper glass microscope coverslip (width × length × thickness: 26 mm × 76 mm × 1 mm) with epoxy resist. The power is brought by a function generator (Model 33220A, Agilent, Santa Clara, CA, USA) with a home-made power amplifier. The transducer spectral response shows several resonance peaks between 400 and 40,000 Hz, from which we chose several values of

frequency from 500 to 3500 Hz. The applied voltage is sinusoidal, within a range between 0 and 60 V peak-to-peak (up to ± 30 V).

The fluids are mixtures of water (W) and glycerin (G) with different rate in W/G. Table 2 presents the main physical properties of different mixtures used in this study and the values of δ for the two extreme values of frequency.

Table 2. Physical properties of water-glycerol mixtures at 20 °C for different mass fraction $w_{\mathtt{glyc}}$ and volume fraction $x_{\mathtt{glyc}}$ of glycerol. Data for the viscosity ν of the water–glycerol mixture are extracted from [43], while the sound speed c_0 (at 25 °C) and the density ρ_0 are extracted from [44]. Additionally indicated are values of the VBL thickness δ at the highest and lowest frequency f, 3500 and 500 Hz.

$w_{\mathtt{glyc.}}$	$x_{\mathtt{glyc.}}$	ν (mm^2/s)	c_0 (m/s)	ρ_0 (kg/m^3)	δ_{3500} (μm)	δ_{500} (μm)
0.00	0.00	1.007	1510	998	9.57	25.3
0.062	0.05	1.158	1580	1012,7	10.3	27.1
0.457	0.4	4.32	1760	1114.5	19.8	52.4
0.654	0.6	13.75	1810	1168.3	35.4	93.6
0.747	0.7	29.44	1840	1193.4	51.7	136.9

2.2. Flow Visualisation and Image Processing

The visualisation is ensured by a fast camera (MotionBLITZ Cube4, Mikrotron) adapted on a binocular microscope. The depth of field of the microscope lens is about 10 μm, and hence five times smaller than the channel depth (p = 50 μm) which, after careful adjustments, enables one to access the streaming velocity near the centre plane. A cold-light beam shines from the bottom of the glass slide. While the seeded particles are fluorescent (excitation wavelength 480 nm, light emission wavelength 515 nm), we found that under some conditions of lighting, and due to the limited sensitivity of the camera, the diffused light could offer better contrast than the fluorescence-emitted light.

By operating under various exposure times and a frame-rate from 500 fps to 25,000 fps (see details in [35]), we can access both the steady streaming velocity $\mathbf{V}_s(x,y)$ and the acoustic velocity $\mathbf{V}_a(x,y) = \mathbf{A}\omega$ (via the vibration amplitude $\mathbf{A}$); see Figure 2. In particular, it is observed that close to the tip, $\mathbf{V}_s$ can be of the same order as $\mathbf{V}_a$. Far from the tip, where the streaming velocity vanishes, the time-cumulated trajectories of individual particles appear as straight segments, along the parallel direction with respect to the channel wall. The measurements of the lengths of these segments, equal to $2A$, allow one to determine the prescribed vibration at infinity $V_a(\infty)$. This appears to us as the most reliable way to quantitatively measure the forcing amplitude, and we denote thereafter for simplicity: $V_a = V_a(\infty)$. As previously shown [35], the relationship between the prescribed voltage V and the vibration velocity V_a is found to be linear over the range 0–60 Volts. For each tested frequency, we proceeded a calibration between voltage and acoustic velocity.

The obtained images are treated with the open-source software ImageJ (https://imagej.net/). The streaming velocity field in the plane (x,y) is determined from the relative displacement of particles at a given phase during several vibration periods. Successive frames are converted into displacement vectors and vorticity maps by the software PIVlab (see: https://pivlab.blogspot.com/).

3. Influence of Viscosity

3.1. Velocity and Vorticity Maps

Figure 3a–d present typical streaming velocity fields obtained from the PIV treatment. The streaming flow appears as a main central jet from the tip, which is symmetric with respect to the y axis (x = 0). It clearly appears that the flow intensity decreases with an increasing viscosity. The jet induces the formation of two symmetric vortices beside the sharp edge. In terms of location,

the eddies are very near to the tip for the lowest viscosity, and for more viscous liquids they are pushed away and more aside from the tip. Let us also remark that at higher viscosity (Figure 3c,d), the flow in the VBL along the lateral walls becomes relatively thicker.

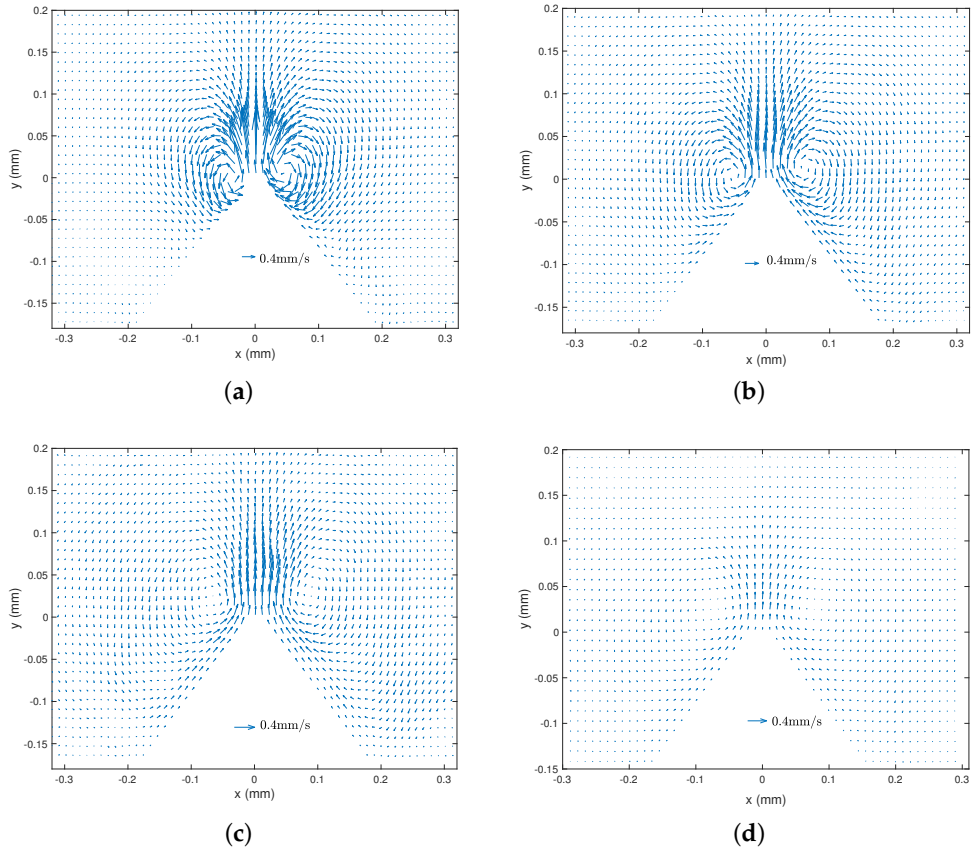

Figure 3. Streaming velocity field $V_s(x, y)$ from PIV measurements, with different liquid viscosities. f = 2500 Hz and V_a = 35 mm/s. (**a**) ν = 1.158 mm^2/s, (**b**) ν = 4.32 mm^2/s, (**c**) ν = 13.75 mm^2/s, (**d**) ν = 29.44 mm^2/s. Scales are the same for the four cases.

Figure 4 shows the vorticity maps corresponding to the fields of Figure 3. The most remarkable point is the decrease of the intensity of the vorticity with increasing viscosity, as testified by the scales of the colourmaps from (a) to (d). However, the size of the vortices, which may characterise the disturbance distance, remains roughly equal for all liquid samples. Additionally, the thickness of the inner vorticity areas, and the absolute vorticity within this specific region appear to be roughly constant for all liquids.

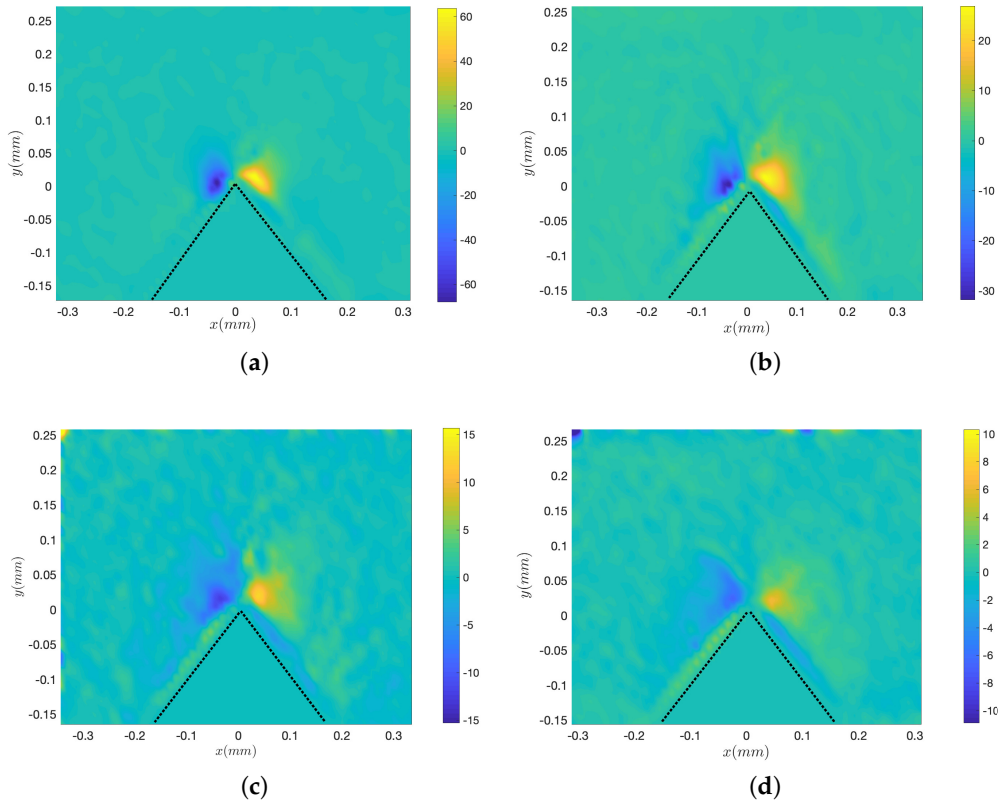

Figure 4. Vorticity maps of the streaming fields corresponding to the cases of Figure 3a–d, with corresponding colour bars that emphasise the decrease of vorticity. f = 2500 Hz and V_a = 35 mm/s. (**a**) ν = 1.158 mm^2/s, (**b**) ν = 4.32 mm^2/s, (**c**) ν = 13.75 mm^2/s, (**d**) ν = 29.44 mm^2/s. Dotted lines show the boundaries of the sharp edge.

3.2. Maximal Streaming Velocity at Different Viscosities

To further quantify the flow pattern, we extract the flow profile along the y axis: $V_s(x = 0, y)$, for different viscosities and forcing amplitudes. Figure 5 shows three examples of profiles for the same V_a = 35 mm/s and Fluids 2, 3 and 4 (see Table 2). It shows a quantitative confirmation that a higher viscosity entrains less intense and relatively more spread profiles. Since the velocity fields are symmetrical with respect to the y axis, the maximal velocity V_{smax} can be extracted from these profiles. It turns out that the maximal velocity is roughly located at a distance $y = \delta$ from the tip.

A more careful examination of the decaying of $V_s(x = 0, y)$ suggests that the influence of viscosity is mainly significant within the region of a few VBLs in thickness. Conversely, the decaying zone further from the tip seems to follow a decreasing exponential behaviour, which is almost independent of ν: the profiles are just shifted from each other by a velocity offset. In addition, at a distance of roughly 130 µm, $V_s(x = 0, y)$ approaches zero for all cases. This length scale seems to depend only on the sharp edge structure, which is in our case characterised by an angle of 60°, and tip height h = 180 µm.

Now we focus on the measurements obtained within a large range of V_a. Quantitatively, we mainly focus on the maximal and characteristic value of $V_s(x, y)$ measured around $y = \delta$ and at x = 0. In what follows, we shall also extract the prefactor θ that relates V_s to V_a^2, from the whole data set where the dependence is linear. Back to Equation (1), θ is equal to $\frac{1}{\nu}\frac{\delta^{2n-1}}{a^{2n-2}}$, from which the dependence on ν and on f can be readily predicted, taking α = 60° as in our experiments:

$$V_s \sim \nu^{-0.9} f^{-0.1}\, V_a^2 \tag{2}$$

To verify this theory, Figure 6 show the results of the experimental maximal streaming velocity $V_{\mathrm{s\,max}}$ versus the square of the acoustic forcing velocity amplitude V_a^2, presented either as raw data (Left) or via the quantity $V_{\mathrm{s\,max}} \times \nu^{-a}$, with a is an exponent deduced from Ovchinnikov et al.'s theory [37], equal to -0.9 for an angle $\alpha = 60°$ as stated above. In the inset, the quantity $V_{\mathrm{s\,max}} \times \nu^{1/2}$ plotted versus V_a^2 shows a partial collapse of data in the range of the smallest values of V_a^2, roughly below 800 mm^2/s. At this stage of our investigations, we are unable to explain such a trend. From these results, we can simply conclude that viscosity strongly influences the streaming flow generated around sharp edges. But the dependence cannot be simply captured by the predictions of the perturbative theory from Ovchinnikov et al. [37], nor by any arbitrary power-law. In any case, the results show the quantitative confirmation that the independence on ν observed in classical Rayleigh–Schlichting streaming is lost in sharp-edge streaming.

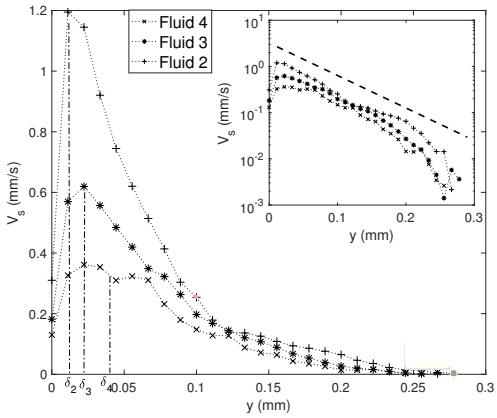

Figure 5. Streaming velocity profile along vertical direction $V_s(y)$, for three different viscosities (Fluids 2, 3 and 4 with ν respectively equal to 1.158, 4.32 and 13.75 mm^2/s). The operation condition is at frequency f= 2500 Hz and acoustic velocity V_a = 35 mm/s. Additionally labelled are the values of the VBL thickness for the three fluids δ_2, δ_3 and δ_4. The inset plots the same data in Lin-log axes.

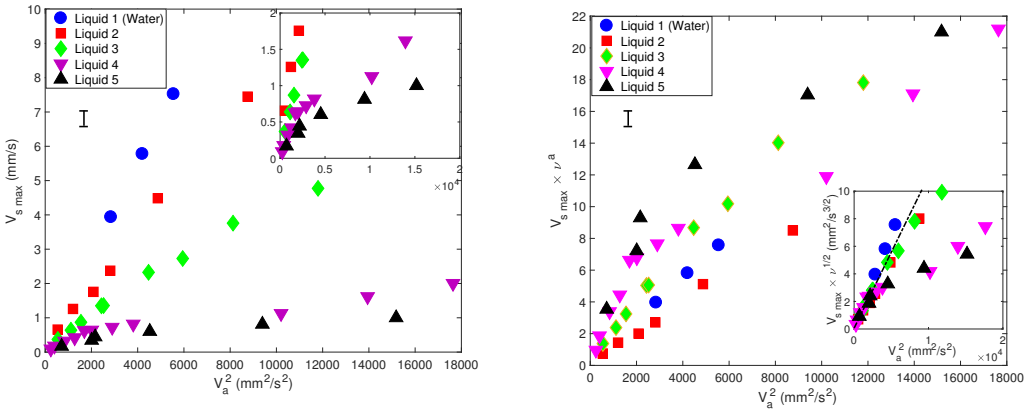

Figure 6. Left —Maximal streaming velocity $V_{\mathrm{s\,max}}$ versus the square of the acoustic forcing velocity V_a^2, for different liquid viscosities ν, indicated in Table 2. Right—Quantity $V_{\mathrm{s\,max}} \times \nu^{-a}$, with a= -0.9. Inset $V_{\mathrm{s\,max}} \times \nu^{1/2}$. All measurements were obtained at f = 2500 Hz. The averaged typical error bar is indicated.

Let us finally point out that for more viscous liquids (4 and 5), there is a clear departure from a linear dependence between V_{smax} and V_a^2, typically as V_a^2 is larger than roughly 800 mm^2/s. For these two liquids, at 2500 Hz, δ_4 = 41.8 µm and δ_5 = 61.2 µm; hence, p^* is of the order of one.

4. Influence of Frequency

4.1. Velocity and Vorticity Maps

Figure 7a–d presents typical streaming velocity fields at different frequencies (f = 3500, 2500, 1250 and 800 Hz) with the same liquid viscosity (ν = 4.32 mm^2/s) and forcing amplitude (V_a = 22.4 mm/s). The same global structure with the main central jet and the inner and outer vortices are observed for all frequencies. The frequency does not seem to significantly influence the order of magnitude of the flow. Figure 8a–d shows the corresponding vorticity maps. Let us note that the colourmap scale is comparable for all four frequencies. As frequency gets lower, one observes a thicker and more intense inner VBL along the walls, while the outer vortices are more spread. The magnitude of vorticity in the outer vortices does not vary much with f.

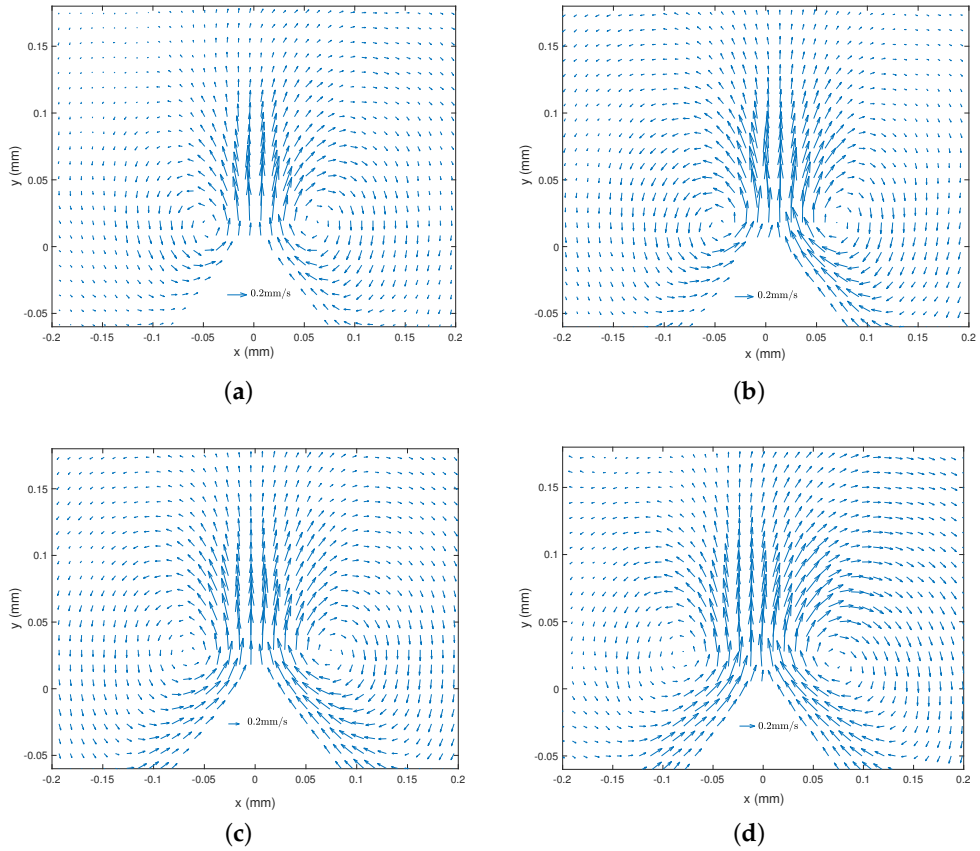

Figure 7. Streaming velocity field $V_s(x, y)$ from PIV measurements, with different excitation frequencies ν = 4.32 mm^2/s (Fluid 3) and V_a = 22.4 mm/s. (**a**) f = 3500 Hz, (**b**) f = 2500 Hz, (**c**) f = 1250 Hz, (**d**) f = 800 Hz. Scales are the same for the four cases.

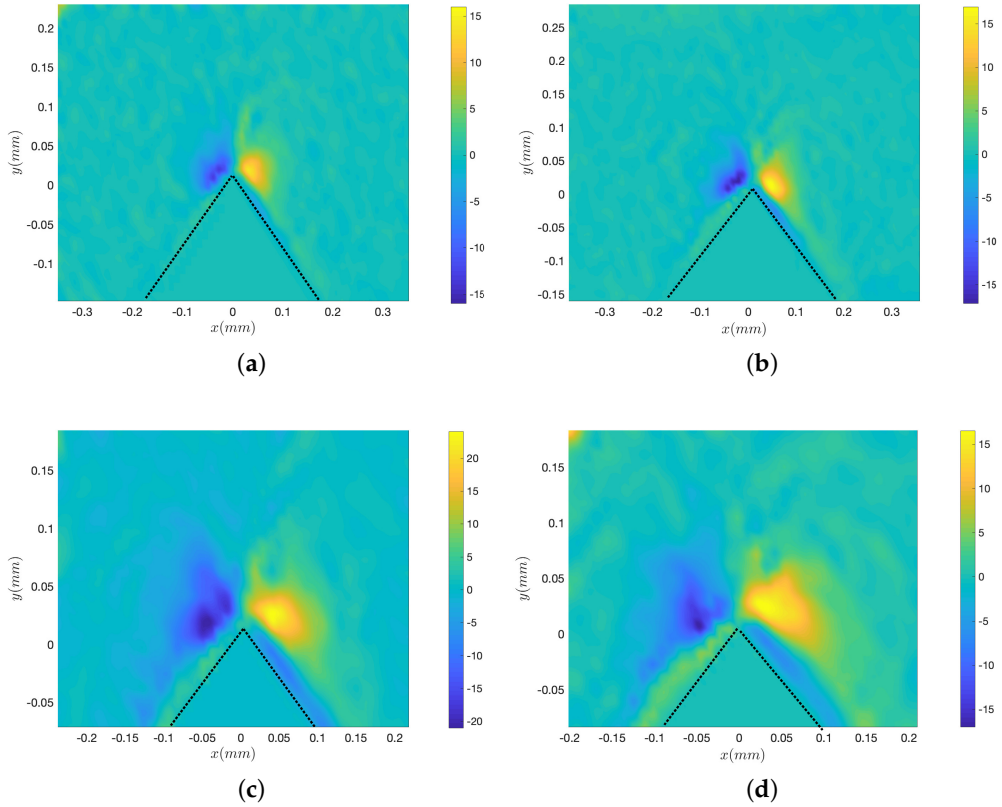

Figure 8. Vorticity maps of the streaming fields corresponding to the cases of Figure 7a–d. ν = 4.32 mm^2/s (Fluid 3) and V_a = 22.4 mm/s. (**a**) f = 3500 Hz, (**b**) f = 2500 Hz, (**c**) f = 1250 Hz, (**d**) f = 800 Hz. Dotted lines show the boundaries of the sharp edge.

4.2. Maximal Velocity at Different Frequencies

We extract the velocity profile $V_s(x = 0, y)$ for the four values of frequency, under the same conditions as those of Figures 7 and 8; in particular, V_a is fixed at 22 mm/s. Results are plotted in Figure 9. The y locations of the maxima roughly correspond to the VBL thickness at respective f: $\delta_{3500} \simeq 19.8$ µm, $\delta_{2500} \simeq 23.4$ µm, $\delta_{1250} \simeq = 33.2$ µm and $\delta_{800} \simeq 41.5$ µm. The maximal velocity itself is very much dependent on f, but the typical length-scale of the decay along y is comparable for all four experiments, as revealed by the Lin-log plot in the insert. The four velocity profiles are shifted from each other with a given offset.

Figure 10 shows the maximal velocity $V_{s\,\max}$ versus the square of the acoustic forcing velocity V_a^2, for different values of frequencies f and the same liquid viscosity ν = 4.32 mm^2/s. Each data group obtained at constant f shows a linear trend: $V_{s\,\max} = \theta V_a^2$. However, the dependence of the prefactor θ on f is unclear. Obviously, the theoretical prediction of [37] shown in Equation (2) fails to predict this strong dependence on f. However, it is possible to make two groups of data:

- One group rather concerns measurements obtained at higher frequencies (2500 and 3500 Hz) and high V_a, for which a good fit is obtained for a value $\theta = 5\times10^{-4}$ s/mm.
- The other group is constituted by measurements obtained at lower frequencies (500, 800 and 1250 Hz) and relatively low V_a; see insert in Figure 10. In this case, the value of the prefactor is θ = 0.0011 s/mm.

To further test the possibility of a scaling law that would capture the dependence of the streaming velocity on f, we attempted to plot $V_{s\,\max}$ versus potential pertinent combinations of

powers of V_a and f. In classical Rayleigh–Schlichting streaming, $V_{s\,max}$ usually depends linearly on $A^2\,f = V_a^2/(4\,\pi^2\,f)$ [42,45]. But it turns out that plotting $V_{s\,max}$ versus $V_a^2/(4\pi^2 f)$ leads to even more scattered data points.

In seeking an empirical law quantifying the dependence on f, we then tried to plot V_s versus other combinations of V_a^2 and f^β, with β being a real exponent, predicted to equal -0.1 from Ovchinnikov et al.'s theory [37]; see Equation (2). Figure 11 show the two most successful attempts:

- Figure 11a: the plot of V_s versus $V_a^2 \times f$ shows a good collapse of data for the three lowest frequency values (500, 800 and 1250 Hz). But the rescaling does not fit with the two other data sets corresponding to the highest frequencies (2500 and 3500 Hz).
- Figure 11b: the plot of V_s versus $V_a^2 \times f^{-1/2}$ shows a fair collapse of data for all frequencies, though it is more convincing at higher acoustic amplitude.

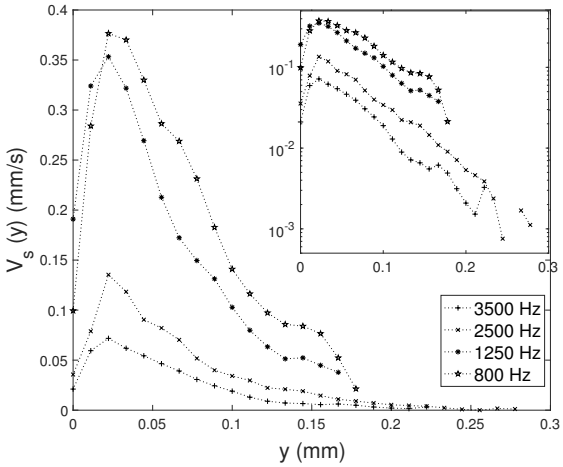

Figure 9. Streaming velocity profile along vertical direction $V_s(y)$, for four different frequencies. Liquid viscosity ν = 4.32 mm^2/s and V_a = 22 mm/s. The inset plots the same data in Lin-log axes.

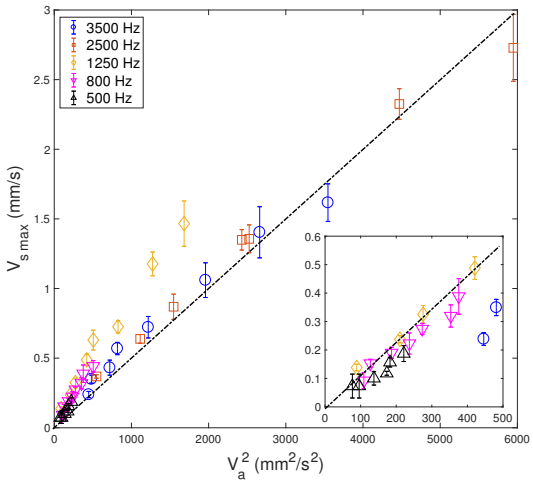

Figure 10. Maximal streaming velocity $V_{s\,max}$ versus V_a^2, for different f and the same viscosity ν = 4.32 mm^2/s. The dashed-dotted line suggests a linear relationship, with a prefactor $\theta = 5\times10^{-4}$ s/mm. The inset represents a magnified view of the plot for the lowest values of V_a^2, suggesting a linear scaling with a prefactor θ = 0.0011 s/mm.

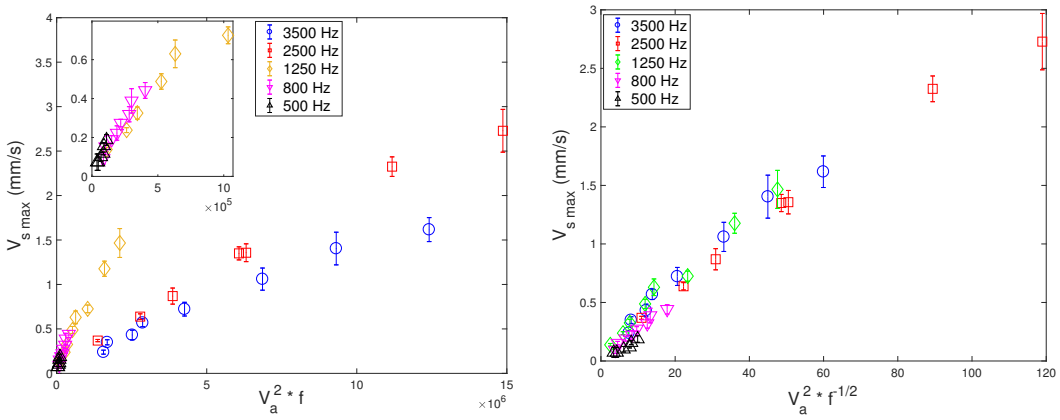

Figure 11. Attempts of data rescalling for $V_{s\,\max}$ (**a**) versus $V_a^2 \times f$ (insert shows data in the lowest range of V_a^2) and (**b**) versus $V_a^2 \times f^{-1/2}$ showing a fair collapse of data.

Still, there is no clear explanation for such trends. Therefore, it is likely that the dependence of the streaming flow on f cannot be captured by simple theoretical predictions.

5. Conclusions

Our study presents qualitative and quantitative results of the streaming flow generated by long-wavelength/low-frequency acoustic fields near a sharp-edge. The main focus has been given to viscosity (ν from pure water to 30 times higher), with frequency f from 500 to 3500 Hz, allowing us to tune the VBL thickness δ from 9.5 to 137 µm. The mechanisms of such a streaming flow, described in previous studies [30–35,37], are distinct from those of the classical Rayleigh–Schlichting streaming. Our results confirm a strong link of sharp-edge streaming to viscosity and frequency. But the dependency on both ν and f seems to be more complex than simple power law descriptions; for instance, those from Ovchinnikov et al.'s study [37]. Let us mention a very recent study [34] where streaming velocity is predicted analytically and numerically. Equations (27)–(28) and (37)–(38) in [34] offer a complete prediction, including the structure of the flow itself. By comparing the scaling laws from this study with our experiments, we could not find agreement. We assume the complex behaviour in our experiments is due to the fact that δ can become comparable to the channel depth. Therefore, we hope our results will provide an interesting challenge for future studies involving complex geometries.

Still, our results allow one to draw several conclusions:

- For any conditions, the maximal streaming velocity is roughly located at a vertical distance of δ from the tip; i.e., just at the limit of the VBL.
- An increase of viscosity leads to globally weaken the streaming velocity and the outer vorticity. Still, the outer vortices keep their size and shape for all liquids, and the thickness of the inner flow along the edge lateral walls roughly remains insensitive to viscosity. This is clearly at odds from what is observed in classical boundary-layer (Rayleigh–Schlichting) streaming.
- At constant V_a, a decrease of frequency tends to increase the streaming velocity. Our results, although unexplained by the current theoretical state of the art, suggests the empirical law: $V_s \sim V_a^2 f^{-1/2}$. Furthermore, the lower the frequency f is, the more spread out the streaming vortices are.
- While the flow near the tip ($r < \delta$) is strongly influenced by ν and f, the flow far from the tip follows an exponential decrease over a length scale of roughly 130 µm, under the test condition and with angle of 60°, and tip height $h = 180$ µm. This length characterises the disturbance distance and seems to be dependent only on the sharp edge structure rather than the operating conditions.

- When the VBL thickness is comparable to the channel depth, i.e., when p^* is of the order one, the dependence of V_{smax} on V_a^2 is no longer linear. It suggests that $p^* \gg 1$ is a necessary condition for this linearity, as otherwise the streaming flow cannot fully develop within the channel.

Author Contributions: X.G., L.R. and P.B. planned the work. C.Z. and P.B. fabricated the device. C.Z. carried out the experiments. C.Z., X.G., L.R. and P.B. discussed the results and their presentation in figures. P.B. wrote the first draft of the paper. C.Z., X.G., L.R. and P.B. wrote the paper. All authors have read and agreed to the published version of the manuscript.

Funding: C.Z. was funded by the China Scholarship Council.

Conflicts of Interest: The authors declare no conflict of interest.

Abbreviations

The following abbreviations are used in this manuscript:

VBL Viscous boundary layer

References

1. Westervelt, P.J. The Theory of Steady Rotational Flow Generated by a Sound Field. *J. Acoust. Soc. Am.* **1953**, *25*, 60–67. doi:10.1121/1.1907009.
2. Nyborg, W.L. Acoustic Streaming due to Attenuated Plane Waves. *J. Acoust. Soc. Am.* **1953**, *25*, 68–75. doi:10.1121/1.1907010.
3. Lighthill, S.J. Acoustic Streaming. *J. Sound Vib.* **1978**, *61*, 391–418.
4. Friend, J.; Yeo, L.Y. Microscale acoustofluidics: Microfluidics driven via acoustics and ultrasonics. *Rev. Mod. Phys.* **2011**, *83*, 647.
5. Eckart, C. Vortices and streams caused by sound waves. *Phys. Rev.* **1948**, *73*, 68–76. doi:10.1103/PhysRev.73.68.
6. Rayleigh, L. On the circulation of air observed in Kundt's tubes, and on some allied acoustical problems. *Philos. Trans. R. Soc. Lond.* **1884**, *175*, 1–21.
7. Schlichting, H.; Gersten, K. *Boundary-Layer Theory*; Springer Nature: Berlin, Germany, 2017.
8. Nyborg, W.L. Acoustic Streaming near a Boundary. *J. Acoust. Soc. Am.* **1958**, *30*, 329–339. doi:10.1121/1.1909587.
9. Riley, N. *Acoustic Streaming*; Springer US: Boston, MA, USA, 1998; Volume 10, pp. 349–356. doi:10.1007/s001620050068.
10. Rayleigh, L. *The Theory of Sound, Volume One*; Dover Publications: New York, NY , USA, 1945; p. 985.
11. Faraday, M. On a Peculiar Class of Acoustical Figures; and on Certain Forms Assumed by Groups of Particles upon Vibrating Elastic Surfaces. *Philos. Trans. R. Soc. Lond.* **1831**, *121*, 299–340. doi:10.1098/rstl.1831.0018.
12. Sritharan, K.; Strobl, C.J.; Schneider, M.F.; Wixforth, A. Acoustic mixing at low Reynold's numbers. *Appl. Phys. Lett.* **2006**, *88*, 054102.
13. Franke, T.; Braunmuller, S.; Schmid, L.; Wixforth, A.; Weitz, D.A. Surface acoustic wave actuated cell sorting (SAWACS). *Lab Chip* **2010**, *10*, 789–794.
14. Lenshof, A.; Magnusson, C.; Laurell, T. Acoustofluidics 8: Applications ofacoustophoresis in continuous flowmicrosystems. *Lab Chip* **2012**, *12*, 1210.
15. Sadhal, S.S. Acoustofluidics 15: Streaming with sound waves interacting with solid particles. *Lab Chip* **2012**, *12*, 2600. doi:10.1039/c2lc40243b.
16. Muller, P.B.; Rossi, M.; Marin, A.G.; Barnkop, R.; Augustsson, P.; Laurell, T.; Kahler, C.J.; Bruus, H. Ultrasound-induced acoustophoretic motion of microparticles in three dimensions. *Phys. Rev. E* **2013**, *88*, 023006.
17. Skov, N.R.; Sehgal, P.; Kirby, B.J.; Bruus, H. Three-Dimensional Numerical Modeling of Surface-Acoustic-Wave Devices: Acoustophoresis of Micro-and Nanoparticles Including Streaming. *Phys. Rev. Appl.* **2019**, *12*, 044028. doi:10.1103/PhysRevApplied.12.044028.

18. Qiu, W.; Karlsen, J.T.; Bruus, H.; Augustsson, P. Experimental Characterization of Acoustic Streaming in Gradients of Density and Compressibility. *Phys. Rev. Appl.* **2019**, *11*, 024018. doi:10.1103/PhysRevApplied.11.024018.
19. Voth, G.A.; Bigger, B.; Buckley, M.R.; Losert, W.; Brenner, M.P.; Stone, H.A.; Gollub, J.P. Ordered clusters and dynamical states of particles in a vibrated fluid. *Phys. Rev. Lett.* **2002**, *88*, 234301.
20. Vuillermet, G.; Gires, P.Y.; Casset, F.; Poulain, C. Chladni Patterns in a Liquid at Microscale. *Phys. Rev. Lett* **2016**, *116*, 184501.
21. Legay, M.; Simony, B.; Boldo, P.; Gondrexon, N.; Le Person, S.; Bontemps, A. Improvement of heat transfer by means of ultrasound: Application to a double-tube heat exchanger. *Ultrason. Sonochem.* **2012**, *19*, 1194–1200. doi:10.1016/J.ULTSONCH.2012.04.001.
22. Loh, B.G.; Hyun, S.; Ro, P.I.; Kleinstreuer, C. Acoustic streaming induced by ultrasonic flexural vibrations and associated enhancement of convective heat transfer. *J. Acoust. Soc. Am.* **2002**, *111*, 875–883.
23. Kamakura, T.; Sudo, T.; Matsuda, K.; Kumamoto, Y. Time evolution of acoustic streaming from a planar ultrasound source. *J. Acoust. Soc. Am.* **1996**, *100*, 132–138.
24. Brunet, P.; Baudoin, M.; Bou Matar, O.; Zoueshtiagh, F. Droplet displacements and oscillations induced by ultrasonic surface acoustic waves: A quantitative study. *Phys. Rev. E* **2010**, *81*, 036315.
25. Moudjed, B.; Botton, V.; Henry, D.; Ben Hadid, H.; Garandet, J.P. Scaling and dimensional analysis of acoustic streaming jets. *Phys. Fluids* **2014**, *26*, 093602.
26. Da Costa Andrade, E.N. On the circulations caused by the vibration of air in a tube. *Proc. R. Soc.* **1931**, *134*, 445.
27. Valverde, J.M. Pattern-formation under acoustic driving forces. *Contemp. Phys.* **2015**, *56*, 338–358.
28. Hamilton, M.F.; Ilinskii, Y.A.; Zabolotskaya, E. Acoustic streaming generated by standing waves in two-dimensional channels of arbitrary width. *J. Acoust. Soc. Am.* **2002**, *113*, 153–160.
29. Wiklund, M.; Green, R.; Ohlin, M. Acoustofluidics 14: Applications of acoustic streaming in microfluidic devices. *Lab Chip* **2012**, *12*, 2438. doi:10.1039/c2lc40203c.
30. Huang, P.H.; Xie, Y.; Ahmed, D.; Rufo, J.; Nama, N.; Chen, Y.; Chan, C.Y.; Huang, T.J. An acoustofluidic micromixer based on oscillating sidewall sharp-edges. *Lab Chip* **2013**, *13*, 3847–3852. doi:10.1039/c3lc50568e.
31. Huang, P.H.; Nama, N.; Mao, Z.; Li, P.; Rufo, J.; Chen, Y.; Xie, Y.; Wei, C.H.; Wang, L.; Huang, T.J. A reliable and programmable acoustofluidic pump powered by oscillating sharp-edge structures. *Lab Chip* **2014**, *14*, 4319–4323.
32. Nama, N.; Huang, P.H.; Huang, T.J.; Costanzo, F. Investigation of acoustic streaming patterns around oscillating sharp edges. *Lab Chip* **2014**, *14*, 2824–2836.
33. Nama, N.; Huang, P.H.; Huang, T.J.; Costanzo, F. Investigation of micromixing by acoustically oscillated sharp-edges. *Biomicrofluidics* **2016**, *10*, 024124.
34. Doinikov, A.A.; Gerlt, M.S.; Pavlic, A.; Dual, J. Acoustic streaming produced by sharp-edge structures in microfluidic devices. *Microfluid. Nanofluid.* **2020**, *24*, 32.
35. Zhang, C.; Guo, X.; Brunet, P.; Costalonga, M.; Royon, L. Acoustic streaming near a sharp structure and its mixing performance characterization. *Microfluid. Nanofluid.* **2019**, *23*, 104. doi:10.1007/s10404-019-2271-5.
36. Zhang, C.; Guo, X.; Royon, L.; Brunet, P. Unveiling of the mechanisms of acoustic streaming induced by sharp edges. *arXiv* **2020**, arXiv:2003.01208.
37. Ovchinnikov, M.; Zhou, J.; Yalamanchili, S. Acoustic streaming of a sharp edge. *J. Acoust. Soc. Am.* **2014**, *136*, 22–29. doi:10.1121/1.4881919.
38. Huang, P.H.; Chan, C.Y.; Li, P.; Wang, Y.; Nama, N.; Bachman, H.; Huang, T.J. A sharp-edge-based acoustofluidic chemical signal generator. *Lab Chip* **2018**, *18*, 1411–1421. doi:10.1039/C8LC00193F.
39. Leibacher, I.; Hahn, P.; Dual, J. Acoustophoretic cell and particle trapping on microfluidic sharp edges. *Microfluid. Nanofluid.* **2015**, *19*, 923–933. doi:10.1007/s10404-015-1621-1.
40. Cao, Z.; Lu, C. A Microfluidic Device with Integrated Sonication and Immunoprecipitation for Sensitive Epigenetic Assays. *Anal. Chem.* **2016**, *88*, 1965–1972. doi:10.1021/acs.analchem.5b04707.
41. Bachman, H.; Huang, P.H.; Zhao, S.; Yang, S.; Zhang, P.; Fu, H.; Huang, T.J. Acoustofluidic devices controlled by cell phones. *Lab Chip* **2018**, *18*, 433–441. doi:10.1039/C7LC01222E.
42. Costalonga, M.; Brunet, P.; Peerhossaini, H. Low frequency vibration induced streaming in a Hele-Shaw cell. *Phys. Fluids* **2015**, *27*, 013101.
43. Cheng, N.S. Formula for the viscosity of a glycerol-water mixture. *Ind. Eng. Chem. Res.* **2008**, *47*, 3285–3288.

44. Slie, W.M.; Donfor, A.R.; Litovitz, T.A. Ultrasonic shear and longitudinal measurements in aqueous glycerol. *J. Chem. Phys.* **1966**, *44*, 3712–3718.
45. Bahrani, S.; Perinet, N.; Costalonga, M.; Royon, L.; Brunet, P. Vortex elongation in outer streaming flows. *Exp. Fluids* **2020**, *61*, 91.

Appendix D

Paper under review in Chemical Engineering Journal

Mixing intensification using sound-driven micromixer with sharp edges

Chuanyu ZHANG[1], Philippe BRUNET[2], Laurent ROYON[1], and Xiaofeng GUO[1,3]

[1]Université de Paris, CNRS, LIED, UMR 8236, F-75006, Paris, France

[2]Université de Paris, CNRS, MSC, UMR 7057, F-75006, Paris, France

[3]Université Gustave Eiffel, ESIEE Paris, F-93162, Noisy le Grand, France

ABSTRACT

Strong acoustic streaming can be generated inside a microchannel near sharp-edge structures. In this study, three Sharp-Edge Acoustic Streaming (SEAS) micromixers with multiple sharp edge patterns actuated by piezoelectric transducers are investigated. Direct Numerical Simulation (DNS) is used to numerically solve the multi-physics phenomenon involving acoustics, fluid dynamics and mass transfer. Experiments are carried out to validate the numerical results by visualization, as well as to evaluate micromixing performance with Iodide-Iodate Reactions. Influence of the sharp edge pattern (i.e. the spacing between individual structures, the number of sharp edges), channel throughput as well as acoustic intensity are studied. The shape of flow streamlines first unveils the interaction between acoustic streaming and main flow, which is shown to be a key for mixing enhancement. Following this, an optimal structure is found among the three mixers which allows achieving a decrease of micromixing time from 0.28 s to 0.03 s. Finally, a comparison with literature on passive mixers confirms the micromixing performance of SEAS mixer in terms of micromixing time at low Reynolds flow.

KEYWORDS

Acoustic Streaming, Sharp-edge, Micromixing, Process intensification, Active enhancement

INTRODUCTION

Mixing is a vital process for operations in microchannels such as chemical reactions, biological syntheses as well as food processing. From the point of view of chemical reactions, homogeneous

and rapid contact between reactants must be realized at the molecular level. As a result, the ability to rapidly create a homogeneous reactant mixture is crucial for the design of microreactors. However, as typical microchannel operations usually involve low-Reynolds number flows, mixing is mainly achieved through molecular diffusion across the interface, especially without external disturbances. Mixing at micro- or millimetric microfluidics is thus very slow for most liquid reagents (DeMello 2006). In such a situation, the mixing efficiency directly affects the quality of a reaction.

Both *passive* and *active* techniques have been used to intensify mixing in microfluidics. Passive techniques optimise the channel geometry, and in turn the flow streamlines, in order to maximize the interface between two fluids. Examples for high and intermediate Reynolds numbers include zigzag-shaped mixing channel (Stroock et al. 2002), tree-like multichannel T-mixer (Guo et al. 2014), chaotic mixer with 3D L-shape channel or with z-connections (DeMello 2006; Qin et al. 2017). For very low Reynolds numbers, structures like staggered-herringbone grooves have been shown to be effective in mixing (Hossain et al. 2010). While passive mixers only relies on hydrodynamic energy dissipation to improve mixing, extra pumping power is required due to the high pressure drop. The strategy of active mixing, on the other hand, introduces external perturbations (mechanical, ultrasonic, among others) within the fluid. For example, (Li and Kim 2017) designed an water-head-driven microfluidic oscillator to generate periodic fluids bands and achieve rapid mixing. Their experimental study showed that at Re= 0.3∼1 with an external activation of 14∼20 Hz oscillation, complete (macro)mixing can be achieved within mixing distances as short as 1.1 cm ∼ 4 cm. Acoustic vibrations as a active enhancement technique are frequently used to enhance heat and mass transfer (Vainshtein 1995; Setareh et al. 2020; Luo et al. 2018). For instance, (Luo et al. 2018) improved micromixing and mass transfer by prescribing high-frequency (20 kHz) ultrasonic wave in a rotating packed bed reactor. The collapse of micro bubbles created by ultrasound waves produces microjets and microstreams that enhance micromixing.

Acoustic streaming (AS), a steady flow generated by an acoustic field in a fluid, can potentially be an effective tool to actively enhance mixing. The AS phenomenon is due to second-order nonlinear effects in the coupling between acoustics and hydrodynamics. Historically, acoustic

streaming was extensively studied in relatively large fluid volumes like in Kundt's tubes excited by kHz-range acoustic forcing (Hutchisson and Morgan 1931). More recently, AS was investigated in microfluidic channels using transducers in pairs or with reflectors in order to realize a condition of resonance (Lei et al. 2013; Bruus 2012). In the latter situation, the acoustic wavelength has to be of the same order of magnitude as the channel width, which imposes a frequency as high as several MHz. However, recently strong streaming flow around sharp structures has been evidenced (Ovchinnikov et al. 2014; Huang et al. 2013; Zhang et al. 2019; Zhang et al. 2020b; Doinikov et al. 2020b; Doinikov et al. 2020a) even in the kHz range or lower, attainable even with low-cost piezo-transducers. Contrary to MHz-range AS, the wavelength of audible acoustic wave at several kHz ($\lambda \approx 0.5$ m) is much larger than the typical dimensions of microfluidic devices (smaller than 1 mm). This means the acoustic amplitude within the fluid is homogeneous and the wave has the same phase everywhere. The presence of sharp edges enables the generation of strong acoustic streaming, which would be null in a smooth channel according to the classical Rayleigh theory (Rayleigh 2013). Thanks to its strong transverse (i.e. perpendicular to the main flow) disturbances within a laminar flow, involving low-cost equipment requirements, such sound-driven steady flows have promising potential applications in Process Intensification (PI), in particular the micromixing enhancement in continuous microfluidics. Another advantage of low-frequency sharp-edge AS is that it can be operated under relatively low power input, avoiding local heating from piezoelectric actuators. This makes it particularly adapted to be used in microfluidic devices with low Reynolds number laminar flows. This study deals with Sharp Edge Acoustic Streaming applied to mixing, which will be abbreviated as SEAS mixers hereafter.

In our earlier experimental (Zhang et al. 2019; Zhang et al. 2020a) and numerical works (Zhang et al. 2020b), the physical mechanisms of streaming flow around a single edge have been thoroughly investigated. Features of SEAS were explored under different conditions, including geometrical (curvature diameters, angles of edge), acoustical (intensity, frequency) and operating ones (flow rate). In (Zhang et al. 2019), we used direct visualisation using fluorescent particles to unveil the streaming generation mechanisms, tracking both the acoustic oscillations and steady

acoustic streaming. The mixing process around one single sharp edge is characterized by dye visualisation, confirming the enhancement of macromixing thanks to streaming flow transverse to the main flow. Disturbance distance, vortex size as well as streaming velocity are retained to quantify the streaming intensity. In a more recent study (Zhang et al. 2020b), we gave guidelines on how to obtain strong acoustic streaming with the combination of acoustic and geometrical configurations. We developed DNS (Direct Numerical Simulation) in the finite-element software COMSOL, which proved to provide better predictions than the classical PT (Perturbation Theory) modelling, especially at relatively large forcing. Finally, the dependency of SEAS on fluid viscosity and acoustic frequency was also experimentally studied in (Zhang et al. 2020a). Following our earlier work, to fabricate a channel with an array of sharp edge structures should be effective to considerably enhance mixing. Although several experimental and PT-based simulation studies focusing on chip-scale SEAS mixing have been reported by (Nama et al. 2016; Ozcelik et al. 2014) and, more recently in (Bachman et al. 2020), the hydrodynamic streaming mixing enhancement mechanism remains unclear. Namely, several critical questions remain unanswered: i) What is the best geometrical sharp-edge configuration that enables the best mixing performance? ii) From a micromixer application perspective, evaluation of micromixing performance of SEAS through parallel chemical reactions (mainly based on micromixing time), to the best of our knowledge, is still absent in the literature. In particular, micromixing time allows a direct comparison with other type of micromixers (both passive and active), in terms of mixing performance and energy cost. iii) Finally, from a methodology point of view, as we have discussed in our previous study (Zhang et al. 2020b), simulation of SEAS with perturbation method can bring in a considerable error, especially under large acoustic intensity. Developing appropriate numerical scheme to resolve the acoustic-hydrodynamic-mass transfer coupling phenomenon is of high reference value for other acoustofluidics researches.

In summary, the current study intends to go further on the use of SEAS on mixing in microchannel. First, we designed three different SEAS mixers with multiple sharp edges in the aim of unveiling the streaming-mixing interaction and finding the best configuration on mixing

performance. Following this design, fluorescence particle visualisation validates the simulation protocol. Then, the effect of streaming on mixing with the three SEAS mixers under specific acoustic conditions are compared. Streamlines of acoustic streaming combined with the main flow, provide valuable clues to design an optimal SEAS mixer. Last, micromixing performance evaluation follows a widely accepted methodology, i.e., Iodide-Iodate reactions. Thanks to performance indicators such as micromixing time and energy dissipation, comparison of SEAS mixer with other previously-reported micromixers illustrates the relative performance of SEAS devices.

THEORETICAL BACKGROUND

Origin of Sharp-Edge Acoustic Streaming (SEAS)

The sharp-edge AS in this study uses acoustic wavelength $\lambda_c = c/f$, of the order of half a meter, hence much larger than the characteristic flow size in microfluidics. There are three velocities involved : acoustic velocity $\mathbf{v}_\omega = Re[\mathbf{v}_a e^{i\omega t}]$ (fluid vibration induced by piezo-transducer, time-dependent part, $\mathbf{v}_a$ is the complex amplitude, $Re[\cdot]$ denotes the real part of a complex term), streaming velocity $\mathbf{v}_s$ (steady-state streaming) and mainstream velocity $\mathbf{v}_0$. All of them being much lower than the sound speed (c=1430 m/s in water), the flow is thus incompressible. According to the classical Perturbation Theory (PT), the steady streaming velocity can be theoretically solved through the time-averaged second-order momentum and continuity equations in Eq.1 and Eq.2 (Ovchinnikov et al. 2014).

$$(\mathbf{v}_s \cdot \nabla)\mathbf{v}_s = -\frac{1}{\rho}\nabla p_s - F_s + \nu\nabla^2\mathbf{v}_s \tag{1}$$

$$\nabla \cdot \mathbf{v}_s = 0 \tag{2}$$

where v_s is the second-order time averaged velocity (streaming flow); $F_s = \frac{1}{2}Re[< (\mathbf{v}_a \cdot \nabla)\mathbf{v}_a^T >]$ is the time averaged inertia term as a result of the first-order oscillatory field. And it's also named averaged *Reynolds Stress Force* (Lighthill 1978), it represents the driving force of the streaming flow in the fluid bulk acting within and beyond the viscous boundary layer.

From the form of F_s, it is clear that a homogeneous acoustic field cannot generate any streaming

flow along straight and smooth walls, as the effective force would be null (Ovchinnikov et al. 2014; Zhang et al. 2019; Zhang et al. 2020b). Within the boundary layer, the oscillations are subjected to spatial variations and vanish along the wall due to the no slip boundary condition. Despite the spatial variations of $\mathbf{v}_a$, the direction of oscillations keeps parallel to the straight horizontal wall, so that F_s remains null (Ovchinnikov et al. 2014; Zhang et al. 2020b). However, the presence of sharp edge structures with strong local curvature on the channel walls induces sharp spatial variations in the acoustic fluid oscillation near the tip (Zhang et al. 2019; Zhang et al. 2020b), which makes F_s non-zero locally. As sketched in Fig.1-(a) for a single sharp edge in a channel, the vibration is uniformly distributed in the channel except for the local zone close to the sharp edge. More specifically, close to the tip, both the orientation of the acoustic field and the vibration amplitude provide favorable conditions to induce an intense streaming force F_s. Far enough from the tip, typically at a distance of a few boundary layers, the force becomes null or negligible. Therefore, the sharp edge induced non-uniformity of the acoustic field makes acoustic streaming at relatively low frequency (several kHz) possible.

Since the streaming force F_s generates a jet shooting from the sharp edge in the transverse direction, a pair of counter-rotating vortices is in turn generated as shown in Fig.1(b). These counter-rotating vortices in the fluid bulk can induce significant disturbance to the main flow at a distance much larger than the boundary layer thickness. Outside the boundary layer, the streaming flow interacts with the main flow, and is susceptible to enhance the advection and mixing of species along the channel. Enhancement of mass transfer of two parallel fluids is thus possible. From the basic flow visualisations for a single sharp edge, our study extends to the case of multiple sharp edges (as shown in Fig.1-(c)). Our expectations are that the interaction and cooperative effects of these several transverse flows and vortices should be suitable for mixing enhancement.

Numerical modelling of acoustic streaming

Although being particularly adapted in qualitative interpretation of the origin of acoustic streaming near sharp edges, the classical Perturbation Theory (PT) fails to accurately predict the magnitude of the streaming velocity. The main reason lies in the particularity of sharp edge streaming for

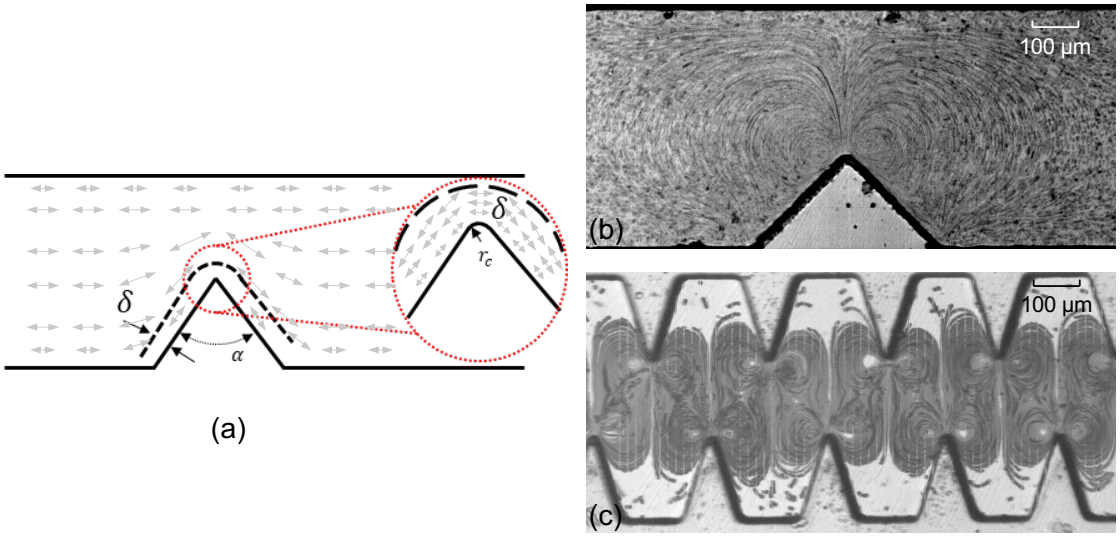

Fig. 1. Origin of the acoustic streaming around the sharp edge. (a) Sharp edge of angle α and curvature diameter $2r_c$ inside a channel, δ shows the boundary layer thickness; Grey arrows represent acoustic oscillations driven by piezoelectric transducer. Particle visualisation of (b) single sharp-edge and (c) multiple sharp-edge acoustic streaming.

which the streaming velocity $\mathbf{v}_s$ can be of the same order of magnitude as the vibration velocity $\mathbf{v}_a$ (Zhang et al. 2019), which is not the case for classical Rayleigh streaming. As discussed above, the velocity field $\mathbf{v}$ and pressure field p can be separated to three parts, shown in Eq.3 and 4. Then the momentum equation Eq.5 can be separated into two parts : the oscillatory terms (Eq.6) and the steady terms (Eq.7). The PT method simplifies the coupling between $\mathbf{v}_a$ and $\mathbf{v}_s + \mathbf{v}_0$ by neglecting the following terms in Eq.6 : $((\mathbf{v}_s + \mathbf{v}_0) \cdot \nabla)\mathbf{v}_a + (\mathbf{v}_a \cdot \nabla)(\mathbf{v}_s + \mathbf{v}_0)$. As a consequence, our earlier work (Zhang et al. 2020b) showed inaccurate resolution of the streaming velocity from PT and the coupling terms in the context of sharp edge streaming are to be considered.

$$\mathbf{v} = \mathbf{v}_0 + \mathbf{v}_\omega + \mathbf{v}_s,\ \mathbf{v}_\omega = Re(\mathbf{v}_a e^{i\omega t}) \tag{3}$$

$$p = p_0 + p_\omega + p_s,\ p_\omega = Re(p_a e^{i\omega t}) \tag{4}$$

$$\begin{aligned} &\frac{\partial \mathbf{v}_\omega}{\partial t} + \left\{[\mathbf{v}_s + \mathbf{v}_0 + Re(\mathbf{v}_a e^{i\omega t})] \cdot \nabla\right\}[\mathbf{v}_s + \mathbf{v}_0 + Re(\mathbf{v}_a e^{i\omega t})] \\ &= -\frac{1}{\rho}\nabla[p_s + Re(p_a e^{i\omega t})] + \nu\nabla^2[\mathbf{v}_s + \mathbf{v}_0 + Re(\mathbf{v}_a e^{i\omega t})] \end{aligned} \tag{5}$$

$$i\omega\mathbf{v}_a + ((\mathbf{v}_s + \mathbf{v}_0) \cdot \nabla)\mathbf{v}_a + (\mathbf{v}_a \cdot \nabla)(\mathbf{v}_s + \mathbf{v}_0) = -\frac{1}{\rho}\nabla p_a + \nu\nabla^2\mathbf{v}_a \tag{6}$$

$$((\mathbf{v}_s + \mathbf{v}_0) \cdot \nabla)(\mathbf{v}_s + \mathbf{v}_0) + \frac{1}{2}Re[(\mathbf{v}_a \cdot \nabla)\mathbf{v}_a^*] = -\frac{1}{\rho}\nabla p_s + \nu\nabla^2(\mathbf{v}_s + \mathbf{v}_0) \tag{7}$$

Recently, we carried out simulations by directly solving the Navier-Stokes equation with periodic boundary conditions, using DNS (Zhang et al. 2020b). With this technique, the time-dependent variable $\mathbf{v} = Re(\mathbf{v}_a e^{i\omega t}) + \mathbf{v}_s + \mathbf{v}_0$ at a given time-step can be obtained by directly solving Eq.(5) in a two-dimensional domain with periodic boundary conditions : $\mathbf{v}_b = Re(\mathbf{v}_{ab} e^{i\omega t}) + \mathbf{v}_{0b}$. $\mathbf{v}_{ab}$ is the $\mathbf{v}_a$ at boundary, and $\mathbf{v}_{0b}$ is the boundary velocity corresponding to channel throughput (cf Fig. 2 (a)). Then the steady velocity $< \mathbf{v} >$ is available by time averaging $\mathbf{v}$ over several acoustic periods. Details about DNS implementation can be found in (Zhang et al. 2020b).

$$\bar{\mathbf{v}} = \mathbf{v}_s + \mathbf{v}_0 = \frac{\int_0^T \mathbf{v} dt}{T} \tag{8}$$

where $\mathbf{v}_0$ is the steady velocity field corresponding to channel throughput, and $T = \frac{1}{f}$ is the acoustic wave period.

Based on the above methodology, simulations of the velocity field can be proceeded as the first step. Then, species transport (macromixing) can be included by adding the classical mass transport equation Eq.9 in a second step with species concentration boundary conditions as shown in Fig.2 (b).

$$-D_i \Delta C_i + \mathbf{v} \cdot \nabla C_i = 0 \tag{9}$$

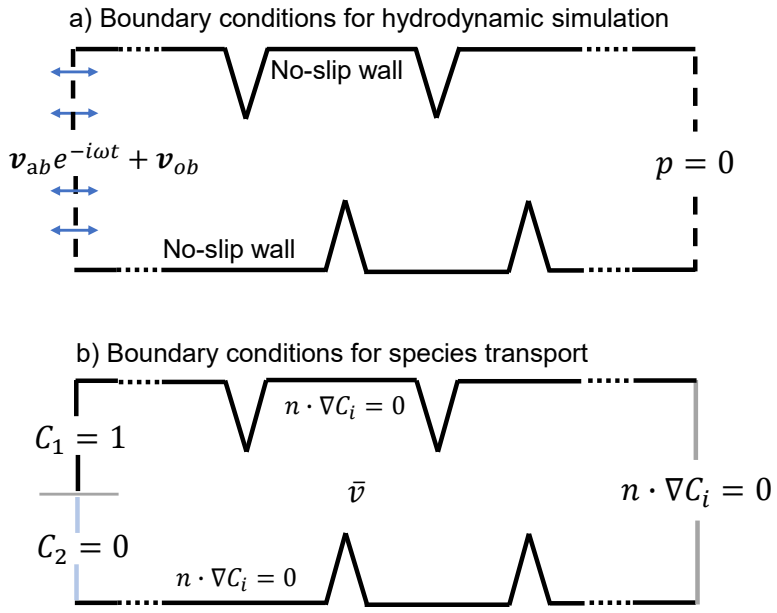

Fig. 2. Boundary conditions used in the DNS modeling

where D_i is the diffusion constant of the i_{th} species. C_i refers to the molar concentration of the i_{th} species. Physically, the equation represents equal value of diffusive part $D_i \Delta C_i$ with convective part $\mathbf{v} \cdot \nabla C_i$ in a steady-state source-less diffusion-convection phenomenon.

It is worth noting that in this step, we use the mean steady velocity $\bar{\mathbf{v}}$ from the hydrodynamic solution as $\mathbf{v}$ in the convective term. In other words, the periodic acoustic oscillation velocity is considered to have no influence on mixing. First, this assertion is based on our experimental visualization to a smooth channel, showing no mixing enhancement effect without acoustic streaming even with acoustic ON. Indeed, the first order vibration, as it mainly follows the longitudinal direction of the mixing channel hence in parallel to the main flow, does not increase the transverse advection of the two species.

Specifically, two solutions with $C_1 = 1$ and $C_2 = 0$ allow to directly obtain dimensionless concentration between 1 to 0 (mixing degree). Then macromixing process between two miscible fluids intensified by streaming phenomenon in the micro channel with sharp edges array can be simulated.

Mixing enhancement by streaming

The present study addresses an advection dominant mixing process which, without any acoustic streaming, would be extremely slow. More specifically, the channel flow is characterized by very low Re, ranging from 0.12 to 0.72 for the tested flow rates of 2 μL/min to 12 μL/min, and considering a channel with smooth walls. It is determined by $Re = \frac{\overline{v_0} D_h}{\nu}$, with D_h being the hydraulic diameter given by $4A/p$; $\overline{v_0}$ is the mean velocity corresponding to the channel flow-rate divided by its sectional area. In terms of relative importance between advection and diffusion, the Peclet number $Pe = Re \cdot Sc$ takes values above 1, typically ranging between 61 and 364, with Sc is the Schmidt number equal to 502 for Methylene dye in water. This implies that the convective transport along the flow direction dominates diffusion in the transverse direction. Under these conditions, and with a laminar Hagen-Poiseuille flow with parabolic velocity field along the channel axial direction, the mixing of the two fluids is strongly limited along a distance as short as $L/w = 14$ with L=7 mm and w=0.5 mm. Jets and vortices driven by acoustic streaming are expected to circumvent this limitation.

Micromixing characterization

General visualization techniques only show the mixing layers between fluids above the micron scale, which is the typical scale of *macromixing*. However, at a molecular scale, especially when mixing is associated with chemical reactions, quantitative characterization to evaluate the *micromixing* becomes necessary. Iodide-Iodate reactions is a commonly accepted protocol to this aim. Also named Villermaux-Dushman method, the protocol involves two competing parallel reactions at two distinct reaction rates : a quasi-instantaneous neutralization reaction and a redox reaction of several order of magnitude slower in terms of reaction rate than the former. This allows to characterize mixing at the molecular scale through the yield of Iodine (I_2) molecules in the final effluent. It is thus particularly useful to interpret the mixing process as a chemical probe. Details of the method are given in the Appendix I.

Additionally, combined with a tubular reactor model IEM (Interaction by Exchange with the Mean), the Iodide-Iodate protocol allows to access micromixing time (t_m). This enables to conduct

a direct and quantitative comparison of performance between different micromixers (Falk and Commenge 2010).

Chemicals and test procedure

Precautions are necessary in the choice of reactant concentrations with which the Absorbance Unit (A) given by the spectrophotometry under all operation conditions should fall in the range $0.1 < A < 3$. This guarantees to remain in the linear range, that enables the use of the Beer-Lambert law to determine the molar concentration of tri-iodide. To this end, we adopt a trial-and-error approach to find the best choice for concentration, as shown in Tab.1. Also, a cuvette with small enough volume (Hellma, QS105, 50 µL) is required, since the flow rate is as low as several µL/min.

	$[H^+]$	[KI]	$[KIO_3]$	[NaOH]	$[H_3BO_3]$
C [mol/L]	0.03	0.016	0.003	0.045	0.045

TABLE 1. Concentration set used to characterize micromixing

Once the spectrometer results are obtained, we use Beer-Lambert law to determine the I_3^- yield (concentration $C_{I_3^-}$). Then, the Segregation Index is determined followed by implementing IEM model to access micromixing time.

Segregation Index

As a quantitative indicator in the Iodide-Iodate reactions scheme, Segregation Index X_S can characterize the mixing efficiency through a given micromixer under a fixed reactant concentration. It is defined by the ratio of the iodine yield (Y) in a test (real case) to the maximum yield of iodine (Y_{ST}) in the case of most inefficient mixing (total segregation case), as in Eq.10.

$$X_S = \frac{Y}{Y_{ST}} \tag{10}$$

In the case of total segregation, the two competitive reactions R1 and R2 (shown in Appendix I) are quasi-instantaneous with respect to the micromixing time, supposed to be infinitely long. Conversely, ideal micromixing implies arbitrarily short micromixing time. Thus, with ideal mi-

cromixing $X_S = 0$, and with total segregation $X_S = 1$. Partial segregation follows the definition $X_S = Y/Y_{ST}$ and it results in a value between 0 and 1. The calculation of Y and Y_{ST} involves all reactant concentrations and it follows the procedure described in the Appendix I.

Micromixing time

Different Segregation Indices X_S can be achieved with different presumed t_m following the procedure in Appendix II. Then the relation between the X_S and t_m can be built up, as shown in Fig.14 (Appendix II), through which, t_m under different conditions can be determined with the segregation index X_S measured by experiment. For t_m, its value can be compared with those under various experimental conditions, like different initial ions' concentrations. However, the value for X_S depends not only on the mixing performance itself but also on the initial ions concentration. Previous investigations opted for concentration values according to the specific mixer design. Hence direct performance comparison between different micromixers by segregation index is not relevant. In such a situation, the only reliable criteria to estimate the mixing performance has to rely on the micromixing time, instead of the segregation index. Therefore several recent comparative micromixing studies have been conducted with the above method (Qin et al. 2017; Li et al. 2019).

EXPERIMENTAL SETUP

Y-type SEAS micromixer

A SEAS mixer is made of Polydimethylsiloxane (PDMS) and contains a Y-mixer and a channel with successive sharp-edges put as a network, with a specific distance between each other. The PDMS channel is pre-fabricated using 2D photo-lithography on a wafer (details have been documented in our previous study (Zhang et al. 2019)) and bonded onto a glass slide by oxygen plasma treatment. Three models (S1, S2, S3) are fabricated and their main geometrical dimensions are detailed in Fig. 3 (b-c). Only the channel section with sharp edge patterns is shown, the Y-mixer being identical for all three models. To provide an acoustic field in a frequency range between 2 and 3 kHz, a piezoelectric transducer is glued with epoxy resist on the glass coverslip slide, next to the channel (Fig. 3-b). After a careful tuning of f corresponding to one of the resonances of the

transducer, streaming clearly appears near each and every tip. The two main control parameters are then the acoustic amplitude (or velocity) and the flow-rate.

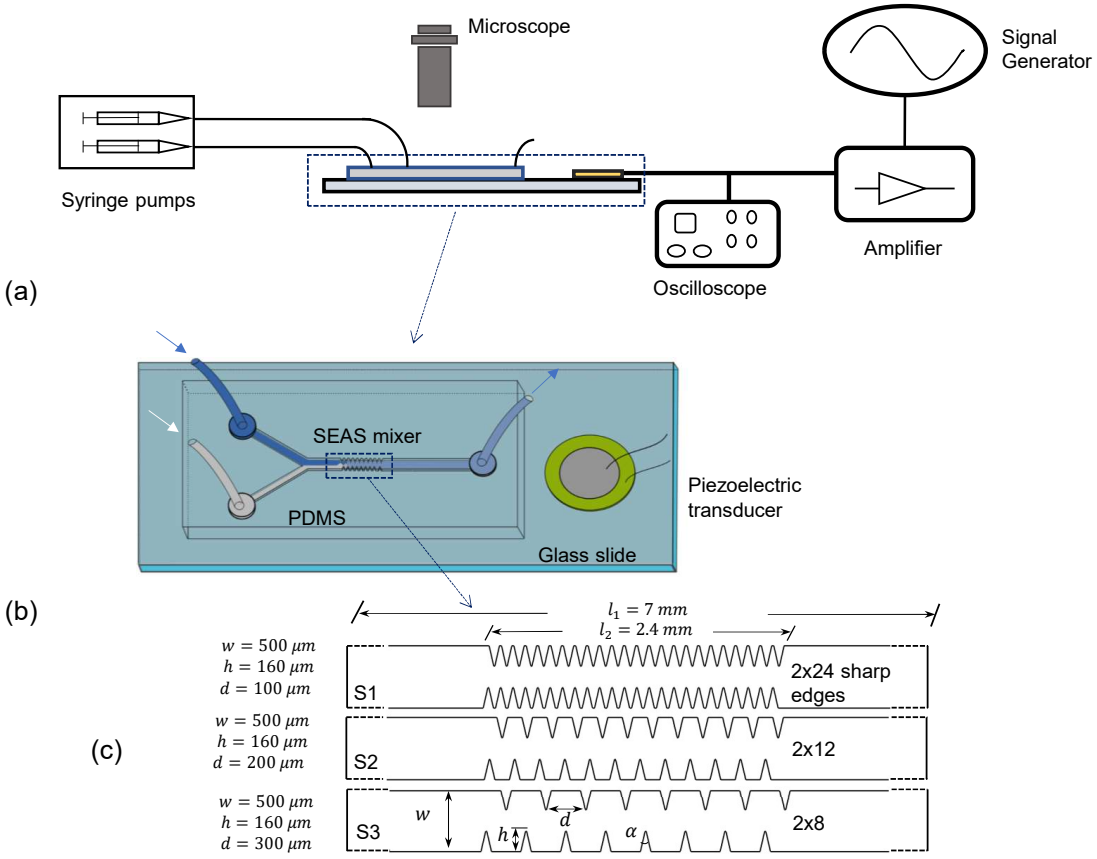

Fig. 3. Schematic of the experiment in this study: (a) Experimental setup with (b) the micro-channel and the transducer glued on the upper coverslip. (c) Three different geometry structures tested, with n_s = 24, 12 or 8, being the number of sharp edges on each side, varying with the distance d between the tip of two consecutive edges.

The experimental setup shown in Fig.3 (a) is composed of two syringe pumps (Newtown Company & Co) that enable the continuous injection of fluid from two syringes, under well-controlled flow-rate via the two inlets through the channel. A function generator (Model 33220A Arbitrary waveform generator, Agilent) with a home-made adjustable power amplifier provides the

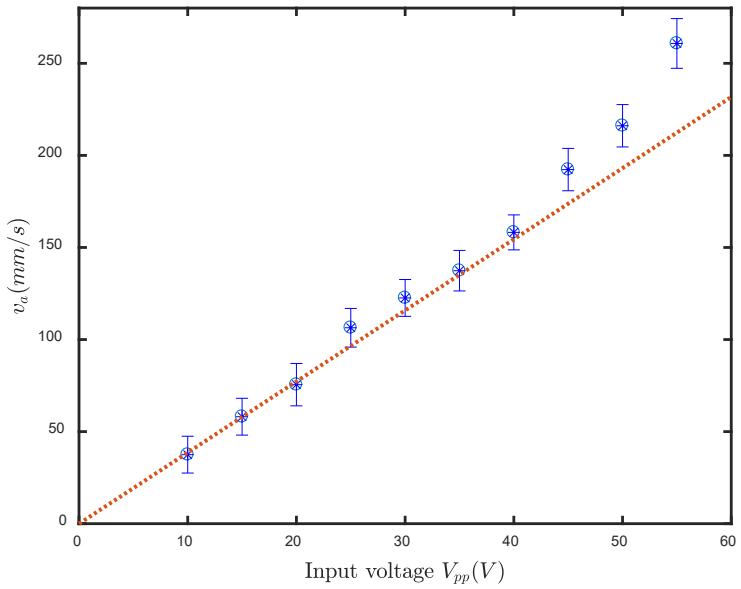

Fig. 4. Acoustic vibration amplitude varies with input voltage

signal supplied to the piezoelectric transducer (Model ABT-455-RC, RS Components). The flow visualization is achieved by a binocular microscope together with a fast camera (MotionBLITZ Cube4, Mikrotron). The piezoelectric transducer (diameter 35 mm and height 0.51 mm) delivers acoustic vibrations to the glass slide and to the whole channel stuck onto it, at various resonance frequencies from 0.1 kHz up to 5 kHz. We chose to operate at a frequency $f = 2.5$ kHz corresponding to one of these resonance peaks. It turns out that the best operating conditions in terms of streaming flow were obtained at this frequency.

The relation between the acoustic vibration amplitude v_a (v_a refer to the norm of $\mathbf{v}_a$) in terms of velocity and input voltage V_{pp} is shown in Fig.4. It turns out that v_a shows a rather linear variation with V_{pp}, except in the upper range of values, typically below 45 Volts. In practice, most of the results shown in this study was obtained in the range $V_{pp} < 45V$. We opted to choose v_a as the control parameter that quantifies the amplitude of the applied acoustic field. Complementary measurements showed a rather complex field of vibrations on the glass slide (Zhang et al. 2019).

Here v_a directly quantifies the real acoustic excitation, which is effective inside the channel and enables comparisons between different experimental studies. Here, it should be noted that v_a is measured far away enough from the sharp edge, and is adopted as the value of v_{ab} in the simulation part. The details of the measurement of v_a are given in a previous study (Zhang et al. 2019).

Mixing measurement procedure

For the Iodide-Iodate reaction protocol, a spectrometer (Jenway 7310) is used to measure the concentration of I_3^-. To cope with the small throughput (Q_c ≤12 µL/min), we use a high-precision micro-cuvette (Hellma, QS105 model, 50 µL, light path 10 mm) to collect the solution as close as possible from the outlet. Each test is conducted under stationary conditions, which is appreciated from direct visualisations. The sample is then put in spectrometer once the cuvette is sufficiently filled. To quantitatively analyze the micromixing process, the Segregation Index (X_s) and Micromixing time (t_m) are determined through the IEM model. For each test, values of t_m and X_s are obtained through the measured concentration I_3^- collected at the outlet. The relation between X_S and t_m at given reactant concentrations is shown in the Appendix II .

Besides micromixing evaluation, the visualisation of the macromixing between two fluids of different colors also helps to track the mixing process. One fluid is a mixture of Methylene blue dye (Fisher BioReagents) into deionized water, while the other one is pure deionized water. These sequences are then used to validate the numerical protocol.

RESULTS AND DISCUSSIONS

Validation of numerical results

Figure 5 shows the validation of numerical results by experimental visualisation (macromixing) with blue dye. The S1 mixer is used under the following operation conditions: v_a=85 mm/s, Q_c=8 µL/min. For the mass transfer, a mass diffusivity of $D = 2.49 \times 10^{-9} m^2/s$ (Leaist 1988) is used in the simulation.

Concentration evolution contours in Fig.5b) and c) obtained both experimentally and numerically show satisfactory agreement, which is also the case over the whole range of tested values

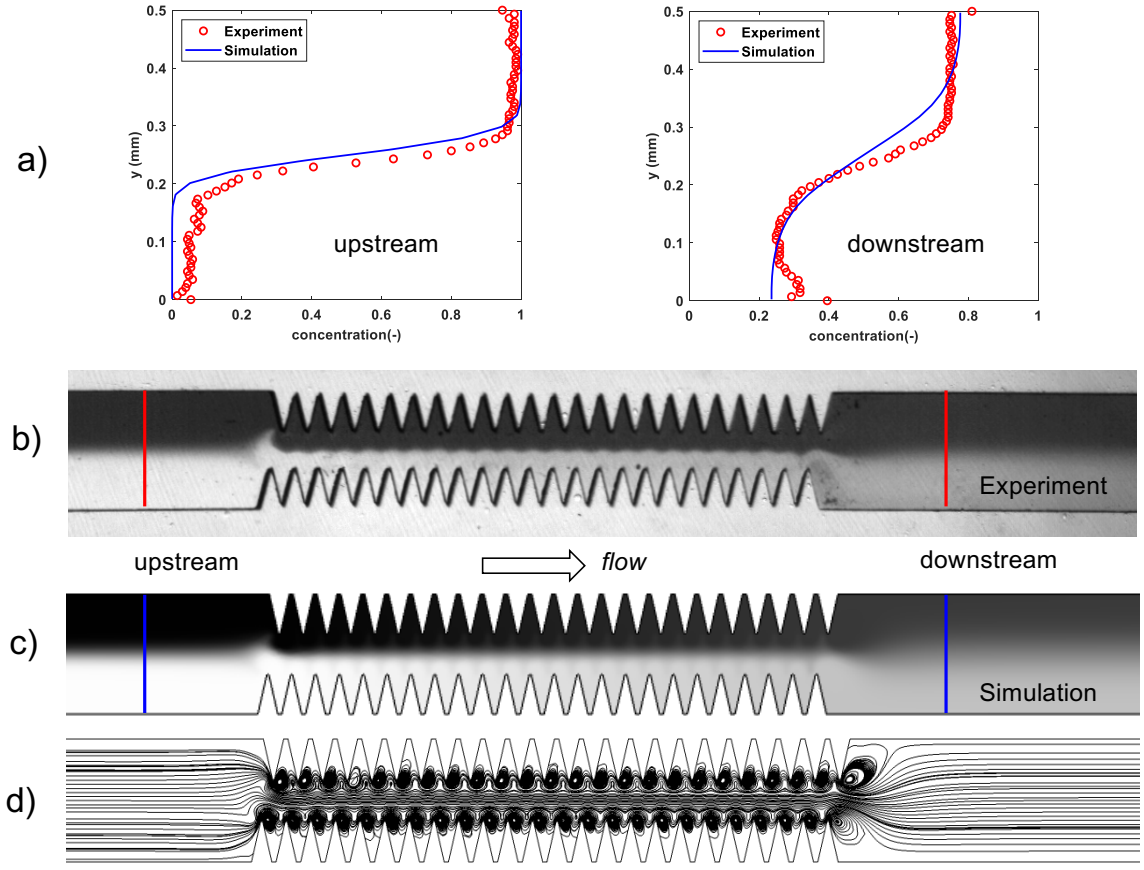

Fig. 5. Experimental validation of numerical results on active acoustic streaming driven mixing of two miscible fluids (water, water with Methylene blue) using micromixer S1. a) Concentration profiles before (upstream, left) and after (downstream, right) the SEAS mixing channel. The concentration profiles are taken at a distance of 0.5 mm before and after the first/last sharp edge, where the profiles are not perturbed by remaining vorticity, b) Experimental concentration evolution in the mixing channel, c) Same concentration field obtained numerically, d) Flow streamlines obtained numerically. The acoustic amplitude is v_a=85 mm/s and the flow rate is Q_c=8 µL/min.

for v_a. Similar grey level distribution - thus tracer concentration, are shown before, through and after the sharp-edge network. Upstream, the two fluids are clearly separated at the centerline of the channel. This is consistent with the advection-dominant flow (Pe≫1) under low-Reynolds laminar regime (Re<1).

As a quantitative comparison, Fig.5-a) confirms the accuracy of the numerical simulations by concentration profiles respectively at the *upstream* and *downstream* locations of the mixing zone.

Before entering the sharp-edges zone, the fluids are perfectly separated and the dye normalized concentration is either close to 0 or to 1. After crossing the sharp-edges region, the two fluids are brought closer to the 50%-50% line (ideal mixing). However, under a relatively low acoustic intensity (v_a=85 mm/s), perfect mixing is not well achieved downstream. For this S1 mixer at least, the generated AS is too weak.

In addition, the steady-state flow streamlines, resulting from the coupling between the main longitudinal flow and the acoustic streaming (disregarding acoustic velocity here), and under the same flow and vibration conditions, are shown in Fig. 5-d). At the centerline, the velocity remains roughly parallel to the main flow and the interface area between the two fluids is only slightly thickened by the space-periodic bending of the streamlines. Moreover, the triangular areas between two adjacent sharp edges do not look disturbed by acoustic streaming. These *dead zones* show a clear limitation of mixing, and are to be avoided from a mixing enhancement prospective.

Based on the experimental validated numerical scheme, we conducted a series of simulations with the three different mixers shown in Fig.3, in the aim of finding the optimal geometry of sharp-edge mixing channels, under the same acoustic and throughput conditions.

Performance comparison of SEAS mixers

Figure 6 shows concentration maps obtained from numerical simulations with the three SEAS mixers, under the same operating conditions : acoustic amplitude v_a=130 mm/s, channel throughput Q_c=8 µL/min. From these maps, one extracts the concentration profiles along the channel width, at five representative longitudinal positions, shown as inserts in Fig.6, with C_{in} and C_{out} being respectively the profiles at the inlet and outlet.

The cross-section concentration profiles extracted at different longitudinal locations, and especially C_{out}, suggest that S2 should be the optimal sharp-edge network for better mixing performance.

Under the same flow conditions, the mixer S2 achieves the best mixing efficiency (evaluated at the outlet) while S1 corresponds to the worst one (Fig.6). A closer examination of the cross-section profiles reveals that S2 and S3 seem to allow larger vortices-induced mixing, both at the entrance (near the first edge) and within the spaces between sharp edges in the middle of the channel. For

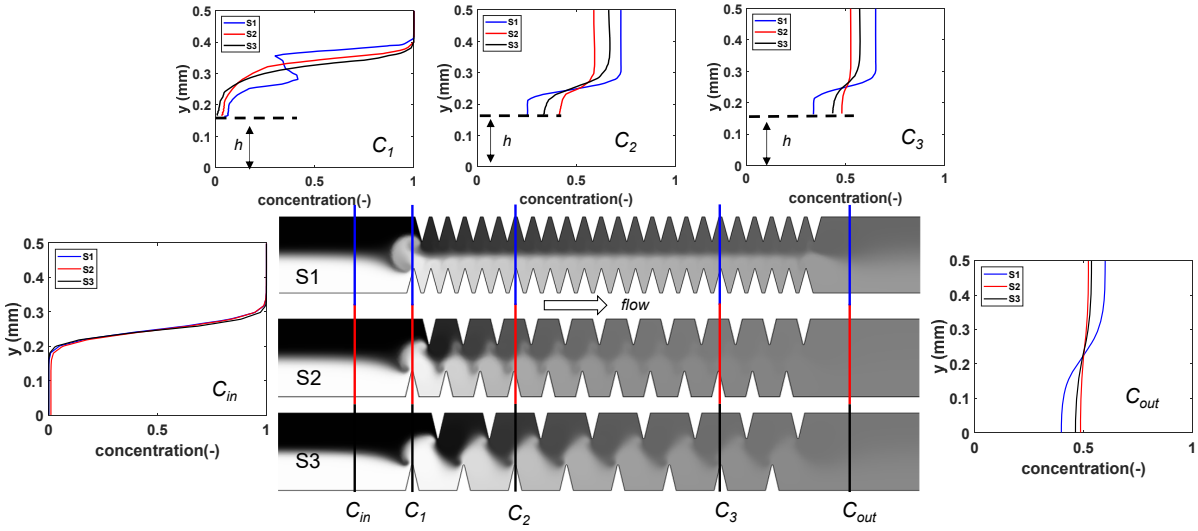

Fig. 6. Comparison of mixing performance of three micromixers S1/S2/S3. Concentration grey level maps from numerical simulation under the same following conditions: v_a=120 mm/s and Q_c= 8 µL/min. Cross-section concentration profiles are shown as inserts, for different longitudinal locations. Concentration curves from C_{in} to C_{out} quantitatively confirms the performance order from S2>S3>S1, with an identical inlet condition C_{in}.

the case of S1, streaming jets vortices are hindered due to the narrow space between each structure. Conversely, S2 and S3 enable each streaming jets from each sharp edge to reach the zones between two consecutive edges at the opposite wall. Therefore, despite S1 corresponds to the densest network, the small space between edges limits the full development of the streaming flow. As a result, AS vortices are within each local fluid instead of being useful for the mixing of them. The first sharp edge of S1, though, seems to play a major role in the mixing before the channel. Strong advection can be achieved at this entrance when the mainstream is subjected to a strong transversal streaming, thus mixing can be enhanced. Also, this effect appears with S2 and S3.

The three grey level maps shown in Fig. 6 comparatively illustrate the performances of the three mixers. With the same inlet C_{in}, a disturbed concentration distribution C_1 can be shown at the entrance, just before the first sharp-edge. At the entrance area, S1 seems to provide stronger disturbances than S2 and S3. Further downstream, S2 shows better mixing performance in the

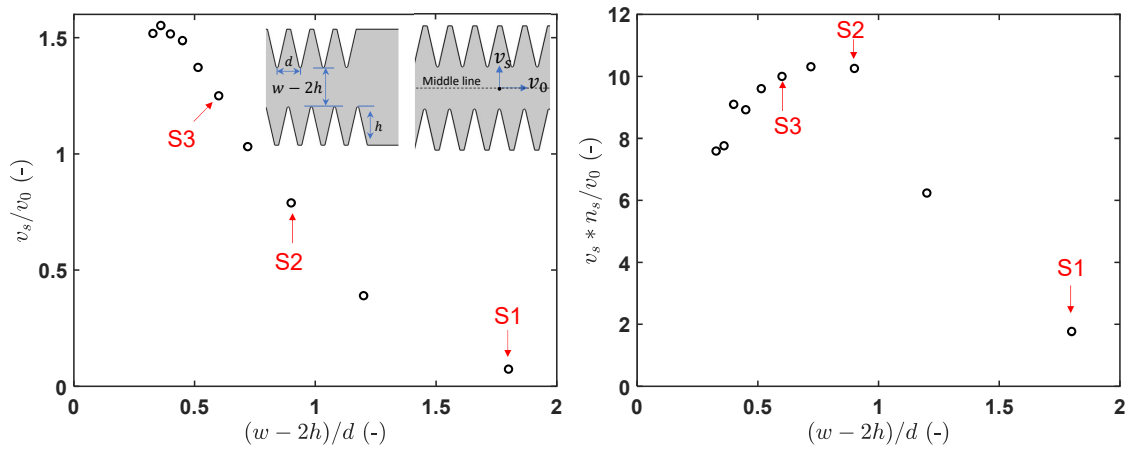

Fig. 7. Parametric simulation of mixing enhancement indicators by adjusting sharp edge patterns. Ratio v_s/v_0 versus $(w-2h)/d$ for different sharp-edge micromixers (left). Quantity $n_s \times v_s/v_0$ versus $(w-2h)/d$, showing S2 as an optimal geometry for mixing (right). The sharp edge section (l_2) is kept the same for the variety of edge densities.

whole area between C_2 and the outlet. This is presumably due to a larger number of effective streaming jets and vortices. The performance of S3 is close to that of S2, although slightly less efficient : it generates effective vortices too, but with less sharp edges. Finally, S1 shows the most segregated fluid at the outlet C_{out}, even though it gets a small advantage at the first sharp edge.

In summary, the above results show a complex nature of SEAS mixing enhancement mechanism, namely in terms of interaction between acoustic streaming and the main flow. It is thus necessary to provide a detailed interpretation on the mixing enhancement mechanism by AS with different structures.

At this stage though, we can propose a coarse optimal performance of the S2 mixer from purely kinetic and geometrical arguments. This optimum results from a compromise between the streaming velocity generated from a single sharp edge, and the length of the mixing area - or the number of mixing elements. In short, if the pattern is too narrow, each streaming jet shall not have enough space to develop toward the opposite wall, reducing the effective transverse velocity. In contrary, if the pattern is too loose, there will be too few transverse streaming jets and the mixing efficiency shall drop.

The orientation angle of the jet is roughly estimated by $\arctan(\frac{v_s}{v_0})$, and this angle should fit with $\arctan(\frac{w-2h}{d})$, which is roughly the angle of the segment relating two consecutive edges at opposite walls. Let us remark that v_s is here evaluated from numerical simulations for the different values of d, taking a typical averaged value from the jet centerline. Dropping the arctan(), we plot the quantity $\frac{v_s}{v_0}$ versus $\frac{w-2h}{d}$ (see Figure 7), confirming that the transverse disturbances are stronger for S2 and S3 geometries. Remarkably, there is a sharp drop beyond $\frac{w-2h}{d} > 1$, i.e. for denser edge structures like S1. In terms of global mixing efficiency, the number of sharp edges also matters, so that the narrowest pattern on the plateau (S2) represents an optimum of efficiency. This is also shown by plotting the quantity $\frac{v_s}{v_0}$ versus $\frac{w-2h}{d}$. Let us mention that this argument remains qualitative, although it has the merit to show where the optimum of efficiency should come from.

Mechanism of SEAS assisted mixing enhancement

We hereby attempt to explain the mixing enhancement mechanism of multiple sharp-edge acoustic streaming mixers, by investigating on the streamline patterns of the streaming flow combined with the main channel flow, see Figure 8. Several parameters can describe the intensity of acoustic streaming, such as maximal streaming velocity, vortex size, disturbance distance, among others (Zhang et al. 2019). Hence, the determination of the crucial driving factors of the mixing process would help to understand the link between streaming and mixing. In a more fundamental aspect, the number of sharp edges, their height, distance, are also influential on the streaming pattern (including intensity). To address these points, we show in Figure 8 a global view of the streamlines for the three mixers (lower figures), as well as magnified views on several key locations (upper figures).

The numerical streamline patterns clearly illustrate two main mechanisms of mixing enhancement from acoustic streaming: entrance effect and interactive vortices. These effects can be shown when focusing on three zones chosen as: i) Entrance, ii) Sharp-Edges, and iii) Outflow.

First, the entrance zone before the first sharp-edge is critical for the pre-mixing. For all three mixers, acoustic streaming creates significant transverse velocity component. Due to the space shift between the sharp edge tips on both sides, the transverse streaming velocity is driven by the

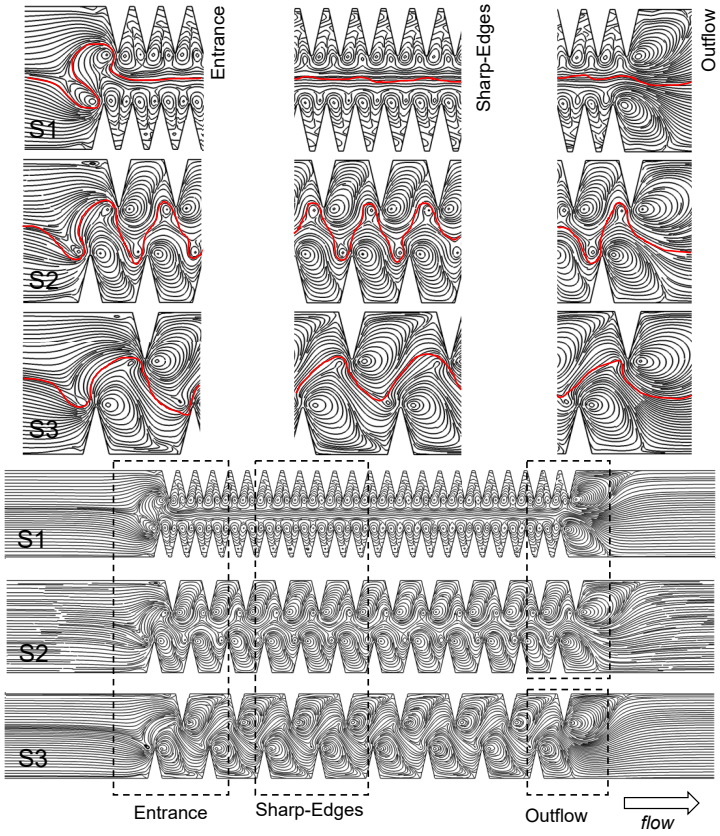

Fig. 8. Streamlines patterns in multiple sharp-edge acoustic streaming, as an explanation support for mixing enhancement. Steady-state velocity streamlines of S1, S2 and S3 (lower figures) under the same condition as in Fig.6. The red line in the zoomed images (upper figures) represents the deflection of the centerline 'interface' between the two fluids. In the spaces between sharp edges, in particular S1, some 'dead zones' appear, where mixing is very limited.

first edge and the jet shoots towards the opposite wall. According to the sectional area, the main stream velocity seem the strongest for S1, followed by S2 and S3.

The entrance perturbation appears with a scale as large as the channel width, in particular for cases S2 and S3. This strong perturbation induces the aforementioned transverse jet, thus disturbing the layer between the two fluids. Fast and effective mixing is shown at this entrance zone.

Second, after the entrance, as the fluids continue to flow within the sharp edge section, the size, shape development of vortices and their interaction are main factors that affect mixing. Large

vortices have more chance to interact with each other and thus to provide larger contact interface between two mixing fluids. From this point of view, structures with less dense edges (S2 and S3) provide stronger disturbances under the same vibration condition (Fig.8). Conversely, the sharp edges network of S1 is too dense, which does not leave enough space for vortices to develop. Also, S1 shows strong independent self-rotating vortices, competing with those from the opposite edges. This only slightly increases the contact area between the two fluids around a wavy center line as vortices are squeezed into narrow spaces.

After the final sharp edge, the streamlines appear as two large vortices, both joining the main flow. They are much larger than the vortices in the sharp edge zone for S1. For S2 and S3, their size is more comparable size as those in the mixing area.

Finally, it is worth noting that we used uniform-density streamline pattern in Fig.8 and in this case, even the dead zones are filled with streamlines. However, a detailed observation shows that the streamlines in the dead zones of S1 are disconnected with the main stream, which testifies again the inefficiency for mixing. Comparatively, no dead zone can be observed for S2 and S3 since all acoustic streaming jets and vortices extend their influence into the space between two consecutive edges along the opposite wall. This is the main reason why the mixing of S2 and S3 is more efficient than that of S1.

To sum up, the above interpretation constitutes a step forward in understanding the multiple SEAS flow on mixing.

Micromixing performance

Since S2 appears to be the most effective SEAS mixer, we keep it to evaluate the micromixing performance, using the experimental method detailed above. Figure 9 shows values of X_S (left axis) and t_m (right axis) versus vibration amplitude v_a, for the mixer S2, and for three different flow-rates Q_c. Firstly, as acoustic intensity v_a increases, X_S and t_m sharply drop, which suggests the achievement of better micromixing performance at the molecular scale. The Segregation Index sharply decreases from 0.06 (at v_a=40 mm/s) down to 0.01 under the strongest acoustic intensity (v_a=150 mm/s). Micromixing time based on IEM decreases by a factor of 10: from 0.28 s under

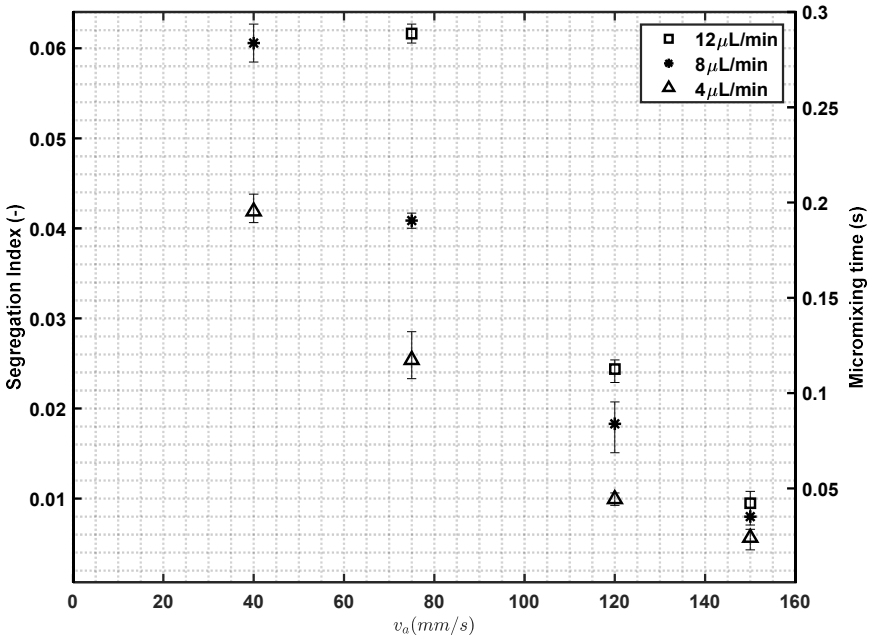

Fig. 9. Micromixing performance of SEAS S2 mixer under different flow-rate and acoustic intensities. Segregation index and Micromixing time are shown respectively at the left- and right-axis. Acoustic intensity is controlled by the input voltage to the piezoelectric actuator, for a range of 10 V, 20 V, 30 V and 40 V, corresponding to acoustic vibration magnitude of v_a from 40-150 mm/s. Error bars are determined by repeated tests for each condition.

mild forcing (v_a=40 mm/s, at 10 V) to 0.03 s under strong acoustic vibration (v_a=150 mm/s at 40 V).

Another influential factor is the flow-rate Q_c. As shown in Figure 9, a lower channel throughput Q_c corresponds to lower X_S and shorter t_m, thus to better micromixing. This results are in agreement with our previous study (Zhang et al. 2019), according to which each SEAS vortex shape and perturbative potential is strongly influenced by the throughput. As Q_c gets higher, the disturbance from the streaming flow on the main one decays, resulting in worse mixing performance. Similarly, the differences of values of X_S and t_m with different throughput are significant. Under weak acoustic field and high throughput, the mixing improvement becomes weak or even negligible.

Notably, the trend of SEAS micromixing performance with respect to Q_c is the opposite to that of passive mixers such as (Commenge and Falk 2011; Falk and Commenge 2010; Guo et al. 2013).

Indeed, passive devices depend on the generation of complex streamlines that in turn can induce Lagrangian chaos. Most often, passive mixers are more efficient under higher throughput.

Micromixing performance comparison with the literature

We now attempt to compare the performance of our micromixers with those of passive mixers on comparable geometries. The review paper (Falk and Commenge 2010) summarized several passive micromixers and proposed a fair agreement between experimental data and a theoretical relation $\frac{t_m}{d_c^2} \sim \frac{ln(Pe)}{Pe}$, with d_c being the characteristic channel dimension. Figure 10 shows the performances of our SEAS mixer S2 with respect to the theoretical line $\frac{t_m}{d_c^2} \sim \frac{ln(Pe)}{Pe}$, with the x-axis being Re. It clearly shows that the SEAS mixer is capable of achieving much faster micromixing that usual passive ones at relatively low Re (lower than one). The quantity t_m/d_c^2 of all tested data ranges from $2\times10^5 s/m^2$ to $6\times10^5 s/m^2$. Comparatively, at this range, mixing without acoustic streaming is almost purely diffusive and t_m/d_c^2 of passive mixers is of the order of molecular diffusion time 1/D, i.e., $0.4\times10^9 s/m^2$ for water.

The energy consumption in the mixing performance improvement is a crucial factor, both for passive and active mixers. In classical passive mixer studies, a well established method consist in using specific energy dissipate rate as an measurement of energy input. The comparison is thus possible with micromixing time obtained from Iodide-Iodate reaction and the specific energy dissipation rate obtained either by experimental pressure loss ΔP or by numerical simulation through CFD (Commenge and Falk 2011). In the case of passive mixers, the specific energy dissipation rate is expressed as ε_p, (in W/kg) given by:

$$\varepsilon_p = \frac{Q_c \cdot \Delta P}{\rho \cdot V} \tag{11}$$

with Q_c the channel volume throughput, m^3/s, V the internal volume of micromixing, including the inlet and outlet tubing parts, m^3, and ΔP pressure loss in Pa. This energy is supposedly exactly balanced by viscous dissipation.

(Commenge and Falk 2011) summarized a large number of micromixing experimental studies

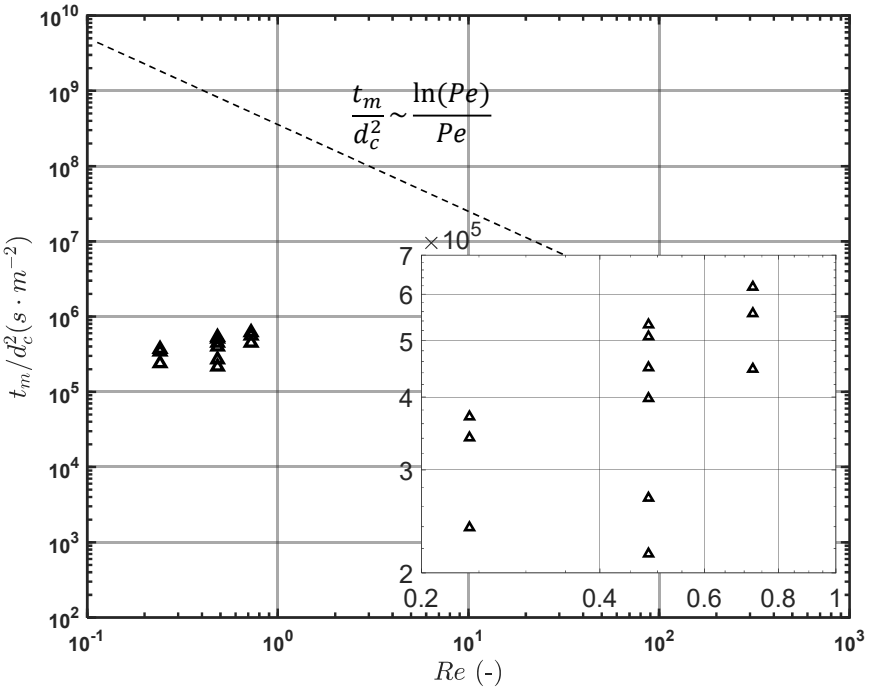

Fig. 10. Quantity t_m/d_c^2 versus channel Reynolds number.

according to which a well established correlation exists between t_m and the specific pumping power dissipation ε_p, see Eq.(12).

$$t_m = 0.15\varepsilon_p^{-0.45} \tag{12}$$

In the case of SEAS mixers, the energy dissipation include both passive (pressure drop) and active mechanisms (acoustic field). The energy dissipation rate (W/kg) thus includes active and passive parts:

$$\varepsilon = \varepsilon_p + \varepsilon_a = \frac{Q_c \Delta P}{\rho V} + \pi f {v_a}^2 sin(4\pi f t) \tag{13}$$

where the first term ε_p represents the energy dissipated into the fluid and is time-independent. The second term $\varepsilon_a = \frac{1}{\rho V}\int_V \partial_t(\frac{1}{2}\rho v_\omega^2)dV = \pi f {v_a}^2 \sin(4\pi f t)$, referring to the definition in (Muller et al. 2012), is estimated as its maximum value $\varepsilon_{a,max} = \pi f {v_a}^2$. More importantly, though, as the characterized length of our SEAS mixer is much smaller than the vibration wavelength in

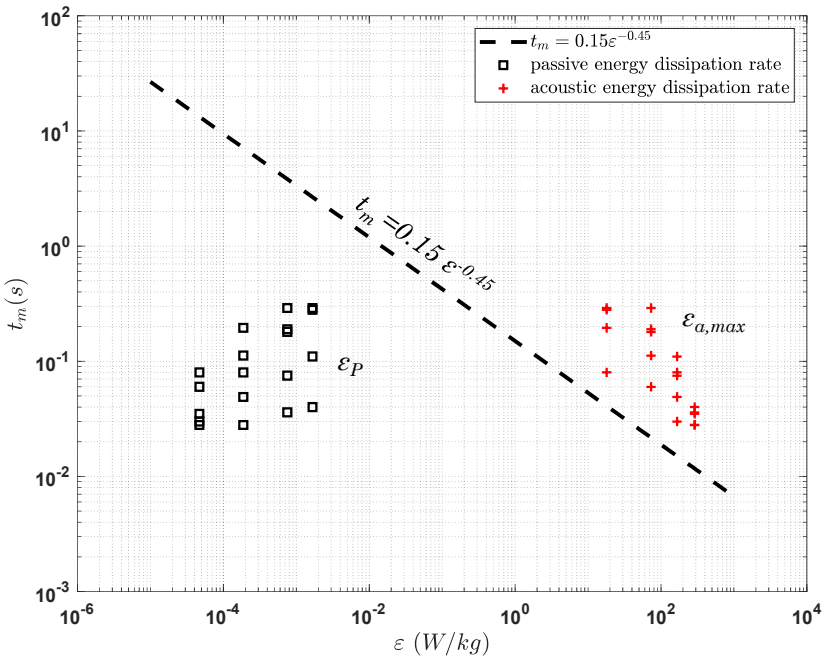

Fig. 11. Micromixing time t_m vs energy dissipation rates ε

kHz-level, acoustic energy is not dissipated into the liquid but travelling through it. It is thus not strictly totally used to enhance the mixing, although it is necessary to generate the streaming. In our estimation, we use numerical pressure drop results (ranging from 71 Pa to 421 Pa, including channel and bending but without the Y part, corresponding throughput Q_c from 2 to 12 µL/min) through the channel to determine the pumping energy dissipation rate ε_p.

Figure 11 gives the relative positioning of our experimental dissipation rate results with respect to the theoretical correlation between t_m and ε. For a micromixing time range t_m = 0.03 to 0.28 s, classic passive mixer would require a specific energy dissipation rate ε from 0.25 to 27 W/kg. With experimental throughputs using SEAS micromixer S2, the viscous dissipation rate ε_p is from 4×10^{-5} to 2×10^{-3} W/kg, far lower than the range of passive mixers. However, as the real mixing enhancement driver, acoustic power with maximal values $\varepsilon_{a,max}$ from 18 to 289 W/kg is necessary. Thus the pressure related dissipation rate in the case of SEAS mixer can be considered negligible compared to the acoustic power. At this stage, as we overestimate the acoustic power, the active

SEAS mixer is not yet competitive with passive mixers in terms of specific energy dissipation rate. The real acoustic energy dissipation rate ε_a should be lower than the values shown in Figure 11, thus closer to passive mixers.

CONCLUSIONS

Acoustic streaming is generated near sharp edges along a microchannel, under low-frequency acoustic wave excitation. The disturbances due to the streaming flow actively enhance the mixing process between two miscible fluids injected at the inlets of a Y-mixer. The micromixing would otherwise be achieved through slow diffusion, due to the low Reynolds number flow - from 0.12 to 0.72. However when SEAS is actuated, the generated vortices strengthen the mixing process. Microchannel SEAS mixer with multiple sharp edges can achieve effective mixing but requires optimal coupling between acoustic streaming and main flow, which is the focus of the current study.

The main findings from our results are:

- With a given microchannel, mixing performance depends on i) acoustic intensity, characterized by acoustic velocity amplitude v_a, which itself depends on the driving input voltage V_{pp}; ii) sharp-edge pattern, including number of sharp edges and pitch distance; and iii) channel throughput Q_c. With V_{pp} increasing from 10 V to 40 V, the best mixing performance using S2 enables X_S and t_m decrease from 0.06 to 0.01 and from 0.28 s to 0.03 s, respectively. SEAS thus achieves much better micromixing performance at high acoustic input. At low acoustic intensity (for instance V_{pp} = 10 V, more sharp edges and lower throughput Q_c are required to achieve relatively low X_S and short t_m.
- From single SEAS microchannel to chip-level micromixer with multiple sharp edges, considering the complex interplay of different parameters underlined in the previous point, a chip-level simulation/experimental study is necessary.
- More specifically, the performance of multiple SEAS micromixers depends on the interaction between the different AS vortices, as well as the specific flow pattern at the upstream of sharp edges; the latter *entrance effect* sometimes plays an important role in the mixing

process.

- In addition, the streamlines patterns confirm the presence of inefficient streaming or dead zones in the case of non-optimal sharp edge design.
- Comparing three different sharp edge patterns, a sufficient number of highly disturbed zigzag flow make SEAS mixer S2 the best in mixing performance. It corresponds to the situation where the ratio of velocities $\frac{v_s}{v_0}$ realises a matching geometrical condition with the pitch between edges and the channel width.
- As an active mixer, a SEAS mixer has better performance at low Re (flow rate) when the residence time is long enough and the vortices disturbance is relatively strong compared to the main flow. With Re lower than 1, we did not observe any passive enhancement effect only due to sharp edges in the channel. Without acoustic actuation, the Reynolds number is too low so that the flow cannot generate significant stretching and folding of the interfacial area between the two fluids. The SEAS mixer thus provides a competitive micromixing solution at low Reynolds regimes.

ACKNOWLEDGEMENTS

We would like to thank the China Scholarship Council for the financial support to the PhD of Chuanyu Zhang.

APPENDIX I. COMPETITIVE IODIDE-IODATE CHEMICAL REACTION AND DATA PROCESSING

Competitive Iodide-Iodate chemical reaction, also named the Villermaux-Dushman method (Fournier et al. 1996), has been extensively used to evaluate micromixing performance of micromixers (Falk and Commenge 2010; Aubin et al. 2010). This reaction scheme is sensitive to mixing at the molecular level through the formation of Iodine (I_2) molecules. This method is based on the competitive parallel reactions involving the neutralization of dihydroborate ions (R1, Eq.14) and a redox reaction (R2, Eq.15):

$$H_2BO_3^- + H^+ \rightleftharpoons 3HBO_3 \tag{14}$$

$$5\,I^- + IO_3^- + 6\,H^+ \rightleftharpoons 3I_2 + 3\,H_2O \tag{15}$$

$$I_2 + I^- \rightleftharpoons I_3^- \tag{16}$$

Once the molecular Iodine is generated (due to ineffective mixing), a equilibrium is established between the iodine and the iodide ion that results in the formation of the tri-iodide ion, I_3^-, through R3 (Eq.16).

Reactions R1 and R3 are quasi-instantaneous; while reaction R2 is by several orders of magnitude slower than the two others. Within a perfect mixing process, the product distribution is solely governed by the chemical kinetics and most H^+ are consumed by $H_2BO_3^-$, resulting in no or very small iodine yields. On the other hand, a significant amount of iodine occurs under a bad mixing conditions, which can be attributed to a local excess of H^+, not only being consumed by reaction R1, but also taking part in the reaction R2 and R3. Under the later condition, tri-iodide appears in the final product and its concentration can characterize the micromixing process. With an absorption peak to ultraviolet (UV) light at a wavelength of 353 nm, the tri-iodide formation

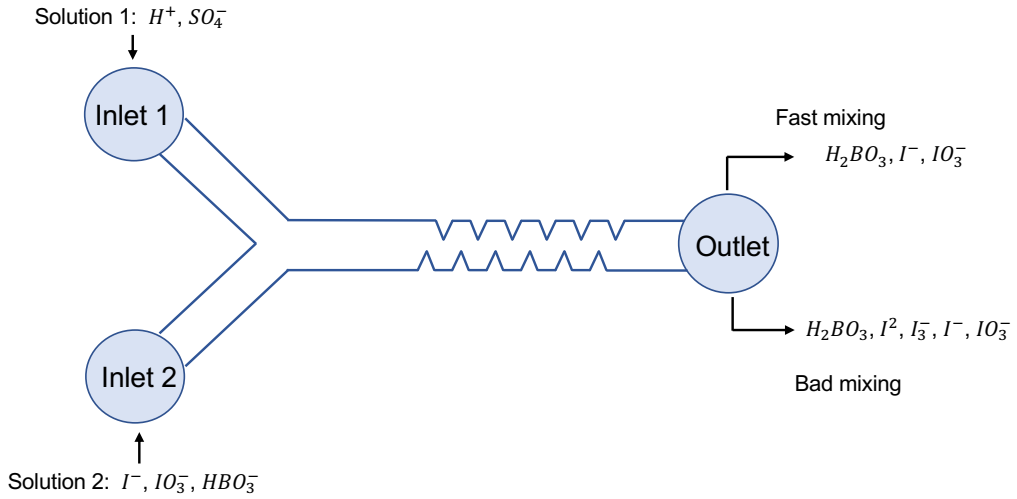

Fig. 12. Sketch of Iodide-Iodate reactions used to micromixing characterization of SEAS micromixers.

can be quantitatively measured by a spectrophotometer. The whole process is thus considered as a chemical probe to assess the micromixing time.

Figure 12 describes the competing reaction mechanism in the case of our SEAS micromixer with two inlets (solution 1 and solution 2, with the same flow-rate). The concentration of H^+ in solution 1 being equivalent or lower than that of $H_2BO_3^-$, all H^+ is consumed by $H_2BO_3^-$ by the rapid reaction R1 as long as the micromixing process is fast. This results in no iodine formation. On the other hand, iodine formation occurs under bad mixing conditions, which can be attributed to a local excess of H^+, not only being consumed by reaction R1, but also taking place in the reaction R2, followed by R3. The concentration of I_3^- is thus positively correlated to the micromixing time.

Beer-Lambert Law

The tri-iodide can be quantified based on the Beer-Lambert Law, which relates the attenuation of light intensity to the absorption properties of materials through which light travels. To determine its concentration from the absorbance unit given by spectrophotometer, we use the classical relation :

$$C_{I_3^-} = A/\epsilon_{353nm} l \tag{17}$$

where A is the Absorbance Unit through the cuvette, (-), ϵ_{353nm} means the molar attenuation coefficient of tri-iodide ions at its peak absorptivity wave-length at 353 nm, $\epsilon_{353nm} = 26047 L/(mol.cm)$, l denotes the optical path length which is $l = 10mm$ in our case.

Calculation of Y and Y_{ST}

Calculation of Y and Y_{ST} from the concentration of reactants as well as that of the tri-iodide yield follows Eqs.18 and 19 (Guo et al. 2013). More specifically, Y is the ratio of acid ion H^+ consumed by reactions R2 and R3 and its initial concentration in the mixture. The quantity C represents the concentration of ions while Q_1 and Q_2 stand for the flow rates of the two solutions, in this study $Q_1 = Q_2$, Y_{ST} is the higher limit of Y in the total segregation case, also based on the initial boric acid and iodate ions concentrations.

$$Y = \frac{2(\mathrm{M}_{I_2} + \mathrm{M}_{I_3^-})}{M_{H^+,0}} = \frac{2(C_{I_2} + C_{I_3^-})(Q_1 + Q_2)}{2C_{H_2SO_4} Q_2} \tag{18}$$

$$Y_{ST} = \frac{6M_{IO_3^-,0}/M_{H_2BO_3^-,0}}{6M_{IO_3^-,0}/M_{H_2BO_3^-,0} + 1} = \frac{6C_{IO_3^-,0} Q_1}{(6C_{IO_3^-,0} + C_{H_2BO_3^-,0})Q_1} \tag{19}$$

With the yield of tri-iodide ions in the final solution, the production of iodine can be determined based on the equilibrium balance of I in R3 Eq.(16):

$$M_{I^-} = M_{I^-,0} - \frac{5}{3}(M_{I_2} + M_{I_3^-}) - M_{I_3^-} \tag{20}$$

$$C_{I^-} = \frac{C_{I^-,0}}{2} - \frac{5}{3}(C_{I_2} + C_{I_3^-}) - C_{I_3^-} \tag{21}$$

with the equilibrium kinetics of reaction R3 given by Eq.(22).

$$-\frac{5}{3}C_{I_2}^2 + (\frac{C_{I^-,0}}{2} - \frac{8}{3}C_{I_3^-})C_{I_2} - \frac{C_{I_3^-}}{K_{eq}} = 0 \tag{22}$$

Then X_S is calculated from Eq.(10).

Reaction kinetics

Thee kinetics for each reaction are listed below (Guichardon and Falk 2000) and they will be used in the IEM model.

$$r_1 = k_1 C_{H^+} C_{H_2BO_3^-} \tag{23}$$

$$r_2 = k_2 C_{H^+}^2 C_{I^-}^2 C_{IO_3^-} \tag{24}$$

$$r_3 = k_{3+} C_{I^-} C_{I_2} - k_{3-} C_{I_3^-} \tag{25}$$

where the k_i stand for the kinetics constants of each reaction. For r_2, fifth-order law are used in the present study. The coefficients k_{3+} and k_{3-} are the forward and reverse reaction rate constants, being respectively equal to $k_{3+} = 5.9 \times 10^9 L \cdot (mol \cdot s)^{-1}$ and $k_{3-} = 7.5 \times 10^6 s^{-1}$ at 25°C.

For reaction R1, as a neutralization reaction, its rate constant is $k_1 = 10^{9.2}$, determined by its acid dissociation constant with Eq.(26).

$$\log_{10}(k_1) = pK_a(H_3BO_3/H_2BO_3^-) = 9.2 \tag{26}$$

The rate constant k_2 of redox reaction R2 is a function of the ion strength μ of ions in the solution. It is determined by Eqs.(28-29) after Eq.(27).

$$\mu = \frac{1}{2}\sum C_i Z_i^2 \tag{27}$$

$$\log_{10}(k_2) = 9.28105 - 3.664\sqrt{\mu} \qquad if\, \mu < 0.166 mol/L \tag{28}$$

$$\log_{10}(k_2) = 8.383 - 1.5115\sqrt{\mu} + 0.23689\mu \qquad if\, \mu >= 0.166 mol/L \tag{29}$$

where C_i and Z_i denotes the concentration and charges of i_{th} specie in the solution.

The equilibrium constant of reaction R3 can be determined by:

$$\frac{\mathrm{C_{I_3^-}}}{\mathrm{C_{I_2}\,C_{I^-}}} = \log_{10}(k_{eq}) = \log_{10}\frac{k_{3+}}{k_{3-}} = \frac{555}{T} + 7.355 - 2.575\log_{10} T \tag{30}$$

where T is temperature in Kelvin. At 25 °C, $k_{eq} = 698 L \cdot mol^{-1}$.

APPENDIX II. DETERMINATION OF MICROMIXING TIME

Interaction by Exchange with the Mean (IEM) model is usually used to build up the relation between Segregation Index and micromixing time. The IEM allows the estimation of the micromixing time (Guo et al. 2013; Falk and Commenge 2010), and makes them independent of the choice of concentration of reactants (Commenge and Falk 2011). The comparison of mixing results is thus possible. One prerequisite of using IEM model is that the residence time of the two solutions from the initial contact and along flow direction being the same. Our sharp edge Y-mixer satisfies this requirement. Besides, another assumption in this model is that the exchange of ions between two solutions occurs at a same micromixing time t_m, which is generally true for microchannel continuous mixers.

At every time step, IEM considers that the concentration of each solution evolves separately and is governed by the following equations:

$$\frac{dC_{k,1}}{dt} = \frac{\overline{C} - C_{K,1}}{t_m} + R_{k,1} \tag{31}$$

$$\frac{dC_{k,2}}{dt} = \frac{\overline{C} - C_{K,2}}{t_m} + R_{k,2} \tag{32}$$

$$\overline{C} = \alpha_v C_{k,1} + (1 - \alpha_v) C_{k,2}, \tag{33}$$

where the coefficient $C_{k,1,2}$ represent the concentration for specie k in solution 1 and 2, mol/L; t_m is the exchange time constant, considered as the micromixing time, s; $R_{k,1,2}$ denotes the change rate of the concentration for species k in solution 1 and 2, $mol/(L \cdot s)$; α_v the volume flow proportion of solution 1, in our case $\alpha_v = 0.5$.

With a given t_m and known initial concentrations of ions, the differential equations can be numerically integrated based on the second-order Runge-Kutta method or an equivalent one, to determine the final concentration $C_{I_3^-}$ and then the value for X_S. For each step, the concentrations and their corresponding mean values, kinetic data are updated by the results from the previous step. The iteration process moves forward step by step until the concentration of H^+ in the solution

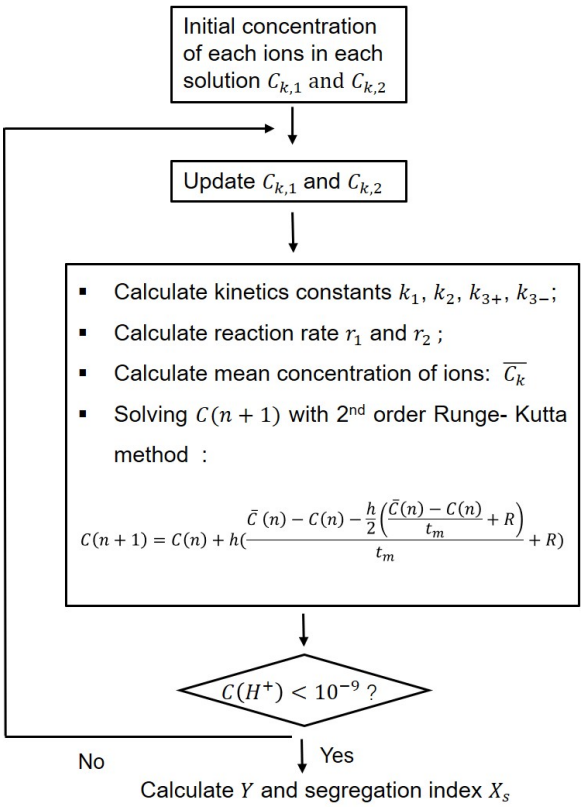

Fig. 13. Algorithmic steps for identifying the relationship between X_S and t_m using IEM model

decrease under a lower threshold value ($10^{-9} mol/L$ in this study). After, H^+ is considered to approach zero and the reactions end. With $C_{I_3^-}$, X_S can be calculated accordingly. An algorithm has been built in Matlab to relate the segregation index with the micromixing time in a large range. This procedure and the resulting relation between X_S and t_m under the concentration condition are shown respectively in Figures 13 and 14. As a result, for each micromixing tests, the segregation index and the corresponding micromixing time can be quantified.

Special attention should be paid on the iteration time step h. On the one hand, the step h should be small enough to avoid unrealistic negative concentrations due to global consumption of ions in the reactions; on the other, a too short time step requires heavier computing costs. In this study, h is kept constant as $10^{-8} s$.

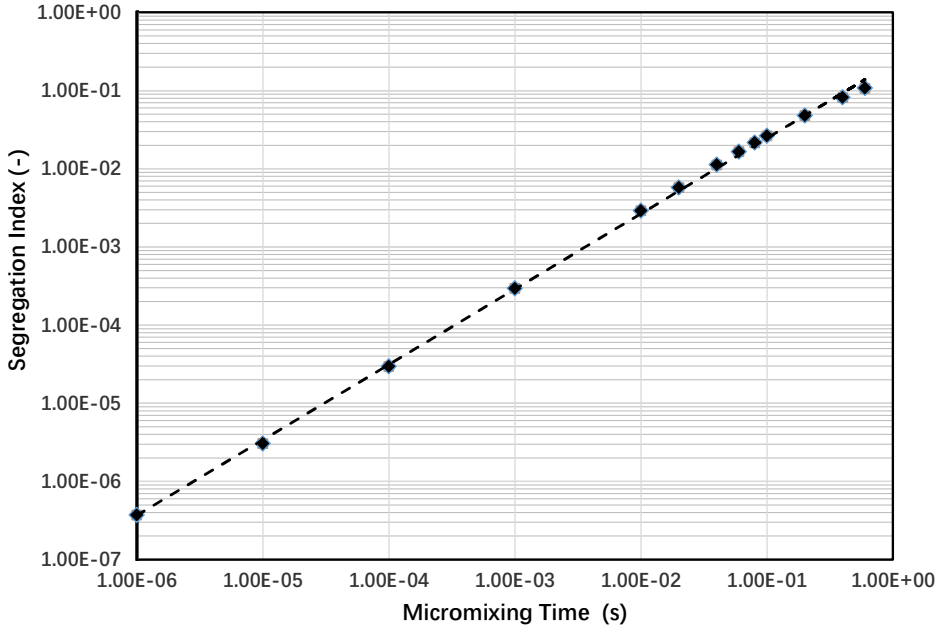

Fig. 14. Segregation index X_S versus micromixing time t_m, for given values of concentrations in Table 1.

APPENDIX III. NOTATION

The following symbols are used in this paper:

Quantity	Abbreviation
Absorbance unit from spectrophotometry	A
Tip angle of sharp edge	α
Height of the sharp edge	h
Width of microchannel	w
Distance between the tip of two consecutive edges on the same side	d
Number of the sharp edges on one side	n_s
Kinematic viscosity	ν
Diffusivity	D
Acoustic vibration velocity	$\mathbf{v}_\omega$
Amplitude of vibration velocity	$\mathbf{v}_a$
Streaming velocity	$\mathbf{v}_s$
Amplitude of vibration velocity at boundary	$\mathbf{v}_{ab}$
Boundary velocity corresponding to channel throughput	$\mathbf{v}_{0b}$
Maximum streaming velocity along y direction	$\mathbf{v}_{sm}$
Concentration	C
Resonance frequency	f
Angular frequency	ω
Molar quantity of reactants or ions	M
Characteristic channel dimension	d_c
Inlet flow rate	Q_c
Peak to peak voltage	V_{pp}
Segregation Index	X_S
Micromixing time	t_m
Pumping energy dissipation rate	ε_p
Acoustic energy dissipation rate	ε_a
Péclet number	Pe
Reynolds number	Re

REFERENCES

Aubin, J., Ferrando, M., and Jiricny, V. (2010). "Current methods for characterizing mixing and flow in microchannels.." Chemical Engineering Science, 65(6), 2065–2093.

Bachman, H., Chen, C., Rufo, J., Zhao, S., Yang, S., Tian, Z., Nama, N., Huang, P.-H., and Huang, T. J. (2020). "An acoustofluidic device for efficient mixing over a wide range of flow rates." Lab on a Chip, 20(7), 1238–1248.

Bruus, H. (2012). "Acoustofluidics 10: Scaling laws in acoustophoresis." Lab on a Chip, 12(9), 1578.

Commenge, J.-M. and Falk, L. (2011). "Villermaux–Dushman protocol for experimental character-

ization of micromixers." Chemical Engineering and Processing: Process Intensification, 50(10), 979–990.

DeMello, A. J. (2006). "Control and detection of chemical reactions in microfluidic systems." Nature, 442(7101), 394–402.

Doinikov, A. A., Gerlt, M. S., and Dual, J. (2020a). "Acoustic Radiation Forces Produced by Sharp-Edge Structures in Microfluidic Systems." Physical Review Letters, 124(15), 154501.

Doinikov, A. A., Gerlt, M. S., Pavlic, A., and Dual, J. (2020b). "Acoustic streaming produced by sharp - edge structures in microfluidic devices." Microfluidics and Nanofluidics, 1–13.

Falk, L. and Commenge, J. M. (2010). "Performance comparison of micromixers." Chemical Engineering Science, 65(1), 405–411.

Fournier, M. C., Falk, L., and Villermaux, J. (1996). "A new parallel competing reaction system for assessing micromixing efficiency - Experimental approach." Chemical Engineering Science, 51(22), 5053–5064.

Guichardon, P. and Falk, L. (2000). "Characterisation of micromixing efficiency by the iodide–iodate reaction system. Part I: experimental procedure." Chemical Engineering Science, 55(19), 4233–4243.

Guo, X., Fan, Y., and Luo, L. (2013). "Mixing performance assessment of a multi-channel mini heat exchanger reactor with arborescent distributor and collector." Chemical Engineering Journal, 227(0), 116–127.

Guo, X., Fan, Y., and Luo, L. (2014). "Multi-channel heat exchanger-reactor using arborescent distributors: A characterization study of fluid distribution, heat exchange performance and exothermic reaction." Energy, 69(0), 728–741.

Hossain, S., Husain, A., and Kim, K. Y. (2010). "Shape optimization of a micromixer with staggered-herringbone grooves patterned on opposite walls." Chemical Engineering Journal, 162(2), 730–737.

Huang, P.-H., Xie, Y., Ahmed, D., Rufo, J., Nama, N., Chen, Y., Chan, C. Y., and Huang, T. J. (2013). "An acoustofluidic micromixer based on oscillating sidewall sharp-edges." Lab on a

Chip, 13(19), 3847.

Hutchisson, E. and Morgan, F. B. (1931). "An experimental study of Kundt's tube dust figures." Physical Review, 37(9), 1155–1163.

Leaist, D. G. (1988). "The effects of aggregation, counterion binding, and added NaCl on diffusion of aqueous methylene blue." Canadian Journal of Chemistry, 66(9), 2452–2457.

Lei, J., Glynne-Jones, P., and Hill, M. (2013). "Acoustic streaming in the transducer plane in ultrasonic particle manipulation devices." Lab on a Chip, 13(11), 2133.

Li, W., Xia, F., Qin, H., Zhang, M., Li, W., and Zhang, J. (2019). "Numerical and experimental investigations of micromixing performance and efficiency in a pore-array intensified tube-in-tube microchannel reactor." Chemical Engineering Journal, 370, 1350–1365.

Li, Z. and Kim, S. J. (2017). "Pulsatile micromixing using water-head-driven microfluidic oscillators." Chemical Engineering Journal, 313, 1364–1369.

Lighthill, S. I. R. J. (1978). "ACOUSTIC STREAMINGt." Journal of Sound And Vibration, 61(April), 391–418.

Luo, Y., Luo, J. Z., Yue, X. J., Song, Y. J., Chu, G. W., Liu, Y., Le, Y., and Chen, J. F. (2018). "Feasibility studies of micromixing and mass-transfer in an ultrasonic assisted rotating packed bed reactor." Chemical Engineering Journal, 331, 510–516.

Muller, P. B., Barnkob, R., Jensen, M. J. H., and Bruus, H. (2012). "A numerical study of microparticle acoustophoresis driven by acoustic radiation forces and streaming-induced drag forces." Lab on a Chip, 12(22), 4617–4627.

Nama, N., Huang, P. H., Huang, T. J., and Costanzo, F. (2016). "Investigation of micromixing by acoustically oscillated sharp-edges." Biomicrofluidics, 10(2).

Ovchinnikov, M., Zhou, J., and Yalamanchili, S. (2014). "Acoustic streaming of a sharp edge." The Journal of the Acoustical Society of America, 136(1), 22–29.

Ozcelik, A., Ahmed, D., Xie, Y., Nama, N., Qu, Z., Nawaz, A. A., and Huang, T. J. (2014). "An acoustofluidic micromixer via bubble inception and cavitation from microchannel sidewalls." Analytical Chemistry, 86(10), 5083–5088.

Qin, H., Zhang, C., Xu, Q., Dang, X., Li, W., Lei, K., Zhou, L., and Zhang, J. (2017). "Geometrical improvement of inline high shear mixers to intensify micromixing performance." Chemical Engineering Journal, 319, 307–320.

Rayleigh, J. W. S. (2013). The Theory of Sound, Volume One. Dover Publications, <http://cds.cern.ch/record/105679>.

Setareh, M., Saffar-Avval, M., and Abdullah, A. (2020). "Heat transfer enhancement in an annulus under ultrasound field: A numerical and experimental study." International Communications in Heat and Mass Transfer, 114, 104560.

Stroock, A. D., Dertinger, S. K., Ajdari, A., Mezić, I., Stone, H. A., and Whitesides, G. M. (2002). "Chaotic mixer for microchannels." Science, 295(5555), 647–651.

Vainshtein, B. P. (1995). "Rayleigh streaming at large Reynolds number and its effect on shear flow." 285, 249–264.

Zhang, C., Guo, X., Brunet, P., Costalonga, M., and Royon, L. (2019). "Acoustic streaming near a sharp structure and its mixing performance characterization." Microfluidics and Nanofluidics, 23(9), 104.

Zhang, C., Guo, X., Royon, L., and Brunet, P. (2020a). "Acoustic Streaming Generated by Sharp Edges: The Coupled Influences of Liquid Viscosity and Acoustic Frequency." Micromachines, 11(6), 607.

Zhang, C., Guo, X., Royon, L., and Brunet, P. (2020b). "Unveiling of the mechanisms of acoustic streaming induced by sharp edges.